The Pennsylvania State University

The Graduate School

College of Earth and Mineral Sciences

INDUCED MICROEARTHQUAKES AND SEISMICITY-PERMEABILITY RELATIONSHIPS IN FRACTURES

A Dissertation in

Energy and Mineral Engineering

by

Yi Fang

Submitted in Partial Fulfillment
of the Requirements
for the Degree of

Doctor of Philosophy

December 2017

The dissertation of Yi Fang was reviewed and approved by the following:

Derek Elsworth
Professor of Energy and Mineral Engineering and Professor of Geosciences
Dissertation Advisor
Chair of Committee

Chris Marone
Professor of Geosciences
Associate Director of Institute for Natural Gas Research at Pennsylvania State University

Tong Qiu
Associate Professor of Civil and Environmental Engineering

Shimin Liu
Assistant Professor of Energy and Mineral Engineering

Luis F. Ayala H.
Professor of Petroleum and Natural Gas Engineering
Associate Department Head for Graduate Education of Energy and Mineral Engineering

*Signatures are on file in the Graduate School

Dedicated to my beloved wife Zihan Ye

携爱而行，倾我所有
携梦而行，唯我所愿

ABSTRACT

In the past several years, induced microearthquakes (MEQs) related to energy development projects have garnered public attention. Large-scale fluid injection in geoengineering activities, such as enhanced geothermal reservoir stimulation, geological storage of CO_2, shale reservoir stimulation, and deep disposal of wastewater can generate significant fluid overpressures and induce microearthquakes by reactivating preexisting faults and fractures that are widely distributed throughout the upper crust. The monitoring of fluid-injection-induced microearthquakes can provide significant information (*e.g.*, timing, special distribution, and moment magnitude) in evaluating reservoir development (*e.g.*, fracture distribution and reservoir hydraulic conductivity evolution), in informing production strategies (*e.g.*, accommodation of production wells), and in assessing the risks of fluid injection activities (*e.g.*, caprock integrity of CO_2 reservoir). The following questions are addressed in this study: (1) what are the mechanisms and implications of in-situ feedbacks (*e.g.*, monitored fluid-injection-induced MEQs distribution, seismic moment magnitudes, and fracture behaviors) in geothermal stimulation? (2) What information can be derived from MEQs to inform geothermal reservoir stimulation strategies? (3) Are there any potential relationships between induced seismic or aseismic slip and permeability evolution of fractures in such unconventional reservoirs and caprocks? (4) What factors play an important role in controlling these relationships? These questions are addressed in the five individual chapters of this thesis.

Chapter 1 describes a case study of anomalous MEQs distribution: A bimodal depth distribution of fluid-injection-induced MEQs was observed in the 2012 stimulation phase of the Newberry Volcano EGS Demonstration project in Oregon, US. During 7 weeks of hydraulic stimulation of well NWG 55-29, 90% of MEQs occurred in the shallow reservoir (~500 m to

~1800 m), only a few occurred adjacent to the bottom of the open borehole (~2500 m to ~3000 m) while almost no seismicity was observed in the intervening interval (~1800 m to ~2500 m). Our analysis of frictional stability using spatial models for fluid pressure diffusion of injected fluids shows that the distribution of MEQs is consistent with observed casing damage, and a possible leak at ~700 m, and is inconsistent with migration of fluids from the casing shoe. The role of fluid injection through the ruptured casing is further supported by the analyses of shear failure and pore-pressure diffusion. Finally, the absence of seismicity at intermediate depths is consistent with our laboratory determinations of frictional stability, showing velocity strengthening frictional behavior for samples from intermediate depths, bracketed by velocity neutral and weakening behavior for samples from shallower and greater depths.

Chapter 2 introduces a method to constrain the evolution of fracture permeability at sufficiently fine resolution with observed *in-situ* MEQs data to define reservoir response. In this method, we propose a model that couples the moment magnitude to fracture aperture and then estimates the reservoir permeability at relatively high resolution. The critical parameters controlling fracture aperture and permeability evolution are stress-drop, the bulk modulus of the fracture embedded matrix, and the dilation angle of fractures. We employ *Oda*'s crack tensor theory and a cubic-law based analog to estimate the permeability of a synthetic fractured reservoir at various scales, demonstrating that the resolution of permeability is largely determined by the cellular grid size. Finally, we map the *in-situ* permeability of the Newberry EGS reservoir using observed MEQs during two rounds of reservoir stimulations in 2014. The equivalent mean permeability evaluated by each method is consistent and unlimited by representative elementary volume (REV) size. With identical parameters, *Oda*'s crack tensor theory produces a more accurate estimation of permeability than that of the cubic law method, but estimate differences are within one order of magnitude. The permeability maps show that the most permeable zone is located within the zone of most dense seismicity providing a reference for the siting of the

production well. This model has the potential for mapping permeability evolution from MEQs data in conventional and unconventional reservoirs and at various scales.

However, the impact of induced seismicity on fracture permeability evolution remains unclear due to the spectrum of modes of fault reactivation (*e.g.*, stable vs. unstable). To better understand the hydro-mechanical behavior of reservoir due to stimulation, it becomes essential to understand the fundamental relationship between induced seismic and aseismic slip and permeability evolution of a fracture. As seismicity is controlled by the frictional response of fractures, **Chapter 3** reports the results of experimental study of friction-stability-permeability relationships through the concurrent measurement of frictional and hydraulic properties of artificial fractures in Green River shale (GRS) and Opalinus shale (OPS). We observe that carbonate-rich GRS shows higher frictional strength but weak neutral frictional stability. The GRS fracture permeability declines during shearing while an increased sliding velocity reduces the rate of permeability decline. By comparison, the phyllosilicate-rich OPS has lower friction and strong stability while the fracture permeability is reduced due to the swelling behavior that dominates over the shearing induced permeability reduction. Hence, we conclude that the friction-stability-permeability relationship of a fracture is largely controlled by mineral composition, and that shale mineral compositions with strong frictional stability may be particularly subject to permanent permeability reduction during fluid infiltration.

Chapter 4 extends previous studies to explore frictional stability-permeability relationships of fractures and identify the role of mineralogy (*i.e.*, tectosilicate, carbonate, and phyllosilicate content). In this study, we perform a series of direct-shear experiments on saw-cut fractures of natural rocks and sintered fractures with distinct mineralogical compositions. Our experimental results indicate that the friction-permeability relationship is controlled by mineralogy. Frictional strength and change in permeability both decrease with an increase in either phyllosilicate or carbonate content as frictional instability (a-b) increases. With this

relationship, we speculate that planar fractures with low frictional stability exhibit permeability enhancement after seismic slip in the frame of rate-state friction theory. This relationship implies a new mechanical-hydro-chemical (MHC) coupling loop *via* a linkage of frictional properties, mineralogy, and permeability.

Previous experiments suggest that frictional strength and stability are primarily controlled by the mineralogical content of fracture material. The permeability of smooth fractures declines monotonically with displacement due to the generation of wear products. **Chapter 5** investigates the effect of roughness on permeability evolution and frictional behavior using artificially fabricated fractures with specified roughness features. The experimental results show that (1) both smooth and rough fracture surfaces exhibit velocity strengthening frictional behavior for small net displacement and evolves to velocity neutral and velocity weakening with greater displacement. (2) Rougher surfaces exhibit higher velocity strengthening frictional behavior and higher frictional strength due to the presence of cohesive interlocking asperities during shearing. Seismicity may not be induced on rough fracture surfaces. (3) The roughness pattern exerts a dominant control on permeability evolution over the entire shearing history. Permeability evolves monotonically for smooth fractures but in a fluctuating pattern for highly roughened fractures. A higher roughness is likely to result in alternating compaction and dilation during shearing. Significant permeability damage may occur for rough samples when asperities are highly worn with wear products blocking fluid pathways. (4) There is no obvious correlation between permeability evolution and frictional behavior for rough fracture samples when fractures are subject to sudden sliding velocity change. Implications of our lab-scale experimental results suggest that characterization of fracture geometry would be beneficial for better understanding and managing induced seismicity and permeability development.

In shale reservoir stimulation, fractures are propped to increase the permeability of the formation. On the other hand, the proppants may also influence the frictional strength

of fractures. Thus, in the appendix, we explore the evolution of friction and permeability of a propped fracture using shearing-concurrent measurements of permeability during constant velocity shearing experiments. We observe that (1) the frictional response is mainly controlled by the normal stress and proppant thickness. High normal stress results in the crushing of proppant particles although this change in particle size distribution has almost no impact on the frictional response of the proppant-fracture system. The depth of shearing-concurrent striations on fracture surfaces suggests that the magnitude of proppant embedment is controlled by the applied normal stress. Moreover, under high normal stress, the reduced friction implies that shear slip is more likely to occur on propped fractures in deeper reservoirs. The increase in the number of proppant layers, from mono-layer to triple-layers, significantly increases the friction of the propped fracture due to the interlocking of the particles and jamming, suggesting that high proppant density during emplacement would help stabilize the fractures during injection. (2) Permeability of the propped fracture is mainly controlled by the magnitude of the normal stress, the proppant thickness, and the proppant size. Permeability of the propped fracture decreases during shearing due to proppant particle crushing and related clogging. Compared to the multi-layered specimen, the mono-layer case which has fewer displacement degrees-of-freedom exhibits the smallest initial permeability due to proppant embedment. Proppants are prone to crushing if the shear loading evolves concurrently with the normal loading. These combined conclusions suggest that the use of high-density proppants not only provides high hydraulic conductivity for hydrocarbon production but may also help to mitigate the risk of induced seismicity.

The chapters of this thesis correspond with a series of six papers either published or in-submittal.

By order of chapter appearance, these papers are (*: corresponding author):

1) **Fang, Y*.**, S.M. den Hartog, D. Elsworth, C. Marone, and T.T. Cladouhos. 2016. Anomalous Distribution of MEQs in Geothermal Reservoir: Mechanisms and Implications. *Geothermics*. Vol. 63, p. 62-73.

2) **Fang, Y*.**, D. Elsworth, and T.T. Cladouhos. 2017. Reservoir Permeability Mapping using MEQ Data. *Geothermics* (In Revision)

3) **Fang, Y*.**, D. Elsworth, C. Wang, and T. Ishibashi, and J.P. Fitts. 2017. Frictional Stability-Permeability Relationships for Fractures in Shales. *J. Geophys. Res. Solid Earth*. DOI: 10.1002/2016JB013435

4) **Fang, Y***., D. Elsworth, C. Wang, and Y. Jia. 2017. Mineralogical controls on frictional strength, stability and shear permeability of fractures. (*Submitted to JGR*)

5) **Fang, Y***., D. Elsworth, T. Ishibashi, and F. Zhang. 2017. Investigation of permeability evolution and frictional behavior on fabricated fractures with specified roughness features. (*Submitted to JGR*)

6) Zhang, F., **Y. Fang***, D. Elsworth, C. Wang, and X. Yang. 2017. Evolution of friction and permeability in a propped fracture under shear. (*Submitted to Geofluids*)

TABLE OF CONTENTS

LIST OF FIGURES

LIST OF TABLES

ACKNOWLEDGEMENTS

"*Three passions, simple but overwhelmingly strong, have governed my life: the longing for love, the search for knowledge, and unbearable pity for the suffering of mankind.*"

Bertrand Russell (1872-1970)

Since I was an undergraduate student, these simple but powerful passions have encouraged me to pursue my degrees, search the unknown and become a better human being.

Having been in Penn State for four years, I am greatly indebted to a number of people who have provided me with unparalleled support, advice, and encouragement throughout the process of developing this thesis. It is with sincere gratitude that I appreciate for everything they have done to assist me in the most ambitious endeavor of my career thus far.

Frist, I would like to express my deepest gratitude to my Ph.D. supervisor, Professor Derek Elsworth, who provided me this invaluable opportunity to work with him and conduct this exciting study. This thesis would not have been possible without his insightful guide and timely help. He is always positive and energetic and is always ready for a new adventure, which has tremendously inspired me to take challenges and to work hard. His enthusiasm and curiosity for science and engineering has motivated me throughout my time at Penn State. Despite his very busy schedule, he has always been keen on sharing his experience and suggesting fascinating ideas and concepts to work on. In addition, I am particularly grateful for the collaborative atmosphere, and abundant opportunities he provided with me to present this work in many conferences, such as ARMA, AGU and GSA. Even more, he is always the person I can turn to when I need help. I am beyond my words in gratitude; thank you is not enough but it is all I have.

I would like to thank Professor Chris Marone, who provided tremendous help and guidance on my research, which significantly improved my experimental methods. I would also

like to thank the other members of my thesis committee – Professor Tong Qiu, and Professor Shimin Liu for their very helpful conversations, feedback, and professional advice.

The journey of pursuing my Ph.D. degree has been inspiring, and at times it was also very intense and frustrating. In this journey, I must thank my unbelievably supportive wife, Zihan Ye. Without her, it would be more difficult for me to make it and I would be a different person today, and this thesis work would likely not have been realized. Being with her, I know who I am, I know what I am striving for. She always kept me in check and helped me stay focused. Thank you for your unconditional love and for motivating me to chase my dream, to keep reaching for excellence.

I also would like to thank my past and present colleagues in the G3 center who have offered me invaluable friendship, unlimited help, and have shared the insightful research discussions: Sabine den Hartog, Takuya Ishibashi, Jeff Fitts, Fengshou Zhang, Chaoyi Wang, Kyungjae Im, Yunzhong Jia, Kasparas Spokas, Sheng Zhi, Jiehao Wang, Taha Husain, Shugang Wang, Xiang Li, Quan Gan and John Leeman. I appreciated their time and help contributing to my Ph.D. research. I am also grateful to our geomechanics laboratory manager Mr. Steven Swavely, who spent great efforts improving the experimental apparatus and ordering the experimental materials for me. Finally, I want to specially thank Dr. Yanhui Han and Professor Younane Abousleiman who provided me with tremendous help during my summer intern at Houston Aramco Research Center.

Last, but never least, I would like to thank my parents Mr. Jinguo Fang and Ms. Qingtao Yang, and my parents in-law. Without their moral support, I might not be courageous enough to overcome all the difficulties I face during these four years at Penn State.

"*Now this is not the end. It is not even the beginning of the end. But it is, perhaps, the end of the beginning.*"

Sir Winston Churchill (1874-1965)

Chapter 1

Anomalous Distribution of Microearthquakes in the Newberry Geothermal Reservoir: Mechanisms and Implications

Abstract

Stimulation of enhanced geothermal system (EGS) reservoirs by fluid injection can enhance the reservoir permeability but may also result in undesired microearthquakes (MEQs). A bimodal depth distribution of fluid-injection-induced MEQs was observed in the 2012 stimulation phase of the Newberry Volcano EGS Demonstration project in Oregon, US. During 7 weeks of hydraulic stimulation of well NWG 55-29, 90% of MEQs occurred in the shallow reservoir (~ 500 m to ~1800 m), only a few occurred adjacent to the bottom of the open borehole (~ 2500 to ~3000 m) while almost no seismicity was observed in the intervening interval (~1800 m to ~2500 m). Our analysis of frictional stability using spatial models for fluid pressure diffusion of injected fluids show that the distribution of MEQs is consistent with observed casing damage, and a possible leak at ~ 700 m, and is inconsistent with migration of fluids from the casing shoe. The role of fluid injection through the ruptured casing is further supported by the analyses of shear failure and pore-pressure diffusion. Finally, the absence of seismicity at intermediate depths is consistent with our laboratory determinations of frictional stability, showing velocity strengthening frictional behavior for samples from intermediate depths, bracketed by velocity neutral and weakening behavior for samples from shallower and greater depths.

Keywords: Fluid-injection-induced microearthquakes, Anomalous distribution, frictional stability

1. Introduction

Enhanced Geothermal Systems (EGS) technology has great potential to utilize Earth's vast thermal resources to meet the world's growing need for energy. Since natural-fractured, high-temperature geothermal systems do not necessarily have high permeability for efficient fluid circulation, they are typically stimulated via hydroshearing to recover geothermal energy sustainably and economically. Hydroshearing is achieved by injecting water at a stimulation pressure that is above the local hydrostatic pore-pressures but below the minimum principal stress. This process induces shear failure of preexisting fractures and self-propped Mode II or Mode III cracks, resulting in zones of enhanced permeability in otherwise typically low permeability crystalline rock (Evans et al., 2005; Tester, 2007). The resulting increased heat exchange area and residence time of injected fluids allows these fluids to reach optimum production temperature (Hubbert and Rubey, 1959; Majer and Peterson, 2007), increasing the production of geothermal energy.

A drawback of the hydroshearing technique is that the elevated pore-pressures during fluid injection can induce low magnitude (M_w) microearthquakes (MEQs) in the reservoir where faults are absent in the stimulated region (Bachmann et al., 2011; Majer et al., 2007; Zoback and Harjes, 1997). Additionally, the short-term thermal cooling of the hot reservoir rock and long-term chemical interactions between the rock and the circulating fluid can also induce shear failure or even tensile failure, further enhancing the occurrence of MEQs (Elsworth and Goodman, 1986; Rutqvist et al., 2008). Clearly, the occurrence of MEQs is the result of complex coupled thermal-hydro-mechanical-chemical processes during the development of EGS.

MEQs, while posing a threat to public acceptance of EGS, provide crucial feedback on the progress of subsurface activities in EGS reservoir stimulation (e.g., crack propagation, permeability evolution, and temperature changes (Izadi and Elsworth, 2013; Majer et al., 2007).

Particularly, the spatial distribution and timing of MEQs are of significance, potentially providing reliable constraints on the progress and effectiveness of stimulation, guiding optimum production of the reservoir, and ensuring the economic maintenance of reservoir life. Of particular interest in this respect are EGS sites where the seismicity distribution is anomalous. Such an anomalous distribution of MEQs was observed in an EGS Demonstration Project at Newberry Volcano, Oregon that has been operated by *AltaRock Energy Inc*. since 2009. The stimulation well (NWG 55-29) of the Newberry EGS system consists of a cased portion to ~1800 m depth followed by an open section to ~3000 m depth and was stimulated in 2012 by fluid-injection. In contrast to the expected MEQ distribution adjacent to the borehole along its entire open zone (**Figure 1-1a**) - including the widely observed progressive movement to greater depths of induced seismicity with time (Fehler, 1989), - the seismicity at the Newberry Geothermal Reservoir exhibited a bimodal depth distribution of MEQs (**Figure 1-1b**). During the seven weeks of hydraulic stimulation, a few MEQs occurred adjacent to the bottom of the open hole (within the initial 4 days) while almost no seismicity was observed in the principal stimulation zone (~1800 m to ~2500 m depth). Anomalously, 90% of the MEQs occurred above the casing shoe (at depths between 500m and 1800m over the next 46 days) adjacent to the cased portion of the well.

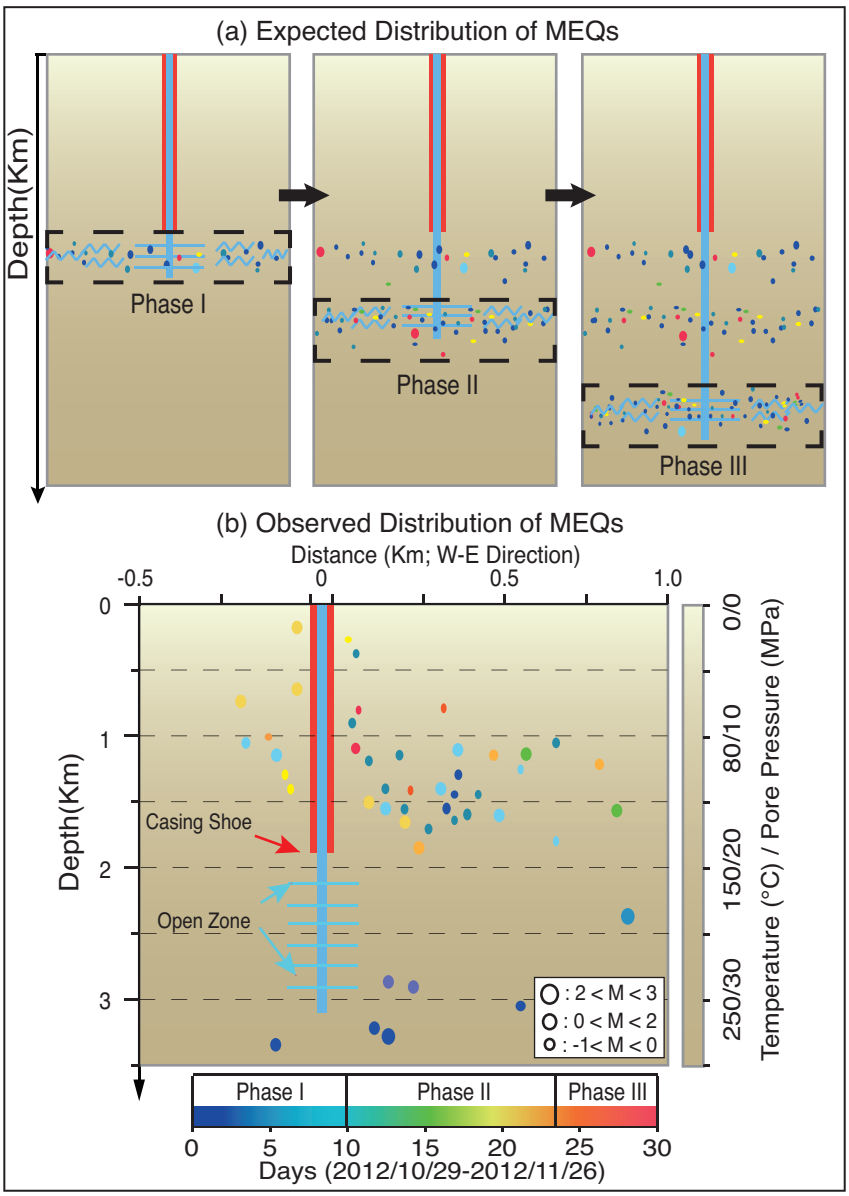

Figure **1-1**: 2012 stimulation of Well NWG 55-29 was completed through three phases. (a) Expected distribution pattern of MEQs in each of stimulation phase. (b) Observed distribution of MEQs, showing both spatial and temporal anomalies.

We propose that the enigmatic distribution of MEQs during the stimulation may have resulted from two alternative causes: (1) Fluid injection through a leak in the casing. A segment of the casing may have been damaged in the shallow reservoir. The resulting leak would have introduced fluid overpressures and thermal stresses that could reactivate fractures. This fluid diversion in the wellbore would reduce pressures in the deep borehole (~1800 to ~3000 m depth)

and staunch the potential for hydroshearing. Alternatively, (2) the shallow casing leak may have been minimal, but migration of the injected fluid from the casing shoe (~1800 m depth) to the shallow zone (~500 m to ~1800 m depth) triggered local seismic events that began after ~5 days - again as a result of elevated pore-pressures and thermal stress.

In this study, we employ both brittle failure analyses and friction experiments to explore the mechanisms behind and implications of the observed anomalous spatial and temporal distribution of seismicity at the Newberry geothermal reservoir. Our results suggest that the bimodal seismicity distribution is due to leakage from the well at shallow depth. Moreover, we show that the absence of seismicity at intermediate depths cannot be explained by the observed stress and presumed stability regime but is consistent with alternate distributions of frictional strength and stability.

We begin with a description of the geological setting of the Newberry Geothermal Reservoir. Next, we provide the rationale behind and approach of various analyses that we conducted to obtain insight into the cause of the anomalous distribution of seismicity in the Newberry Geothermal Reservoir. Our analysis consists of four consecutive steps: we (i) define the controls on frictional stability within the shallow crust, (ii) define the anticipated timing of these events if driven by fluid migration, (iii) use the depth-stability analysis to show that if MEQs occur at depth, then they should also be present at all depths, and then (iv) explore reasons for the missing seismicity through inferred strain-hardening/velocity-strengthening behavior, constrained by experimental characterization. We assume constant frictional properties in efforts (i)-(iii) and test this assumption via the shear experiments (part (iv)). In addition, throughout theoretical analyses (i-iii), we adopt the in-situ stresses and pore-pressures as estimated in the geological setting and treat these quantities as constants.

2. Geological Setting and Methods

2.1 Geological Setting

The Newberry Volcano has been active for 0.5 Myr and is located in Deschutes County, Oregon, ~ 40 km south of Bend and ~ 56 km east of the crest of the Cascade Range. Well NWG 55-29 cuts through a thick flat-lying sequence of tuffs and reaches a depth of ~3km west of the caldera rim of Newberry Volcano (**Figure 1-2a**) (Cladouhos et al., 2011). Neither ring fractures nor faults transect the stimulated injection well (Davatzes and Hickman, 2011), eliminating the possibility of vertical conduits to transmit fluids. However, pre-existing fractures are observed in the borehole (Davatzes and Hickman, 2011). We consider a normal faulting stress regime according to the World Stress Map (Heidbach et al., 2010) and take the vertical σ_v, maximum horizontal σ_H, and minimum horizontal σ_h, stresses to be zero at the surface and use gradients of 24.1, 23.5 (N-S) and 14.9-15.8 (E-W) MPa/km, respectively with an initial hydrostatic pore-pressure P_f gradient of 8.8 MPa/km. The volcanic stratigraphy and the in-situ stress regime are indicated in **Figure 1-2b**. The average wellhead pressure during the stimulation was ~6 MPa (Cladouhos et al., 2011; Davatzes and Hickman, 2011).

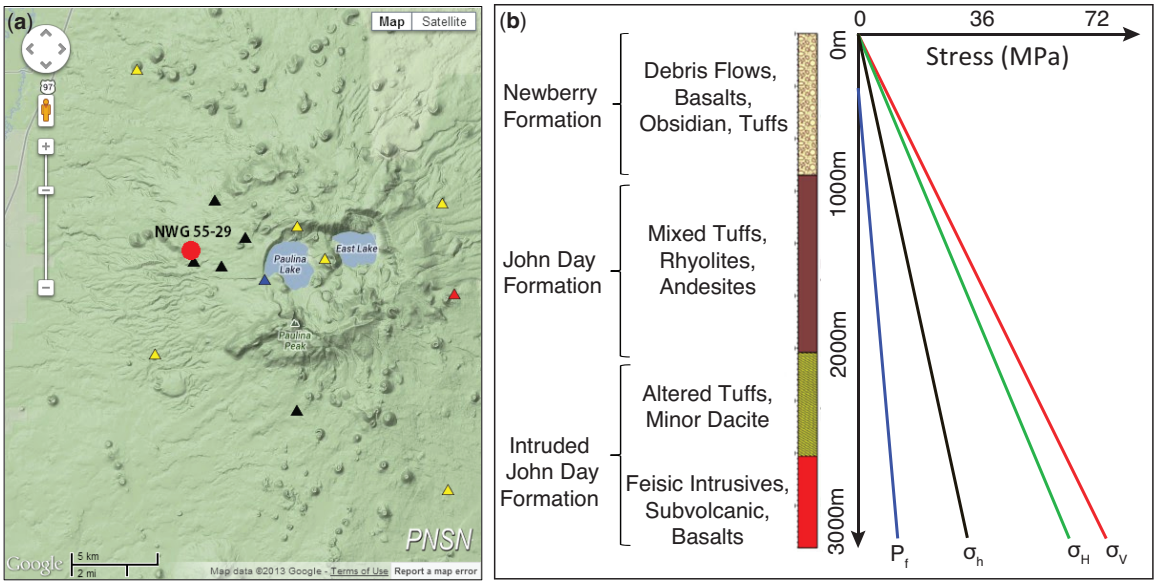

Figure **1-2**: **(a)** Location of well NWG 55-29 (from Google Earth). **(b)** Stratigraphy and stress regime of well NWG 55-29.

2.2 Shear Failure Analysis

Observations such as in-situ stress measurements in deep boreholes (Zoback and Healy, 1992), seismicity induced by fluid injection (Pine et al., 1983; Raleigh et al., 2013) and earthquake triggering of secondary earthquakes (Stein et al., 1992) all suggest a state of dynamic equilibrium within the upper continental crust (Townend and Zoback, 2000). Here, we explore the potential for shear failure of critically stressed fractures throughout the depth of the geothermal reservoir. We use the Mohr-Coulomb failure criterion (**Figure 1-3**) to define the shear strength, τ_s, for brittle failure of pre-existing fractures:

$$\tau_s = C_0 + \mu_s \cdot \sigma_{neff} = C_0 + \mu_s \cdot (\sigma_{tot} - \alpha_b \cdot P_f) \quad (1)$$

where C_0 is cohesion; μ_s is the coefficient of friction (tangent of friction angle φ); σ_{neff} is the effective normal stress; σ_{tot} is the total normal stress; and α_b is the Biot coefficient.

The pre-existing fractures are considered to be optimally oriented for shear failure with the fracture normal at an angle θ to the maximum principal stress σ_1 (**Figure 3**).

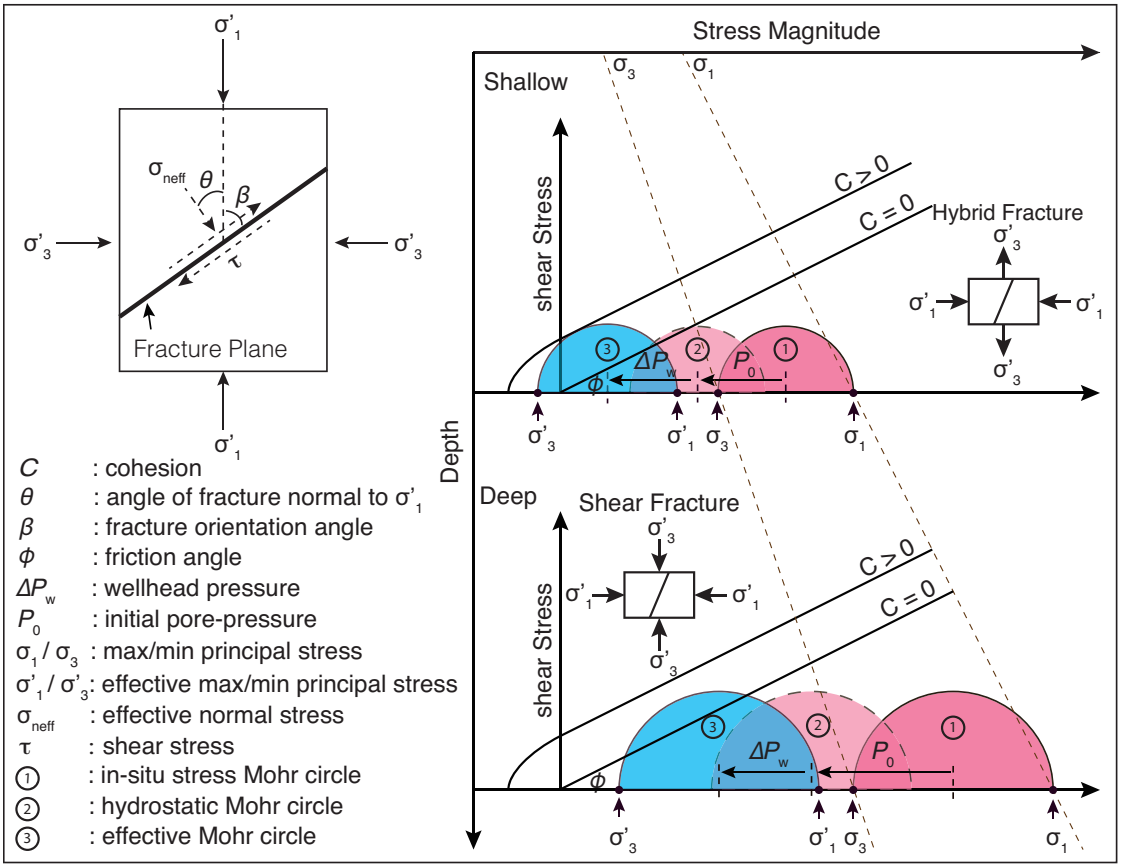

Figure **1-3**: Schematic fracture plane with respect to stress configuration (left side) and depth and fluid pressure dependent Mohr circles (right side)

Thus, we have:

$$\sigma_{neff} = \frac{(\sigma_1' + \sigma_3')}{2} + \frac{(\sigma_1' - \sigma_3')}{2}\cos 2\theta \tag{2}$$

$$\tau = -\frac{\sigma_1' - \sigma_3'}{2}\sin 2\theta \tag{3}$$

where τ is the critical shear stress; σ_1' and σ_3' are the effective maximum and minimum principal stresses, respectively; and 2θ is equal to $\varphi+\pi/2$. In this study, σ_1 and σ_3 denote the vertical and minimum horizontal stresses, respectively. Combining Eq. (1) and Eq. (3), yields:

$$\frac{\sigma_1'}{\sigma_3'} = \frac{(\mu_s^2+1)^{1/2} + \mu_s + 2C/\sigma_3'}{(\mu_s^2+1)^{1/2} - \mu_s} \tag{4}$$

Extending the principal stress as a function of in-situ stress gradients, reservoir depth, initial hydrostatic pore-pressure, and applied wellhead pressure, we can rewrite Eq. (4) as follows:

$$F_{pot} = \frac{\sigma_1'}{\sigma_3'} = \frac{(\gamma_1 - \alpha_b \cdot \gamma_f)\cdot z - \alpha_b \cdot \Delta P_w}{(\gamma_3 - \alpha_b \cdot \gamma_f)\cdot z - \alpha_b \cdot \Delta P_w} \tag{5}$$

$$F_{crt} = \frac{(\mu_s^2+1)^{1/2} + \mu_s + 2C/\sigma_3'}{(\mu_s^2+1)^{1/2} - \mu_s} = \frac{(\mu_s^2+1)^{1/2} + \mu_s + 2C/[(\gamma_3 - \alpha_b \cdot \gamma_f)\cdot z - \alpha_b \cdot \Delta P_w]}{(\mu_s^2+1)^{1/2} - \mu_s} \tag{6}$$

where γ_1, γ_3, and γ_f, represent the gradients of σ_1, σ_3, and P_f, respectively; z is the reservoir depth and ΔP_w is the local wellhead pressure (**Figure 1-3**). We define Eq. (5) as the shear failure potential F_{pot} and Eq. (6) as the critical failure index F_{crt} to determine whether a critically stressed fracture would fail at a given reservoir depth. If the cohesion C_0 is null, then the critical failure index F_{crt} is controlled only by the coefficient of friction of the pre-existing fractures.

Before stimulation, F_{pot} is a constant value defined by the initial in-situ pore-pressure and in-situ stresses. During fluid injection, F_{pot} becomes a function of both depth and the fluid pressure. More realistically, injecting cold fluid in the hot reservoir induces thermal contraction of the rock, reducing the effective stresses acting on the fracture. The upper-bound for the induced thermal stress is approximated as:

$$\sigma_{thermal} = \alpha \cdot \Delta T \cdot E \tag{7}$$

where α is the linear thermal coefficient; ΔT is temperature change; E is the Young's modulus of the reservoir rocks and a full displacement constraint is assumed. This yields the shear failure potential:

$$F_{pot} = \frac{(\gamma_1 - \alpha_b \cdot \gamma_f)\cdot z - \alpha_b \cdot \Delta P_w - \sigma_{thermal}}{(\gamma_3 - \alpha_b \cdot \gamma_f)\cdot z - \alpha_b \cdot \Delta P_w - \sigma_{thermal}} \tag{8}$$

Thus the relation between F_{pot} and F_{crt} with respect to the shear failure events in the geothermal reservoir can be described as: (1) If F_{pot} is equal to or greater than F_{crt}, then shear failure may occur. (2) If F_{pot} is less than F_{crt}, then no failure occurs.

For the scenario of a casing leak in the shallow reservoir, we assume that the wellhead pressure in the leaking window is transmitted to the open zone. Thus, we use this method to examine the shear failure potential on pre-existing fractures exposed to the same ΔP_w.

2.3 Pore-Pressure Diffusion Analysis

In well injection scenarios, pore-pressure diffusion is an important factor that may influence the timing of seismicity (Evans et al., 2005; Lee and Wolf, 1998; Shapiro et al., 1997). In the low-frequency limit of Biot's (1962) equations, the pore-pressure diffusion from a borehole in a fluid-saturated porous medium is expressed as (Biot, 1956; Shapiro et al., 2002):

$$\beta\phi\frac{\partial p}{\partial t}=\frac{\partial}{\partial r}\left[\frac{\kappa}{\eta}\cdot r^2\cdot\left(\frac{\partial p}{\partial r}\right)\right] \tag{9}$$

where β is the compressibility coefficient; Φ is the porosity; p is the pressure; t is the diffusion time; r is the diffusion length; η is the viscosity of the fluid; κ is the permeability. The solution to Eq. (9) for a Heaviside pressure pulse applied at the origin (Shapiro et al., 1997) suggest that the distance from the injection point to the triggering front can be described as:

$$r^2=4\pi Dt=4\pi t\frac{N\kappa}{\eta} \tag{10}$$

where D is the hydraulic diffusivity and N is a poroelastic modulus defined as follows (Delépine et al., 2004; Lachenbruch, 1980; Shapiro et al., 1997):

$$N=[\frac{\phi}{K_f}+\frac{\alpha}{K_g}]^{-1} \tag{11}$$

where α =1-K_d/K_g; K_d is the drained bulk modulus of the dry frame; K_g is the bulk modulus of the grains; and K_f is the bulk modulus of the fluid.

We use Eq. (10) to estimate the time necessary for injected fluid to diffuse from the top of the open hole (base of the casing) to the shallow reservoir and test whether this can explain the observed timing of anomalous seismicity at shallow depths in the reservoir. We assume spherical pore-pressure diffusion in a homogeneous medium, and we focus on upward diffusion along a vertical path as this is the shortest distance to reach the shallow reservoir and thus defines the shortest critical diffusion time t_c.

2.4 Friction Experiments

In the foregoing analyses, we have assumed constant frictional properties of the geothermal reservoir rocks. However, in reality, the frictional characteristics are expected to depend on factors such as rock composition and the depth-dependent in-situ pressure and temperature conditions (den Hartog and Spiers, 2013). Hence, we performed friction experiments to determine the frictional properties of pre-existing fractures as a function of depth and as such provide insight into the mechanisms of the anomalous distribution of seismicity.

2.4.1 Sample Material and Experimental Procedure

We collected 5 samples from drilling cuttings from well NWG 55-29 for friction experiments. Samples 1 and 2 were collected from the shallow reservoir where abundant MEQs occurred, while samples 3 to 5 were taken from the missing seismic zone at depths between ~1800 m and ~3000 m. After cleaning the samples to remove the drilling mud and possible drill bit fragments, the samples were crushed and powdered in a disc mill, and finally sieved to a

particle size less than 150 μm. The mineralogical composition of the samples was characterized via X-Ray Diffraction analysis (XRD), which shows that the samples were dominated by three groups of minerals: carbonate (mainly calcite), phyllosilicates and tectosilicates (**Table 1-1**).

The experiments were performed with a biaxial testing apparatus (**Figure 1-4a**), using the same set-up and following similar procedures as (Samuelson et al., 2008). In this machine, two gouge layers are sandwiched between three roughened steel forcing blocks with a contact area of 50 x 50 mm^2. We performed experiments at room temperature on water-saturated gouge layers with an initial thickness of 5 mm. To ensure that gouge layers were flat and identical in each experiment, they were constructed using a leveling jig and a measured mass (Frye and Marone, 2002).

Table **1-1**: Information of drilling core samples from stimulation well NWG 55-29

No.	Depth (m)	Formation	Mineral Compositions
S1	~701	Newberry	81% albite, 17% clinopyroxene, 2% hematite
S2	~1407	John Day	49% andesine, 14% calcite, 13% montmorillorite, 11% clinochlore, 7% quartz, 3% vermiculite
S3	~2139	Intruded John Day	60% albite, 20% quartz, 14.8% clinochlore, 3.5% calcite, 2.6% muscovite
S4	~2603	Intruded John Day	70% albite, 12% quartz, 11% phlogopite, 2.5% chlorite, 2.1% stilbite, 0.5% calcite, 1.9% others
S5	~2904	Intruded John Day	56.4% albite, 23.6% quartz, 14.6% orthoclase, 4.4% clinochlore, 0.6% muscovite, 0.4% calcite

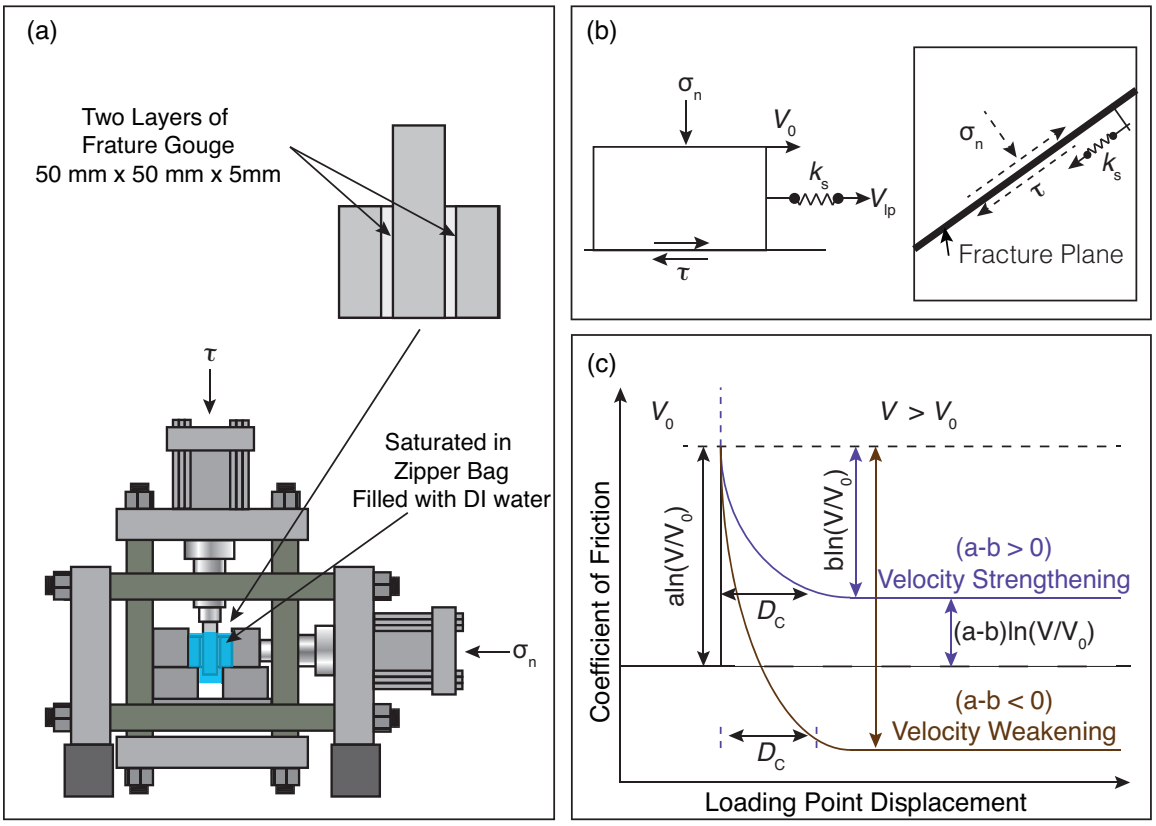

Figure **1-4**: **(a)** Double-direct shear geometry in a biaxial load frame. **(b)** Conceptual sliding model representing the fracture/fault sliding behavior. **(c)** Idealized RSF friction response to an increased velocity step showing two alternative frictional behaviors: velocity strengthening and velocity weakening.

Shear loading was attained by forcing the central block down at a constant velocity of 10 μm/s, while applying a normal load of 15 MPa perpendicular to the shear direction. After the achievement of steady-state friction, the sliding velocity was stepped in the range from 1 μm/s to 300 μm/s until a displacement of 9 mm was reached. The normal stress was next raised to 45 MPa and the velocity sequence was repeated, reaching a final displacement of 18-20 mm. The effect of calcite on the frictional properties of the Newberry samples was tested by performing additional experiments on samples 2 and 4 after leaching with 12% hydrochloric acid to remove the calcite.

2.4.2 Data Analysis

We calculated the coefficient of friction μ as a function of shear displacement for our experiments using $\mu = \tau / \sigma_n$. The velocity dependence of friction was interpreted in the framework of the rate and state friction (RSF) theory (**Figure 1-4b**) (Dieterich, 1979, 1978; Ruina, 1983). In the RSF approach to modeling fracture slip, the friction coefficient is written as (Dieterich, 1978; Marone, 1997; Scholz, 1998):

$$\mu = \mu_0 + a \ln\left(\frac{V}{V_0}\right) + b \ln\left(\frac{V_0 \theta}{D_c}\right) \tag{12}$$

$$\frac{d\theta}{dt} = 1 - \frac{V\theta}{D_c} \tag{13}$$

where μ_0 is the coefficient of friction at a reference velocity V_0; θ is a state variable, a and b are friction parameters which represent, respectively, the effect of instantaneous and displacement-dependent changes in friction from V_0 to V=eV_0; and D_c is the critical slip distance over which evolution to a new steady state takes place. Frictional slip instability is determined in part by the parameter (a-b) derived from Eq. (12) for a finite step in velocity, yielding (Dieterich, 1979; Ruina, 1983; Scholz, 1998):

$$a - b = \frac{\Delta \mu_{ss}}{\Delta \ln V} \tag{14}$$

A positive value of (a-b) denotes velocity-strengthening behavior indicative of stable, aseismic slip (Gu et al., 1984), while a negative a-b indicates velocity-weakening behavior, which is potentially unstable (**Figure 1-4c**). The RSF friction parameters were determined from our experiments by solving Eqns. (12) and (13), coupled with an equation describing elastic interaction with the testing machine, using the fitting method described by Marone (1998) and Blanpied et al. (1998).

Frictional stability depends on the critical stiffness K_c defined as:

$$K_c = \frac{\sigma_n (b-a)}{D_c} \tag{15}$$

As shown by Gu et al. (1984), instability may occur if the loading stiffness K is smaller than the effective-rheologic stiffness K_c. If we assume a circular dislocation (fracture) in a homogeneous medium, the effective shear stiffness around a fracture of diameter L is (Chinnery, 1969; Scholz, 2002; Starr, 1928):

$$K = \eta \cdot \frac{G_s}{L} \tag{16}$$

where η is a geometric factor and G_s is the shear modulus. Assuming the crack in the reservoir is penny-shaped, η has the value of $7\pi/24$. Combing Eq. (15) and Eq. (16), we find that the critical fracture length L_c for instability is:

$$L_c = \eta \cdot \frac{G_s \cdot D_c}{\sigma_n \cdot (b-a)} \tag{17}$$

For fractures smaller than L_c, (i.e., $K > K_c$) stable sliding will occur, while for those larger than L_c (i.e., $K < K_c$), unstable slip can result.

3. Results

3.1 Shear Failure Analysis

Failure may be induced on critically oriented fractures in the reservoir by the application of sufficient wellhead pressure. **Figure 1-5a** shows that when the friction angle of fractures is 30° and the wellhead pressure is 3 MPa, the F_{pot} at each depth is larger than that of F_{crt}, implying that all the critically stressed fractures will fail to slip at all depths. If fractures are frictionally stronger, the F_{crt} in the deeper reservoir will be larger than F_{pot}, resulting in a stable region in the

deep reservoir, but rendering the shallow reservoir unstable ($F_{pot} > F_{crt}$). Increasing wellhead pressure (e.g., from 3 MPa to 6 MPa) can both enlarge the regions of hybrid fracturing (shear failure and tensile failure) and hydroshearing where $F_{pot} > F_{crt}$ (**Figure 1-5b**). In addition, when thermal stresses are considered at each depth (quenching), the zones of instability spread.

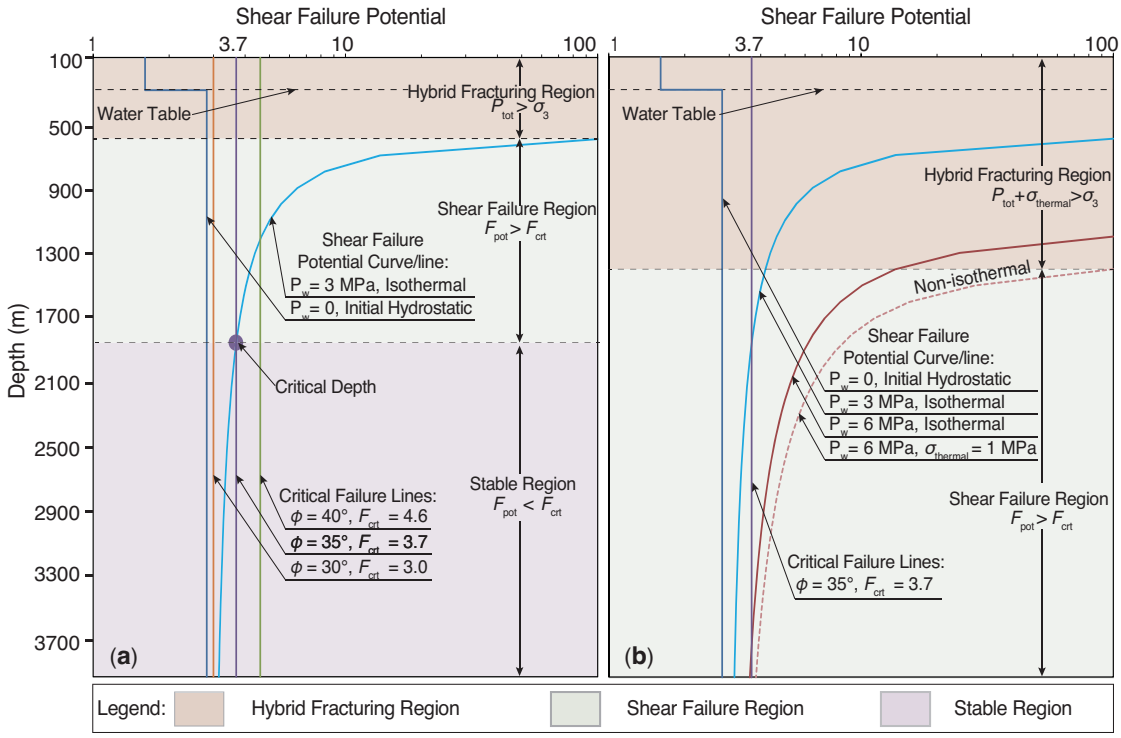

Figure **1-5**: Shear failure potential and critical failure as a function of depth for wellhead pressure applied at all depths. **(a)** Effect of coefficient of friction of pre-existing fractures. Assuming the friction angle is 35°, the value of shear failure potential (blue curve) is greater than that of the critical failure line (purple line) above the critical depth at ~1900 m, while it is smaller below this depth. If the fracture has a larger (or smaller) friction angle than 35° (or 30°), the stability region will increase (or decrease). **(b)** Effects of magnitude of wellhead pressure and thermal stress. When wellhead pressure increases from 3 MPa to 6 MPa, the shear failure region will be enlarged with depth. Thermal stress will enhance the instability along the depth.

3.2 Pore-Pressure Diffusion

We consider a possible migration of fluids from the deep open zone (top of the open zone at ~ 2000m) to the shallow seismic zone and calculate pressure-diffusion under two end-member

permeability scenarios: 1) migration through high permeability fractures (k = 10 mD) and 2) migration through low permeability matrix (k =10 µD). During the stimulation, injection of water was completed in three cycles: about 7 days for the first cycle, then 7 days for the second cycle and 14 days for the third cycle after a hiatus of 7 days (**Figure 1-6a**). The depths of seismic events with time are indicated in **Figure 1-6b**. The timing of these seismic events indicates an appropriate synchronous response to the injected wellhead pressure. The rate of pore-pressure diffusion in the fractures and rock matrix shows a significant difference that in the first injection cycle, the vertical distances from the depths of all seismic events to the reference depth are larger the pore-pressure diffusion length through the matrix.

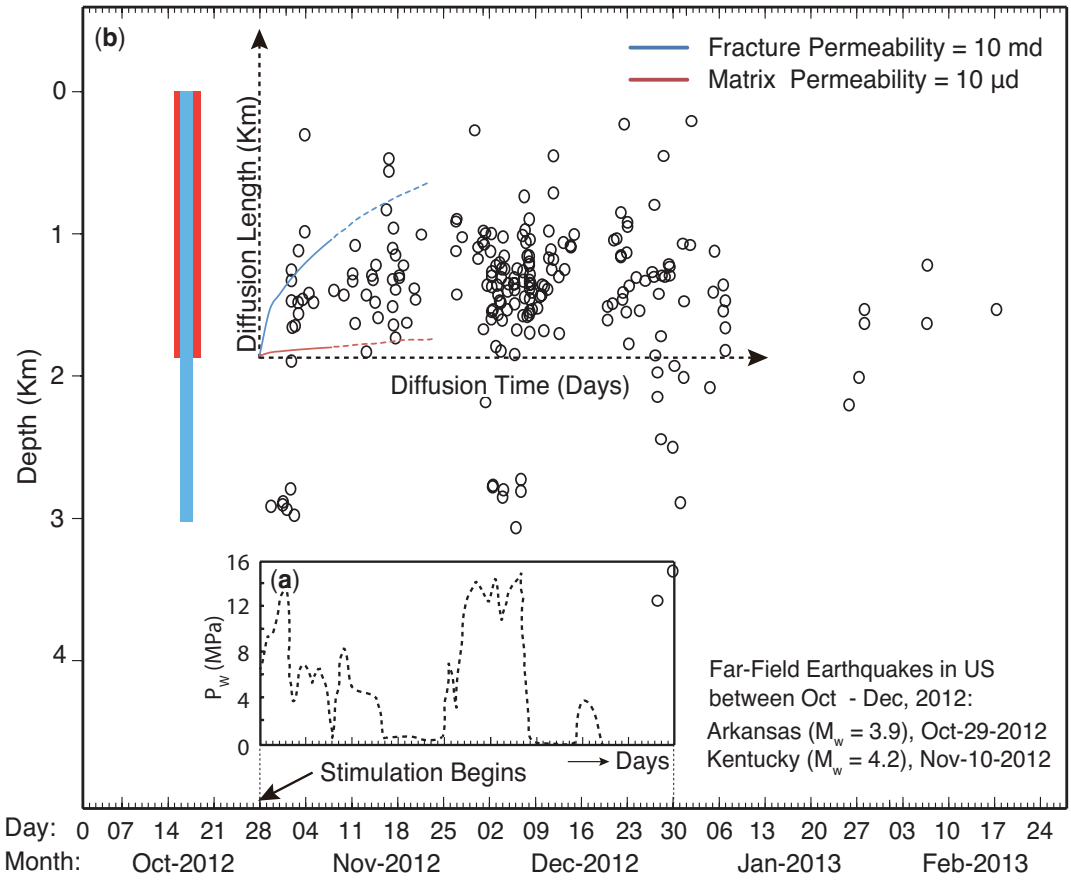

Figure **1-6**: (**a**) Injection wellhead pressure with time. (**b**) Pore-pressure diffusion length with time compared with elevations of seismic events with time. The vertical distances between the top of uncased wellbore portion and some seismic events in shallow reservoir (above 1000 m) are beyond the maximum diffusion front when reservoir permeability is 10 md.

3.3 Friction Experiments

A preliminary appraisal of the observed seismicity by both lithostatic (Section 3.1) and distributed parameter models (Section 3.2) suggests that if shear failure occurred in the deep reservoir (~3000 m) it should also occur in the upper open zone. Thus the observed bimodal distribution of seismicity cannot be fully explained by a model with uniform frictional properties with depth. Therefore, we determined the frictional slip stability as a function of depth from our shear experiments to clarify the distribution of MEQs.

The composition of the samples used for the experiments is plotted versus depth in **Figure 1-7a**. All samples are dominated by tectosilicates with lesser amounts of phyllosilicates and calcite. The phyllosilicates and calcite contents reach a maximum at a depth of ~1500 m while the amount of tectosilicates is lowest at this depth. The friction curves of all shear experiments were similar (**Figure 1-7b**). The friction coefficient measured at the end of each constant normal stress portion (i.e. at displacements of 9 and 18 mm for 15 and 45 MPa, respectively) are plotted in **Figure 1-8** versus depth, while (*a*-*b*) values at 15 and 45 MPa normal stress are shown versus depth in **Figure 1-9** and **1-10.**

The measured (*a*-*b*) values of samples are predominantly positive (velocity strengthening) at the conditions of our experiments. At shallow depth (~700 m) and at the base of the open zone (~ 2900 m), the (*a*-*b*) magnitudes are near zero or close to velocity neural, while at ~1400 m, (*a*-*b*) is more positive, representing more velocity strengthening behavior. The (*a*-*b*) values of samples with/without calcite at 15 MPa and 45 MPa normal stress are shown in **Figure 1-11**.

The results show similar trends of composition of samples and friction properties with depth, suggesting a possible mineralogical control on the MEQs at intermediate depth. The critical friction slip distance increases with post-step velocity (**Figure 1-12a**). We used the

modeled RSF parameters along with a bulk modulus of 17 GPa and Poisson ratio of 0.27 (Izadi and Elsworth, 2013; Li et al., 2012) to estimate the critical fracture radius L_c for frictional instability and earthquake nucleation. The fracture length increases with increasing sliding velocity (**Figure 1-12b**). Our data suggest a minimum fracture radius of ~7 m.

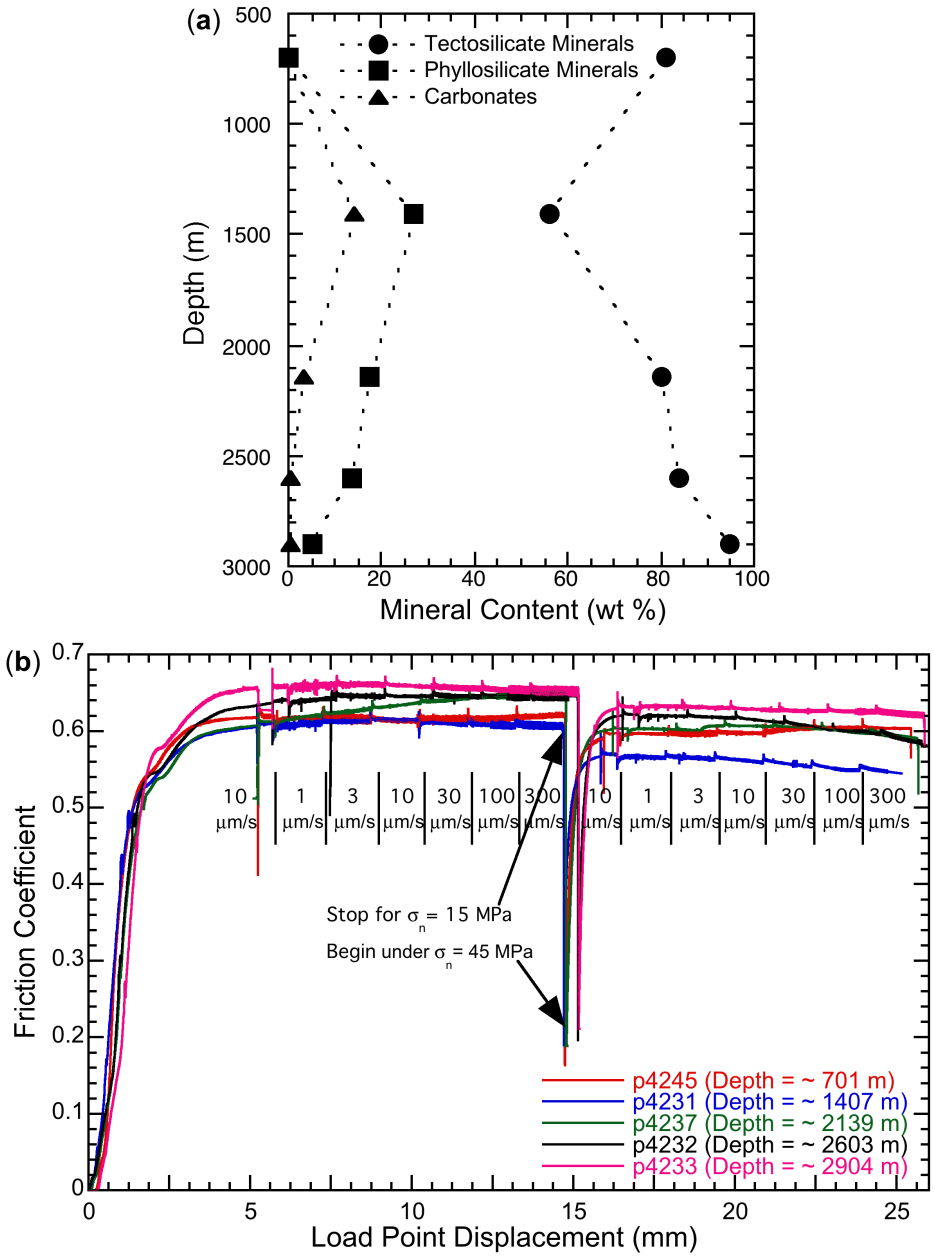

Figure **1-7**: **(a)** Mineral contents with depths. **(b)** Friction-load point displacement curves of examined samples under normal stresses of 15 MPa and 45 MPa, respectively.

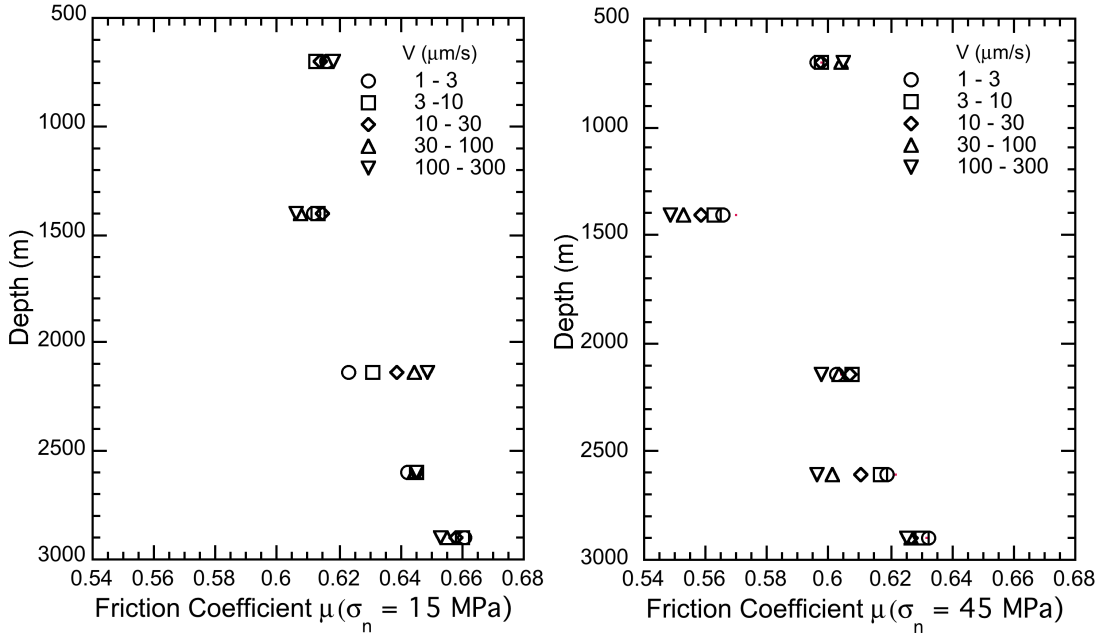

Figure **1-8**: Steady sliding friction μ of examined samples with depths before each velocity step under normal stresses of 15 MPa and 45 MPa, respectively

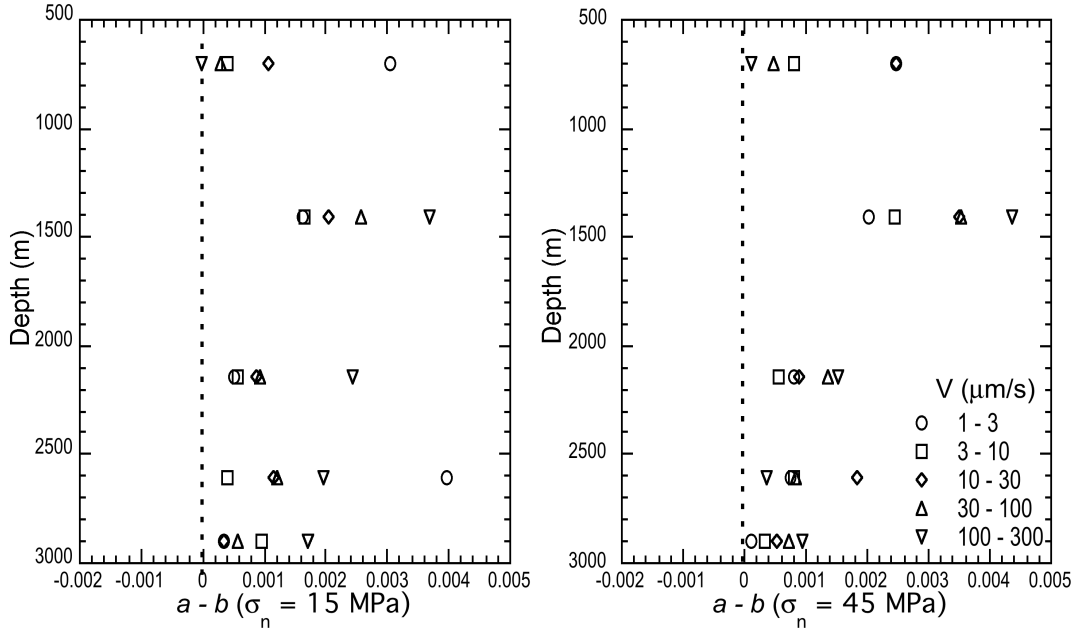

Figure **1-9**: Friction parameter (*a*-*b*) of examined samples with depths for each velocity step under normal stresses of 15 MPa and 45 MPa, respectively

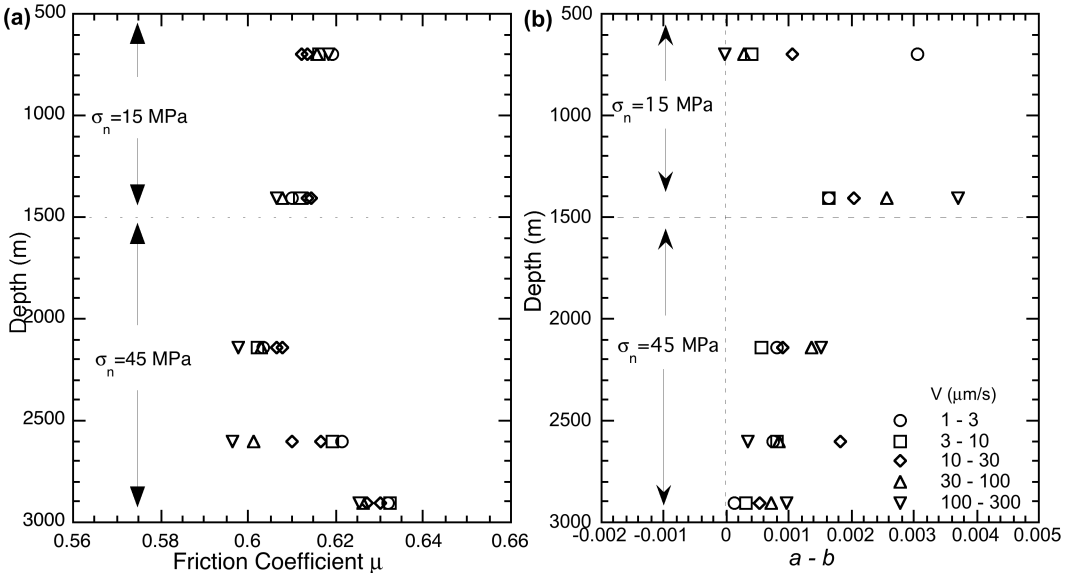

Figure **1-10**: **(a)** Friction coefficient μ and **(b)** parameter (*a-b*) with depths of approximate in-situ normal stress

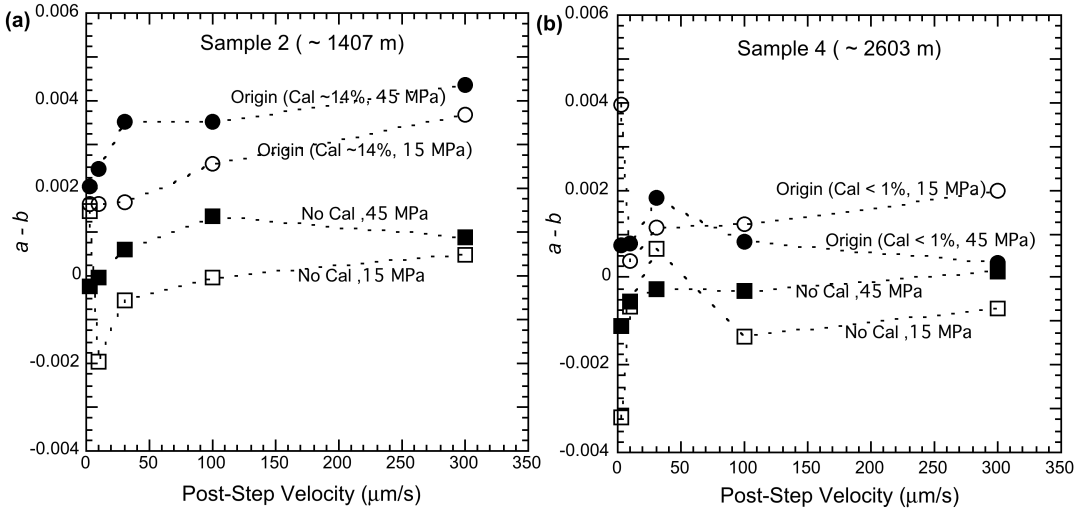

Figure **1-11**: Comparison of frictional parameter (*a-b*) between calcite contained and calcite removed sample 2 and 4.

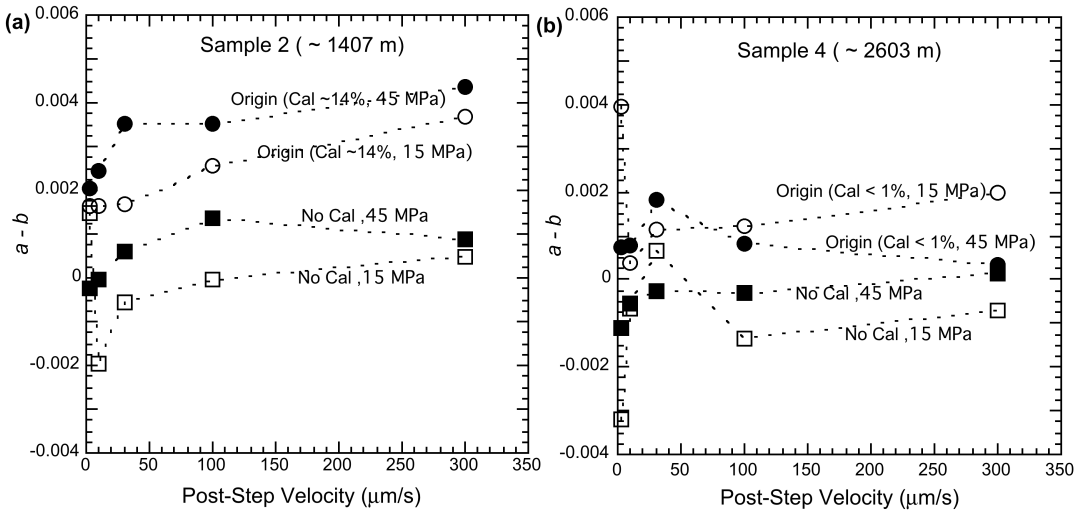

Figure **1-12**: **(a)** Critical slip distance and **(b)** critical fracture length with increasing velocity.

4. Discussion

Considering the first possible cause that the casing leak in the shallow reservoir may contribute to the bimodal distribution of the MEQs, shear failure analysis indicates that the newly introduced fluid penetrating the shallow reservoir (above ~ 1800 m) due to casing leak will enhance local instability of fractures and induce MEQs. The less critically oriented fractures in the shallow reservoir could also be reactivated due to the higher shear potential F_{pot} compared to that of the deep reservoir (~ 3000 m), resulting in more seismic events. Meanwhile, wellhead pressure ΔP_w in the open zone (below ~ 2000 m) will decrease due to the shallow casing leak. As a result, the residual ΔP_w in the open zone may not be sufficient to continue reactivating local pre-existing fractures, which explains why the MEQs diminish in the deep zone (~ 3000 m).

For the second possible cause, pore-pressure diffusion analysis demonstrates that, for reservoir fractures with a permeability of 10 mD, the estimated fluid migration time does not match the timing of the observed shallow MEQs within the initial 4 days of stimulation.

Furthermore, the previous logging and testing of well NWG 55-29 suggests that the pre-existing fractures lack significant permeability (estimated at ~10 μD in impermeable zone and ~3.25 mD in permeable zone) (Petty et al., 2013; Spada et al., 2013). Hence, a realistic diffusion length should be considerably shorter than the upper-limit end-member scenario and it is plausible that the water cannot migrate upwards and generate critical overpressures sufficiently quickly. As a result, the unmatched timing between MEQs and fluid migration (**Figure 1-6**) implies that the deep injected fluid is unlikely to be the major cause of early shallow seismic events.

Based on our friction experiments, and previous studies, we consider four factors that may be important to explain the missing seismicity at intermediate depths: *viz.* contrasting mineral compositions, pore-pressures, temperatures and fracture sizes at the sampled depths in the reservoir. In terms of mineralogy, frictional strength μ shows the opposite trend compared to parameter (a-b) with depth. The phyllosilicate-rich materials exhibit low frictional strength and velocity-strengthening behavior while tectosilicate-rich materials show high frictional strength with velocity-neutral (or minimum velocity-weakening behavior) (**Figure 1-7a** and **Figure 1-10**) suggesting that (a-b) and μ are strongly mineral group dependent. This relation is also observed in previous studies (Ikari et al., 2011; Kohli and Zoback, 2013; Niemeijer and Collettini, 2013). The comparison of (a-b) values between samples with calcite and those in which the calcite was removed shows that dissolving the calcite decreases (a-b) at room temperature (**Figure 1-11**), implying that the dissolution of calcite can decrease frictional stability. Because wet calcite-rich fault gouge exhibits stable slip below 80°C ~100°C, unstable slip at 100°C ~ 550°C, and is stable again at 590°C (Verberne et al., 2014), (a-b) values of samples at in-situ temperatures (100°C ~ 250°C) are expected to be lower than the values measured in the current experiments conducted at room temperature. However, the effects of calcite on (a-b) values are expected to be minimal in the deep reservoir where the calcite content is negligible. This is supported by our result showing similar (a-b) values for sample with and without (~0.5%) calcite.

Pore pressure is another important factor that may influence frictional slip stability (Scholz, 1998). In our experiments, we observed that the (*a*-*b*) values of samples from the shallow reservoir are slightly lower when deformed at a normal stress of 15 MPa as opposed to 45 MPa. Samples from the deep reservoir, on the other hand, show slightly higher values at 15 MPa than at 45 MPa. Although the differences are small, they suggest that a reduction of the effective normal stress brought about by an increase in the pore pressure due to plausible casing leak in the shallow reservoir may result in a lower local (*a*-*b*) value, while increasing the pore pressure due to fluid injection in the deep reservoir can increase the local (*a*-*b*) value.

In summary, from the above we infer that the *in-situ* frictional slip stability of the shallow reservoir could have been less than implied by our measured (*a*-*b*) data, because: 1) the temperature of the calcite-rich shallow reservoir (~1400 m) is about 100°C and previous studies suggest that (*a*-*b*) values are lower at this higher temperature; 2) An abrupt increase in fluid pressure as a result of casing leak in this calcite-rich region also decreases frictional stability and 3) low temperature leaking fluid dissolves the calcite, resulting in a further reduction of (*a*-*b*). In addition, (*a*-*b*) values at these depths are very small and close to velocity neutral. Thus the perturbation by the increased pore-pressure as well as the temperature effect may result in a shift of local *a*-*b* magnitudes from positive to negative.

In the zone where seismic events are absent, the calcite content of samples decreases with depth and is negligible at the base of the open zone. Thus the measured positive (*a*-*b*) values in the deep reservoir may be slightly influenced by the temperature that promotes velocity-weakening behavior in calcite (i.e., (*a*-*b*) values may be slightly lower than the measured ones). However, this slight effect is offset by the pore-pressure perturbation that increasing local fluid pressure (or decreasing effective normal stress) at greater depths will have, thereby increasing local *a*-*b* values (i.e., local frictional stability is enhanced). As a result, the measured positive *a*-*b* values may be close to the in-situ values, implying that only aseismic events could occur in the

deep zone. Furthermore, the migration of cold injected fluid through the fractures could remove the retrograde-soluble calcite and may gradually decrease the (*a*-*b*) values. In this manner the initial velocity strengthening properties of preexisting fractures could be transformed to velocity weakening, with the potential for frictional instability.

In addition to mineralogical influences on stability, the distribution of fracture sizes is an important factor to determine the potential for instability when (*a*-*b*) values are negative. Our results suggest that only fractures with negative (*a*-*b*) values and lengths (radius) greater than ~7 m may slip unstably. However, fractures with length less than 7 m are conditionally stable. If *in-situ* fault creep velocities are slower than the experimental sliding velocity, the real critical fracture length could be smaller than the lowest fracture length derived from our data. Based on this analysis, we can speculate that, if the (*a*-*b*) values of the preexisting fractures were initially negative, then fracture lengths in the stable aseismic zone must be smaller than this threshold of ~7 m. This speculation needs to be validated by further *in-situ* reservoir fracture characterization.

5. Conclusion

Differing from other expected distribution patterns of induced MEQs with depth, this bimodal depth distribution of MEQs at the Newberry geothermal reservoir suggests unusual controls by fluid permeation and reservoir mineralogy and state. Our analyses introduce the following conclusions: (1) The unusual and unexpected penetration of excess fluid pressures in the shallow zone is plausible mainly due to the casing leak in the shallow reservoir. This result is further confirmed by the second observation that indeed the casing is damaged at shallow depth (~700 m). (2) The diminished seismicity in the deep open zone is plausibly associated by fluid loss (wellhead pressure drop) as a result of the shallow leak. (3) An upward-migrating fluid pressure pulse is incapable of inducing seismicity in the shallow reservoir (above ~1000 m), but

may partially contribute to the occurrence of seismicity near the top of casing shoe (~1800 m). (4) The observation of missing seismic events between ~1800 m and ~2500 m during the stimulation plausibly results from slight velocity strengthening properties in the reservoir and in particular on local preexisting fractures. Aseismic events may still occur in this intermediate zone, in the form of slow sliding slip or creep events, but may be below the threshold observed by the seismic monitoring.

Acknowledgement

This work is the result of partial support provided by DOE Grant DE-EE002761 and NSF grants EAR1045825, and EAR1215856. This support is gratefully acknowledged.

Appendix

Table **1-2**: List of experiment names (*Exp*), normal stresses (σ_n), pre-step velocity (V), friction coefficient (μ), frictional stability (a-b) and critical slip (D_c)

Exp	σ_n (MPa)	V (μm/s)	μ	(a-b)	D_c (mm)
p4245	15	1	0.61614	0.003050	0.02
		3	0.61220	0.000402	0.011
		10	0.61362	0.001063	0.011
		30	0.61587	0.000296	0.009
		100	0.61819	-0.00003	0.008
p4245	45	1	0.59620	0.002462	0.022
		3	0.59771	0.000805	0.011
		10	0.58782	0.002460	0.008
		30	0.60394	0.000463	0.012
		100	0.60485	0.000113	0.023
p4231	15	1	0.61189	0.001625	0.011
		3	0.61354	0.001651	0.011
		10	0.61451	0.002036	0.02
		30	0.60770	0.002571	0.02
		100	0.60636	0.003693	0.051
p4231	45	1	0.56541	0.002037	0.013
		3	0.56280	0.002448	0.023
		10	0.55870	0.003509	0.016
		30	0.55272	0.003525	0.029
		100	0.54883	0.004376	0.055
p4237	15	1	0.62286	0.000509	0.022
		3	0.63110	0.000566	0.023
		10	0.63879	0.000869	0.022
		30	0.64465	0.000943	0.036
		100	0.64870	0.002449	0.007
p4237	45	1	0.60232	0.000807	0.015
		3	0.60764	0.000568	0.02
		10	0.60650	0.000886	0.021
		30	0.60320	0.001374	0.035
		100	0.59790	0.001524	0.084
p4232	15	1	0.64223	0.003969	0.014
		3	0.64513	0.000387	0.037
		10	0.64554	0.001143	0.043
		30	0.64469	0.001213	0.023
		100	0.64511	0.001975	0.052
p4232	45	1	0.61920	0.000760	0.02
		3	0.61678	0.000796	0.025
		10	0.61023	0.001833	0.017
		30	0.60133	0.000840	0.036
		100	0.59638	0.000355	0.094

Table **1-2** Continued

Exp	σ_n (MPa)	V (μm/s)	μ	(a-b)	D_c (mm)
p4233	15	1	0.66063	0.000344	0.032
		3	0.65985	0.000959	0.016
		10	0.65768	0.000345	0.019
		30	0.65543	0.000560	0.021
		100	0.65268	0.001697	0.028
p4233	45	1	0.63220	0.000120	0.021
		3	0.63021	0.000327	0.018
		10	0.62703	0.000524	0.018
		30	0.62645	0.000722	0.027
		100	0.62525	0.000957	0.061
p4274	15	1	0.57300	0.001498	0.014
		3	0.57354	-0.001939	0.008
		10	0.57110	-0.000570	0.012
		30	0.57067	-0.000036	0.025
		100	0.57107	0.000467	0.125
p4274	45	1	0.61850	-0.000229	0.017
		3	0.61623	-0.000020	0.039
		10	0.62140	0.000587	0.063
		30	0.60780	0.001358	0.067
		100	0.60198	0.000878	0.170
p4246	15	1	0.62542	-0.003200	0.013
		3	0.62747	-0.000662	0.023
		10	0.62800	0.000665	0.069
		30	0.62992	-0.001342	0.078
		100	0.62871	-0.000689	0.114
p4246	45	1	0.61511	-0.001117	0.022
		3	0.61452	-0.000527	0.040
		10	0.61267	-0.000251	0.084
		30	0.61126	-0.000307	0.094
		100	0.60840	0.000135	0.084

References

Bachmann, C.E., Wiemer, S., Woessner, J., Hainzl, S., 2011. Statistical analysis of the induced Basel 2006 earthquake sequence: Introducing a probability-based monitoring approach for Enhanced Geothermal Systems. Geophys. J. Int. 186, 793–807. doi:10.1111/j.1365-246X.2011.05068.x

Biot, M.A., 1956. Theory of Propagation of Elastic Waves in a Fluid-Saturated Porous Solid. II. Higher Frequency Range. J. Acoust. Soc. Am. doi:10.1121/1.1908241

Blanpied, M.L., Marone, C.J., Lockner, D.A., Byerlee, J.D., King, D.P., 1998. Quantitative measure of the variation in fault rheology due to fluid-rock interactions. J. Geophys. Res. Solid Earth 103, 9691–9712. doi:10.1029/98JB00162

Chinnery, M.A., 1969. Theoretical fault models, in A symposium on Processes in the Focal Region, 37, edited by K. Kasahar and A.E. Stevens. Publ. Dom. Obs. Ottawa 211–223.

Cladouhos, T.T., Petty, S., Callahan, O., Osborn, W., Hickman, S., Davatzes, N., 2011. The Role of Stress Modeling in Stimulation Planning at the Newberry Volcano EGS Demonstration Project, in: Thirty Sixth Workshop on Geothermal Reservoir Engineering. Stanford University, Stanford, California, 8 p.

Davatzes, N.C., Hickman, S.H., 2011. Preliminary analysis of stress in the Newberry EGS Well NWG 55-29.

Delépine, N., Cuenot, N., Rothert, E., Parotidis, M., Rentsch, S., Shapiro, S.A., 2004. Characterization of fluid transport properties of the Hot Dry Rock reservoir Soultz-2000 using induced microseismicity. J. Geophys. Eng. doi:10.1088/1742-2132/1/1/010

Den Hartog, S.A.M., Spiers, C.J., 2013. Influence of subduction zone conditions and gouge composition on frictional slip stability of megathrust faults. Tectonophysics 600, 75–90. doi:http://dx.doi.org/10.1016/j.tecto.2012.11.006

Dieterich, J.H., 1978. Time-dependent friction and the mechanics of stick-slip. Pure Appl. Geophys. PAGEOPH 116, 790–806. doi:10.1007/BF00876539

Dieterich, J.H., 1979. Modeling of rock friction 1. Experimental results and constitutive equations, in: Journal of Geophysical Research: Solid Earth. pp. 2161–2168. doi:10.1029/JB084iB05p02161

Elsworth, D., Goodman, R.E., 1986. Characterization of rock fissure hydraulic conductivity using idealized wall roughness profiles. Int. J. Rock Mech. Min. Sci. Geomech. Abstr. 23, 233–243. doi:http://dx.doi.org/10.1016/0148-9062(86)90969-1

Evans, K.F., Genter, A., Sausse, J., 2005. Permeability creation and damage due to massive fluid injections into granite at 3.5 km at Soultz: 1. Borehole observations. J. Geophys. Res. Earth 110. doi:Artn B04203 Doi 10.1029/2004jb003168

Fehler, M.C., 1989. Stress control of seismicity patterns observed during hydraulic fracturing experiments at the Fenton Hill hot dry rock geothermal energy site, New Mexico. Int. J. Rock Mech. Min. Sci. Geomech. Abstr. 26, 211–219. doi:http://dx.doi.org/10.1016/0148-9062(89)91971-2

Frye, K.M., Marone, C., 2002. Effect of humidity on granular friction at room temperature. J. Geophys. Res. Earth 107. doi:Artn 2309 Doi 10.1029/2001jb000654

Gu, J.-C., Rice, J.R., Ruina, A.L., Tse, S.T., 1984. Slip motion and stability of a single degree of freedom elastic system with rate and state dependent friction. J. Mech. Phys. Solids 32, 167–196. doi:http://dx.doi.org/10.1016/0022-5096(84)90007-3

Heidbach, O., Tingay, M., Barth, A., Reinecker, J., Kurfeß, D., Müller, B., 2010. Global crustal stress pattern based on the World Stress Map database release 2008. Tectonophysics 482, 3–15. doi:10.1016/j.tecto.2009.07.023

Hubbert, M.K., Rubey, W.W., 1959. Role of fluid pressure in mechanics of overthrust faulting I. Mechanics of fluid-filled porous solids and its application to overthrust faulting. Geol. Soc. Am. Bull. 70, 115–166.

Ikari, M.J., Marone, C., Saffer, D.M., 2011. On the relation between fault strength and frictional stability. Geology 39, 83–86. doi:10.1130/g31416.1

Izadi, G., Elsworth, D., 2013. The effects of thermal stress and fluid pressure on induced seismicity during stimulation to production within fractured reservoirs. Terra Nov. 25, 374–380. doi:10.1111/ter.12046

Kohli, A.H., Zoback, M.D., 2013. Frictional properties of shale reservoir rocks. J. Geophys. Res. Earth 118, 5109–5125. doi:Doi 10.1002/Jgrb.50346

Lachenbruch, A.H., 1980. Frictional heating, fluid pressure, and the resistance to fault motion. J. Geophys. Res. doi:10.1029/JB085iB11p06097

Lee, M.K., Wolf, L.W., 1998. Analysis of fluid pressure propagation in heterogeneous rocks: Implications for hydrologically-induced earthquakes. Geophys. Res. Lett. 25, 2329–2332. doi:Doi 10.1029/98gl01694

Li, Y., Wang, J., Jung, W., Ghassemi, A., 2012. Mechanical Properties of Intact Rock and Fractures in Welded Tuff from Newberry Volcano, in: Thirty-Seventh Workshop on Geothermal Reservoir Engineering. Stanford University, Stanford, California, 12 p.

Majer, E.L., Baria, R., Stark, M., Oates, S., Bommer, J., Smith, B., Asanuma, H., 2007. Induced seismicity associated with Enhanced Geothermal Systems. Geothermics 36, 185–222. doi:http://dx.doi.org/10.1016/j.geothermics.2007.03.003

Majer, E.L., Peterson, J.E., 2007. The impact of injection on seismicity at The Geysers, California Geothermal Field. Int. J. Rock Mech. Min. Sci. 44, 1079–1090. doi:http://dx.doi.org/10.1016/j.ijrmms.2007.07.023

Marone, C., 1997. On the rate of frictional healing and the constitutive law for time- and slip-dependent friction. Int. J. Rock Mech. Min. Sci. Geomech. Abstr. 34, 347. doi:10.1016/S1365-1609(97)00054-3

Marone, C., 1998. Laboratory-derived friction laws and their application to seismic faulting. Annu. Rev. Earth Planet. Sci. 26, 643–696. doi:Doi 10.1146/Annurev.Earth.26.1.643

Niemeijer, A., Collettini, C., 2013. Frictional Properties of a Low-Angle Normal Fault Under In Situ Conditions: Thermally-Activated Velocity Weakening. Pure Appl. Geophys. 1–24. doi:10.1007/s00024-013-0759-6

Petty, S., Nordin, Y., Glassley, W., Cladouhos, T.T., Swyer, M., 2013. Improving Geothermal Project Economics with Multi-zone Stimulation: Results from the Newberry Volcano EGS Demonstration, in: PROCEEDINGS, Thirty-Eighth Workshop on Geothermal Reservoir Engineering. Stanford University, Stanford, California.

Pine, R.J., Ledingham, P., Merrifield, C.M., 1983. In-situ stress measurement in the Carnmenellis granite—II. Hydrofracture tests at Rosemanowes quarry to depths of 2000 m. Int. J. Rock Mech. Min. Sci. Geomech. Abstr. 20, 63–72. doi:10.1016/0148-9062(83)90328-5

Raleigh, C.B., Healy, J.H., Bredehoeft, J.D., 2013. Faulting and Crustal Stress at Rangely, Colorado, in: Flow and Fracture of Rocks. American Geophysical Union, pp. 275–284. doi:10.1029/GM016p0275

Ruina, A., 1983. Slip instability and state variable friction laws. J. Geophys. Res. Solid Earth 88, 10359–10370. doi:10.1029/JB088iB12p10359

Rutqvist, J., Freifeld, B., Min, K.B., Elsworth, D., Tsang, Y., 2008. Analysis of thermally induced changes in fractured rock permeability during 8 years of heating and cooling at the Yucca Mountain Drift Scale Test. Int. J. Rock Mech. Min. Sci. 45, 1373–1389. doi:http://dx.doi.org/10.1016/j.ijrmms.2008.01.016

Samuelson, J., Marone, C., Voight, B., Elsworth, D., 2008. Laboratory investigation of the frictional behavior of granular volcanic material. J. Volcanol. Geotherm. Res. 173, 265–279. doi:http://dx.doi.org/10.1016/j.jvolgeores.2008.01.015

Scholz, C.H., 1998. Earthquakes and friction laws. Nature 391, 37–42. doi:Doi 10.1038/34097

Scholz, C.H., 2002. The Mechanics of Earthquakes and Faulting, 2nd Edition. ed. Cambridge University Press.

Shapiro, S.A., Huenges, E., Borm, G., 1997. Estimating the crust permeability from fluid-injection-induced seismic emission at the KTB site. Geophys. J. Int. 131, F15–F18. doi:Doi 10.1111/J.1365-246x.1997.Tb01215.X

Shapiro, S.A., Rothert, E., Rath, V., Rindschwentner, J., 2002. Characterization of fluid transport properties of reservoirs using induced microseismicity. Geophysics. doi:10.1190/1.1451597

Spada, M., Tormann, T., Wiemer, S., Enescu, B., 2013. Generic dependence of the frequency-size distribution of earthquakes on depth and its relation to the strength profile of the crust. Geophys. Res. Lett. 40, 709–714. doi:Doi 10.1029/2012gl054198

Starr, A.T., 1928. Slip in a crystal and rupture in a solid due to shear. Math. Proc. Cambridge Philos. Soc. 24, 489–500. doi:doi:10.1017/S0305004100014626

Stein, R.S., King, G.C., Lin, J., 1992. Change in failure stress on the southern San Andreas fault system caused by the 1992 magnitude = 7.4 Landers earthquake. Science 258, 1328–1332. doi:10.1126/science.258.5086.1328

Tester, J., 2007. The Future of Geothermal Energy: Impact of Enhanced Geothermal Systems (EGS) on the United States in the 21st Century. MIT.

Townend, J., Zoback, M.D., 2000. How faulting keeps the crust strong. Geology 28, 399–402. doi:10.1130/0091-7613(2000)28<399:HFKTCS>2.0.CO

Verberne, B.A., Spiers, C.J., Niemeijer, A.R., De Bresser, J.H.P., De Winter, D.A.M., Plümper, O., 2014. Frictional Properties and Microstructure of Calcite-Rich Fault Gouges Sheared at Sub-Seismic Sliding Velocities. Pure Appl. Geophys. 171, 2617–2640. doi:10.1007/s00024-013-0760-0

Zoback, M.D., Harjes, H.-P., 1997. Injection-induced earthquakes and crustal stress at 9 km depth at the KTB deep drilling site, Germany. J. Geophys. Res. Solid Earth 102, 18477–18491. doi:10.1029/96JB02814

Zoback, M.D., Healy, J.H., 1992. In situ stress measurements to 3.5 km depth in the Cajon Pass Scientific Research Borehole: Implications for the mechanics of crustal faulting. J. Geophys. Res. doi:10.1029/91JB02175

Chapter 2

Reservoir Permeability Mapping using Microearthquake Data

Abstract

Evaluating hydraulic properties of fractured reservoirs both during and after stimulation is vital for the development of Enhanced Geothermal System (EGS) and hydrocarbon reservoirs. To constrain the evolution of fracture permeability at sufficiently fine resolution to define reservoir response, we propose a model that couples the moment magnitude to fracture aperture and then estimates the reservoir permeability at relatively high resolution. The critical parameters controlling fracture aperture and permeability evolution are stress-drop, the bulk modulus of the fracture embedded matrix, and the dilation angle of fractures. We employ Oda's crack tensor theory and a cubic-law based analog to estimate the permeability of a synthetic fractured reservoir at various scales, demonstrating that the resolution of permeability is largely determined by the cellular grid size. These methods are applied to map the in-situ permeability of the Newberry EGS reservoir using observed microearthquakes (MEQ) induced during the 1st and 2nd reservoir stimulations in 2014. The equivalent mean permeability evaluated by each method is consistent and unlimited by representative elementary volume (REV) size. With identical parameters, Oda's crack tensor theory produces a more accurate estimation of permeability than that of the cubic law method, but estimates are within one order of magnitude. The permeability maps show that the most permeable zone is located within the zone of most dense seismicity providing a reference for the siting of the production well. This model has the potential for mapping permeability evolution from MEQ data in conventional and unconventional reservoirs and at various scales.

Keywords: EGS, Stimulation, Microearthquake, Permeability

1. Introduction

Some unconventional resources, such as geothermal energy, have the potential to enable a transition to a more sustainable energy future. Enhanced Geothermal Systems (EGS) have the potential to tap the Earth's vast thermal resource. Since fractures are the most abundant structural feature in the upper crust (*Warren and Root*, 1963) and a fracture surface may have much higher permeability than the surrounding rock matrix and therefore operate as a conduit for fluids, a key capability for the successful development of EGS is to generate sufficient permeability in naturally fractured reservoirs via hydroshearing and to optimally accommodate the production well according to the identified locations of clustered fractures (*Rinaldi et al.*, 2015; *Cladouhos et al.*, 2016). Traditionally, information on fracture attributes has come from well data (*Barthélémy et al.*, 2009; *Zeeb et al.*, 2013), but for reservoirs undergoing active stimulation at a greater depth, microseismic monitoring is the most effective and useful method to characterize the spatial distributions of fractures as well as fluid migration in the subsurface (*Maxwell and Urbancic*, 2001; *Maxwell et al.*, 2010; *Downie et al.*, 2013). This reservoir feedback occurs since the injected fluid reactivates pre-existing fractures and thus triggers microearthquakes (MEQs) (*Nicholson and Wesson*, 1990; *Majer et al.*, 2007; *Suckale*, 2009; *Ellsworth*, 2013; *Guglielmi et al.*, 2015). Hence it is of particular interest to evaluate the properties of fractures and to estimate the evolution of permeability - it has become essential and necessary to establish a model that accurately captures the hydraulic properties using the crucial feedback on stimulation contained within the observed MEQs.

A number of previous studies have provided insight into connections between in-situ MEQ data, inferred subsurface fluid migration and reservoir state. For example, the hydraulic diffusivity may be defined from the analysis of the spatio-temporal growth of the fluid-injection-induced seismic cloud (*Shapiro et al.*, 1997, 2006). If the leading edge of the seismic cloud is

presumed coincident with the fluid pressure front, then fluid diffusivity may be evaluated at reservoir scale (Hummel and Shapiro, 2012). However, this method ignores local geomechanical effects and variations in fracture permeability caused by hydroshearing. As a result, it cannot constrain permeability at finer resolution. In addition, a viable approach estimates a linkage between triggering fluid pressures and in-situ MEQ data (*Terakawa et al.*, 2010, 2012). This method integrates focal mechanism tomographic techniques and the Mohr-Coulomb failure criterion to indicate the fluid pressure along the fracture plane at the time of slip. Though this work provides constraint of a 3D distribution of fluid pressures in the stimulated zone of the reservoir, it does not include the contribution of the fracture network to the evolution of hydraulic properties (i.e. permeability heterogeneity) that are of principal interest for long-term EGS production. Meanwhile, *Ishibashi, et al.,* (2016) have tried to link the microseismicity to the permeability evolution by considering the topography of fracture/fault surfaces.

In the following, we propose a model to couple in-situ MEQ data and in-situ permeability at various reservoir scales. This model assumes that induced seismicity is controlled by the Mohr-Coulomb failure criterion and applies the moment magnitude of MEQs to recover fracture shear slip (*Stein and Wysession*, 2009). We explore two alternate approaches - (1) the cubic law based equivalent porous-medium method (EPM) and (2) Oda's crack tensor theory (*i.e.*, discrete fracture network (DFN)) to approximately define the permeability at a suitable representative elementary volume of the reservoir (REV).

The cubic law may be used to link permeability of the reservoir to the aperture of fractures, as a fundamental parameter that, in turn, may be indexed to seismicity. As fluid is usually channeled in permeable fractures that occupy only a small volume of the rock mass, it is important to characterize such hydraulic properties with consideration of the appropriate length scale. The hydraulic properties of the fracture network are captured as an equivalent permeability (*Snow*, 1969; *Tsang and Witherspoon*, 1981) for parallel or ubiquitous joints. An alternate

approach is to use a discrete fracture model (*Oda*, 1982) in the evaluation of permeability. Thus a model-fabric tensor may be used to describe the geometric characteristics of fractured rock and to determine transport characteristics (*Oda*, 1982, 1984).

In this study, we are primarily interested in the sensitivity of parameters that control stress state and fracture properties, and their significance in influencing the moment magnitude of MEQs and the evolution of permeability before and after seismic slip. We use a synthetic model to explore the features of the two methods and indicate the most significant factors that dominate the resolution of the evaluated permeability. The significance of this model lies in two aspects: (1) it allows abundant observations of MEQs to constrain the structure and distribution of in-situ permeability evolution of the reservoir; and (2) it reinforces the importance of determining high fidelity in-situ geomechanical parameters (*e.g.*, fracture orientation, fracture stiffness, dilation and friction) and moment tensors, as crucial in successfully constraining permeability evolution.

2. Methods

In the following, we first identify the assumptions and define the key features of the model, and use these to provide the rationale to recover the physical relations that couple both cubic law based equivalent porous medium method and Oda's crack tensor theory to the hydraulic behavior of fractures. The detailed coupling mechanism is introduced in Appendix A.

2.1 Assumptions

Naturally fractured reservoirs are complex and difficult to characterize due to the significant uncertainty in the subsurface. Experimental observations provide some constraints on the fluid-mechanical coupling (*Elsworth and Goodman*, 1986; *Polak et al.*, 2003) as illustrated in

Figure 2-1. Key concepts include that: **(1)** the seismicity induced by hydroshearing of fractures is controlled by the Mohr-Coulomb shear failure criterion. **(2)** The frictional coefficient of fractures evolves during seismic slip; in a seismic event, a velocity weakening fracture slips while friction drops from a static to a dynamic value. **(3)** In the reservoir, two types of fractures are considered **(i)** seismic fractures and **(ii)** aseismic fractures – the latter being fractures smaller than a critical radius such that stick slip cannot be triggered by increased fluid pressure and "failure" proceeds aseismically (*Fang et al.*, 2016). However, aseismic slip may also contribute to the permeability change of fractures (*Guglielmi et al.*, 2015), but its occurrence may not be on the same scale of a timeframe of the reservoir stimulation (*Peng and Gomberg*, 2010). In addition, fractures that slip seismically, but whose signal is below the recording threshold of $M_w < 0.0$ will not be recorded. For the stress drop selected here, these missing fractures have a radius less than ~10 m. **(4)** Neighboring fractures are mechanically isolated and do not interact. The direction and magnitude of the maximum principal stress (total stress) applied to the population of fractures remains unchanged.

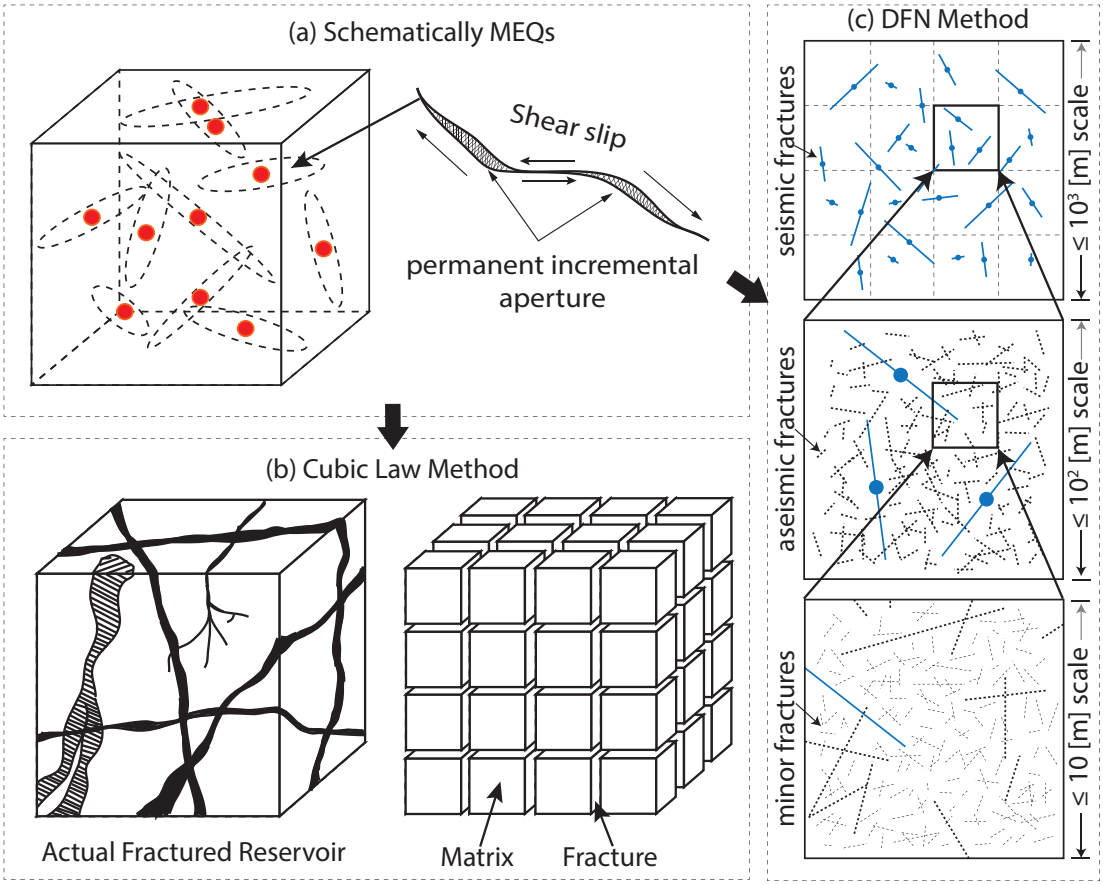

Figure **2-1**: **(a)** Schematic representation of observed MEQs and shear slip of fractures. **(b)** Equivalent porous-medium models of a heterogeneous fractured reservoir at a defined scale (modified from *Warren and Root* (1963)). **(c)** Schematic of distributed seismic fractures and aseismic fractures with scales from 10^1 to 10^3 m.

2.2 Equivalent Porous Medium Method

Pre-existing natural fractures are the most abundant structures in EGS reservoirs where fractures play a governing role in defining the hydraulic evolution of the reservoir (*Murphy et al.*, 1981; *Breede et al.*, 2013). The reservoir may be represented as an equivalent dual-porous medium with orthogonal fractures as illustrated in **Figure 2-1(b)**. The equivalent permeability of a rock mass can be expressed using the cubic law as (*Witherspoon et al.*, 1980):

$$k_m = \frac{{b_f}^3}{12 S_f} \tag{1}$$

where k_m, b_f, S_f are permeability, fracture aperture, and fracture spacing, respectively. As an important attribute of natural fracture systems, the fracture spacing can be problematic to estimate in the subsurface. Several methods of estimating fracture spacing have been previously introduced (*Priest et al.*, 1976; *Priest and Hudson*, 1981; *Bour and Davy*, 1999; *Ortega et al.*, 2006). As spatial variation in permeability is an important feature in this study, we intentionally use a simple scale-dependent approach to measure the average spacing expressed as:

$$\bar{S} = \frac{1}{n}\sum_{i=1}^{n} S_f^i = \frac{L_s}{n} \tag{2}$$

where $\bar{S}$ is the average fracture spacing and n is the number of fractures along a reference scan line length L_s. Because the fracture size can range from microscopic (*e.g.*, microcracks, veins and joints) to regional scales (large-scale joints, dikes and joint networks), we consider the fractures with size smaller than a critical length as aseismic fractures, and separately estimate the equivalent permeability for seismic fracture sets and aseismic fracture sets. These results are then superposed over a representative reservoir volume. Ignoring low-velocity stable sliding effects on the change in aperture of aseismic fractures, we extend **Eq. (1)** as follows:

$$k_{tot} = k_{seis} + k_{aseis} + k_{matrix} = \begin{cases} \dfrac{b_{nIni}^3}{12 S_{seis}} + \dfrac{b_{nIni}^3}{12 S_{aseis}} + k_{matrix}(Before) \\ \dfrac{b_{nFin}^3}{12 S_{seis}} + \dfrac{b_{nFin}^3}{12 S_{aseis}} + k_{matrix}(After) \end{cases} \tag{3}$$

Where k_{tot} is the total mean permeability; k_{seis} is the mean permeability of the seismic fracture network with fracture spacing S_{seis}; k_{aseis} is the mean permeability of aseismic fracture networks with fracture spacing S_{aseis}; and k_{matrix} is the mean permeability of matrix rock; b_{nIni} is the initial normal aperture of fracture and b_{nFin} is the final normal aperture after stimulation. In this scenario,

S_{aseis} is a constant value assuming an evenly distributed aseismic fracture network in the reservoir while S_{seis} varies with local seismic fracture network density that is defined by the scan line length L_s (*i.e.*, the imaginary mapping grid size).

2.3 Oda's Crack Tensor Theory

If greater details of reservoir fracture attributes (*e.g.*, the fracture size and orientation illustrated in **Figure 2-1(c)**) are available, then Oda's crack tensor theory can be used as an alternative method to map reservoir permeability. In a representative elementary volume V_{rev}, a fabric tensor considers the position, density, shape, dimension and orientation of fractures and averages these features in each arbitrary direction (*Oda*, 1982, 1984) as

$$F_{ij} = \rho_{frac} \frac{\pi}{4} \int_0^b \int_0^l \int_\Omega l^3 n_i n_j E(\bar{n}, l, b) d\Omega \cdot dl \cdot db \tag{4}$$

where F_{ij} is the fabric tensor; ρ_{frac} is the density of centers of fracture planes in the control volume; $E(\bar{n}, b, l)$ is a probability density function that describes the number of fractures with size (*i.e.*, trace length) in the range $l \sim (l + dl)$ and with apertures in the range $b \sim (b + db)$; $\boldsymbol{n}$ is the unit vector to the fracture plane oriented within a small solid angle $d\Omega$. This concept has been extended (*Oda*, 1985) to represent a permeability tensor based on the assumption that (i) the rock matrix is impermeable and (ii) the fluid is channeled in parallel fracture planes with volumetric flow rate proportional to b^3. Thus the permeability tensor k_{ij} is represented as,

$$k_{ij} = \lambda (P_{kk} \delta_{ij} - P_{ij}) \tag{5}$$

$$P_{ij} = \rho_{frac} \frac{\pi}{4} \int_0^b \int_0^l \int_\Omega l^2 b^3 n_i n_j E(\bar{n}, l, b) d\Omega \cdot dl \cdot db \tag{6}$$

where $\lambda = \lambda(F_{ij})$ is a dimensionless constant associated with fracture interconnectivity and is restricted between 0 and 1/12; δ_{ij} is the Kronecker delta; i and j represent Cartesian coordinate directions x, y, z. For a 2D problem, i and j are defined within x and y. In this method, the flow properties obtained from the fracture models consider the total sum of the areas of the fractures contained in each representative element volume. As fracture aperture is determined by injection pressure, fracture length, moment magnitude, and fracture orientation, the permeability tensor takes an average of all these attributes. For the purpose of comparing the results with EPM method, the mean permeability is calculated from the trace of permeability tensor in Oda's method.

3. In-Situ MEQ Data Analysis

According to the physical relations in **Figure 2-A1** in the appendix, we first explore the roles of essential parameters that control the MEQ-permeability coupling. The results of parametric analysis are reported in **Appendix B.1**. For demonstration purpose, we then define a synthetic discrete fracture network and perform a model study in **Appendix B.2**. We apply both EPM and Oda methods to estimate the reservoir permeability. Finally we discuss the limitation of study on the potential application for in-situ data analysis in **Appendix B.3**.

Differing from the synthetic fracture networks, natural reservoir fracture networks are notably more complex and difficult to characterize due to the uncertainties of in-situ stress and geologic discontinuities. For in-situ characterization, statistical field measurement of surface outcrops and fracture statistics from borehole imaging are essential and useful methods to reveal correlated fracture structure in near-surface formations. However, microseismic monitoring is the best way to characterize stimulated fracture networks at depth. In this section, we apply the

methods introduced in **Section 2** and **Appendix A** to analyze MEQ data from the first two rounds of the 2014 Newberry EGS stimulation (first round from Sept 24th to Oct 15th and second round from Nov 11th to Nov 20th) that followed an earlier 2012 stimulation (*Cladouhos et al*., 2016; *Fang et al*., 2016).

3.1 MEQ Observations and Assumptions

During the 2014 stimulation, about 350 MEQs were located by a fifteen-station microseismic array (**Figure 2-2**) [http://fracture.lbl.gov/Newberry/Location.txt] and the moment tensors analyzed (*Julian et al.*, 1998; *Miller et al.*, 1998). **Figure 2-3 (a)** indicates that all of these MEQs were located within a depth range from ~ 2000 *m* to ~ 3300 *m* while more than 75% of these seismic events occurred within the range ~ 2500 *m* to ~ 3300 *m*. Among all the MEQs, moment tensors (MT) are available for the 99 events with the best quality and identify the strikes and dip angles of corresponding fault planes. The possibility that these MEQs may be triggered by dynamic stresses associated with distant earthquakes is ruled out (*van der Elst and Brodsky*, 2010; *van der Elst et al.*, 2013), thus all the MEQs are considered to be the results of the stimulations.

The stress regime is a determining factor that defines the shear failure behavior of the fractures. For the Newberry EGS reservoir we use the normal faulting regime with E-W extension (minimum principal stress) according to World Stress Map. However, the observed focal mechanism solutions show combined double-couple (DC) and non-double-couple (non-DC) results, suggesting a possible strike-slip regime. Due to insufficient evidence to resolve this ambiguity, we use the stress regime aligned with the previous in-situ investigation and related THM simulations [*Cladouhos et al.*, 2011; *Davatzes and Hickman*, 2011; *Fang et al.*, 2016; *Rinaldi et al.*, 2015]. We constrain the vertical σ_v, maximum horizontal σ_H, and minimum

horizontal σ_h, stresses to be zero at the surface and use gradients of 24.1, 23.5 (N-S) and 14.9 (E-W) MPa/km.

To analyze all seismic events, we use these 99 focal mechanism solutions as a statistical reference and randomly assign the strike and dip angle values to non-MT seismic fractures based on a normal distribution. Apparent from **Figure 2-3 (b)** and **(c)**, strike orientations of the fractures from the John Day formation share similar ranges with those from the Intruded John Day formation. The dip angles of fractures in the "intruded" John Day formation, in comparison to those in the John Day formation, are more widely distributed.

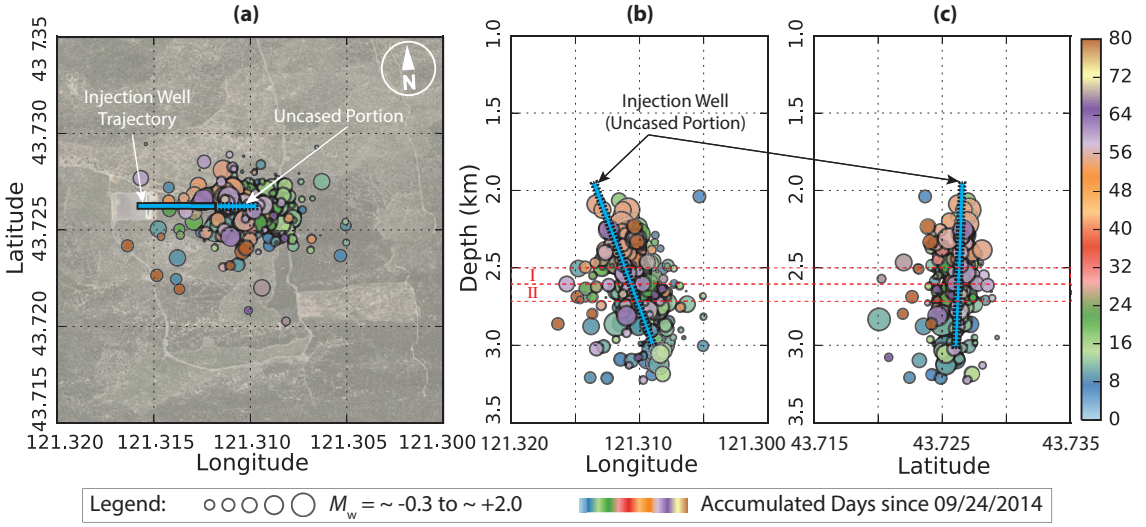

Figure **2-2**: **(a)** Map view of the distribution of seismic events in Newberry EGS stimulation (MEQ catalog from LBNL relocations). **(b)** Vertical view of MEQ distribution with Longitude. **(c)** Vertical view of MEQ distribution with Latitude. Circle size shows the magnitudes of MEQ from M_w = ~ -0.3 to ~ 2.0 and the color bar highlights the accumulated time since the beginning of the first round stimulation in 2014.

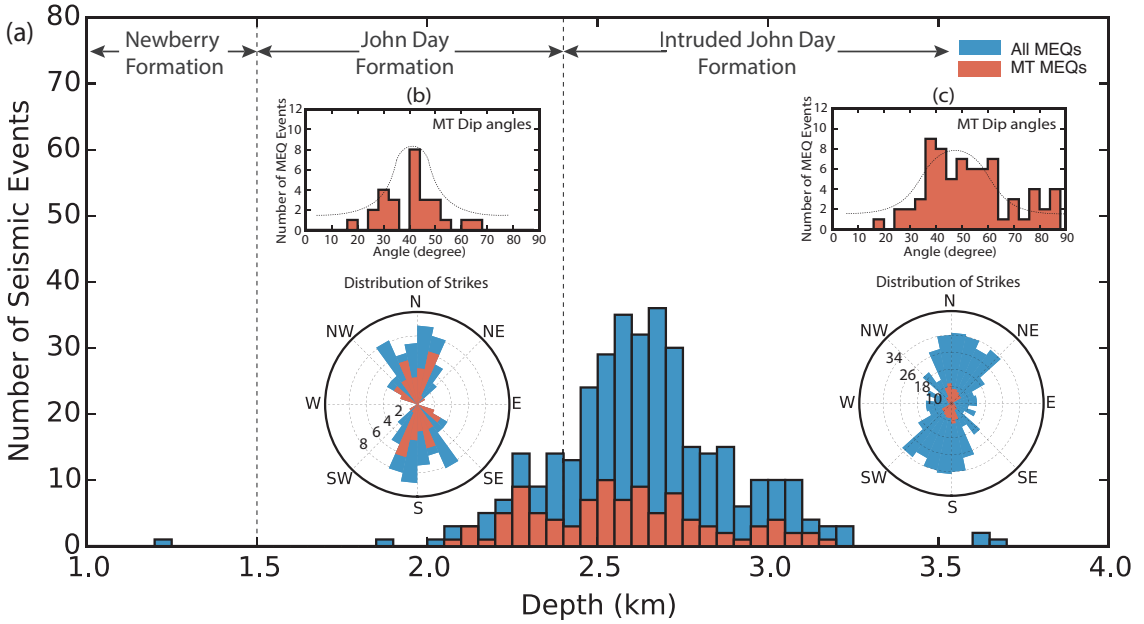

Figure **2-3**:**(a)** Histogram of MEQ frequency with depth. Red bars represent the events for which moment tensors are derived. **(b)** Dip angle and strike distribution of fractures in the John Day formation. **(c)** Dip angle and strike distribution of fractures in the "intruded" John Day formation.

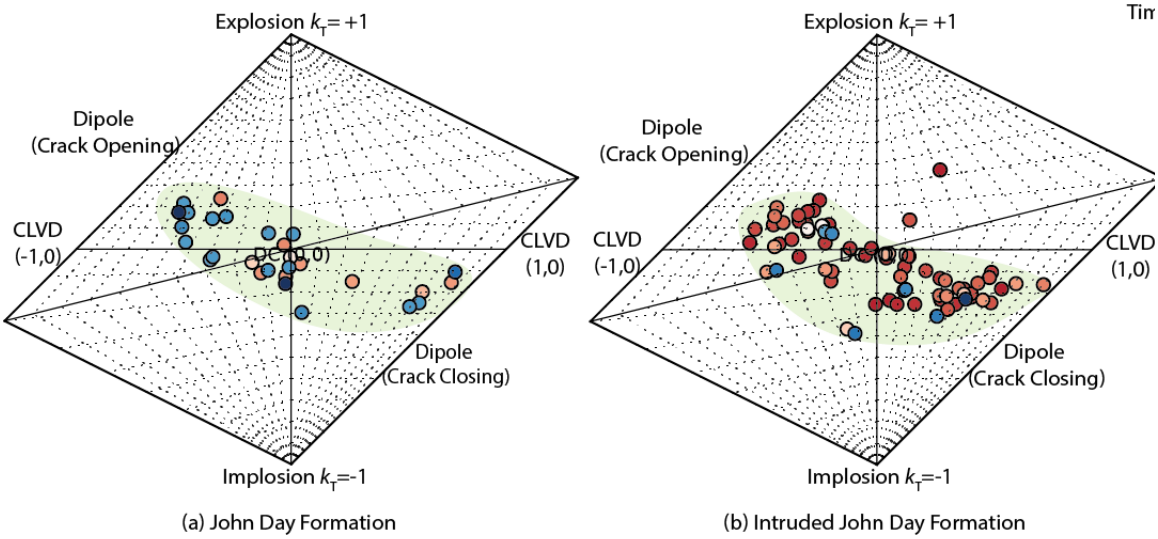

Figure **2-4**: **(a)** Source type (k_T value) plot of seismic events in the John Day formation **(b)** Source type plot of seismic events in the "intruded" John Day formation

The observed moment magnitudes of the MEQs are constrained between -0.28 and 2.0 with a *b*-value close to unity. This suggests that the sizes of the seismic fractures in the Newberry EGS reservoir are between meters and one-hundred meters and cannot exceed a thousand meters. Because these observed MEQs do not overprint each other spatially, this implies that each fracture is reactivated once. Thus each distinct seismic event is assumed to represent a pre-existing fracture in the reservoir. The source type, derived from the moment tensors of the observed seismic events in each geologic formation, is displayed on a two dimensional diagram in **Figure 2-4**. The statistical analysis of the source type indicates a negative averaged k_T value (mean = -0.055, standard deviation = 0.18) and suggests a slight volumetric compaction (*i.e.,* fracture closing) of fractures, which seems to contradict the expected dilatational behavior of fracture shearing and volume increase caused by injecting ~ 25000 m^3 of water. We resolve this contradiction by considering the combined effects of perturbation of thermal contraction of the reservoir matrix and the sequential shear compaction and dilation behaviors of fractures. Based on this assumption, we assign a statistically calculated k_T value to the non-moment tensor derived seismic events. Hence we are able to estimate the size of each fracture using **Eqs. (A3)** to **(A10)** and **Eqs. (A14)** to **(A21)** with the parameters in **Table 2-1**. The calculated radii of seismic fractures range from ~ 10 *m* to ~ 150 *m* and are illustrated in **Figure 2-5 (a)**, agreeing with the widely observed power-law distribution of fracture sizes in natural reservoirs (*Bonnet et al.*, 2001).

We assume that the fluid flow is essentially horizontal and in order to analyze spatial variations of permeability in the reservoir, we select two horizontal zones with the highest concentration of seismic events as an example where fracture traces are projected to a plane of zero-thickness (*Bundschuh and Arriaga*, 2010). The selected zones are constrained to between the depths of 2500 *m* ~ 2600 *m* and 2600 *m* ~ 2700 *m* respectively, and are bounded by latitude 43.715° to 43.735° and longitude -121.32° to -121.30° as indicated in **Figure 2-2 (b)** and **(c)**.

Compared to the reservoir scale (~$10^3 m$), the lengths of fracture traces (10^1 *m* to 10^2 *m*) are approximately one to two orders of magnitude smaller, suggesting a poor interconnection of these seismic fractures. Due to the low permeability of the rock matrix, there must be abundant pre-existing fractures within the reservoir as fluid conduits and connecting each observed seismic fracture (**Figure 2-1**). These particular small "infill" fractures remain aseismic due to their small size [*Scholz*, 1998]. In this study, the calculated critical fracture radius is ~10 *m*. Though the accuracy is limited by the seismic sensitivity, the size still appropriately agrees with previous frictional experimental results showing the smallest possible seismic fracture radius to be ~7 *m* (*Fang et al.*, 2016). Given the total number of seismic fractures N_{seis}, which denotes the number of MEQs in the interval represented by *l* and *l*+*dl*, the total number of aseismic fractures is estimated using the power law frequency-length of the fractures as described by **Eq. (B1)** in the appendix. Thus the total number of fractures N_{tot} is expressed as follows:

$$N_{tot} = N_{aseis} + N_{seis} = N_{aseis} + N_f + N_{uf} \tag{31}$$

where N_{aseis} is the population of aseismic fractures with fracture size less than critical length; N_{seis} is the number of seismic fractures including the population (N_{f}) of activated fractures with favorably oriented fractures and the population (N_{uf}) of unactivated fractures with relatively unfavorably oriented fractures. In this relation, it is noted that when wellhead pressure increases sufficiently, the non-activated fractures convert to "activated" fractures. In **Figure 2-5 (b)**, the number of non-activated fractures decreases with elevated wellhead pressures and declines to zero at P_{w}= ~20 MPa (relaxed with ~5 MPa thermal stress) that is close to the maximum operating wellhead pressure in the field. Over the period of the two rounds of the stimulation, we assume that N_{f} within the stimulated area has reached a maximum while N_{uf} approaches zero. Thus we set the known number of N_{f} to be the same as the number of observed MEQs and use the identified power-law distribution to invert for the approximate number of small fractures (aseismic fractures with size smaller than minimum size limit for unstable slip) within the

reservoir. However, the orientation and locations of the sub-seismic fractures are poorly characterized in the Newberry EGS reservoir. As a result, we use a homogeneous Poisson process to define the coordinates of the fracture centers that are uniformly but randomly distributed within the domain as illustrated in **Figure 2-6 (a)** to **(d)**. Thus the total reservoir permeability can be regarded as a superposition of seismic fracture permeability, aseismic fracture permeability and matrix permeability using **Eq. (3)**. The presumed matrix permeability and calculated aseismic/minor fracture permeability of each selected seismic zone are listed in **Table 2-1**.

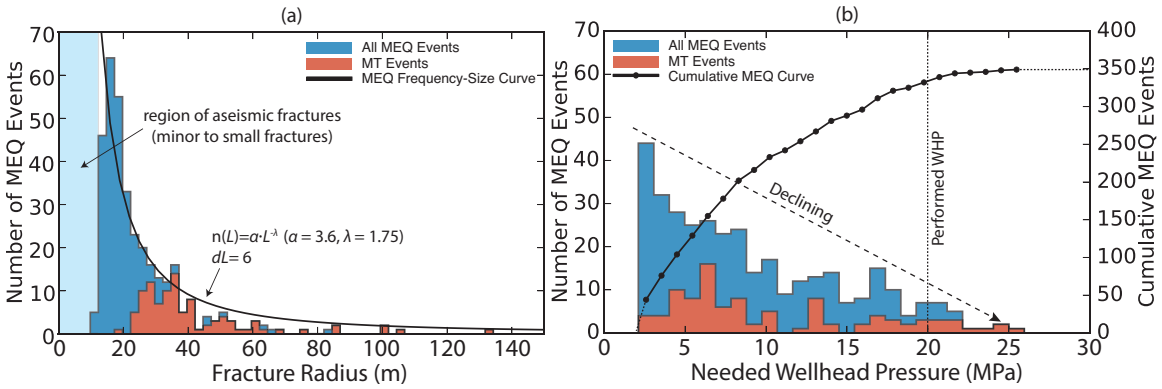

Figure **2-5**: **(a)** Size distribution of in-situ fractures calculated from MEQ data. **(b)** Fracture frequency with corresponding required reactivating wellhead pressures (extra fluid pressure).

3.2 Results and Interpretation

The relation between slip distances of seismic fractures and fracture size is presented in **Figure 2-6 (e)**, showing that slip increases linearly (from ~0.1 *mm* to ~2.1 *mm*) with growing fracture trace length. **Figure 2-7** presents the stimulated permeability map of the resulting discrete fractures in **Figure 2-6**, illustrating that the most permeable zone is created adjacent to the injection well in the first round stimulation (northwestern quadrant). After the second stimulation, the permeability is enhanced around the injection well. In the depth range 2500 *m* to

2600 *m*, enhanced permeability develops preferentially towards the southwest while in the depth range 2600 *m* to 2700 *m* the trend changes to the southeast. Comparing the mapped cellular permeability recovered by both the cubic law method and by Oda's crack tensor theory, it is expected that the cellular permeability evaluated by the cubic law is slightly higher than that by Oda's crack tensor theory - which is similar to observations within the synthetic reservoir. Thus it is more appropriate to adopt the equivalent mean permeability values estimated by Oda's crack tensor theory. The corresponding estimated equivalent mean permeability of each selected zone at both local reservoir scale (400 *m* × 400 *m*) and global reservoir scale (1500 *m* × 1500 *m*) are listed in **Table 2-2** and labeled in **Figure 2-8**. Confirmatory and independent estimates of the equivalent mean permeability may be recovered at reservoir scale using pore-pressure diffusion lengths (*Shapiro et al.*, 1997) and the 99 MT events. The diffusion-length versus time curves are shown in **Figure 2-8**, suggesting that the reservoir permeability evolved from $\sim 0.7\times10^{-15} m^2$ to $\sim 1.3\times10^{-15} m^2$ which are bounded by the estimated permeability values.

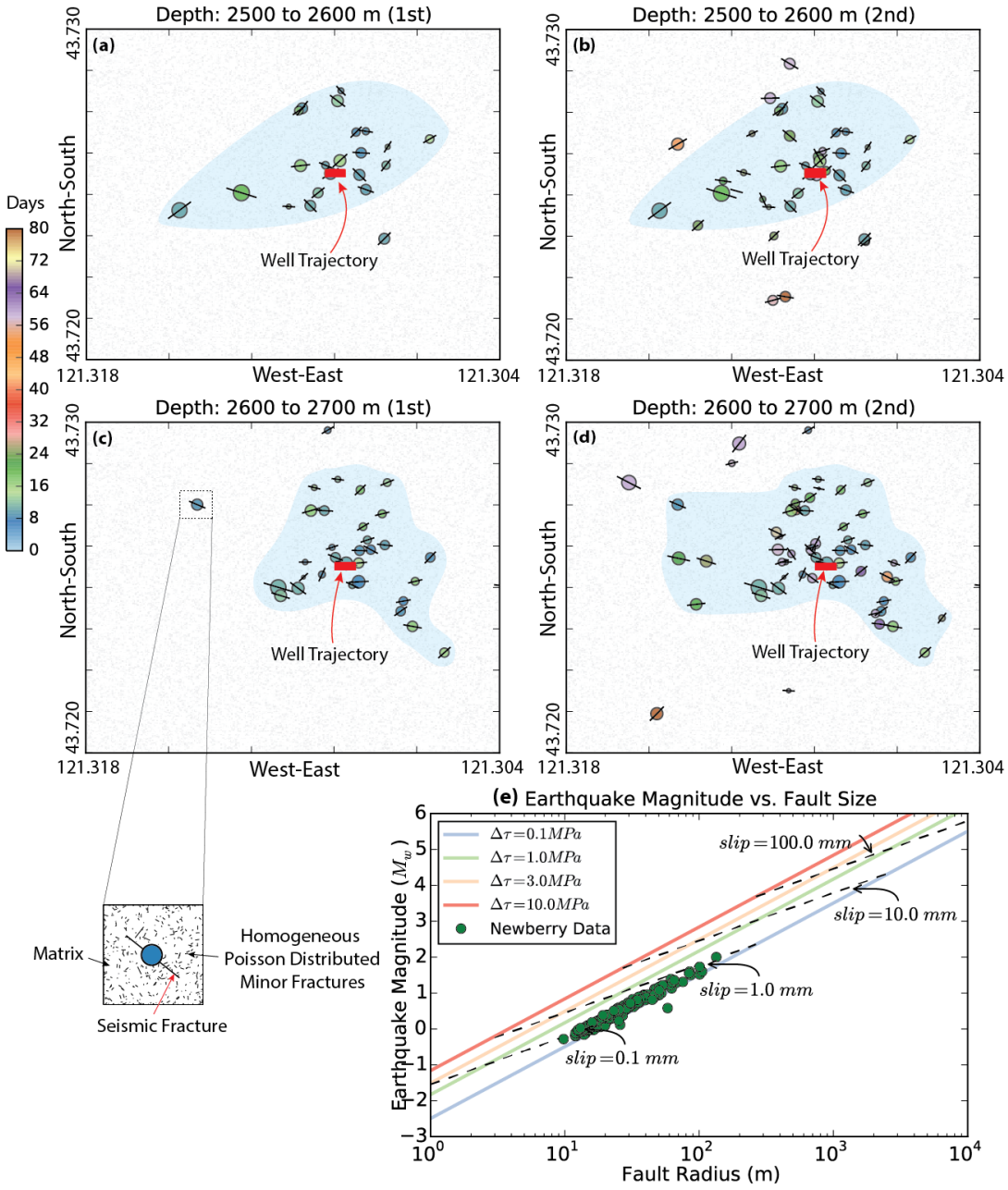

Figure **2-6**: **(a)** and **(b)** Map view of fracture distributions derived from microseismic events (both 1st and 2nd round stimulation) at a depth of 2500 *m* to 2600 *m*. **(c)** and **(d)** Map view of fracture distributions derived from microseismic events (both 1st and 2nd round stimulation) at a depth of 2600 *m* to 2700 *m*. **(e)** Relationship of fracture size and moment magnitude and the corresponding slip distances. Slip distances of fractures in Newberry EGS reservoir labeled as greed dots (Modified from *Zoback and Gorelick*, 2012 with parameters in **Table 2-1**)

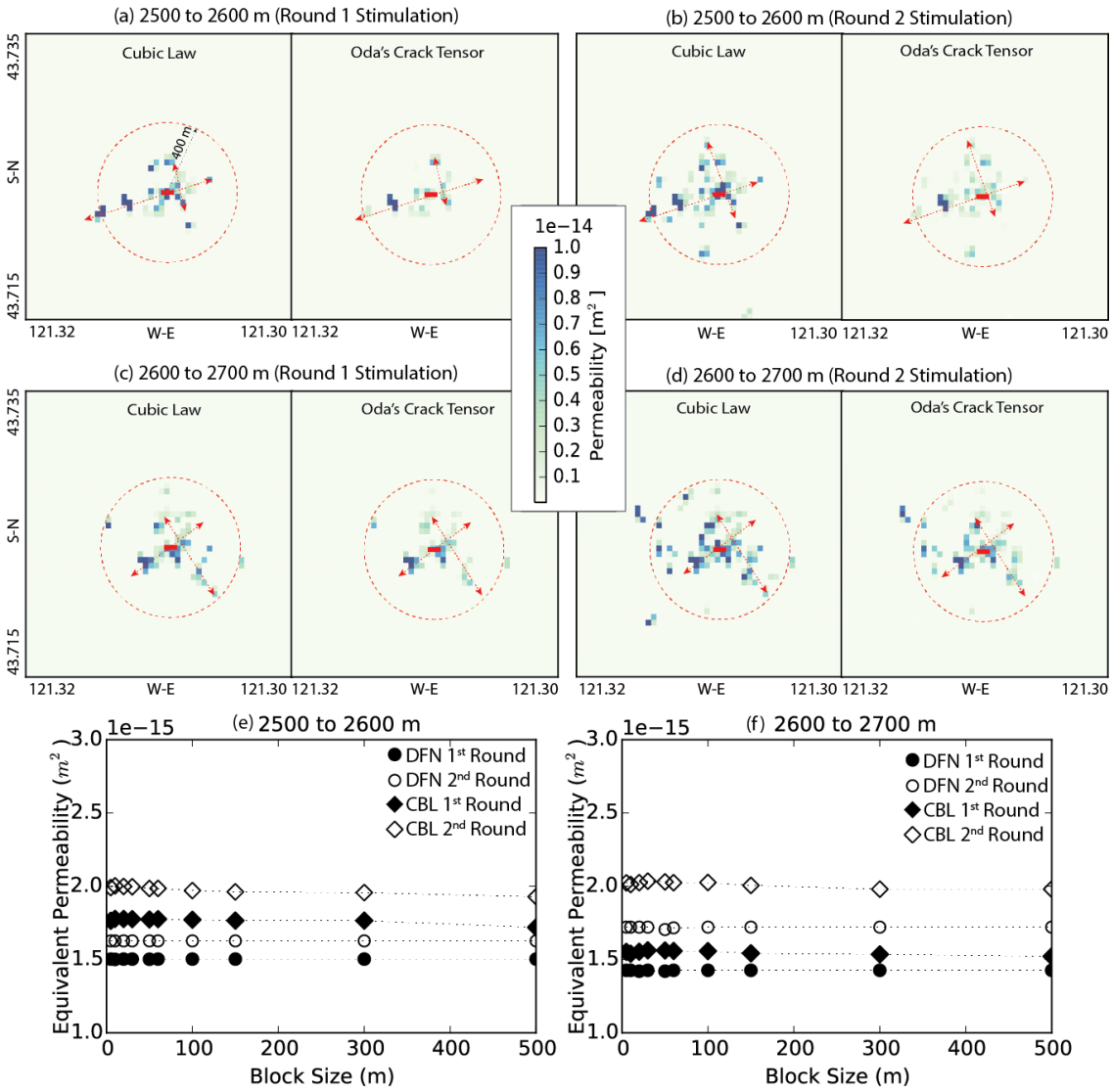

Figure **2-7**: **(a)** to **(d)** Celluar grid of stimulated permeability created using both cubic law and Oda's crack tensor methods for both 1st and 2nd round stimulation at a depth of 2500 *m* to 2600 *m* and 2600 *m* to 2700 *m* respectively. The grid size is 30 *m*. The effective diffusion length from the injection well is labeled as red circle with a radius of 400 *m*. **(e)** and **(f)** Comparison of effects of the grid size on the evaluated permeability using both cubic law and Oda's crack tensor methods.

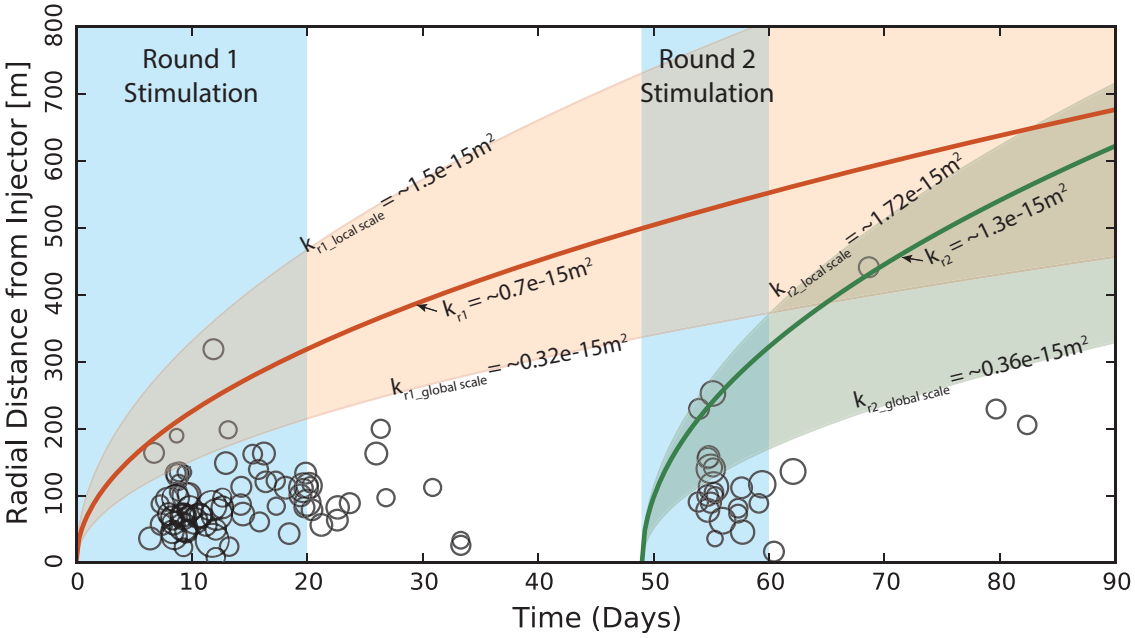

Figure **2-8**: Spatio-temporal distribution of induced MEQ during the 2014 Newberry EGS stimulation. Diffusion-length versus time curves constrain the equivalent permeabilities at both local and global reservoir scale.

Table **2-1**: Parameters used in the in-situ MEQ data

Parameters	**Symbol**	**Value**	**Units**
Frictional Parameter	$(a^*\text{-}b^*)$	0.0005	-
Reference velocity	V_0	1 ~ 2	*mm*/yr
Coseismic velocity	V_f	1	*m*/s
Vertical stress gradient	S_v/D_p	24.1	MPa/*km*
Max-horizontal stress gradient	S_H/D_p	23.5	MPa/*km*
Min-horizontal stress gradient	S_h/D_p	15.0	MPa/*km*
Pore-pressure gradient	P_0/D_p	8.8	MPa/*km*
Residual aperture	b_r	5.0e-5	*m*
Dilation angle	ψ	5.0	°
Bulk modulus	K	17.0	GPa
Poisson ratio	v	0.27	-
Non-linear fracture stiffness	α_s	0.218	1/MPa
Power law scaling exponent	e	0.5	$m^{1/2}$
Constant stress intensity factor	K_{IC}	8.0	MPa·$m^{1/2}$
REV size	L_{rev}	30	*m*
Matrix Permeability	k_{matrix}	1.0e-18	m^2
Minor Frac Perm (2500 to 2600 m)	k_{aseis}	2.6e-16	m^2
Minor Frac Perm (2600 to 2700 m)	k_{aseis}	2.1e-16	m^2

Table **2-2**: Parameters calculated from the model

Parameters	Units	Value	Units
Frictional drop	$\Delta\mu$	0.012	-
Fracture radius length	l_h	9.79 to 134.25	m
Slide distance	Δu_s	0.1 ~ 2.1	mm
Local Equiv Perm (Zone I, 1st)	k_{local_z1r1}	1.50e-15	m^2
Local Equiv Perm (Zone I, 2nd)	k_{local_z1r2}	1.63e-15	m^2
Local Equiv Perm (Zone II, 1st)	k_{local_z2r1}	1.43e-15	m^2
Local Equiv Perm (Zone II, 2nd)	k_{local_z2r2}	1.72e-15	m^2
Global Equiv Perm (Zone I, 1st)	k_{global_z1r1}	0.34e-15	m^2
Global Equiv Perm (Zone I, 2nd)	k_{global_z1r2}	0.36e-15	m^2
Global Equiv Perm (Zone II, 1st)	k_{global_z2r1}	0.32e-15	m^2
Global Equiv Perm (Zone II, 2nd)	k_{global_z2r2}	0.38e-15	m^2

Note: The local equivalent permeability refers to the permeability averaged over the area of the red dashed circle in **Figure 2-8** and the global equivalent permeability refers to the permeability averaged over the rectangular area in **Figure 2-8**.

4. Conclusion

In this work we present a model that links observed MEQs to the permeability of the fractured reservoir. The model links the established physical coupling between hydraulic and mechanical properties of fractures, hydroshearing-induced seismicity, and fracture permeability. We first investigate all the controlling parameters in the governing equations and define the most significant geophysical properties that determine the aperture of the fracture, for example, frictional evolution, fracture dilation angle, moment magnitude and the distribution of spatial seismicity (*i.e.* fracture populations, locations, spacing) and apply both the cubic law and Oda's crack tensor theory to a synthetic reservoir model as a demonstration. We then evaluate the

permeability distribution and its evolution using MEQ data from the stimulation of the Newberry EGS reservoir. Comparison of predicted permeabilities derived from each method identifies that **(1)** the resolution of permeability is largely determined by the cellular grid size and the fracture size for both Oda's crack tensor theory and cubic law methods while the evaluated equivalent permeability is independent of the limitation of the REV size. **(2)** With identical parameters, although Oda's crack tensor theory produces a more accurate estimation of permeability than that of the cubic law, the difference between the two estimates is less than one order magnitude. **(3)** In the reservoir, the most permeable zone is located within the densest zone of MEQs. This model has potential application for mapping permeability evolution using in-situ monitored MEQ data in both conventional and unconventional reservoirs at various scales. The study also suggests that higher reliability of the results can be achieved through improving the accuracy of the parameters that are used in the model. Particularly in practical operations, the quality of the observed moment tensors recovered through microseismic monitoring is key in determining the accuracy of the properties of the in-situ fractures and the recovered permeability of the EGS reservoir.

Appendix

A. Mechanism of MEQ-permeability Coupling

In **Eq. (3)** and **Eq**. **(6)**, the fracture aperture is an essential parameter in both the EPM and DFN (Oda) methods for estimating the permeability. Thus the central requirement for MEQ-permeability coupling is to correlate the fracture aperture to the moment magnitude. When pre-existing fractures are reactivated, the aperture changes due to the combined effects of normal opening, shear dilation and thermal expansion/contraction. It may be expressed as an integration of nonlinear normal stress-dependent aperture b_n and shear stress-dependent aperture b_s (*Rutqvist and Tsang*, 2003; *Rutqvist et al.*, 2004) as,

$$b = b_n + b_s \tag{A1}$$

$$b_n = b_r + (b_m - b_r) \cdot \exp[-\alpha_s \cdot (\sigma_n - P_f)] \tag{A2}$$

where b_r is the irreducible or residual aperture at maximum mechanical loading; b_m is the mechanical aperture under a small reference stress or zero stress; the difference of b_r and b_m is the maximum opening b_{max}; α_s [1/MPa] is the stiffness parameter determined from experiments; σ_n is the remote normal stress perpendicular to the fracture surface; and P_f is the internal fluid pressure in the fracture.

In this work, the local normal stress σ_n on the fracture plane can be determined via principal stresses at depth as,

$$S = diag[S_1, S_2, S_3] \tag{A3}$$

with stresses in a local coordinate system obtained by tensor transformation as,

$$S_G = R_G^T \cdot S \cdot R_G \tag{A4}$$

where R_G is the rotation matrix. Hence, the normal stress on a fault plane coordinate system can be calculated as,

$$\sigma_n = (S_G \cdot \hat{n}) \cdot \hat{n} \tag{A5}$$

The shear stresses τ_d and τ_s are defined in terms of both dip and strike directions as,

$$\tau_d = (S_G \cdot \hat{n}) \cdot \hat{n}_d \tag{A6}$$

$$\tau_s = (S_G \cdot \hat{n}) \cdot \hat{n}_s \tag{A7}$$

where $\hat{n}$ $\hat{n}_s$ $\hat{n}_d$ are vectors defined by the strike and dip angle of fracture planes.

According to the Mohr-Coulomb failure criterion, we assume that shear failure of a pre-existing fracture occurs at the critical normal stress σ_n^{crt} and critical fluid pressure $P_f = P_f^{crt}$, expressed as,

$$P_f^{crt} = \sigma_n - \tau / \mu_s \tag{A8}$$

$$\sigma_n^{crt} = \sigma_n - P_f \tag{A9}$$

$$P_{wf} = P_f^{crt} - P_0 \tag{A10}$$

where τ is the magnitude of total shear stress acting on the fracture plane; μ_s is the static frictional coefficient of the fracture; P_{wf} is the minimum wellhead pressure required to reactivate pre-existing fractures and P_0 is the hydrostatic pore pressure of the reservoir before the injection of fluids. When the increased fluid pressure triggers fracture reactivation, the shear aperture b_s will increase and its magnitude is controlled by the slip distance Δu_s and fracture dilation angle ψ, as,

$$b_m = \alpha_f \cdot l_h^e \tag{A12}$$

$$\alpha_f = \frac{K_{IC} \cdot (1-\nu^2)}{E \cdot \sqrt{\pi / 8}} \tag{A13}$$

where α_f is the pre-factor defined by the constant stress intensity factor K_{IC} with units of m^{1-e}, Young's modulus E, and Poisson's ratio ν; l_h refers to fracture radius or half length; and e is the power-law scaling exponent. However, the shear aperture component b_s is only applicable when shear failure occurs during a seismic event. If fluid pressure is insufficient to induce shear failure on fractures, the permeability evolution is dominated by the effective normal stress. When shear failure occurs, seismic energy M_0^s (seismic moment) is released during shear slip. The seismic moment is determined from the moment tensor M of individual seismic events and can be further correlated to the moment magnitude as,

$$M_0 = M_0^s = G \cdot A \cdot \Delta u_s \tag{A14}$$

$$M_w = \frac{2}{3}(\log M_0 - 16.1) \tag{A15}$$

where G is the average shear modulus of the fracture embedded within the rock mass, A is the area of the fracture surface, and Δu_s is the average displacement over the entire fracture surface quantified as (*Brune*, 1970),

$$\Delta u_s = \frac{2}{3}\Delta u_{\max} = \frac{2}{3}\frac{\Delta\tau}{K_s} \tag{A16}$$

$$\Delta\tau = \Delta\mu \cdot \sigma_n^{crt} \tag{A17}$$

$$K_s = \frac{G \cdot \eta}{l_h} \tag{A18}$$

where $\Delta u_{\max}$ is the maximum final dislocation for 100% stress drop $\Delta\tau$; K_s is the fracture stiffness; l_h is the fracture radius; assuming that fractures in the reservoir are penny-shaped, thus the

geometric factor η has the value of $7\pi/24$ (*Dieterich*, 1986, 1992); $\Delta\mu$ is the frictional change in shear slip and can be further extended as,

$$\Delta\mu = \left|a^* - b^*\right| \cdot \ln(\frac{V_f}{V_0}) \tag{A19}$$

where (a^*-b^*) is the frictional parameter (*i.e.,* (a^*-b^*) < 0 for velocity weakening and (a^*-b^*) > 0 for velocity strengthening), V_f is the coseismic shear velocity (~10^0 *m*/*s* to 10^2 *m*/*s*) of fractures, and V_0 is the reference velocity or background velocity (~ 1 to 2 *mm*/*yr*) of fractures.

In reality, the moment tensor of observed MEQs in EGS reservoirs may indicate mixed failure modes (*Julian et al.*, 1998; *Miller et al.*, 1998). The focal mechanism solutions of these events show combined double-couple (DC) and non-double-couple (non-DC) components, suggesting both fracture shearing and opening/closing and making the estimation of fracture size more difficult. To simplify the complexity, we define two end-member MEQ scenarios: (i) pure double-couple MEQs as a result of pure shear failure, in which the seismic moment can be expressed by **Eq. (A14)** and (ii) pure non-double-couple MEQs due to pure tensile failure where the seismic moment is defined as follows (*Foulger and Long*, 1984),

$$M_0 = M_0^n = 2G \cdot A \cdot \Delta u_n \tag{A20}$$

where Δu_n refers to the normal displacement of crack opening or closing. Most fracture deformations occur between these two end-members. To quantify the deformational contribution from each end-member, *Hudson et al.*, (1989) defines the source-type parameter k_T as the measure of the relative size of the dilatational component of the moment tensor. Assuming a linear decomposition from the seismic moment, the quantitative relation of the two end-member MEQ scenarios can be defined as,

$$M_0 = M_0^s + M_0^n = c_s \cdot M_0 + c_n \cdot M_0 = G \cdot A(c_s \cdot \Delta u_s + 2c_n \cdot \Delta u_n) \tag{A21}$$

$$c_s = 1 - \left|k_T\right| \tag{A22}$$

$$c_n = |k_T| \tag{A23}$$

where parameters c_s and c_n denote the contributions from each end-member MEQ mode and parameter k_T ranges between -1 to 1. In this case, the fracture is assumed to be in opening when k_T is greater than 0 and in closing when k_T is smaller than 0 (*Hudson et al.*, 1989).

These prior physical relations (*i.e.*, **Eq. (A1)** to **(A21)**) are schematically illustrated in **Figure 2-A1**. The spatial distribution of MEQs can imply local stress magnitudes on fractures if reservoir stress gradients are well constrained. The reservoir stress state and reservoir material properties, which control the fracture properties, can be quantitatively correlated to MEQ magnitudes by fracture size. As a result, the permeability enhancement resulting from shear slip or crack opening during EGS stimulation can be estimated.

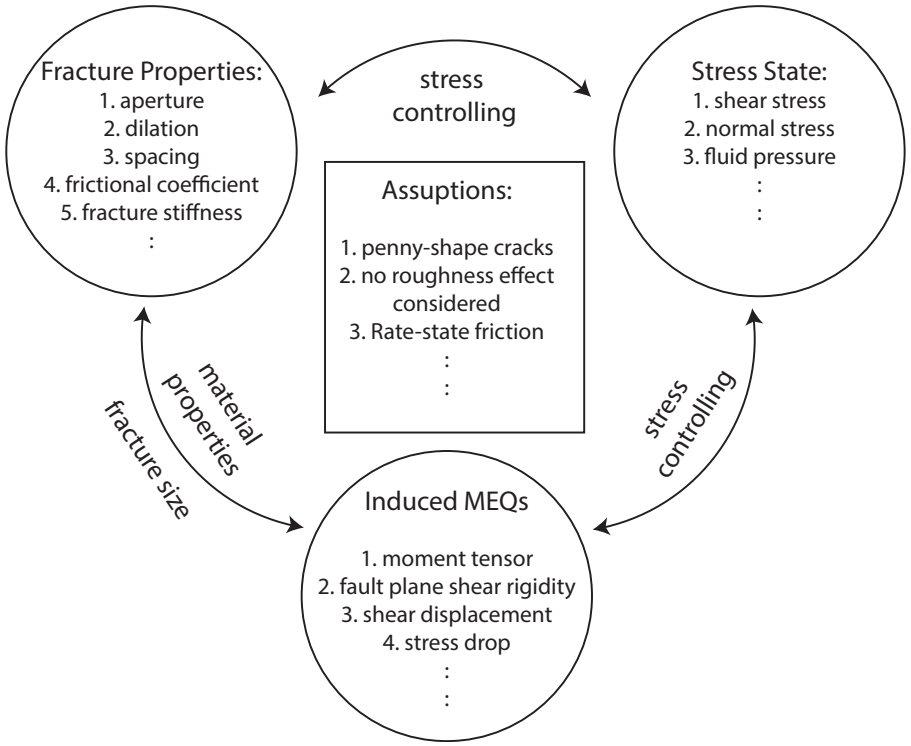

Figure **2-A1**: Schematic of relations among physical properties and variables that controlling MEQ-permeability coupling.

B. Model Study

B.1 Parametric Analysis

The physical relations described in **Appendix A** involve parameters that may influence the variations of the hydraulic properties of fractures. These geomechanical controls can be attributed to both normal and shear stress effects on the fracture aperture and permeability. To understand how sensitive the permeability evolution of fractures is to these parameters, and the potential effects of these sensitivities on the interpretation of the *in-situ* MEQ data, we perform a parametric study on permeability evolution of fractures with radius from 1 *m* to 1000 *m* at a depth of 3 *km*. The values of parameters are listed in **Table 2-B1**. The fractures are assumed to fail in shear.

First, a log-linear relationship between seismic moment magnitude (M_w) and the fracture size is indicated in **Figure 2-B1**. For a fracture with a fixed orientation (defined by θ), a larger frictional drop results a larger moment magnitude. If the frictional drop is fixed, shear slip of a fracture with a favorable orientation induces a slightly larger moment magnitude than that of unfavorably oriented fractures. Since friction is a function of the minerals comprising the fractures (*Ikari et al.*, 2011; *Fang et al.*, 2016) and the fracture orientation (*i.e.*, strike and dip) can be partially reflected through the moment tensor, it can be speculated that, for a precisely calculated seismic moment magnitude and a well-determined fracture orientation, an accurately measured frictional change can reduce the error in calculating the fracture size.

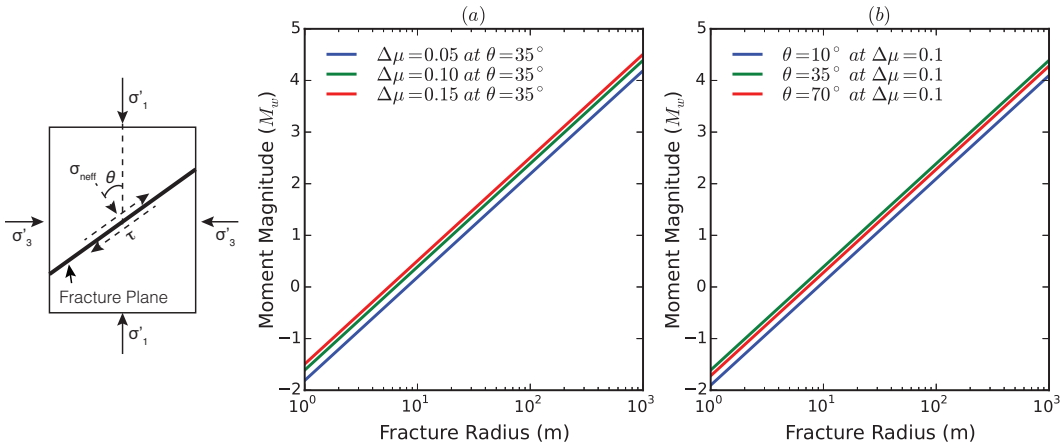

Figure **2-B1**: Log-linear relationship between seismic moment magnitude (M_w) and the fracture size for a single fracture: **(a)** Effect of frictional difference $\Delta\mu$ on moment magnitude M_w; **(b)** Effect of localized orientation of fracture (defined as the angle between fracture plane normal and direction of maximum principal stress) on moment magnitude M_w. The stresses are listed in **Table 2-B1**.

The variation of fracture aperture with respect to fracture radius may be defined. The initial aperture and evolving aperture of fractures without shear failure, termed b_{ini} and b_n respectively, are controlled by the fluid pressure that acts on the fracture walls and enlarges the normal aperture of fractures. When the fluid pressure reaches the critical magnitude P_f^{crt} and the shear stress acting on the fracture exceeds its strength, shear slip occurs, resulting in an enhancement of aperture, b_s. Therefore, the fluid pressure plays a role as a trigger for seismic slip. According to **Eq. (A9)**, **(A16)** and **(A17)**, the magnitude of the shear aperture b_s is constant when the fluid pressure reaches and exceeds a critical value. Changes in normal aperture and to permeability are largely reversible in the elastic loading and unloading cycle. When fluid pressure is dissipated, the reduced changes in normal aperture are negligible compared to those changes in the aperture that are permanently enhanced by shear slip. Hence, the fluid pressure is an important factor in triggering failure but exerts less significant control in the evolution of permanent aperture. In addition to fluid pressure, the following parameters may affect the evolution of aperture in normal, b_n and in shear, b_s modes as separated into three categories: (1)

reservoir deformability characteristics, for example, the bulk modulus K of the reservoir; (2) fracture deformability characteristics, such as residual aperture b_r and dilation angle ψ; and (3) fracture material properties, such as fracture toughness K_{IC} and frictional drop $\Delta\mu$. As presented in **Figure 2-B2 (a)** and **(b)**, both the bulk modulus K and the fracture toughness K_{IC} have little effect on the normal aperture b_n, particularly for fracture radii less than ~10 m. The effect of residual aperture b_r on normal aperture is apparent in comparing results for both K and K_{IC} (**Figure 2-B2 (c)**). From **Figure 2-B2 (d)** to **(f)**, the change in aperture due to shear slip of fractures larger than ~10^2 m is mainly controlled by the bulk modulus K, the shear dilation angle ψ and the frictional drop $\Delta\mu$. In summary, the physical linkage between the moment magnitude of seismic events and the fracture aperture is most strongly influenced by the controlling factors of frictional drop, fracture dilation angle, and fracture embedded bulk modulus that define the magnitudes of stress drop, shear deformation and the resistance to shear deformation respectively. However, these parameters have only a limited effects on small fractures (< 10 m) where the corresponding moment magnitude is less than ~0 to ~ +0.2.

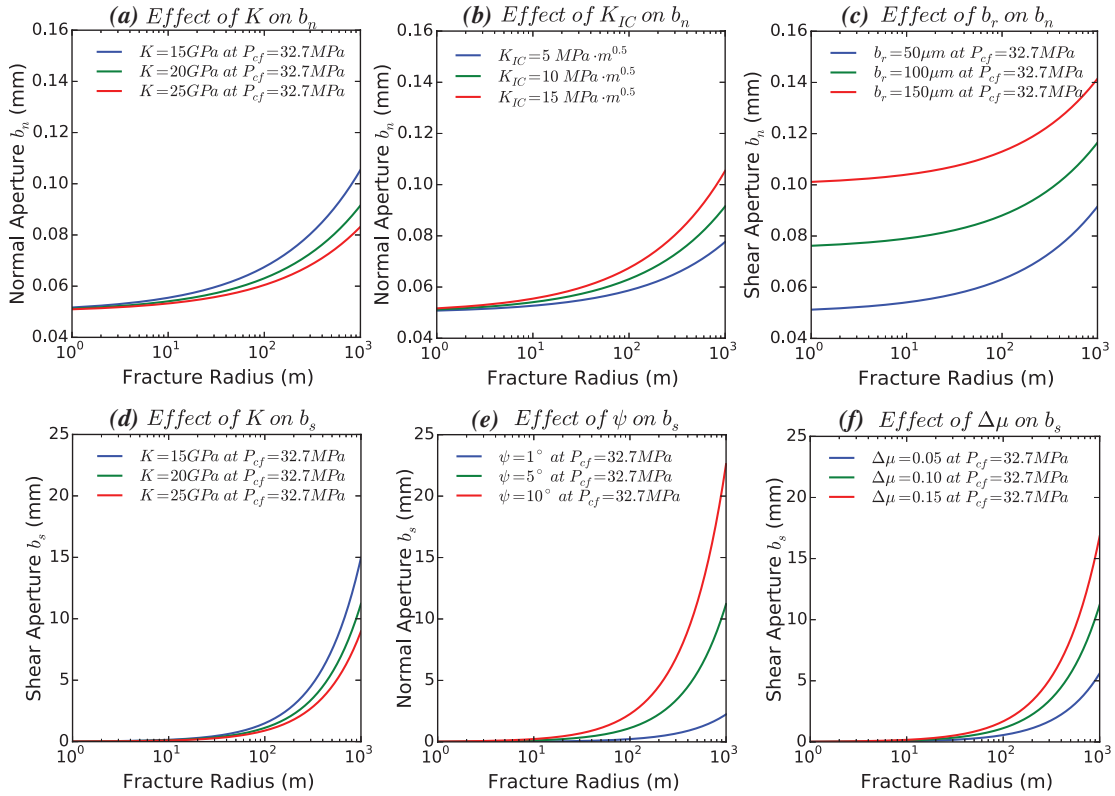

Figure **2-B2**: Graph panel shows the geomechanical parameters that may affect the evolution of aperture in normal, $b_{n,}$ and in shear, b_s. **(a)** Effect of bulk modulus K on normal aperture b_n; **(b)** Effect of fracture toughness K_{IC} on normal aperture b_n; **(c)** Effect of residual aperture b_r on normal aperture b_n; **(d)** Effect of bulk modulus K on shear aperture b_s ; **(e)** Effect of fracture dilation angle ψ on shear aperture b_s; **(f)** Effect of frictional difference $\Delta\mu$ on shear aperture b_s.

Table **2-B1**: Ranges of values used in parametric study

Parameters	Symbol	Value	Units
Fracture radius	l_h	1-1000	m
Frictional drop	$\Delta\mu$	0.05, 0.10, 0.15	-
Maximum Principal Stress	S_1	72.0	MPa
Minimum Principal Stress	S_3	45.0	MPa
Pore-pressure	P_0	30.0	MPa
Residual aperture	b_r	5.0e-5, 1.0e-4, 1.5e-4	m
Dilation angle	ψ	1, 5, 10	°
Bulk modulus	K	15, 20, 25	GPa
Poisson ratio	v	0.25	-
Non-linear fracture stiffness	α_s	0.3	1/MPa
Power law scaling exponent	e	0.5	$m^{1/2}$
Constant stress intensity factor	K_{IC}	5, 10, 15	MPa·$m^{1/2}$

B.2 A Synthetic Model Study

The parametric study of physical relations described in **Appendix B.1** suggests that the most important factors determining the evolution of fracture aperture are the geomechanical fracture properties (*i.e.*, residual aperture, frictional drop and dilation angle). To create a reliable map of permeability in the fractured reservoir using the EPM or Oda's crack tensor theory, it is essential to identify the distribution and orientation of discrete fractures and to define the size of the representative element volume (REV) of the fractured domain in which the reservoir permeability is to be mapped. We build a synthetic forward DFN-MEQ-Permeability model to quantify the relationship between the induced MEQs and the permeability of the reservoir, and to explore how the mapped permeability varies with the selected size of the REV.

In the synthetic model, we set 300 penny-shaped discrete fractures at a prescribed depth of 3 *km* within a reservoir with an edge dimension of 1500 *m* × 1500 *m* (**Figure 2-B3 (a)**). The strike of these fractures are randomly oriented at azimuths (to North) within 30° to 150° and 210° to 330°, with arbitrary dip magnitudes within 0° to 90°. The lengths of fractures are statistically arranged from 20 *m* to 300 *m* (**Figure 2-B3 (b)**), which can be described *via* the fracture length-frequency power law as follows,

$$n(l) = \rho_c \cdot l^{-\xi} \tag{B1}$$

where $n(l)$ is the density distribution of the number of fractures present in the interval [l, l+dl]; ρ_c is a fracture density constant and ξ is an exponent.

Assuming a gravitational lithostatic stress gradient of 24 MPa/km (2,450 kg/m^3) and hydrostatic pore pressure gradient of 10 MPa/*km*, the total vertical stress on the synthetic reservoir is fixed at S_v=72 MPa. We set three potential Andersonian (*Anderson*, 1905) stress regimes (normal faulting: S_v=72 MPa, S_{Hmax}=63 MPa, S_{hmin}=45 MPa P_p=30 MPa; strike-slip faulting: S_{Hmax}=75 MPa, S_v=72 MPa, S_{hmin}=45 MPa; reverse faulting: S_{Hmax}=78 MPa, S_{hmin}=75 MPa, S_v=72 MPa) for the fractured reservoir. Before fluid injection, the stress states in each faulting regime are plotted in **Figure 2-B4 (c)** to **(e)**. The fractures in the normal faulting and strike-slip faulting regimes are much closer to the Mohr-Coulomb failure than those of the reverse faulting regime, suggesting that the fractures in the normal and strike-slip faulting regimes will be most prone to fail by fluid injection. Based on observations from the World Stress Map, most current EGS projects are located in normal faulting or strike-slip faulting regime. Hence, in the following analysis, we particularly select the normal faulting stress regime where the maximum horizontal and minimum horizontal stresses are in the North-South and the East-West directions respectively. Moreover, the wellhead pressure is imposed on the entire domain rather than originating from a point source. The geomechanical parameters of fractures are listed in **Table 2-B2**.

When a wellhead pressure of 5 MPa is applied to the fractured reservoir, the most favorably oriented fractures are reactivated first, as indicated in **Figure 2-B4 (a)**. The resulting seismic moment magnitudes range from M_w= ~ -0.3 to ~ +2.4. Increasing the wellhead pressure to 15 MPa (**Figure 2-B4 (b)**) evidently reactivates the fractures that are less favorably oriented. Although the population of MEQs increases significantly due to the elevated fluid pressure, the variation of moment magnitudes remains within this confined range – this is a result of the fracture size distribution. It can be speculated that large moment magnitude seismic events are more likely to occur in the reservoir only where large-radius fractures are embedded. It is also noted that the apertures of fractures are enhanced by the seismic events and are proportional to the moment magnitudes.

The previous analysis implies that a zone within the reservoir with a high density of seismic events is expected to be more permeable. This prediction is examined by mapping the permeability of the synthetic reservoir after injection at wellhead pressures of 5 MPa and 15 MPa respectively and by employing both cubic law and Oda's crack tensor methods. The results obtained from these two methods (**Figures 2-B5** and **2-B6**) indicate that the permeability is relatively high in the block where fractures are present. The evaluated permeability in each block is not constant but varies with the selected size of the REV. When the block size is increased, the hydraulic properties of fractures are averaged over a larger area, resulting in a declining magnitude of permeability in the block. The evaluated permeability from the cubic-law method in each block is slightly larger than that evaluated from Oda's crack tensor theory.

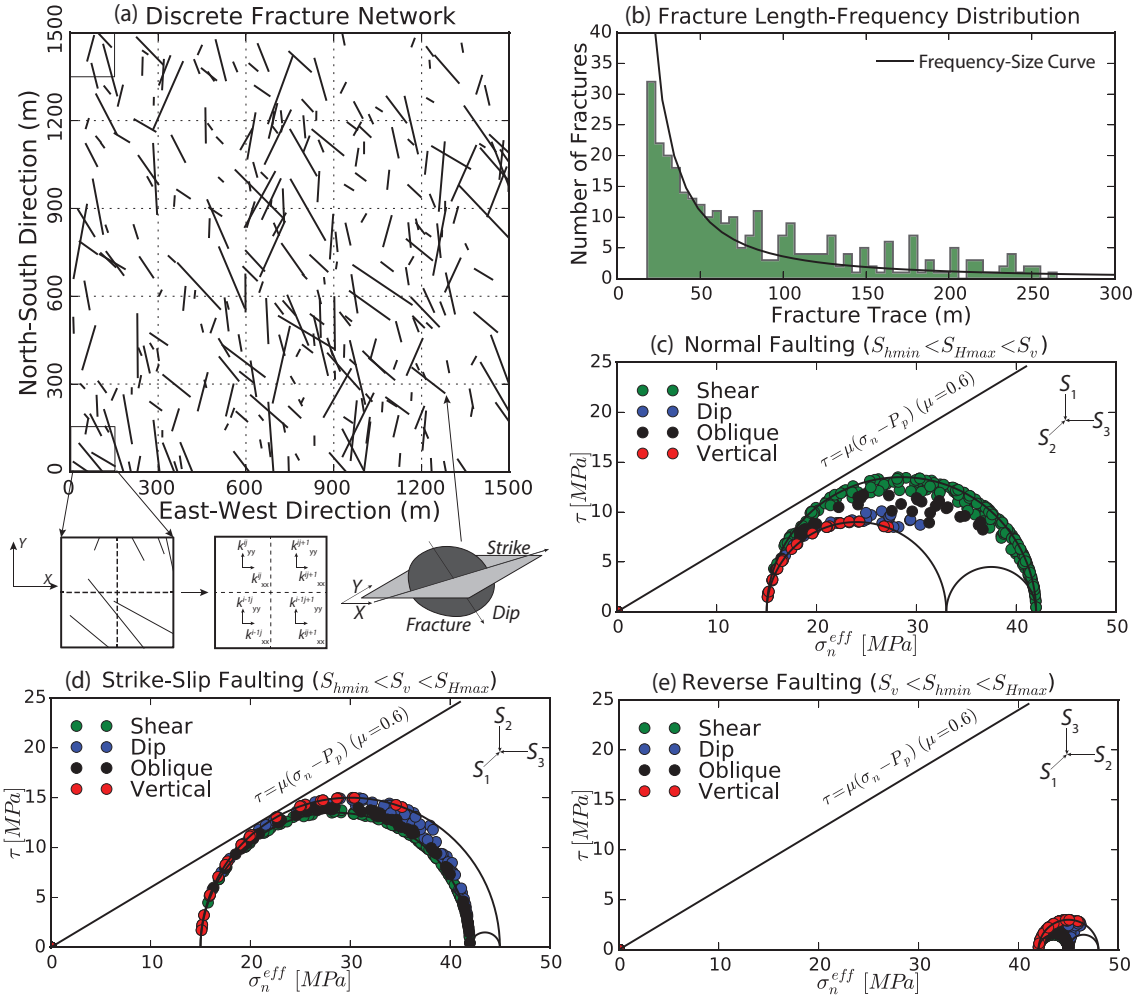

Figure **2-B3**: **(a)** Generated 2D discrete fracture network where the fracture diameters cut the same plane; **(b)** Size-frequency distribution of generated fractures; **(c)** to **(e)** Mohr circles of discrete fractures subject to hydrostatic stresses of three faulting regimes at a depth of 3 km with known vertical stress gradient (normal faulting: S_v=72 MPa, S_{Hmax}=63 MPa, S_{hmin}=45 MPa P_p=30 MPa; strike-slip faulting: S_{Hmax}=75 MPa, S_v=72 MPa, S_{hmin}=45 MPa; reverse faulting: S_{Hmax}=78 MPa, S_{hmin}=75 MPa, S_v=72 MPa).

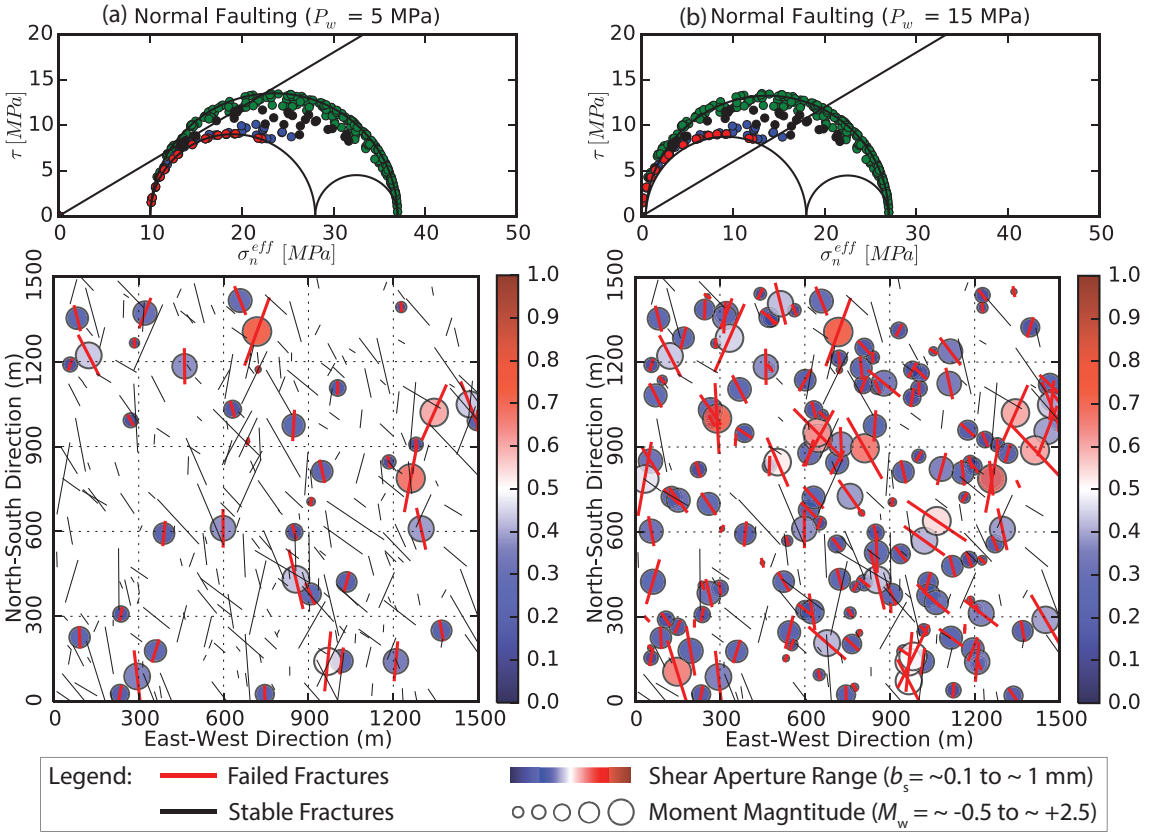

Figure **2-B4**: **(a)** and **(b)** Mohr circles of discrete fractures in the domain that are respectively subject to a wellhead pressure of 5 MPa and 15 MPa in the normal faulting stress regime (S_v=72 MPa, S_{Hmax}=63 MPa, S_{hmin}=45 MPa P_p=30 MPa). Stable fractures and reactivated fractures are explicitly illustrated in the reservoir domain. The moment magnitude and the fracture apertures are correlated for each shear-reactivated fracture.

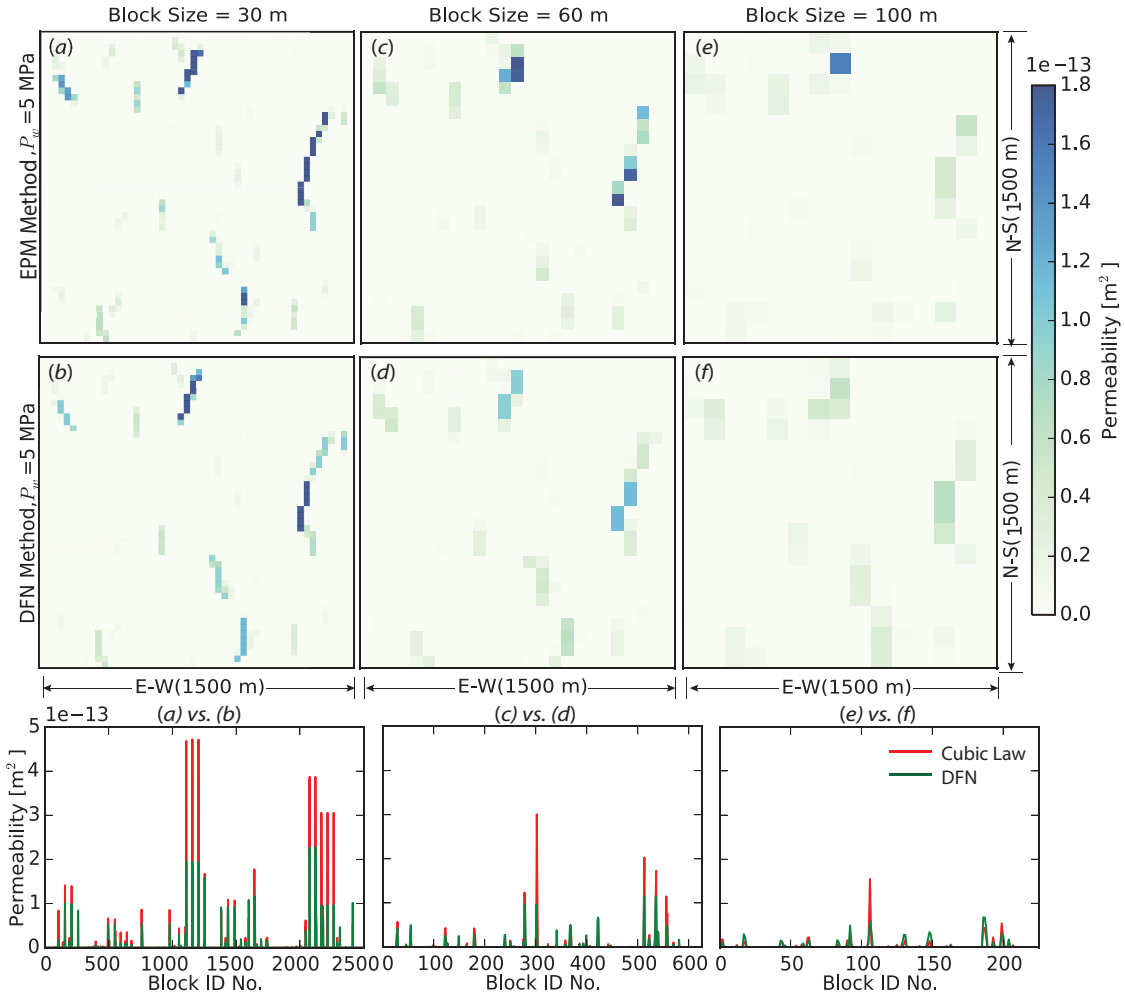

Figure **2-B5**: Map of the estimated mean permeability of the synthetic fractured reservoir with different REV sizes. The reservoir is subject to a wellhead pressure at 5 MPa using the EPM method versus the DFN method. **(a)** to **(b)**: the comparison of permeability map of a small REV (30 m) by each method; **(c)** to **(d)**: the comparison of permeability map of a small REV (60 m) by each method; **(e)** to **(f)**: the comparison of permeability map of a small REV (100 m) by each method. The comparisons of permeability of each block are show in the lower portion of the diagram.

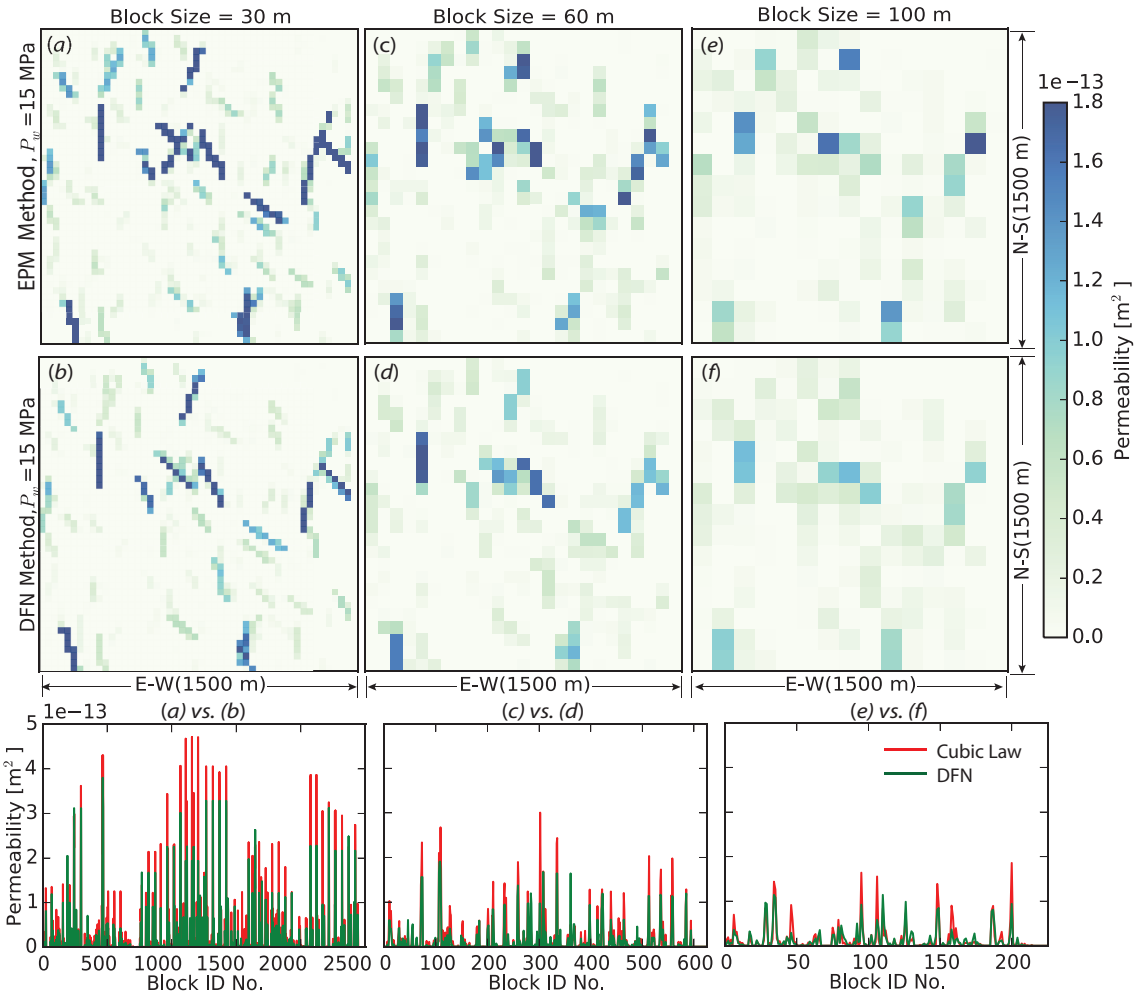

Figure **2-B6**: Map of the estimated mean permeability of the synthetic fractured reservoir with different REV sizes. The reservoir is subject to a wellhead pressure at 15 MPa using the EPM method versus DFN method. **(a)** to **(b)**: the comparison of permeability map of a small REV (30 m) by each method; **(c)** to **(d)**: the comparison of permeability map of a small REV (60 m) by each method; **(e)** to **(f)**: the comparison of permeability map of a small REV (100 m) by each method. The comparisons of permeability of each block are show in the lower portion of the diagram.

B.3 Discussion

In reality, the in-situ stress conditions and observed MEQ data are far more complex than those assumed in the model. For the future prospect of this application method, three essential improvements are recommended to lift the limitations of the model: (1) Couple the real-time dynamic stress balance in the MEQ-perm coupled model. On the framework of this model, a rigorous DFN implemented mechanical model can be developed but may at the expenses of computational efficiency at reservoir scale. (2) Understand the fundamental relationship between shear deformation and permeability evolution. This model employed simple shear dilation – permeability enhancement relation. However, some laboratory and numerical experiments have revealed the contradictory observations that permeability decreases with shear slip due to the generated wear product or gouge (*Vogler et al.*, 2016; *Fang et al.*, 2017; *Wang et al.*, 2017). In addition, thermal contraction induced aseismic deformation may play a significant role in changing fracture permeability in reservoir stimulation. This process may particularly occur in the aseismic domain. These effects of governing relationships are worth considering in the model. (3) Enhance the accuracy of the measured geophysical parameters. From the parametric analysis and the synthetic model study, the reliability of these methods is affected by the geomechanical properties, populations, location and orientations of fractures. These properties, for example, the frictional drop during fracture slip, the modulus of the matrix, and the residual fracture apertures can be measured in the laboratory. The population and spatial information of fractures can be confirmed from geophysical observations with high resolution.

Table **2-B2**: Parameters used in the synthetic model analysis

Parameters	**Symbol**	**Value**	**Units**
Frictional drop	$\Delta\mu$	0.050	-
Vertical stress	S_V	72.0	MPa
Max-horizontal stress	S_H	63.0	MPa
Min-horizontal stress	S_h	45.0	MPa
Pore-pressure	P_p	30.0	MPa
Injection pressure	P_w	5, 15	MPa
Residual aperture	b_r	5.0e-5	m
Dilation angle	ψ	5.0	°
Bulk modulus	K	20.0	MPa
Poisson ratio	ν	0.25	-
Non-linear fracture stiffness	α_s	0.3	1/MPa
Power law scaling exponent	e	0.5	$m^{1/2}$
Constant stress intensity factor	K_{IC}	10.0	MPa·$m^{1/2}$
REV size	ΔL	30, 60, 100	m
Fracture number	n_f	300	-
Fracture trace length	L_f	20 to 300	m
Matrix Permeability	k_m	1.0e-18	m^2
Source Plot Parameter	k_T	0	-

Nomenclature

a^*	Frictional parameter (direct effect)
A	Area of the fracture surface
b	b-value
b^*	Frictional parameter (evolution effect)
b_f	Fracture aperture
b_m	Mechanical aperture at low reference stress
b_n	Normal aperture
b_nIni	Normal aperture before fluid injection
b_nFin	Normal aperture after fluid injection
b_r	Residual aperture
b_s	Shear aperture
c_n	Contribution coefficient of tensile failure
c_s	Contribution coefficient of shear failure
D_p	Reservoir depth
e	Power-law scaling exponent
E	Young's modulus
F_ij	Fabric tensor
G	Average shear modulus of fracture embedded rock mass
k_ij	Permeability Tensor
k_m	Mean permeability
k_matrix	Matrix permeability
k_T	Source-type parameter
k_tot	Total mean permeability
k_aseis	Mean permeability of aseismic fracture networks
k_seis	Mean permeability of seismic fracture networks
K	Bulk modulus
K_IC	Stress intensity factor
K_s	Fracture stiffness
l	Fracture trace length
l_h	Fracture radius or half length
L_rev	Scan line or imaginary grid size (REV size)
M	Moment tensor
M_0	Seismic moment
M_0^s	Seismic moment for pure shear failure
M_0^n	Seismic moment for pure tensile failure
M_w	Moment magnitude
n	Number of fracture
$\boldsymbol{n}$	Unit vector of the fracture plane
N_tot	Total population of fractures
N_aseis	Population of aseismic fractures with size less than critical length
N_seis	Population of seismic fractures
N_f	Number of activated fractures
N_uf	Number of unactivated fractures

P_0	Initial hydrostatic pore pressure
P_f	Total fluid pressure
P_f^{crt}	Critical fluid pressure at which the pre-existing fracture is reactivated
P_w	Wellhead pressure
P_wf	Minimum wellhead pressure required to reactivate pre-existing fractures
$\bar{S}$	Average fracture spacing
S_{aseis}	Spacing of aseismic fractures
S_{seis}	Spacing of seismic fractures
S_f	Fracture spacing
S_H	Maximum horizontal stress
S_h	Minimum horizontal stress
S_v	Vertical stress
S_1	Maximum principal stress
S_3	Minimum principal stress
Δu_max	Maximum final dislocation for 100% stress drop
Δu_n	Average normal opening
Δu_s	Average shear displacement
V_rev	Representative elementary volume
V_0	Reference velocity
V_f	Coseismic velocity
α_f	Pre-factor of aperture-to-length scaling law
α_s	Stiffness parameter
ρ_frac	Density of centers of fracture planes
ρ_c	Density constant in fracture length-frequency power law
δ_{ij}	Kronecker delta
η	Fracture geometric factor
θ	Fracture orientation
λ	Nondimensional coefficient
μ_s	Static friction coefficient
$\Delta\mu$	Frictional drop
ν	Poisson's ratio
ξ	Exponent in the fracture length-frequency power law
σ_n	Normal stress
σ_n^{crt}	Critical normal stress at which the pre-existing fracture is reactivated
τ	Shear stress
$\Delta\tau$	Stress drop
$d\Omega$	Solid angle
ψ	Dilation angle

Acknowledgement

This work is a partial result of support provided by DOE Grant DE-EE002761. This support is gratefully acknowledged. The authors would like to thank the anonymous reviewers for their valuable comments and suggestions to improve the quality of the paper.

References

Anderson, E. M. (1905), The dynamics of faulting, *Trans. Edinburgh Geol. Soc.*, *8*(3), 387–402.

Barthélémy, J. F., M. L. E. Guiton, and J. M. Daniel (2009), Estimates of fracture density and uncertainties from well data, *Int. J. Rock Mech. Min. Sci.*, *46*(3), 590–603, doi:10.1016/j.ijrmms.2008.08.003.

Bonnet, E., O. Bour, N. E. Odling, P. Davy, I. Main, P. Cowie, and B. Berkowitz (2001), Scaling of fracture systems in geological media, *Rev. Geophys.*, *39*(3), 347–383, doi:10.1029/1999RG000074.

Bour, O., and P. Davy (1999), Clustering and size distributions of fault patterns: Theory and measurements, *Geophys. Res. Lett.*, *26*(13), 2001, doi:10.1029/1999GL900419.

Breede, K., K. Dzebisashvili, X. Liu, and G. Falcone (2013), A systematic review of enhanced (or engineered) geothermal systems: past, present and future, *Geotherm. Energy*, *1*(1), 4, doi:10.1186/2195-9706-1-4.

Brune, J. N. (1970), Tectonic stress and the spectra of seismic shear waves from earthquakes, *J. Geophys. Res.*, *75*(26), 4997–5009, doi:10.1029/JB075i026p04997.

Bundschuh, J., and M. C. S. Arriaga (2010), Introduction to the Numerical Modeling of Groundwater and Geothermal Systems: Fundamentals of Mass, Energy and Solute Transport in Poroelastic Rocks. Taylor & Francis, Boca Raton

Cladouhos, T. T., S. Petty, O. Callahan, W. Osborn, S. Hickman, and N. Davatzes (2011), The Role of Stress Modeling in Stimulation Planning at the Newberry Volcano EGS Demenstration Project, in *Thirty Sixth Workshop on Geothermal Reservoir Engineering*, vol. SGP-TR-191, p. 8, Stanford University, Stanford, California.

Cladouhos, T.T., Petty, S., Swyer, M.W., Uddenberg, M.E., Grasso, K., Nordin, Y., 2016. Results from Newberry Volcano EGS Demonstration, 2010–2014. Geothermics 63, 44–61. doi:https://doi.org/10.1016/j.geothermics.2015.08.009

Davatzes, N. C., and S. H. Hickman (2011), Preliminary analysis of stress in the Newberry EGS Well NWG 55-29. GRG Trans. 35, 323-332.

Dieterich, J. H. (1986), A model for the nucleation of earthquake slip, in *Earthquake Source Mechanics*, vol. 37, pp. 37–47, AGU, Washington, DC.

Dieterich, J. H. (1992), Earthquake nucleation on faults with rate-and state-dependent strength, *Tectonophysics*, *211*(1–4), 115–134, doi:http://dx.doi.org/10.1016/0040-1951(92)90055-B.

Downie, R., J. Xu, D. Grant, R. Malpani, and A. Viswanathan (2013), Microseismic parameters help to calibrate complex hydraulic fracture models, *World Oil*, (SPEC. SUPPL. MARC), 13–16.

Ellsworth, W. L. (2013), Injection-Induced Earthquakes, *Science (80-.).*, *341*(6142), 142–149, doi:10.1126/science.1225942.

van der Elst, N. J., and E. E. Brodsky (2010), Connecting near-field and far-field earthquake triggering to dynamic strain, *J. Geophys. Res. Solid Earth*, *115*(B7), B07311, doi:10.1029/2009JB006681.

van der Elst, N. J., H. M. Savage, K. M. Keranen, and G. A. Abers (2013), Enhanced Remote Earthquake Triggering at Fluid-Injection Sites in the Midwestern United States, *Science (80-.).*, *341*(6142), 164–167, doi:10.1126/science.1238948.

Elsworth, D., and R. E. Goodman (1986), Characterization of rock fissure hydraulic conductivity using idealized wall roughness profiles, *Int. J. Rock Mech. Min. Sci. Geomech. Abstr.*, *23*(3), 233–243, doi:http://dx.doi.org/10.1016/0148-9062(86)90969-1.

Fang, Y., S. A. M. den Hartog, D. Elsworth, C. Marone, and T. Cladouhos (2015), Anomalous distribution of microearthquakes in the Newberry Geothermal Reservoir: Mechanisms and implications, *Geothermics*, doi:10.1016/j.geothermics.2015.04.005.

Fang, Y., Elsworth, D., Wang, C., Ishibashi, T., Fitts, J.P., 2017. Frictional stability-permeability relationships for fractures in shales. J. Geophys. Res. Solid Earth 122, 1760–1776. doi:10.1002/2016JB013435

Foulger, G., and R. E. Long (1984), Anomalous focal mechanisms: tensile crack formation on an accreting plate boundary, *Nature*, *310*(5972), 43–45.

Guglielmi, Y., F. Cappa, J.-P. Avouac, P. Henry, and D. Elsworth (2015), Seismicity triggered by fluid injection–induced aseismic slip, *Sci.* , *348* (6240), 1224–1226, doi:10.1126/science.aab0476.

Hudson, J. A., R. G. Pearce, and R. M. Rogers (1989), Source type plot for inversion of the moment tensor, *J. Geophys. Res.*, *94*(B1), 765, doi:10.1029/JB094iB01p00765.

Hummel, N., Shapiro, S.A., 2012. Microseismic estimates of hydraulic diffusivity in case of non-linear fluid-rock interaction. Geophys. J. Int. 188, 1441–1453. doi:10.1111/j.1365-246X.2011.05346.x

Ikari, M. J., C. Marone, and D. M. Saffer (2011), On the relation between fault strength and frictional stability, *Geology*, *39*(1), 83–86, doi:10.1130/g31416.1.

Ishibashi, T., N. Watanabe, H. Asanuma, and N. Tsuchiya (2016), Linking microearthquakes to fracture permeability evolution, *Geofluids Special Thermatic Issues "Crustal Permeability"* 49-64.

Julian, B. R., A. D. Miller, and G. R. Foulger (1998), Non-double-couple earthquakes 1. Theory, *Rev. Geophys.*, *36*(4), 525, doi:10.1029/98RG00716.

Majer, E. L., R. Baria, M. Stark, S. Oates, J. Bommer, B. Smith, and H. Asanuma (2007), Induced seismicity associated with Enhanced Geothermal Systems, *Geothermics*, *36*(3), 185–222, doi:http://dx.doi.org/10.1016/j.geothermics.2007.03.003.

Maxwell, S. C., and T. I. Urbancic (2001), The role of passive microseismic monitoring in the instrumented oil field, *Lead. Edge*, *20*(6), 636, doi:10.1190/1.1439012.

Maxwell, S. C., J. Rutledge, R. Jones, and M. Fehler (2010), Petroleum reservoir characterization using downhole microseismic monitoring, *Geophysics*, *75*(5), 75A129, doi:10.1190/1.3477966.

Miller, A. D., G. R. Foulger, and B. R. Julian (1998), Non-double-couple earthquakes 2. Observations, *Rev. Geophys.*, *36*(4), 551, doi:10.1029/98RG00717.

Murphy, H. D., J. W. Tester, C. O. Grigsby, and R. M. Potter (1981), Energy extraction from fractured geothermal reservoirs in low-permeability crystalline rock, *J. Geophys. Res.*, *86*(B8), 7145, doi:10.1029/JB086iB08p07145.

Nicholson, C., and R. L. Wesson (1990), Earthquake hazard associated with deep well injection: A report to the U.S. Environmental Protection Agency, *US Geol. Surv. Bull.*, *1951*, 74pp.

Oda, M. (1982), *Fabric Tensor for Discontinuous Geological Materials*. *Soils and Foundations*, 22(4), 96-108

Oda, M. (1984), Similarity rule of crack geometry in statistically homogeneous rock masses, *Mech. Mater.*, *3*(2), 119–129, doi:http://dx.doi.org/10.1016/0167-6636(84)90003-6.

Oda, M. (1985), Permeability tensor for discontinuous rock masses, *Geotechnique,* 35(4), 483-495.

Olson, J. E. (2003), Sublinear scaling of fracture aperture versus length: An exception or the rule?, *J. Geophys. Res. Solid Earth*, *108*(B9), 2413, doi:10.1029/2001JB000419.

Ortega, O. J., R. A. Marrett, and S. E. Laubach (2006), A scale-independent approach to fracture intensity and average spacing measurement, *Am. Assoc. Pet. Geol. Bull.*, *90*(2), 193–208, doi:10.1306/08250505059.

Peng, Z., Gomberg, J., 2010. An integrated perspective of the continuum between earthquakes and slow-slip phenomena. Nat. Geosci. 3, 599–607. doi:10.1038/ngeo940

Polak, A., D. Elsworth, H. Yasuhara, A. S. Grader, and P. M. Halleck (2003), Permeability reduction of a natural fracture under net dissolution by hydrothermal fluids, *Geophys. Res. Lett.*, *30*(20), doi:Artn 2020Doi 10.1029/2003gl017575.

Priest, S. D., and J. a. Hudson (1981), Estimation of discontinuity spacing and trace length using scanline surveys, *Int. J. Rock Mech. Min. Sci. Geomech. Abstr.*, *18*(3), 183–197, doi:16/0148-9062(81)90973-6.

Priest, S. D., S. D. Priest, J. A. Hudson, and J. A. Hudson (1976), Discontinuity spacings in rock, *Int. J. Rock Mech. Min. Sci. Geomech. Abstr.*, *13*(5), 135–148, doi:10.1016/0148-9062(76)90818-4.

Rinaldi, A. P., J. Rutqvist, E. L. Sonnenthal, and T. T. Cladouhos (2015), Coupled THM

modeling of hydroshearing stimulation in tight fractured volcanic rock, *Transp. Porous Media*, *108*(1), 131–150, doi:10.1007/s11242-014-0296-5.

Rutqvist, J., and C. F. Tsang (2003), Analysis of thermal-hydrologic-mechanical behavior near an emplacement drift at Yucca Mountain, *J. Contam. Hydrol.*, *62–63*, 637–652, doi:10.1016/S0169-7722(02)00184-5.

Rutqvist, J., C. F. Tsang, and Y. Tsang (2004), Analysis of stress and moisture induced changes in fractured rock permeability at the yucca mountain drift scale test, in *Elsevier Geo-Engineering Book Series*, vol. Volume 2, edited by S. Ove, pp. 161–166, Elsevier.

Scholz, C. H. (1998), Earthquakes and friction laws, *Nature*, *391*(6662), 37–42, doi:Doi 10.1038/34097.

Shapiro, S. A., E. Huenges, and G. Borm (1997), Estimating the crust permeability from fluid-injection-induced seismic emission at the KTB site, *Geophys. J. Int.*, *131*(2), F15–F18, doi:Doi 10.1111/J.1365-246x.1997.Tb01215.X.

Shapiro, S. A., C. Dinske, and E. Rothert (2006), Hydraulic-fracturing controlled dynamics of microseismic clouds, *Geophys. Res. Lett.*, *33*(14), doi:Artn L14312Doi 10.1029/2006gl026365.

Snow, D. T. (1969), Anisotropic Permeability of Fractured Media, *Water Resour. Res.*, *5*(6), 1273–&, doi:Doi 10.1029/Wr005i006p01273.

Stein, S., and M. Wysession (2009), *An Introduction to Seismology, Earthquakes, and Earth Structure*, Wiley.

Suckale, J. (2009), Induced seismicity in hydrocarbon fields, *Adv. Geophys.*, *51*(09), 1976–1984, doi:10.1016/S0065-2687(09)05107-3.

Terakawa, T., A. Zoporowski, B. Galvan, and S. A. Miller (2010), High-pressure fluid at hypocentral depths in the L'Aquila region inferred from earthquake focal mechanisms, *Geology*, *38*(11), 995–998, doi:10.1130/g31457.1.

Terakawa, T., S. A. Miller, and N. Deichmann (2012), High fluid pressure and triggered earthquakes in the enhanced geothermal system in Basel, Switzerland, *J. Geophys. Res. Solid Earth*, *117*(B7), B07305, doi:10.1029/2011JB008980.

Tsang, Y. W., and P. A. Witherspoon (1981), Hydromechanical behavior of a formable rock fracture subject to normal stress, *J. Geophys. Res.*, *86*(B10), 9287–9298.

Vogler, D., F. Amann, P. Bayer, and D. Elsworth (2016), Permeability Evolution in Natural Fractures Subject to Cyclic Loading and Gouge Formation, *Rock Mech. Rock Eng.*, *49*(9), 3463–3479, doi:10.1007/s00603-016-1022-0.

Wang, C., D. Elsworth, and Y. Fang (n.d.), Influence of Weakening Minerals on Ensemble Strength and Slip Stability of Faults, *J. Geophys. Res. Solid Earth*, n/a-n/a, doi:10.1002/2016JB013687.

Warren, J. E., and P. J. Root (1963), The Behavior of Naturally Fractured Reservoirs, *Soc. Pet. Eng. J.*, *3*(3), 245–255, doi:10.2118/426-PA.

Witherspoon, P. A., J. S. Y. Wang, K. Iwai, and J. E. Gale (1980), Validity of Cubic Law for fluid flow in a deformable rock fracture, *Water Resour. Res.*, *16*(6), 1016–1024, doi:10.1029/WR016i006p01016.

Zeeb, C., E. Gomez-Rivas, P. D. Bons, and P. Blum (2013), Evaluation of Sampling methods for fracture network characterization using Outcrops, *Am. Assoc. Pet. Geol. Bull.*, *97*(9), 1545–1566, doi:10.1306/02131312042.

Zoback, M. D., and S. M. Gorelick (2012), Earthquake triggering and large-scale geologic storage of carbon dioxide, *Proc. Natl. Acad. Sci. U. S. A.*, *109*(26), 10164–10168, doi:Doi 10.1073/Pnas.1202473109.

Chapter 3

Frictional Stability-Permeability Relationships for Fractures in Shales

Abstract

There is wide concern that fluid injection in the subsurface, such as for the stimulation of shale reservoirs or for geological CO_2 sequestration (GCS), has the potential to induce seismicity that may change reservoir permeability due to fault slip. However, the impact of induced seismicity on fracture permeability evolution remains unclear due to the spectrum of modes of fault reactivation (*e.g.*, stable vs. unstable). As seismicity is controlled by the frictional response of fractures, we explore friction-stability-permeability relationships through the concurrent measurement of frictional and hydraulic properties of artificial fractures in Green River shale (GRS) and Opalinus shale (OPS). We observe that carbonate-rich GRS shows higher frictional strength but weak neutral frictional stability. The GRS fracture permeability declines during shearing while an increased sliding velocity reduces the rate of permeability decline. By comparison, the phyllosilicate-rich OPS has lower friction and strong stability while the fracture permeability is reduced due to the swelling behavior that dominates over the shearing induced permeability reduction. Hence, we conclude that the friction-stability-permeability relationship of a fracture is largely controlled by mineral composition, and that shale mineral compositions with strong frictional stability may be particularly subject to permanent permeability reduction during fluid infiltration.

Keywords: Friction, Stability, Permeability, and Induced Seismicity

1. Introduction

Large-scale fluid injection into the subsurface (*e.g.,* shale reservoir stimulation, geological storage of CO_2, deep disposal of wastewater, enhanced geothermal stimulation) [*Healy et al.*, 1968; *Raleigh et al.*, 1976; *Kanamori and Hauksson*, 1992; *Shapiro et al.*, 2006; *Majer et al.*, 2007; *Suckale*, 2009; *Ellsworth*, 2013; *Walsh and Zoback*, 2015; *Guglielmi et al.*, 2015] can generate overpressures and induce seismicity by reactivating pre-existing faults and fractures that are widely distributed throughout the upper crust [*Anderson and Zoback*, 1982; *McGarr et al.*, 2002] (**Figure 3-1**). The key to the success of these activities relies on (1) type of induced seismicity (*i.e.*, low frequency and slow energy release rate in the form of aseismic events or fast-slip and high energy release rate seismic events) and (2) desired permeability evolution - such as increased permeability for energy recovery systems and retained low permeability for caprock sealing systems. Hence, it is of particular interest to evaluate the relationship between the mode of fault reactivation (*i.e.*, induced fault slip, including both seismic and aseismic modes) and fracture permeability evolution.

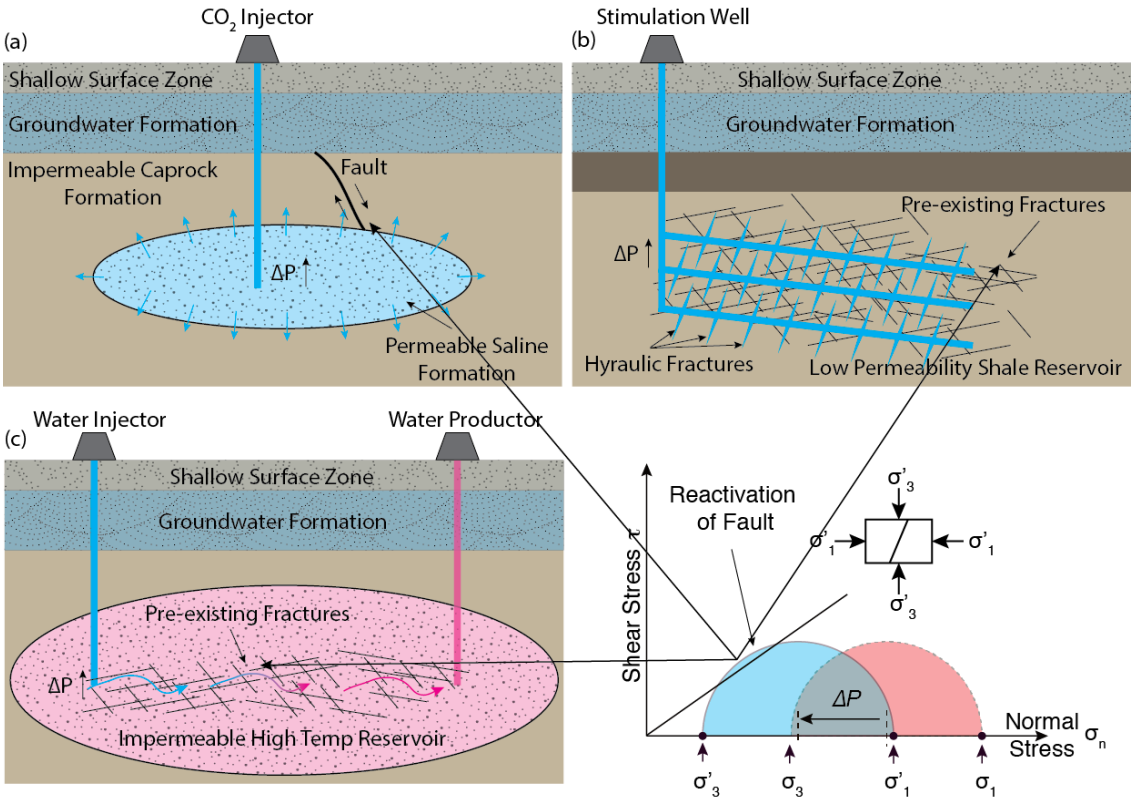

Figure **3-1**: Schematic diagram illustrating three scenarios of fluid injection into the subsurface. **(a)** Geological CO_2 Sequestration: the pre-existing fault is embedded in the caprock formation at the boundary of saline formation. **(b)** Hydraulic Fracturing of Shale Reservoir: pre-existing faults are stimulated. **(c)** Enhanced Geothermal System: hydraulic shearing in low permeability volcanic rocks. The Coulomb-Mohr circle shows that overpressure may destabilize and reactivate the fault.

The permeability of faults is known to change during shear deformation due to the rearrangement and destruction of bridging asperities [*Elsworth and Goodman*, 1986]. When shear deformation occurs on a fracture, permeability may increase due to significant dilation [*Barton et al.*, 1985; *Ishibashi et al.*, 2016] or decrease as a result of progressive formation of gouge [*Faoro et al.*, 2009]. During fracture shearing, the frictional strength of the fracture is affected by the state of true area of solid-solid contact between the displacing surfaces [*Dieterich*, 1978]. This contact relationship provides a potential physical explanation for the rate-and-state friction laws that can evaluate whether a fault fails stably (aseismically) at slow creep rates of long duration (order of 1~100 mm/yr) or unstably (seismically) at fast frictional sliding rates of short duration (order of 1 m/s) under certain boundary conditions [*Brune*, 1968; *Anderson et al.*, 1996; *Schmidt*

et al., 2005; *Peng and Gomberg*, 2010]. Fault movement is governed by the frictional behavior of the fault gouge within the fault. This frictional behavior is adequately defined by rate-and-state friction laws [*Dieterich*, 1978; *Ruina*, 1983; *Marone*, 1998; *Scholz*, 1998]. Friction measurements indicate that the frictional strength and stability of simulated fault gouges are a function of mineralogy. This relationship is due to the distinct crystalline structure and mechanical properties (e.g., plasticity, brittleness and ductility) [*Ikari et al.*, 2011; *Kohli and Zoback*, 2013; *Niemeijer and Collettini*, 2013; *Fang et al.*, 2016] of different minerals as well as their swelling characteristics [*Heidug and Wong*, 1996; *Xu and Pruess*, 2004; *Mazumder and Wolf*, 2008]. Clay minerals, such as kaolinite, montmorillorite, chlorite, illite, smectite, muscovite and mixed layer phases react with water-based fluids, leading to various degrees of swelling, dispersion, and migration characteristics [*Mohan et al.*, 1993; *Amorim et al.*, 2007]. Smectite and mixed layer clays exhibit crystalline swelling and hydration properties in an aqueous environment and experience significant volume expansion, which reduces the porosity and permeability of rocks [*Norrish*, 1954; *Norrish and Quirk*, 1954; *Young and Smith*, 2000]. Non-swelling clays, such as kaolinite and illite have less interaction with water than those of swelling clays, can easily disperse and migrate and lead to permeability damage [*Dodd et al.*, 1955]. At grain scale, with the effect of elevated temperature, stress-induced chemical dissolution of contacting asperities minerals may also change the contact area and alter the fracture conductivity [*Yasuhara et al.*, 2004, 2006; *Zhong et al.*, 2016]. A microphysical model has explained a competition between shear-induced dilatation and compaction via pressure solution transfer processes with respect to frictional stability in a simulated fault gouge [*Niemeijer and Spiers*, 2007]. These studies provide valuable insights into the formation-specific rheological response of fractures to deformation as seismic or aseismic – with implications for whether permeability evolution will be associated with these modes. Notwithstanding, it is still unclear whether there are different styles of

permeability evolution for different frictional responses and whether the different styles can be inferred or predicted based on formation mineralogy.

In this study, we explore the possible link between frictional stability and the evolution of fracture permeability under upper crustal conditions where mineral reactions and thermally activated deformation mechanisms are too slow to be relevant (with the exception of clay swelling). We select two mineralogically distinct shale samples: Green River shale and Opalinus shale to perform frictional-permeability experiments, static non-shearing hydraulic tests, and imaging by X-ray computed tomography (CT) of both shale samples to probe the following key questions: **(1)** what is the fracture friction-permeability interaction that may occur during shear slip; **(2)** what is the influence of mineral composition of shale samples on friction and permeability behavior; and **(3)** what are the engineering implications of the friction-permeability relationships to activities such as caprock selection and pressure management for CO_2 geologic storage?

2. Experimental Methods

From the foregoing, it is clear that many parameters influence friction-permeability relationships, so it is important to capture the most critical factors at all scales. Thus, we first define key features that capture the most fundamental characteristics that influence permeability evolution during aseismic or seismic events and how these might be captured in experiments. We then introduce sample materials and preparation methods, and finally define the experimental setup and procedures.

2.1 Assumptions and Conditions

To capture the key features of permeability-slip coupling we list the following assumptions:

(1) The pre-existing fault is assumed to be a parallel plate model in the experiment and the cubic law is assumed to be valid for the fluid flow within the fracture. Although this model differs from a natural fracture with complex geometric surfaces, it provides the essential link between aperture and fluid transmission rate [*Snow*, 1969] and is consistent with the geometry of fracture slip [*Dieterich*, 1992].

(2) The normal stress applied in the experiment is equivalent to the in-situ effective normal stress that acts on the most favorably orientated fractures after an overpressure is applied. Considering the shallow depths of shale reservoirs [*Allis et al.*, 2001], we assume that the local effective normal stress on the surface of a shale fracture is relatively low (**Figure 2-2a**), so the effective normal stress used in the experiments might be comparable to some potential GCS reservoirs. However, for reliable extrapolation to deeper GCS fields, we need a microphysical model accommodating the effects of temperature and effective normal stress.

(3) The applied experimental loading velocity (10^0 μ m/s to 10^1 μ m/s) does not purport to cover the full spectrum of possible seismic or aseismic transient slip velocities, but represents a narrow range where contrasting responses of different mineralogies may be explored, with velocity as a control parameter. As the sliding velocity in these experiments is approximately two orders of magnitude lower than similar experiments, no thermal pressurization effect is considered [*Rice*, 2006; *Tanikawa et al.*, 2010, 2014].

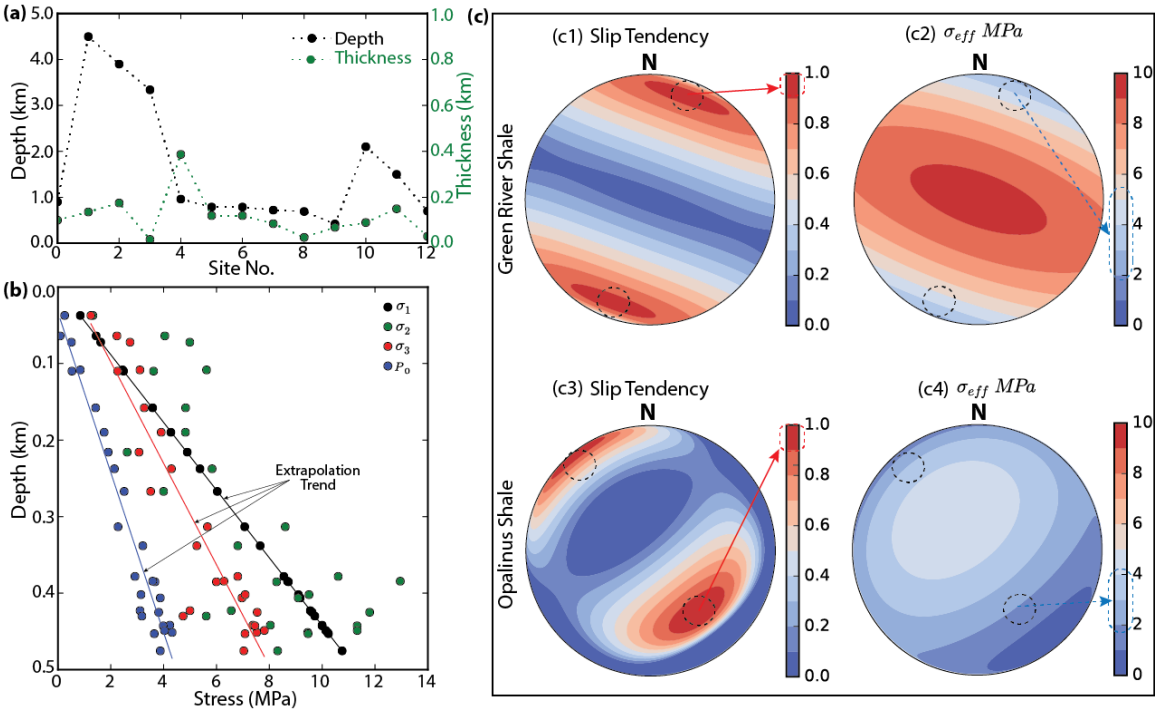

Figure **3-2**: **(a)** Depth and thickness of shale reservoirs (Data adopted from the report by *Allis et al.*, [2001]); **(b)** In-situ stress field of Green River Formation, Piceance Basin, Colorado (Data adopted from hydraulic fracturing experiments by *Bredehoeft and Shuter,* [1976]); **(c)** Lower stereographic projection of slip tendency and effective normal stress of fractures with required overpressure $\Delta P_f = 3.2$ MPa at the bottom (~ 950 m) of Green River Formation, Colorado (**c1** and **c2**) and with required overpressure $\Delta P_f = 1.70$ MPa at the depth of ~ 270 m of Opalinus shale (c3 and c4) [*Corkum and Martin*, 2007].

2.2 Sample Materials and Preparation

In this experiment, we select two natural shales with distinctly mineralogy - Green River shale and Opalinus shale. Green River shale is deposited in a fresh water lacustrine environment. The samples are recovered from the sequence at Grand Junction, Colorado. The in-situ stress field of the Green River formation [*Bredehoeft et al.,* 1976] suggests a strike slip faulting regime near the surface and a normal faulting stress regime below a depth of ~200 m (**Figure 3-2b**), with the maximum horizontal stress σ_H trending N70W. Stratigraphic analysis indicates that the base of the Green River shale formation is at a depth of ~ 950 m [*Dyni*, 2006]. Thus, from the measured

stress gradient in **Figure 3-2b**, local in-situ stresses and fluid pressures are estimated as σ_v = 21.5 MPa, σ_H = 20.0 MPa, σ_h = 14.9 MPa and P_0 = 8.8 MPa respectively. The Opalinus shale is clay rich shale (**Figure 3-3d**) and is representative of caprock materials for a large number of reservoirs targeted for carbon dioxide storage. The Opalinus core sample is taken from a horizontal borehole (BEZ-G50) at the Mont Terri underground rock laboratory in Switzerland, where the in-situ stresses are σ_v = 6.5 MPa, σ_H = 4.0 MPa, σ_h = 2.2 MPa, P_0 = 1.7 MPa and a fracture cohesion C_f = 1.0 MPa [*Corkum and Martin*, 2007].

For the experiments, cores with longitudinal lengths of 5 cm and diameters of 2.5 cm are drilled and carefully saw-cut and polished into two halves, representing a parallel plate model (**Figure 3-3a** and **3-3b**). The planar surfaces are uniformly roughened with grinding powder (#60 Grit) at constant rate. The mineralogical composition of the samples was characterized via X-ray diffraction, suggesting that GRS is carbonate-rich with an equivalent proportion of tectosilicate while OPS is primarily composed of phyllosilicates (**Figure 3-3c** and **3-3d**).

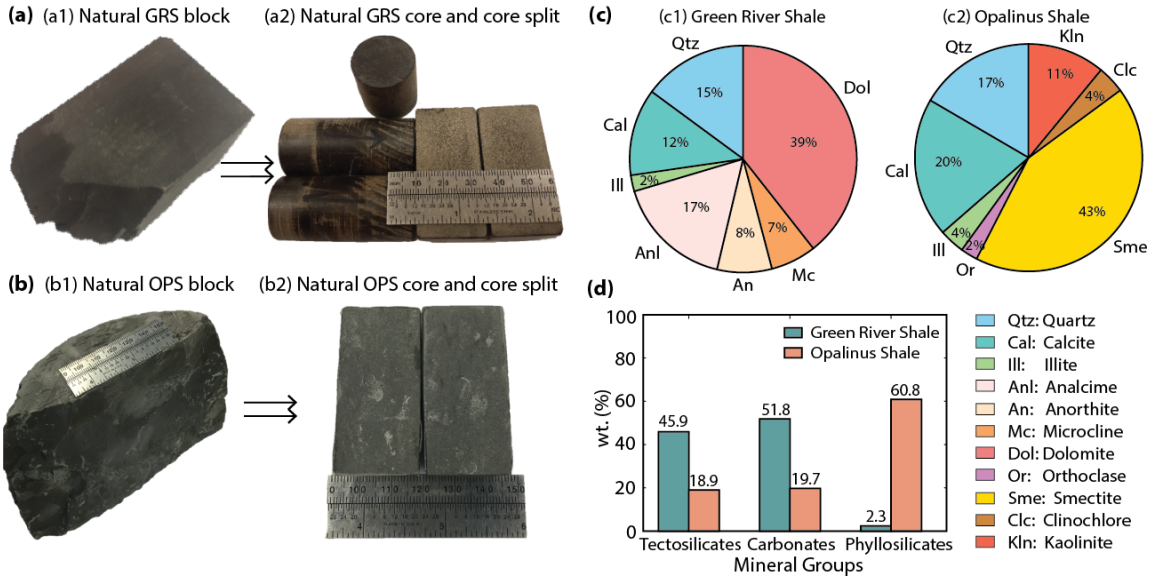

Figure **3-3**: **(a)** Natural (intact) Green River shale block and cores and saw-cut half split of the cores; **(b)** Natural (intact) Opalinus shale block and cores and saw-cut half split of the cores; **(c)** XRD analysis of mineral compositions of both Green River shale and Opalinus shale **(d)** Comparison of mineral groups (tectosilicate, carbonate, and phyllosilicate) between Green River shale and Opalinus shale.

2.3 Experimental Setup and Procedure

2.3.1 Friction-Permeability Experiments

The friction-permeability experiments were performed in a triaxial testing apparatus that independently applies confining pressure and differential (end-to-end) pore pressure while the sample is sheared at a prescribed velocity. This allows the concurrent measurement of the evolution of fracture permeability and friction (**Figure 3-4**). The reassembled split samples were packed within a latex membrane with an initial offset of 10 mm for slip displacement during sliding. An aluminum ring is placed at 10 mm offset to prevent fluid extruding. To reduce the friction between the outer wall of the sample, aluminum ring and the membrane, we wrapped the sample in Teflon tape.

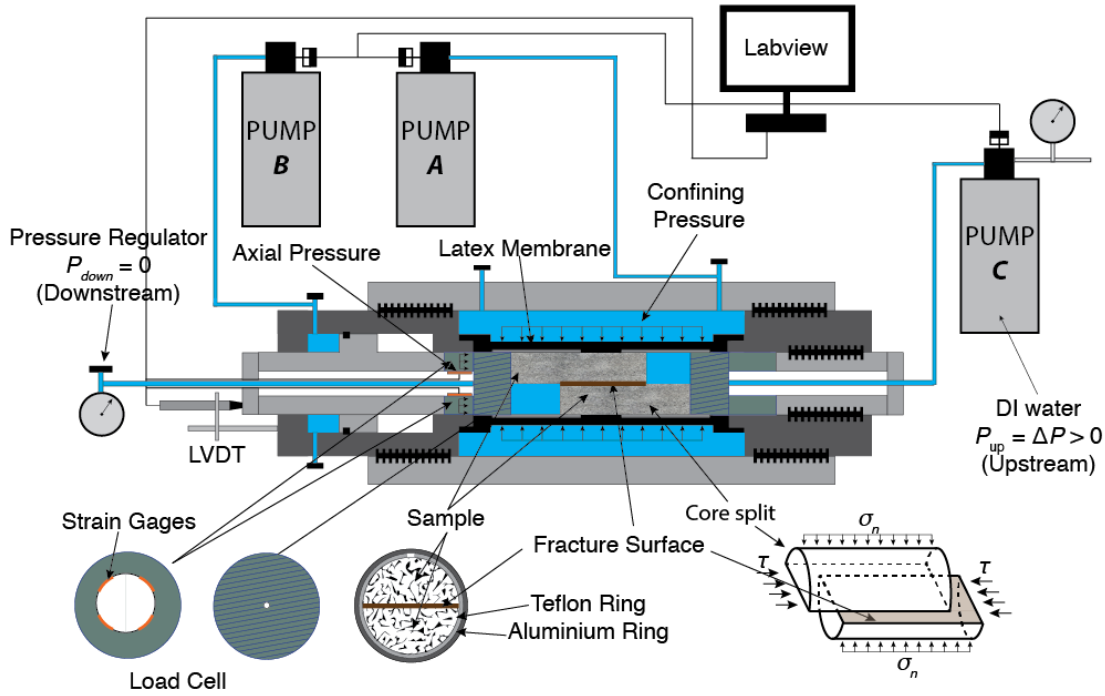

Figure **3-4**: Picture of experimental setup for friction-permeability evolution test: Pump A (ISCO500D) controls the confining pressure (normal stress) applied on the fracture. Pump B (ISCO500D) controls pressure that provides the source of shear stress applied on the fracture. Pump C (ISCO500D) injects the fluid at a prescribed flow rate or pressure, allowing the fluid source locates at the origin of the fracture and flow along the fractures.

From the estimated in-situ stresses in **section 2.2**, the equivalent effective normal stresses at which critically stressed fractures will fail range from 2 MPa to 5 MPa (**Figure 3-2c**). Thus, we apply a confining stress (normal stress) of 3 MPa (pump A) and set a constant upstream fluid pressure (pump C) during axial shear displacement at constant rate (pump B) and measured force. The minimum flow rate of each pump is 0.001 ml/min and the display resolution of the pump pressure transducer is 1.0 kPa. A load cell with a resolution of 0.3 kPa is used to measure the axial stress. At room temperature, the minimum measurable transient fracture permeability is $1.0x10^{-14}m^2$.

We conducted both constant velocity and velocity-stepping experiments to compare the hydraulic behavior response to varying velocities. For the Green River shale, the shear velocity was set to 1 μm/s (monotonic) and switched by up-steps and down-steps between 1 μm/s and 10 μm/s, until a displacement of ~10 mm was reached. These conditions were repeated for Opalinus shale, but with an initial shear velocity at 10 μm/s to minimize the competing time-dependent swelling effect of clay minerals, with up-steps and down-steps completed (1 μm/s and 10 μm/s) to a final shear offset of ~8 mm. All the experiments were performed at room temperature (25 C°), with shear displacements recorded by LVDT (Linear Variable Differential Transformer) located outside the vessel.

2.3.2 Static Non-Shearing Hydraulic Experiments

The XRD analysis (**Figure 3-3**) of both the Green River and Opalinus shales show that Green River shale is carbonate-rich and is assumed to be more brittle while the Opalinus shale is clay-dominated and shows ductile macro-swelling behavior during excavation [*Bossart et al.*, 2004]. Due to the inhomogeneity of the shale samples from the sedimentation processes, mineral

phase contents of these shale samples are variously reported [*Wenk et al.*, 2008; *Kaufhold et al.*, 2013].

To examine the swelling effect and to isolate its influence on the permeability from the shearing response, we measure permeability under the same uniform stress as before but for null shearing velocity in the sample configuration of **Figure 3-5**. We apply identical initial fracture roughness to both samples. The initial upstream pressure of 0.01 MPa is incrementally increased when the flow rate reaches steady state. For Opalinus shale, we directly apply an initial hydraulic pressure at 0.5 MPa to ensure fluid migration through the fracture at the first hydraulic pressure step. The detailed hydraulic pressure and flow rate results of both samples are illustrated in **Figure 3-7**.

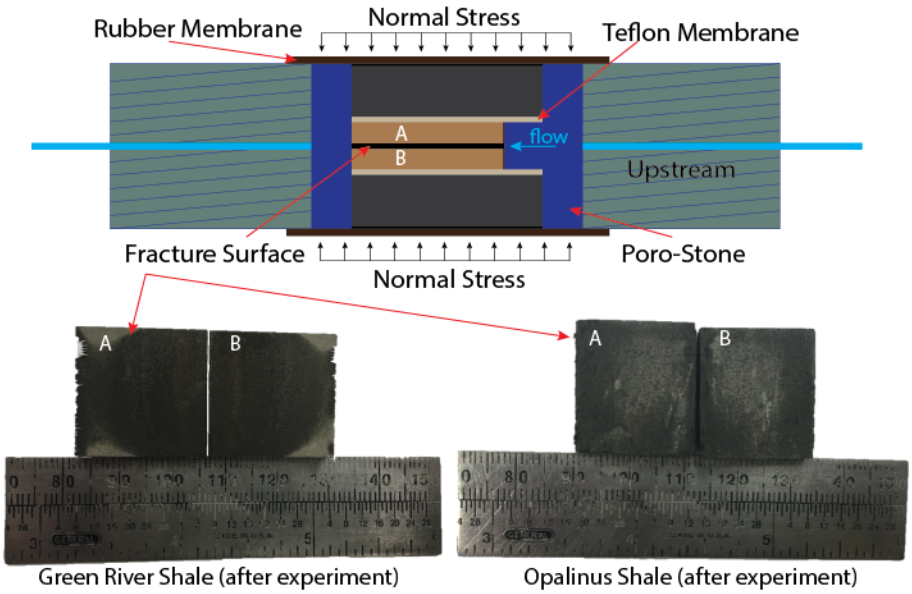

Figure **3-5**: Experimental configuration and sample geometry for static non-shearing hydraulic experiments for both Green River shale and Opalinus shale

2.3.3 Tomographic Imaging

Samples are characterized by white light optical profilometry and 3D X-ray imaging to: (1) control and ensure that the statistical fracture roughness before the friction-permeability and static non-shearing experiments are of the same magnitude; (2) measure the evolved fracture roughness after the experiments; (3) observe the wear products generated during the experiments at analogous in-situ conditions; and (4) monitor the short-term swelling effect of the clay-rich Opalinus shale fracture under wetting.

White light interferometry was performed using a Zygo NewView 7300 with a 10X objective (**Figure 3-6a**) and data were processed with Mx^{TM} software (Zygo). The Root Mean Square (RMS) asperity height is characterized on the sample fields of 1.66 mm × 1.66 mm as an index of fracture surface roughness of both Green River and Opalinus samples both before and after the friction-permeability and static non-shearing experiments (**Figure 3-6c**).

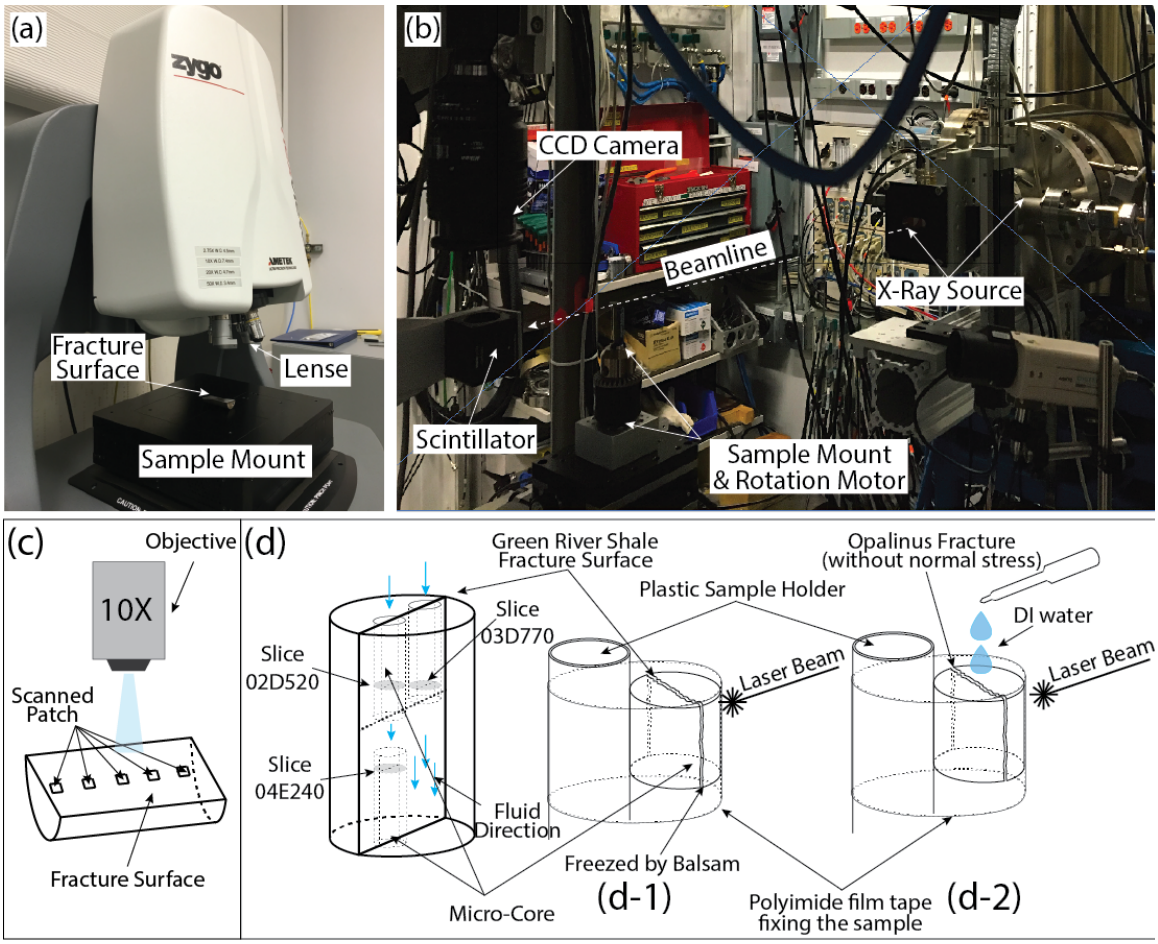

Figure **3-6**: **(a)** 3D optical surface profiler for characterizing statistical roughness of fracture surface. **(b)** APS GSECARS Beamline 13BMD Experimental Setup for characterizing the fracture asperity contacts at post-mortem conditions **(c)** Fracture surface for white light scanning (**d-1**) Micro cores of Green River shale for x-CT imaging (**d-2**) Opalinus shale fracture with DI water for x-CT imaging

To capture the features of the wear products that are generated during sliding, we first manually inject Canada balsam (diluted by 40% ethyl alcohol) by syringe to freeze the state of the fracture immediately after the sliding experiment with the normal stress unchanged. We then apply X-ray computed tomography (xCT) to produce 3D images of fracture contacts. We also use xCT in rapid data collection mode to observe the temporal evolution of swelling in response to aqueous fluid flow within fractures of the clay-rich Opalinus shale. The Green River shale subcore is scanned at standard mode (~12 mins/scan) with larger voxel dimension. On the

contrary, to avoid the effect of time-dependent water evaporation during the wetting process for the Opalinus shale, we use a rapid scanning mode (~1.5 mins/scan) to observe the swelling behavior of Opalinus shale. X-ray tomography data were collected on the bending magnet beamline 13BMD at the GeoSoilEnviroCARS sector 13 of the Advanced Photon Source (APS), Argonne National Laboratory (ANL), Illinois, USA (**Figure 3-6b and 3-6d**). Tomograms were obtained with a monochromatic x-ray beam (34.5keV), sample rotation scheme, and downstream scintillator, focusing optics and CCD detector combination that produced reconstructed 3D images with a 2.88 μm voxel dimension. See *Gualda and Rivers* (2006) for detailed descriptions of data collection and processing methods.

3. Results and Discussion

We interpret measurements of concurrent flow and deformation to recover friction-stability-permeability evolution in the context of rate-state friction models. This analysis consists of (1): rate and state friction response to calculate the frictional parameters from measured data; (2) cubic law representation to estimate permeability and (3) parametric stress and slip dependent aperture analysis that reveals the mechanism of evolving permeability. Additionally, we perform an analysis of the permeability evolution measured by the static non-sheared hydraulic experiments and tomographic characterizations, in order to segregate and interpret the swelling behavior and its effect on the friction-permeability relationship.

3.1 Data Analysis

We calculate the coefficient of friction μ as a function of shear displacement using $\mu = \tau/\sigma_n$, ignoring cohesion. The velocity dependence of friction can be interpreted in the framework

of rate and state friction (RSF) theory [*Dieterich*, 1978, 1979; *Ruina*, 1983]. In the RSF approach to modeling fracture shear slip, the friction coefficient is written as [*Dieterich*, 1978; *Marone*, 1997; *Scholz*, 1998]:

$$\mu(V,\theta) = \mu^i + a\ln\left(\frac{V^i}{V^{i-1}}\right) + b\ln\left(\frac{V^{i-1}\theta^i}{D_c^i}\right) \tag{1}$$

$$\frac{d\theta^i}{dt} = 1 - \frac{V^i\theta^i}{D_c^i} \tag{2}$$

where μ_0 is the coefficient of friction at a reference velocity V^{i-1}; θ^i is a state variable that evolves after the velocity is incremented (stepped up- or down-) to V^i; a and b are the friction parameters which represent the direct effect (a) and the evolutionary effect due to a step velocity change (b); and D^i_c is the critical slip distance, over which evolution to a new steady state takes place. Frictional slip instability is determined in part by the parameter (a-b) derived from **Eq. (1)** for a finite step in velocity, yielding [*Dieterich*, 1979; *Ruina*, 1983; *Scholz*, 1998]:

$$a - b = \frac{(\mu_{ss}^i - \mu_{ss}^{i-1})}{\ln(V^i / V^{i-1})} \tag{3}$$

A positive value of (a-b) denotes velocity-strengthening behavior, suggesting stable, aseismic slip, while a negative (a-b) indicates velocity-weakening behavior, which is potentially unstable. The RSF constitutive parameters were determined by fitting experimental and modeled data *via* Eqs. (1) and (2).

The measured fracture permeability k_m [m^2] can be expressed in terms of measured hydraulic aperture b_m [m] based on the cubic law,

$$b_m = -\left(\frac{12\mu_{vis}\cdot L(t)\cdot Q(t)}{W\cdot\Delta P_f}\right)^{1/3} \text{ and } k_m = \frac{b_m^2}{12} \tag{4}$$

where μ_{vis} [Pa·s] is the viscosity of fluid; $L(t)$ [m] is the contact length of the fracture surface; W [m] is the fracture width; $Q(t)$ [m^3/s] is the measured flow rate and ΔP_f [Pa] is the differential pressure between the upstream and downstream extent of the fracture.

Elastic and plastic deformations of asperity contacts are the key physical processes to interpret the frictional evolution during sliding [*Rabinowicz*, 1951; *Yoshioka and Scholz*, 1989; *Wang and Scholz*, 1994; *Yoshioka*, 1997; *Misra*, 2002]. Correspondingly, fracture permeability is governed by the evolution of fracture aperture that is mainly stress-dependent. In the laboratory, the aperture distribution of a fracture at laboratory scale (10^{-2} m to 10^{0} m), can be determined by measuring the asperity heights of a fracture [*Brown and Scholz*, 1985]. Here we define a constitutive aperture model that describes the relationship between friction and permeability considering the effects of both shear slip displacement and velocity change. Before the pre-existing fracture is reactivated, the fracture aperture may be expressed as a nonlinear normal stress-dependent b_0 [*Rutqvist et al.*, 2004],

$$b_0 = b_r + (b_{\max} - b_r) \cdot \exp[-\alpha_n \cdot (\sigma_n - P_f)] \tag{5}$$

where b_r [m] is the residual hydraulic aperture; b_{max} [m] is the maximum opening; α_n [1/MPa] is the normal stiffness parameter determined from experiments; σ_n [MPa] is the normal stress perpendicular to the fracture surface; and P_f [MPa] is the internal fluid pressure in the fracture. After the reactivation of a pre-existing fracture, the shear slip dependent aperture b_{slip} [m] may be empirically defined as,

$$b_{slip}^{i} = b_f + (b_{S0} - b_f) \cdot \exp\left[-\alpha_s \cdot \frac{u(V^i,t)}{L_0} \cdot \mu(V^i,\theta^i) \cdot (\sigma_n - P_f) \right] \tag{6}$$

where the index i refers to the i^{th} velocity step (if the velocity is constant throughout the shear slip, $i = 0$); b_f [m] is the final aperture after sufficient shear displacement to reach steady state; b_{s0} [m] is the initial shear slip aperture; α_s [1/MPa] is the shear stiffness parameter; $u(V^i,t)$ [m] is the

shear displacement as a function of sliding velocity and time; L_0 [m] is the contact length of the fracture surface before shear slip; and $\mu(V^i, \theta^i)$ is the concurrently measured frictional strength.

Analogous to the shear dilation relationship of *Samuelson et al.*, 2009, we define a dilation or compaction parameter $\Delta\phi^i$ to represent the volumetric response after failure as,

$$\Delta\phi^i = \frac{\Delta b^i_{vel}}{b^{i-1}_{slip}} = \psi^i \cdot \ln\left(\frac{V^{i-1}}{V^i}\left[1 + \left(\frac{V^i}{V^{i-1}} - 1 \right) \cdot e^{-V^i \cdot t^i / D^i_c} \right] \right) \tag{7}$$

where Δb^i_{vel} [m] is the aperture change due to the i^{th} velocity change in the slip history; b^{i-1}_{slip} [m] is the aperture at the moment before the shear velocity is stepped; ψ^i is a compaction/dilation factor that pertains to the fracture material and generated wear products; t^i [s] is the time since the i^{th} velocity step. Hence, the modeled fracture aperture b_{evo} [m] that evolves during shear slip and the corresponding permeability k_f [m^2] are expressed as,

$$b_{evo} = b^{i-1}_{slip}(1 + \Delta\phi^i) \text{ and } k_f = \frac{b^2_{evo}}{12} \tag{8}$$

3.2 Analysis of Measured Data

3.2.1 Friction-Permeability Relationship

Asperity damage is manifested as a change in roughness of the fracture surface. In **Figure 3-7**, the root mean square (RMS) asperity height of a monotonically sheared fracture of Green River shale (black triangles at 1 to 3 MPa) and Opalinus shale (black circles and squares at 3 MPa) are significantly reduced due to the shearing and increased normal stress, suggesting that the surface roughness evolves by progressive removal of the highest asperities from the surface.

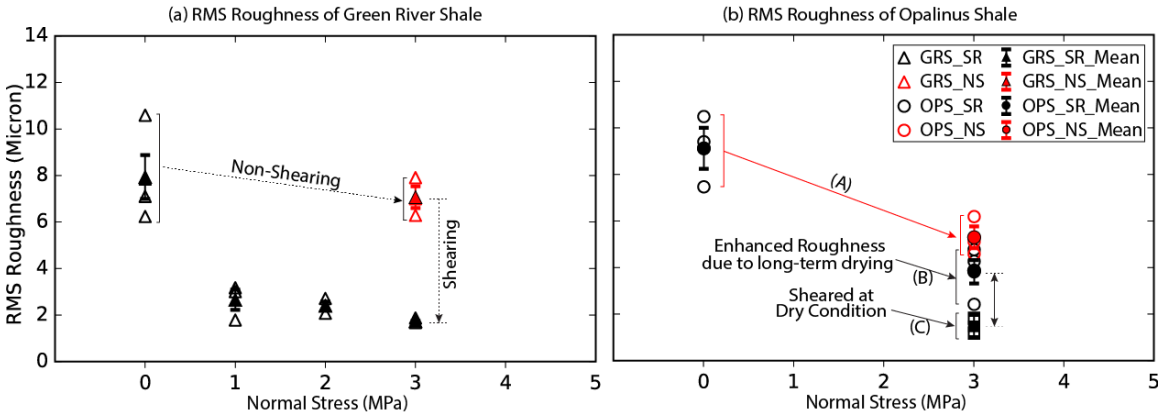

Figure **3-7**: Root mean square (RMS) roughness of planar fracture surface of a split core of **(a)** Green River shale and **(b)** Opalinus shale. Plots with normal stress at 0 refer to the initial asperity before shear sliding. Plots with normal stress at 1 to 3 MPa refer to the asperity after shear sliding (SR stands for the sheared experiments). Plots in red at 3 MPa refer to static non-shearing hydraulic experiments (NS refers to non-shearing). In figure (b), the black squares refer to friction experiments at dry condition. Arrow (A) refers to the reduced roughness by swelling in a non-shearing experiment. Arrow (B) refers to the roughness value when fracture is sheared at wet condition. Due to the long-term drying, the measured roughness value is higher than its real value when the shearing was just finished. Arrow (C) refers to roughness value of fracture sheared at dry condition.

The frictional constitutive parameters of Green River shale and Opalinus shale are listed in **Table 3-1**. The average friction coefficient value of Green River shale (μ = 0.573) is larger than that of Opalinus shale (μ = 0.502). The experimental slip displacement is at the same scale of displacement (*e.g.*, 0.1 mm to 10 mm) in micro-earthquakes (M_w < 2.5) or aseismic slip events [*Zoback and Gorelick*, 2012; *Guglielmi et al.*, 2015]. The (*a*-*b*) value of Green River shale decreases with displacement from 0.0027 to 0.0022 with an average value of 0.0025, showing a slight velocity strengthening when the velocity step is applied. The (*a*-*b*) value of Opalinus shale decreases with displacement from 0.0155 to 0.0140 with an average value of 0.0152, suggesting a much stronger velocity strengthening behavior than that of Green River shale under same experimental conditions. This implies that fractures in Opalinus shale tend to fail aseismically at low effective normal stresses congruent with rate-and-state friction theory.

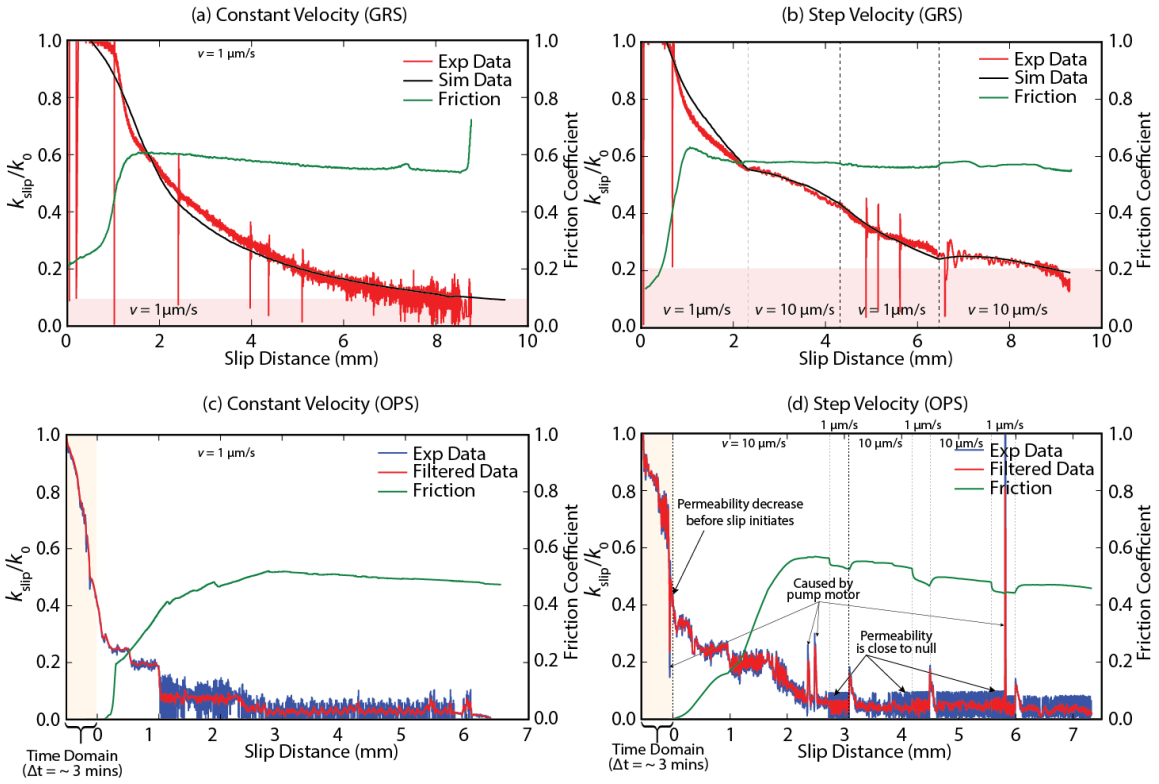

Figure **3-8**: Diagrams showing relationship between measured friction (green curve), measured permeability (red curve) and sliding velocity (constant vs. stepped velocity) for Green River shale (GRS) and Opalinus shale (OPS). Simulated permeability is shown in black. **(a)** Scenario of constant slip velocity (1 μm/s) for GRS with initial permeability k_0 of $82.302\times10^{-12}m^2$; **(b)** Scenario of stepped slip velocity (1 μm/s, 10 μm/s, 1 μm/s, 10 μm/s) for GRS with k_0 of $74.332\times10^{-12}m^2$. The shaded area at the bottom of both diagrams highlight final permeability magnitude after shearing. **(c)** Scenario of constant slip velocity (1 μm/s) for OPS with k_0 of $7.301\times10^{-12}m^2$; **(d)** Scenario of stepped slip velocity (10 μm/s, 1 μm/s, 10 μm/s, 1 μm/s, 10 μm/s, 1 μm/s) for OPS with k_0 of $8.801\times10^{-12}m^2$.

For the case of Green River shale, the impact of asperity reduction is reflected in **Figure 3-8a** and **3-8b**, where the frictional strength (green curve) decreases slightly after reaching a peak and stabilizes within the range of ~ 0.57 to ~ 0.59 at a slip distance of ~ 8 mm. The removed asperities contribute to the generation of wear products of various particle sizes. The largest (with diameter size > ~10 μm) are captured in the xCT images while the smaller ones are removed from the sample with the impregnation by the highly viscous Canada balsam (**Figure 3-9**). In addition, the reconfigured asperities change the hydraulic properties of Green River shale as illustrated in

Figure 3-8a and **3-8b** (red curve). The measured permeability declines exponentially at a constant sliding velocity (**Figure 3-8a**). Although **Figure 3-8b** shows a similar declining trend of the measured permeability, the change in sliding velocity from 1 to 10 μm/s clearly slows down the rate of permeability decrease. Conversely, when the sliding velocity drops from 10 to 1 μm/s, the rate of permeability decrease accelerates. Clearly, after a shear slip of 6 to 8 mm, the slope of the decrease in permeability flattens, suggesting that the asperity height distribution experienced a relatively small change. It is noteworthy that the eventual permeability for the up-stepped velocity is enhanced by ~10% compared to that at constant velocity. This implies that a high velocity may, to some extent, enhance fracture permeability.

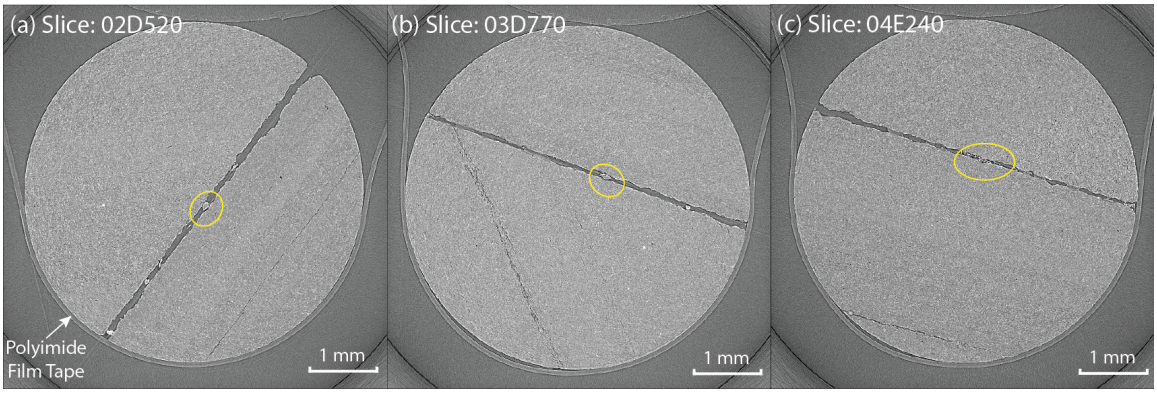

Figure **3-9**: Subcores of Green River shale fracture (see **Fig. 6d**) for the xCT experiments. The fracture is filled with Canada balsam. **(a)** The xCT image from subcore 02. **(c)** The xCT image from subcore 03. **(d)** The xCT image from subcore 04. Yellow circles locate the large particles (wear product generated during shearing).

To yield a better understanding of the mechanisms of permeability evolution, we represent the permeability evolution using **Eqs. (5)** to **(8)** and show the results (black curve) in **Figure 3-8a** and **3-8b**. The parameters adopted in the model are listed in **Table 3-2**. The modeled permeability matches well with the measured permeability for both constant velocity and stepped-velocities. These results may be interpreted as follows: **(1)** within the slow slip velocity domain, permeability always declines as shear slip increases due to the reduction of asperity height up to the time that a steady state asperity height is reached; **(2)** with the generated wear products

embedded within the two fracture walls, changing the sliding velocity may enhance or diminish the rate of change of permeability *via* dilation or by compaction. Thus comminution will favor a reduction in permeability, by reducing pore-throat size, and dilation in the absence of comminution will favor permeability increase.

For the case of Opalinus shale, though the trends of friction and permeability evolution of **Figure 3-8c** and **3-8d** are similar to those of Green River shale, we do observe some differences in their hydraulic and frictional behaviors. First, there is significant damage (reduction in permeability) during the first ~3 minutes before the initiation of shear slip for both constant velocity and stepped velocity. When the permeability reduced to ~35% of its initial magnitude, shear slip was started at a sliding velocity of 10 μm/s. The declining rate of permeability starts increasing until the frictional strength curve becomes flat at a sliding displacement of ~1.8 mm. When the frictional strength reaches steady state (~0.55), at a sliding displacement of ~2.7 mm, the permeability drops to a stable level (equal to ~null). In contrast with the velocity-stepped permeability evolution of the Green River shale (**Figure 3-8b**), the permeability change of the Opalinus shale is smaller than the measurement error at these low permeabilities. This implies that friction and permeability are decoupled if the fracture is fully sealed with swelling clay-rich particles. In terms of frictional stability, the strong strengthening behavior is the result of clay-rich materials that may promote swelling during fluid infiltration. Correspondingly, we postulate that strong frictional stability may result in permeability destruction.

The experimental results are broadly honored by the model (**Figure 3-8a** and **3-8b**). From **Eqs. (5)** to **(8),** geomechanical controls can be attributed to both normal and shear stress effects on the fracture aperture and asperities, which define the hydraulic behavior of the fractures. To understand how sensitive the permeability evolution of fractures is to these parameters, and the potential effects of these sensitivities on the interpretation of the measured data, we perform a parametric study to isolate the individual effect of each parameter from the ensemble of

integrated effects. In the model, the velocity step is applied at a displacement of 4 mm, before which wear products and friction are assumed to reach steady state.

Individually, in **Figure 3-10a** higher D_c values (critical slip distance) result in a smooth change of permeability, due to the fracture asperities taking longer to reconcile and relocate relative to each other. Increasing the velocity will inevitably enhance the dilation effects (if the dilation parameter ψ is positive) (**Figure 3-10b**). However, this enhancement asymptotes to an upper limit when upstep velocity grows to infinity, indicating that the velocity change is only the trigger for the permeability change but not the dominant controlling process. In comparison, an increase of the dilation parameter (ψ) can significantly enhance the permeability after a velocity step occurs (**Figure 3-10c**). In **Figure 3-10d**, the reduced final aperture crucially determines the background permeability evolution where a large final aperture would result in a small permeability decrease. This behavior is largely controlled by the applied normal stress and the strength of the asperity where high normal stress and a weak asperity would result in a larger contact area of the fracture surfaces. Likewise, the shear stiffness parameter α_s determines how fast the asperities are destroyed during the shearing and controls the timing of the permeability reduction with slip distance (**Figure 3-10e**). For example, a higher shear stiffness parameter α_s suggest that the permeability declines faster to its steady state. The effect of frictional strength (μ) is illustrated in **Figure 3-10f**, indicating that high frictional strength leads to a smaller permeability decline. As frictional strength is a function of mineral composition, where strong minerals resist deformation, this leads to a minimal decline in permeability.

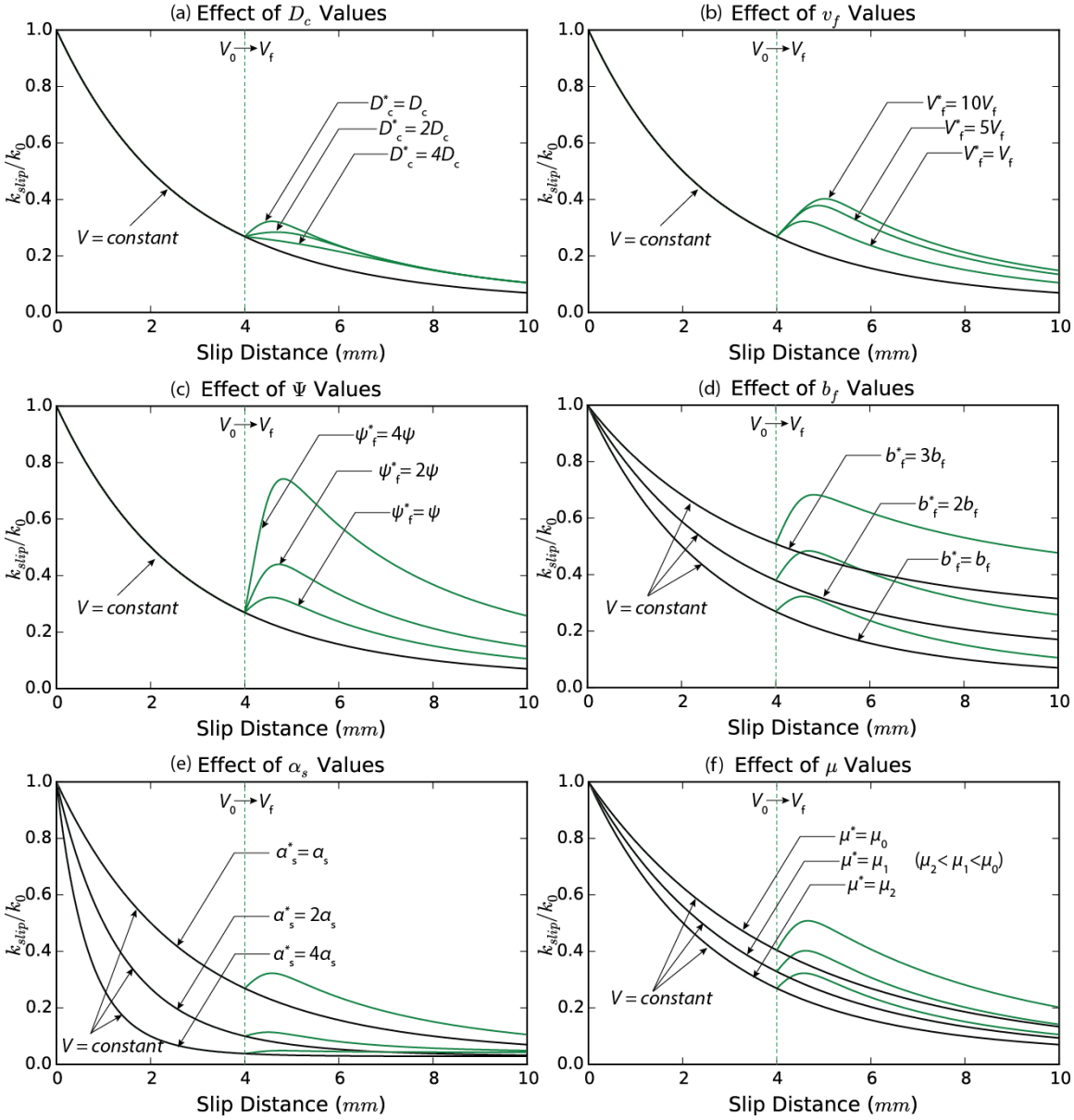

Figure **3-10**: Parametric analysis: **(a)** Effect of critical displacement (D_c). **(b)** Effect of velocity upstep (V_f). **(c)** Effect of dilation or compaction parameter (ψ). **(d)** Effect of reduced final aperture (b_f). **(e)** Effect of shear stiffness parameter (α_s). **(f)** Effect of frictional strength (μ). The black curves show the permeability evolution under constant velocity shearing while the green curves represent the permeability change after a velocity step applied. Model reference case parameters in each plot (D^*_c=D_c, V^*_f=V_f, ψ^*=ψ, b^*_f=b_f, α^*_s=α_s, μ^*=μ) are referred from experimental values.

Summarized from the above analysis, **Figure 3-7** shows that critical displacement (D_c), incremented-velocity (V_f) and the dilation or compaction parameter (ψ) only play a role in influencing the permeability after a velocity change (**Figure 3-10a** to **3-10c**) while the influences

of the final aperture (b_f), shear stiffness parameter (α_s) and frictional strength (μ) accompany the entire shearing process (**Figure 3-10d** to **3-10f**).

3.2.2 Effect of Swelling

The static non-shearing hydraulic experiments demonstrate that swelling plays a significant role in the friction-permeability relationship for the clay-rich Opalinus shale but only a negligible role for the carbonate-rich Green River shale. The flow rate through the fracture in Green River shale increases or decreases linearly with fluid pressure (**Figure 3-11a**). The fluid percolates through the fracture of Green River shale at a very low pressure (e.g., 0.01 MPa), while flow initiates only above 0.5 MPa for the Opalinus shale. At constant pressure, the flow rate within the Opalinus shale is reduced to only 6% of its initial rate within ~10 minutes and essentially stops (~0 ml/min) at ~120 minutes (**Figure 3-11b**) due to closure of the fracture by the swelling of clay minerals. A high fluid pressure (~1.5 MPa) is required to reopen the fracture. In **Figure 3-11c**, the permeability of the Green River shale remains constant for the first ~10 minutes and declines slightly when the fluid pressure is stepped to 0.06 MPa and eventually rebounds back to its initial magnitude after the fluid pressure drops to 0.01 MPa. In contrast, the permeability of the Opalinus shale drops permanently to a value sufficiently low (*i.e.*, not resolvable by experimental setup) over the same time scale (~120 minutes), implying that permeability damage is occurring (**Figure 3-8c** and **3-8d)** and is primarily a result of the swelling induced sealing of the fracture.

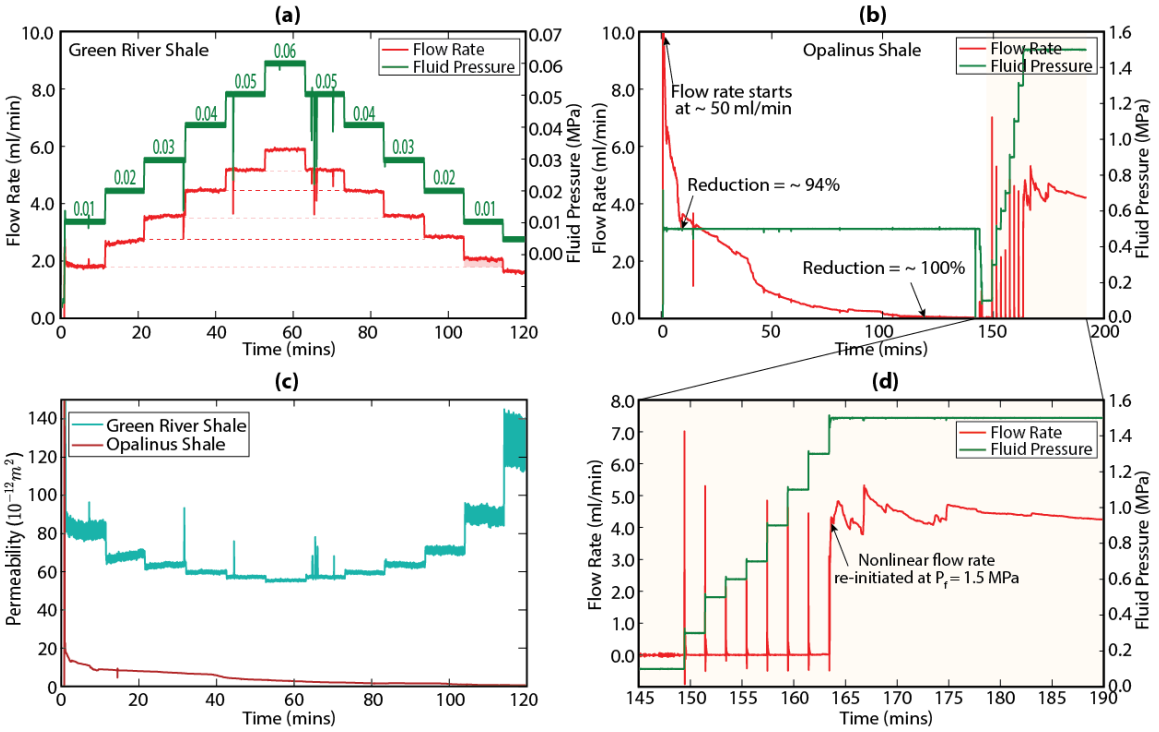

Figure **3-11**: Results of static non-shearing hydraulic experiments of Green River shale and Opalinus shale. **(a)** Temporal evolution of gauge pressure and injected flow rate for Green River shale. **(b)** Temporal evolution of gauge pressure and injected flow rate for Opalinus shale. **(c)** Comparison of temporal evolution of permeability between Green River shale and Opalinus shale. **(d)** The pink shading highlights a condensed data section in **(b)**.

A comparison of fracture roughness after the non-shearing hydraulic experiments is shown in **Figure 3-7**. It is observed that the roughness of the fracture in Green River shale reduces (red triangles at 3 MPa in **Figure 3-7a**) in comparison to its initial state (black triangles at 0 MPa). This may be due to the irreversible deformation of the asperities under the increased normal stress. However, the apparent roughness of the fracture in the Opalinus shale reduced markedly after the experiment (red circles at 3 MPa in **Figure 3-7b**) compared to before the experiment (black circles at 0 MPa). This decrease is likely a result of swelling and attendant flattening of the fracture surface (**Figure 3-7b**). It is worth noting that the roughness of the sheared Opalinus fracture surface (black circles at 3 MPa) is slightly enhanced due to drying for the unconstrained situation where the fracture is exposed to the air.

Furthermore, swelling-induced fracture sealing within the Opalinus shale was independently observed using time-dependent xCT imaging (**Figure 3-12**). The time sequence of xCT images shows that within a short time period after the wetting (< 3mins), the shale matrix expansion is captured. The unconfined fractures begin to adhere to each other. After a period of 30 mins, the partial fracture surfaces are filled with swelled minerals, demonstrating how swelling in clay-rich shales under confining pressure can result in fracture closure and permeability reduction. However, during this process, the swelling effect is gradually reduced due to the fast water evaporation.

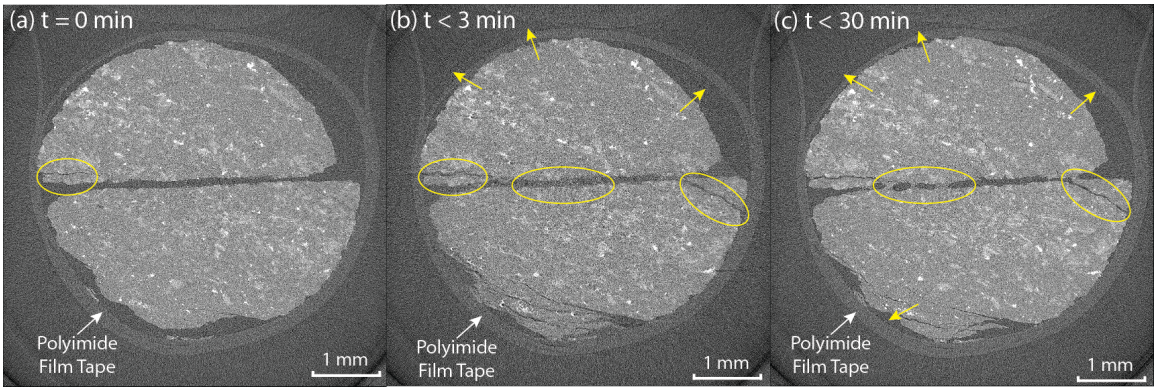

Figure **3-12**: xCT images of Opalinus shale fracture under wetting conditions without confining pressure **(a)** Dry Opalinus shale fracture. **(b)** Wet Opalinus shale fracture 3 minutes after wetting. **(c)** Wet Opalinus shale fracture 30 minutes after wetting when water drop is fully evaporated. The yellow arrows point the swelling expansion direction. The highlighted circles points out where swelling occurring on fracture surfaces.

3.3 Summary

These observed responses, can be summarized with a proposed conceptual model that considers three distinct modes of friction-stability-permeability evolution in a low effective normal stress regime (**Figure 3-13**). These different conditions include where: **(1)** The fracture asperities are composed of strong-brittle minerals that are difficult to comminute into finer particles during shearing - this results in significant dilation when subject to an increased sliding velocity and an

enhancement in permeability. Such fractures are likely frictionally unstable to neutral [*Niemeijer and Spiers*, 2007], which means that the induced fault slip is on the boundary between seismic slip and aseismic slip. **(2)** The fracture comprises weak-brittle minerals are relatively easier to be crushed into small particles. When the shearing rate increases, the generated wear products initiate dilation but then continue to comminute into finer particles that are subsequently compacted during shearing. These types of fractures tend to be frictionally neutral to stable. **(3)** The fracture material is weak-ductile and clay-rich, with velocity strengthening property and dominated by swelling caused by fluid infiltration. While fluid passes through the fracture, the swelling clays close the aperture. Concurrently, the shearing process comminutes the swelling fracture asperities into fine particles, and distorts particles, resulting in the formation of fabric layer – thin clay-rich foliae, along which the frictional strength is reduced but the stability is increased and the fluid pathway is fully sealed. When the permeability is significantly reduced to its steady state, a change in shearing velocity does not change the permeability. This conceptual model, although not supported by an exhaustive suite of experimental observations on all natural shale rocks, is consistent with the experiments reported here and with the grain packing framework model from previous experimental studies on shales and other sedimentary rocks [*Crawford et al.*, 2008; *Tembe et al.*, 2010; *Kohli and Zoback*, 2013]. Additionally, there are other factors influencing frictional stability, such as fluid pressure, temperature, sliding velocity and presence of carbonate-rich material content [*Niemeijer and Collettini*, 2013; *Verberne et al.*, 2014], while in this study, keeping these potential influencing factors constant will help us better capture fundamental features of the frictional stability – permeability relationship under the simplest variation (*i.e.*, mineralogy). Integrated effects with multiple influencing factors are worth investigating in the further work.

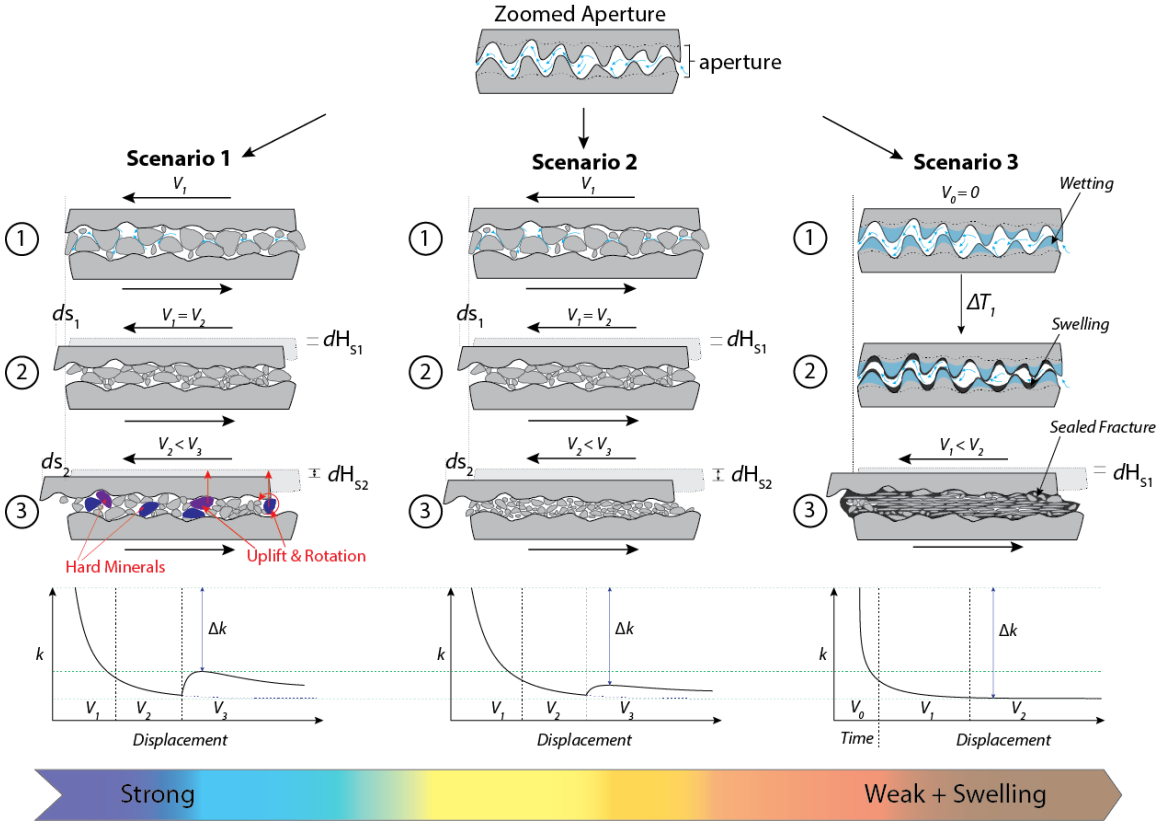

Figure **3-13**: Conceptual model of asperity and permeability evolution of planar saw-cut fractures. Scenario 1: End member of clay-poor, brittle-like fracture material that is composed of hard minerals. During the shearing, the hard minerals are difficult to comminute into small particles and the fracture may dilate significantly. Scenario 2: Intermediate case between clay-poor and clay-rich end member. The fracture material is brittle and comprises weak minerals that are easier to be crushed into fine particles and compacted with shear displacement. Scenario 3: End member of clay-rich and weak-ductile fracture material that is composed of soft minerals. When subject to shearing, the soft minerals readily deform and comminute into smaller particles and fill the trough. With effect of fluid infiltration, clay swelling leads to a thin layer of clay-rich foliae that seals the fracture.

4. Conclusion

In order to understand the mode of fracture reactivation and permeability evolution in shales in a low effective normal stress regime, we performed direct-shearing experiment to measure the frictional strength and stability while also measuring permeability changes. We find that, under low effective normal stress, phyllosilicate-rich shale (OPS) exhibits weaker frictional

strength but much stronger frictional stability and larger permeability reduction than that of carbonate-rich shale (GRS). Our experimental and analytical results show that this observed friction-stability-permeability relationship may be explained via an integration of three interconnected physical mechanisms: (1) different mineral composition of fractures has a distinct effect on frictional strength and frictional stability. At low effective normal stress, phyllosilicate-rich OPS tends to be more frictionally stable than that of carbonate-rich GRS. (2) Generated wear products of low surface roughness fractures, would seal the fluid conduits of fracture aperture, countering the effect of fracture dilation. The competition between wear product and fracture dilation depends on material strength and brittleness – strong-brittle asperities may result in higher frictional strength, lower frictional stability and larger permeability than that of weak-ductile asperities. (3) Swelling of clay-rich asperities and clay-rich wear products directly seals the fracture aperture, and therefore reduces the permeability. This relationship implies that a comprehensive mineralogical characterization of reservoir rock and fractures may help in a preliminary understanding of potential permeability evolution subject to fluid injection in shale rocks. In context of shale reservoir site selection, we speculate that shallow depth overpressure may induce aseismic events in clay-rich shales causing low roughness fractures to seal and secure the integrity of shale reservoir.

Acknowledgement

This work is the result of support provided by U.S. Department of Energy (DOE) under Grant No. DE-FE0023354. This support is gratefully acknowledged. We thank Senior Research Scientist Dr. Mark Rivers for help with the x-ray tomography data collection and processing, which were performed at GeoSoilEnviroCARS (The University of Chicago, Sector 13), Advanced Photon Source (APS), Argonne National Laboratory. GeoSoilEnviroCARS is

supported by the National Science Foundation - Earth Sciences (EAR-1128799) and DOE-Geosciences (DE-FG02-94ER14466). The APS, is a DOE Office of Science User Facility operated under Contract No. DE-AC02-06CH11357. We would like to thank the editor Dr. Michael Walter for handling the manuscript and both reviewers Dr. André Niemeijer and Dr. Peter Eichhubl and an anonymous reviewer whose careful reading and many insightful comments and constructive suggestions helped improve the work. The data for this paper are available by contacting the corresponding author at yi.fang@psu.edu.

Appendix

Table **3-1**: Friction experiment data summary

Sample	Normal Stress (MPa)	Velocity Step	Velocity (μm/s)	Friction Coefficient	(a-b)	D_c ((μm)
Green River	3	1	1 to 10	0.576	0.0027	600
		2	10 to1	0.578	0.0026	500
		3	1 to 10	0.565	0.0022	500
Average[1]				0.573	0.0025	533
Opalinus	3	1	10 to 1	0.569	0.0155	370
		2	1 to 10	0.521	0.0152	430
		3	10 to 1	0.532	0.0173	360
		4	1 to 10	0.466	0.0149	460
		5	10 to 1	0.482	0.0146	330
		6	1 to 10	0.442	0.0140	440
Average[1]				0.502	0.0152	398
Green River	3	Constant[2]	1	0.571	-	-
Opalinus	3	Constant[2]	1	0.498	-	-

Note: (1) The average value of friction coefficient and (a-b) values are obtained from averaging the results of all velocity steps. (2) The friction coefficients of GRS and OPS at constant velocity are evaluated by averaging the friction values after the frictional peak.

Table **3-2**: Parameters used in permeability modeling in Figure 3-8

Parameters	Symbol	Value	Units
Residual hydraulic aperture	b_r	1.0e-5	[m]
Maximum aperture	b_{max}	2.2e-5	[m]
Final aperture after shear	b_f	2.5e-6	[m]
Critical slip distance	D^i_c	600,500,500	[μm]
Loading velocity	V^i	1,10,1,10	[μm/s]
Compaction/Dilation factor	ψ^i	0.09,0.03,0.09	[-]
Effective normal stress	σ_{neff}	3.0	[MPa]
Initial contact length	L_0	18.8	[mm]
Non-linear normal stiffness	α_n	0.3	[1/MPa]
Non-linear shear stiffness	α_s	0.064	[1/MPa]

Note: Loading velocity V^i and effective normal stress σ_{neff} are applied experimental conditions. Critical slip distance D^i_c can be estimated by frictional experiments. Residual hydraulic aperture b_r, maximum aperture b_{max} and final aperture b_f after shearing can be measured using surface characterization method as illustrated in **Figure 3-6(c)**. Non-linear normal stiffness α_n and non-linear shear stiffness α_s are empirical parameters that can be estimated by the curvature of aperture-normal/shear stress function in normal- and shear deformation experiments [*Davies and Davies*, 2001; *Rutqvist et al.*, 2002]. Initial contact length L_0 is known in initial experimental setup. Compaction/Dilation factor ψ^i is an estimated fitting parameter.

References

Allis, R., T. Chidsey, W. Gwynn, C. Morgan, S. White, M. Adams, and J. Moore (2001), Natural CO2 reservoirs on the Colorado Plateau and southern Rocky Mountains: Candidates for CO2 sequestration, in *Proceedings of the First National Conference on Carbon Sequestration*, pp. 14–17.

Anderson, J. G., S. G. Wesnousky, and M. W. Stirling (1996), Earthquake Size as a Function of Fault Slip Rate, *Bull. Seismol. Soc. Am.*, *86*(June), 683–690.

Anderson, R. N., and M. D. Zoback (1982), Permeability, underpressures, and convection in the oceanic crust near the Costa Rica Rift, eastern equatorial Pacific,

Amorim, C. L. G., R. T. Lopes, R. C. Barroso, J. C. Queiroz, D. B. Alves, C. A. Perez, and H. R. Schelin (2007), Effect of clay–water interactions on clay swelling by X-ray diffraction, *Nucl. Instruments Methods Phys. Res. Sect. A Accel. Spectrometers, Detect. Assoc. Equip.*, *580*(1), 768–770, doi:10.1016/j.nima.2007.05.103.

Barton, N., S. Bandis, and K. Bakhtar (1985), Strength, deformation and conductivity coupling of rock joints, *Int. J. Rock Mech. Min. Sci.*, *22*(3), 121–140, doi:10.1016/0148-9062(85)93227-9.

Bossart, P., T. Trick, P. M. Meier, and J.-C. Mayor (2004), Structural and hydrogeological characterisation of the excavation-disturbed zone in the Opalinus Clay (Mont Terri Project, Switzerland), *Appl. Clay Sci.*, *26*(1), 429–448.

Bredehoeft, J. D., W. R. G, K. W. S, and E. Shuter (1976), Hydraulic fracturing to determine the regional in situ stress field , Piceance Basin , Colorado, *Geol. Soc. Am. Bul87letin*, *87*, 250–258, doi:10.1130/0016-7606(1976)87.

Brown, S. R., and C. H. Scholz (1985), Broad bandwidth study of the topography of natural rock surfaces, *J. Geophys. Res.*, *90*(B14), 12575, doi:10.1029/JB090iB14p12575.

Brune, J. N. (1968), Seismic moment, seismicity, and rate of slip along major fault zones, *J. Geophys. Res.*, *73*(2), 777, doi:10.1029/JB073i002p00777.

Corkum, A. G., and C. D. Martin (2007), Modelling a mine-by test at the Mont Terri rock laboratory, Switzerland, *Int. J. Rock Mech. Min. Sci.*, *44*(6), 846–859, doi:10.1016/j.ijrmms.2006.12.003.

Crawford, B. R., D. R. Faulkner, and E. H. Rutter (2008), Strength, porosity, and permeability development during hydrostatic and shear loading of synthetic quartz-clay fault gouge, *J. Geophys. Res. Solid Earth*, *113*(3), 1–14, doi:10.1029/2006JB004634.

Davies, J. P., and D. K. Davies (2001), Stress-Dependent Permeability: Characterization and Modeling, SPE Journal, 6(2), 224-235, doi:10.2118/71750-PA.

Dieterich, J. H. (1978), Time-dependent friction and the mechanics of stick-slip, *Pure Appl. Geophys. PAGEOPH*, *116*, 790–806, doi:10.1007/BF00876539.

Dieterich, J. H. (1979), Modeling of rock friction 1. Experimental results and constitutive equations, in *Journal of Geophysical Research: Solid Earth*, vol. 84, pp. 2161–2168.

Dieterich, J. H. (1992), Earthquake nucleation on faults with rate-and state-dependent strength, *Tectonophysics*, *211*(1–4), 115–134, doi:http://dx.doi.org/10.1016/0040-1951(92)90055-B.

Dyni, J. R. (2006), *Geology and resources of some world oil-shale deposits*, US Department of The Interior, US Geological Survey.

Ellsworth, W. L. (2013), Injection-Induced Earthquakes, *Science (80-.).*, *341*(6142), 142–149, doi:10.1126/science.1225942.

Elsworth, D., and R. E. Goodman (1986), Characterization of rock fissure hydraulic conductivity using idealized wall roughness profiles, *Int. J. Rock Mech. Min. Sci. Geomech. Abstr.*, *23*(3), 233–243, doi:http://dx.doi.org/10.1016/0148-9062(86)90969-1.

Fang, Y., S. A. M. den Hartog, D. Elsworth, C. Marone, and T. Cladouhos (2016), Anomalous distribution of microearthquakes in the Newberry Geothermal Reservoir: Mechanisms and implications, *Geothermics*, *63*, 62–73, doi:http://dx.doi.org/10.1016/j.geothermics.2015.04.005.

Faoro, I., A. Niemeijer, C. Marone, and D. Elsworth (2009), Influence of shear and deviatoric stress on the evolution of permeability in fractured rock, *J. Geophys. Res. Solid Earth*, *114*(1), doi:10.1029/2007JB005372.

Gualda, G. A. R., and M. Rivers (2006), Quantitative 3D petrography using x-ray tomography: Application to Bishop Tuff pumice clasts, *J. Volcanol. Geoth. Res. 154* (1-2), 48-62. doi: 10.1016/j.jvolgeores.2005.09.019

Guglielmi, Y., F. Cappa, J.-P. Avouac, P. Henry, and D. Elsworth (2015), Seismicity triggered by fluid injection–induced aseismic slip, *Sci.* , *348* (6240), 1224–1226, doi:10.1126/science.aab0476.

Healy, J. H., W. W. Rubey, D. T. Griggs, and C. B. Raleigh (1968), The Denver Earthquakes., *Science*, *161*(3848), 1301–1310, doi:10.1126/science.161.3848.1301.

Heidug, W. K., and S. Wong (1996), Hydration swelling of water□absorbing rocks: A constitutive model, *Int. J. Numer. Anal. methods Geomech.*, *20*(6), 403–430.

Ikari, M. J., C. Marone, and D. M. Saffer (2011), On the relation between fault strength and frictional stability, *Geology*, *39*(1), 83–86, doi:10.1130/g31416.1.

Ishibashi, T., N. Watanabe, H. Asanuma, and N. Tsuchiya (2016), Linking microearthquakes to fracture permeability change: The role of surface roughness, *Geophys. Res. Lett.*, *43*(14), 7486–7493, doi:10.1002/2016GL069478.

Kanamori, H., and E. Hauksson (1992), A Slow Earthquake in the Santa Maria Basin, *Bull. Seismol. Soc. Am.*, *82*(5), 2087–2096, doi: .

Kaufhold, A., W. Gräsle, I. Plischke, R. Dohrmann, and S. Siegesmund (2013), Influence of carbonate content and micro fabrics on the failure strength of the sandy facies of the Opalinus Clay from Mont Terri (Underground Rock Laboratory), *Eng. Geol.*, *156*, 111–118, doi:10.1016/j.enggeo.2013.01.014.

Kohli, A. H., and M. D. Zoback (2013), Frictional properties of shale reservoir rocks, *J. Geophys. Res. Earth*, *118*(9), 5109–5125, doi:Doi 10.1002/Jgrb.50346.

Majer, E. L., R. Baria, M. Stark, S. Oates, J. Bommer, B. Smith, and H. Asanuma (2007), Induced seismicity associated with Enhanced Geothermal Systems, *Geothermics*, *36*(3), 185–222, doi:http://dx.doi.org/10.1016/j.geothermics.2007.03.003.

Marone, C. (1997), On the rate of frictional healing and the constitutive law for time- and slip-dependent friction, *Int. J. rock Mech. Min. Sci. Geomech. Abstr.*, *34*, 347, doi:10.1016/S1365-1609(97)00054-3.

Marone, C. (1998), Laboratory-derived friction laws and their application to seismic faulting, *Annu. Rev. Earth Planet. Sci.*, *26*, 643–696, doi:Doi 10.1146/Annurev.Earth.26.1.643.

Mazumder, S., and K. H. Wolf (2008), Differential swelling and permeability change of coal in response to CO 2 injection for ECBM, *Int. J. Coal Geol.*, *74*(2), 123–138.

McGarr, a., D. Simpson, and L. Seeber (2002), 40 Case histories of induced and triggered seismicity, *Int. Geophys.*, *81*(PART A), 647–661, doi:10.1016/S0074-6142(02)80243-1.

Misra, A. (2002), Effect of asperity damage on shear behavior of single fracture, *Eng. Fract. Mech.*, *69*(17), 1997–2014, doi:10.1016/S0013-7944(02)00073-5.

Mohan, K. K., R. N. Vaidya, M. G. Reed, and H. S. Fogler (1993), Water sensitivity of sandstones containing swelling and non-swelling clays, *Colloids Surfaces A Physicochem. Eng. Asp.*, *73*, 237–254, doi:10.1016/0927-7757(93)80019-B.

Niemeijer, A. R., and C. J. Spiers (2007), A microphysical model for strong velocity weakening in phyllosilicate-bearing fault gouges, *J. Geophys. Res. Solid Earth*, *112*(B10), B10405, doi:10.1029/2007JB005008.

Niemeijer, A., and C. Collettini (2013), Frictional Properties of a Low-Angle Normal Fault Under In Situ Conditions: Thermally-Activated Velocity Weakening, *Pure Appl. Geophys.*, 1–24, doi:10.1007/s00024-013-0759-6.

Norrish, K. (1954), The swelling of montmorillonite, *Discuss. Faraday Soc.*, *18*(0), 120–134,

doi:10.1039/DF9541800120.

Norrish, K., and J. P. Quirk (1954), Crystalline Swelling of Montmorillonite: Use of Electrolytes to Control Swelling, *Nature*, *173*(4397), 255–256.

Peng, Z., and J. Gomberg (2010), An integrated perspective of the continuum between earthquakes and slow-slip phenomena, *Nat. Geosci.*, *3*(9), 599–607, doi:10.1038/ngeo940.

Rabinowicz, E. (1951), The nature of the static and kinetic coefficients of friction, *J. Appl. Phys.*, *22*(1951), 1373–1379, doi:10.1063/1.1699869.

Raleigh, C. B., J. H. Healy, and J. D. Bredehoeft (1976), An experiment in earthquake control at rangely, colorado., *Science*, *191*(4233), 1230–7, doi:10.1126/science.191.4233.1230.

Rice, J. R. (2006), Heating and weakening of faults during earthquake slip, *J. Geophys. Res. Solid Earth*, *111*(5), 1–29, doi:10.1029/2005JB004006.

Ruina, A. (1983), Slip instability and state variable friction laws, *J. Geophys. Res. Solid Earth*, *88*(B12), 10359–10370, doi:10.1029/JB088iB12p10359.

Rutqvist, J., Y.-S. Wu, C.-F. Tsang, and G. Bodvarsson (2002), A modeling approach for analysis of coupled multiphase fluid flow , heat transfer , and deformation in fractured porous rock, *Int. J. Rock Mech. Min. Sci.*, *39*(4), 429–442, doi:10.1016/S1365-1609(02)00022-9.

Rutqvist, J., C. F. Tsang, and Y. Tsang (2004), Analysis of stress and moisture induced changes in fractured rock permeability at the yucca mountain drift scale test, in *Elsevier Geo-Engineering Book Series*, vol. Volume 2, edited by S. Ove, pp. 161–166, Elsevier.

Samuelson, J., D. Elsworth, and C. Marone (2009), Shear-induced dilatancy of fluid-saturated faults: Experiment and theory, *J. Geophys. Res. Solid Earth*, *114*(12), 1–15, doi:10.1029/2008JB006273.

Schmidt, D. A., R. Bürgmann, R. M. Nadeau, and M. D'Alessio (2005), Distribution of aseismic slip rate on the Hayward fault inferred from seismic and geodetic data, *J. Geophys. Res. B Solid Earth*, *110*(8), 1–15, doi:10.1029/2004JB003397.

Scholz, C. H. (1998), Earthquakes and friction laws, *Nature*, *391*(6662), 37–42, doi:Doi 10.1038/34097.

Shapiro, S. A., C. Dinske, and E. Rothert (2006), Hydraulic-fracturing controlled dynamics of microseismic clouds, *Geophys. Res. Lett.*, *33*(14), doi:Artn L14312Doi 10.1029/2006gl026365.

Snow, D. T. (1969), Anisotropic Permeability of Fractured Media, *Water Resour. Res.*, *5*(6), 1273–&, doi:Doi 10.1029/Wr005i006p01273.

Suckale, J. (2009), Induced seismicity in hydrocarbon fields, *Adv. Geophys.*, *51*(09), 1976–1984, doi:10.1016/S0065-2687(09)05107-3.

Tanikawa, W., M. Sakaguchi, O. Tadai, and T. Hirose (2010), Influence of fault slip rate on shear-induced permeability, *J. Geophys. Res. Solid Earth*, *115*, 1–18, doi:10.1029/2009JB007013.

Tanikawa, W., O. Tadai, and H. Mukoyoshi (2014), Permeability changes in simulated granite faults during and after frictional sliding, *Geofluids*, 14(4), 481-494, doi: 10.1111/gfl.12091.

Tembe, S., D. A. Lockner, and T. F. Wong (2010), Effect of clay content and mineralogy on frictional sliding behavior of simulated gouges: Binary and ternary mixtures of quartz, illite, and montmorillonite, *J. Geophys. Res. Solid Earth*, *115*(3), doi:10.1029/2009JB006383.

Walsh, F. R., and M. D. Zoback (2015), Oklahoma's recent earthquakes and saltwater disposal, *Sci. Adv.*, *1*(5).

Weibin Wang, and C. H. Scholz (1994), Wear processes during frictional sliding of rock: a theoretical and experimental study, *J. Geophys. Res.*, *99*(B4), 6789–6799, doi:10.1029/93JB02875.

Wenk, H. R., M. Voltolini, M. Mazurek, L. R. Van Loon, and A. Vinsot (2008), Preferred orientations and anisotropy in shales: Callovo-oxfordian shale (France) and opalinus clay (Switzerland), *Clays Clay Miner.*, *56*(3), 285–306, doi:10.1346/CCMN.2008.0560301.

Xu, T., and K. Pruess (2004), Numerical simulation of injectivity effects of mineral scaling and clay swelling in a fractured geothermal reservoir, *Lawrence Berkeley Natl. Lab.*

Yasuhara, H., D. Elsworth, and A. Polak (2004), Evolution of permeability in a natural fracture: Significant role of pressure solution, *J. Geophys. Res. Earth*, *109*(B3), doi:Artn B03204Doi 10.1029/2003jb002663.

Yasuhara, H., A. Polak, Y. Mitani, A. S. Grader, P. M. Halleck, and D. Elsworth (2006), Evolution of fracture permeability through fluid-rock reaction under hydrothermal conditions, *Earth Planet. Sci. Lett.*, *244*(1–2), 186–200, doi:10.1016/j.epsl.2006.01.046.

Yoshioka, N. (1997), A review of the micromechanical approach to the physics of contacting surfaces, *Tectonophysics*, *277*(1-3), 29–40, doi:10.1016/S0040-1951(97)00076-0.

Yoshioka, N., and C. H. Scholz (1989), Elastic properties of contacting surfaces under normal and shear loads: 2. Comparison of theory with experiment, *J. Geophys. Res.*, *94*, 17691, doi:10.1029/JB094iB12p17691.

Young, D. A., and D. E. Smith (2000), Simulations of clay mineral swelling and hydration: dependence upon interlayer ion size and charge, *J. Phys. Chem. B*, *104*(39), 9163–9170.

Verberne, B. A., C. J. Spiers, A. R. Niemeijer, J. H. P. De Bresser, D. A. M. De Winter, and O. Plümper (2014), Frictional Properties and Microstructure of Calcite-Rich Fault Gouges Sheared at Sub-Seismic Sliding Velocities, *Pure Appl. Geophys.*, *171*(10), 2617–2640, doi:10.1007/s00024-013-0760-0.

Zhong, Z., D. Elsworth, and Y. Hu (2016), Evolution of Strength and Permeability in Stressed Fractures with Fluid–Rock Interactions, *Pure Appl. Geophys.*, *173*(2), 525–536.

Zoback, M. D., and S. M. Gorelick (2012), Reply to Juanes et al.: Evidence that earthquake triggering could render long-term carbon storage unsuccessful in many regions, *Proc. Natl. Acad. Sci. U. S. A.*, *109*(52), E3624–E3624, doi:Doi 10.1073/Pnas.1217264109.

Chapter 4

Mineralogical Controls on Frictional Strength, Stability and Shear Permeability Evolution of Fractures

Abstract

Massive fluid injection into the subsurface can reactivate pre-existing faults or fractures as seismic or aseismic slip. Such seismic or aseismic shear deformations may result in different modes of permeability evolution. Previous studies have explored frictional stability-permeability relationships of carbonate-rich and phyllosilicate-rich samples under shear, suggesting that friction-permeability relationship may be primarily controlled by fracture minerals. We examine this relationship and identify the role of mineralogy (*i.e.*, tectosilicate, carbonate, and phyllosilicate content) using direct-shear experiments on saw-cut fractures of natural rocks and sintered fractures with distinct mineralogical compositions. These results indicate that the friction-permeability relationship is controlled by mineralogy. Frictional strength and change in permeability both decrease with an increase in either phyllosilicate or carbonate content as frictional instability (*a*-*b*) increases. This relationship implies a new closed hydro-mechanical-chemical (HMC) coupling loop.

Key words: fracture minerals, frictional strength, stability, and permeability evolution

1. Introduction

The stimulation of shale gas reservoirs, of enhanced geothermal system (EGS), and the long term geological sequestration of CO_2 involve massive fluid injection that may reactivate pre-existing faults and fractures and induce seismicity. This deformation may occur as seismic slip, slow slip and aseismic slip [*Cornet et al.*, 1997; *Zoback et al.*, 2012; *Guglielmi et al.*, 2015b; *Fang et al.*, 2016]. In-situ observations show that these deformations may affect the transport characteristics of the reservoir formation. For example, locally elevated permeabilities at seismogenic depths are observed in IODP drill holes on the Cascadia margin [*Davis et al.*, 1995]. In-situ experiments show permeability enhancement associated to small dilatant slip event in reactivation of both Tournemire shale and carbonate faults [*Guglielmi et al.*, 2015a, 2015b]. At laboratory scale, experimental observations indicate that when a fracture slips, permeability may increase due to significant dilation or decrease as a result of progressive formation of gouge [*Barton et al.*, 1985; *Faoro et al.*, 2009]. These relationships between fluid flow and fault slip pose a ubiquitous question in understanding how fault permeability evolves during fault movement. This further provides significant insight of how fluids may be trapped by sealing layers, how hydrocarbons may migrate within fractures, and how the integrity of seal systems may be degraded or enhanced. Theoretical treatments and experimental results suggest that fault movement is independent of fault strength but governed by the frictional behavior within the fault associated with slip velocity perturbations [*Brune*, 1970; *Johnson and Scholz*, 1976; *Ikari et al.*, 2011]. This frictional behavior is empirically defined by rate-and-state friction laws [*Dieterich*, 1978, 1979; *Ruina*, 1983], in which the friction coefficient μ (also known as the frictional strength) is written as :

$$\mu = \mu_0 + a \cdot \ln\left(\frac{V}{V_0}\right) + b \cdot \ln\left(\frac{V_0 \theta}{D_c}\right) \tag{1}$$

$$\frac{d\theta}{dt} = 1 - \frac{V\theta}{D_c} \tag{2}$$

where μ_0 is the coefficient of friction at a reference fault slip velocity; θ is a state variable, a and b are friction parameters which represent the effect of instantaneous and displacement-dependent changes in friction from V_0 to V; and D_c is the critical slip distance over which evolution to a new steady state takes place. Frictional slip instability is determined in part by the parameter $(a-b)$ for a finite step in velocity, yielding [*Dieterich*, 1979; *Ruina*, 1983; *Scholz*, 1998]:

$$a - b = \frac{\Delta\mu_{ss}}{\Delta \ln V} \tag{3}$$

The μ value defines the propensity for failure while $(a-b)$ values define the mode of slip, as stable, aseismically (*i.e.*, $a-b>0$), or unstable, seismically (*i.e.*, $a-b<0$) [*Samuelson and Spiers*, 2012; *Kohli and Zoback*, 2013].

Abundant experimental studies have revealed the values of frictional strength and frictional stability of a variety of rock materials, such as shales, tuffs, carbonates, clays, mineral mixtures, and natural fault gouge. Behavior may be divided among three mineral groups: tectosilicates, carbonates, and phyllosilicates (**Figure 4-1a**) [*Stesky et al.*, 1974; *Numelin et al.*, 2007; *Smith and Faulkner*, 2010; *Verberne et al.*, 2010, 2014, *Ikari et al.*, 2011, 2015; *Moore and Lockner*, 2011; *Boulton et al.*, 2012; *Samuelson and Spiers*, 2012; *Kohli and Zoback*, 2013; *Carpenter et al.*, 2015; *Giorgetti et al.*, 2015; *Fang et al.*, 2016]. These frictional strength and stability values follow a reversal relationship (**Figure 4-1b**). The time or rate dependence of frictional strength is due to processes that affect the true area of solid-solid contract between the sliding surfaces. Microphysical models explain these experimental observations by examining the mechanics of surface contact and rheology of microstructure of crystalline phases during shear deformation. This suggests that the frictional stability of a simulated fault gouge is associated

with shear-induced dilation or compaction [*Niemeijer and Spiers*, 2007; *Niemeijer and Collettini*, 2013]. Hence, the frictional strength and stability values may be linked to permeability evolution of a fracture during shearing.

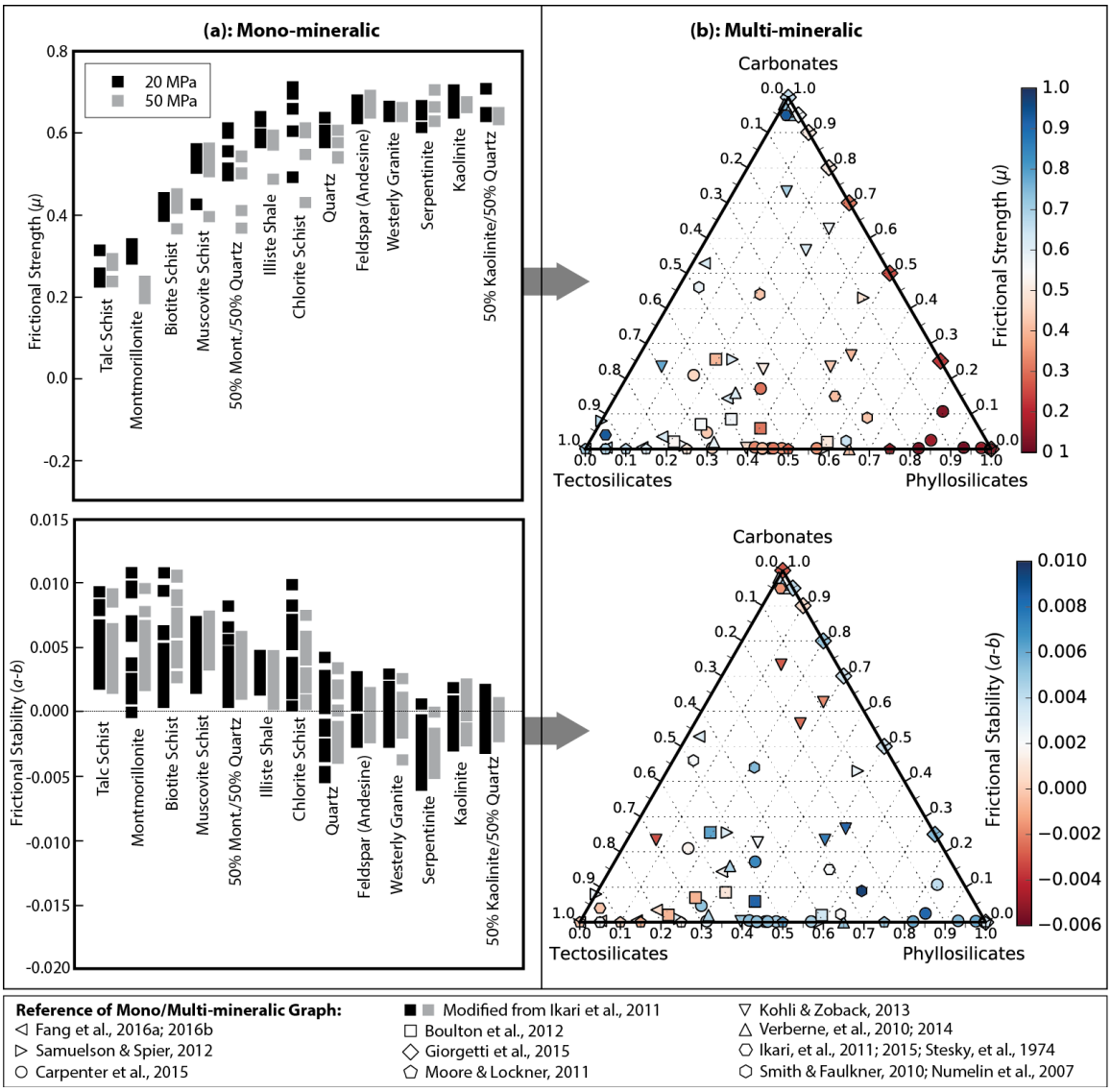

Figure **4-1**: **(a)** Frictional strength μ and stability (a-b) of mono-mineralogical samples. **(b)** Frictional strength μ and stability (a-b) of samples with varied proportions of Carbonate-Tectosilicate-Phyllosilicate mixtures. Source data of this ternary graph is listed in **Appendix Table 4-A1**.

Previous experimental studies have explored friction-stability-permeability relationships of carbonate-rich and phyllosilicate-rich samples during shear deformation, suggesting that phyllosilicate-rich shale has a lower frictional strength, but higher frictional stability and larger permeability reduction than that of carbonate-rich shale [*Fang et al.*, 2017]. This result, implying the effect of mineralogy on friction-stability-permeability, however, may not be sufficient to identify the role of each mineral group (*i.e.*, tectosilicate, carbonate, and phyllosilicate content). It is still uncertain whether or not a systematic relationship of friction-stability-permeability relationships of fractures can be constrained.

In this study, we explore friction-stability-permeability relationships with respect to mineralogical compositions of fractures through a series of direct-shear experiments on saw-cut fractures of natural rocks (Green River shale, Opalinus shale, Longmaxi shale, Tournemire shale, Marcellus shale, and Newberry tuff). These represent distinct mineralogical compositions, as do sintered fractures with specially controlled weight percentages of mineral groups. In particular, we address questions including: Can mineralogical compositions predict the frictional strength, stability and shear permeability evolution of fractures? What is the implication of the friction-stability-permeability relationship to fluid rock interaction in fluid-injection involved engineering activities, such as, long-term heat recovery and geological sequestration of CO_2?

2. Experimental Method

In the following we define experimental assumptions, introduce sample materials and methods of preparation and finally define the experimental setup and procedures.

2.1 Assumptions

The experimental conditions and data analysis are based on following assumptions: **(1)** Frictional strength and stability are primary controlled by three mineralogical end-members: carbonates (*C*), tectosilicates (*T*), and phyllosilicates (*P*) while keeping other factors (*e.g.*, effective normal stress, fracture roughness and temperature) constant (**Figure 4-1**). **(2)** The sintered fractures comprise an assemblage of three mineral groups: carbonates, tectosilicates and phyllosilicates. The percentage of each mineral group is defined from lithofaces classifications of shale rock in **Figure 4-A1** [*Gamero-Diaz et al.*, 2013]. **(3)** The frictional strength of sintered samples is shown to be representative of natural samples with the same lithology. The frictional strength of natural Green River shale and sintered Green River shale (powdered and reconsolidated) shows a difference of <10%, suggesting a reliable analogue (**Figure 4-A2)**. **(4)** The linkage between the evolution of friction, stability, and permeability are explored in the brittle regime where mechanical controls dominate response and thermally and chemically activated effects are too slow to be manifest.

2.2 Sample Materials and Preparation

In this experiment, we prepare two types of samples (1) intact natural samples and (2) sintered samples. We collect six intact natural samples including five shales (*i.e.,* Green River shale, Opalinus claystone, Marcellus shale, Tournemire shale, and Longmaxi shale) and one tuff (*i.e.,* Newberry tuff). The Green River shale is deposited in a freshwater lacustrine environment and is recovered from the sequence at Grand Junction, Colorado. The Opalinus shale, known as a clay-rich caprock, is taken from horizontal borehole (BEZ-G50) at the Mont Terri underground rock laboratory in Switzerland. The Marcellus shale is taken from outcrop from the Middle

Devonian Marcellus Formation at Frankstown, PA (New Enterprise Quarry off Locke Mountain Road, Coordinates: N40°26'00", W78°20'28"). The Tournemire shale sample is cored from a fault zone in the shale formations at Tournemire Underground Research Laboratory in France. The Longmaxi shale sample is collected from the major gas production formation, Sichuan Province, China. The Newberry tuff is cored from well N2 at Newberry geothermal site, Oregon.

The sintered samples are consolidated from five different minerals: dolomite, calcite, albite, quartz and illite that are common in major fault zones. The mineral chips are purchased from Ward Science Company (**Figure 4-2a**) and then powdered with a particle size less than 100 μm. Based on the weight percentage in **Figure 4-A1**, the powders of each mineral phase are uniformly mixed with deionized water. The mixed mineral slurry is filled into the pressing vessel, and then drained and consolidated under an overburden stress of 150 MPa (**Figure 4-2b**). When consolidation ceases, the samples are removed from the pressure vessel and dried at room temperature for 48 hours. The natural samples are saw cut into twin coupons with a dimension of 0.22 inch × 1.5 inch × 0.75 inch (**Figure 4-2c**). The artificial samples are directly pressed into the same dimension as that of natural samples. The planar surfaces of the coupons are uniformly roughened with grinding powder (#60 Grit) at constant rate to ensure the surface roughness of the same order. The mineral compositions of the natural samples are characterized via X-ray diffraction and the data are listed in **Table 4-A2** in **Appendix**. The basic properties of those samples are listed in **Table 4-A3**. The weight percentage of each group of all samples is illustrated in **Figure 4-3**.

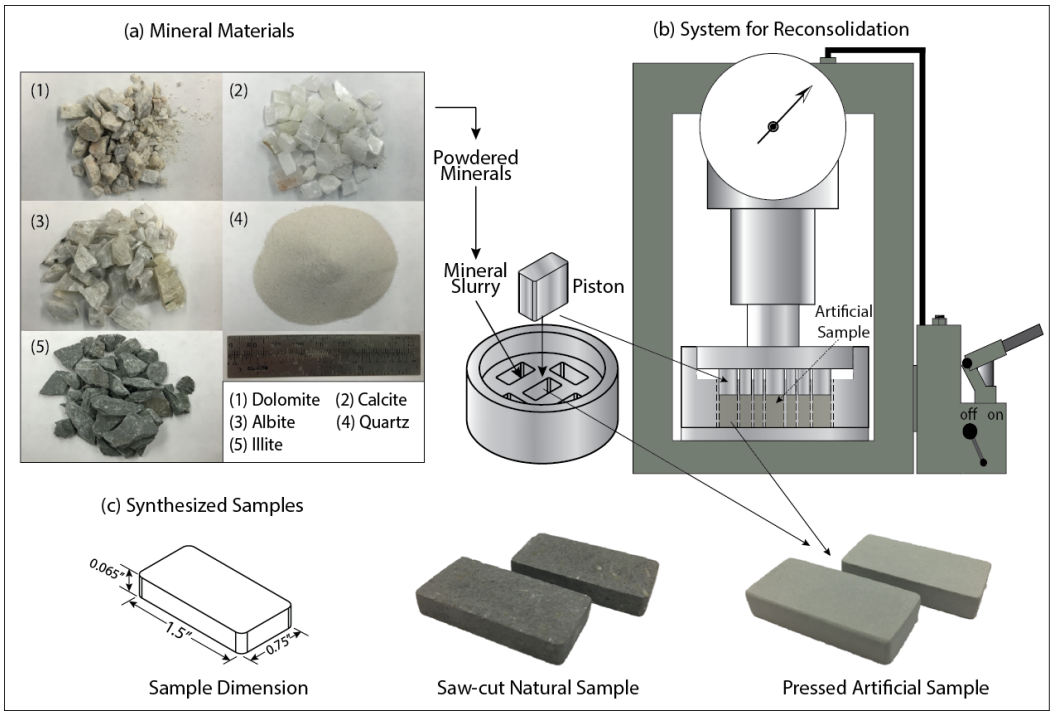

Figure **4-2**: **(a)** Minerals for artificial samples. **(b)** System for reconsolidation comprising a pressuring system, sample vessel, draining base and piston. **(c)** Dimension of saw-cut natural and artificial samples.

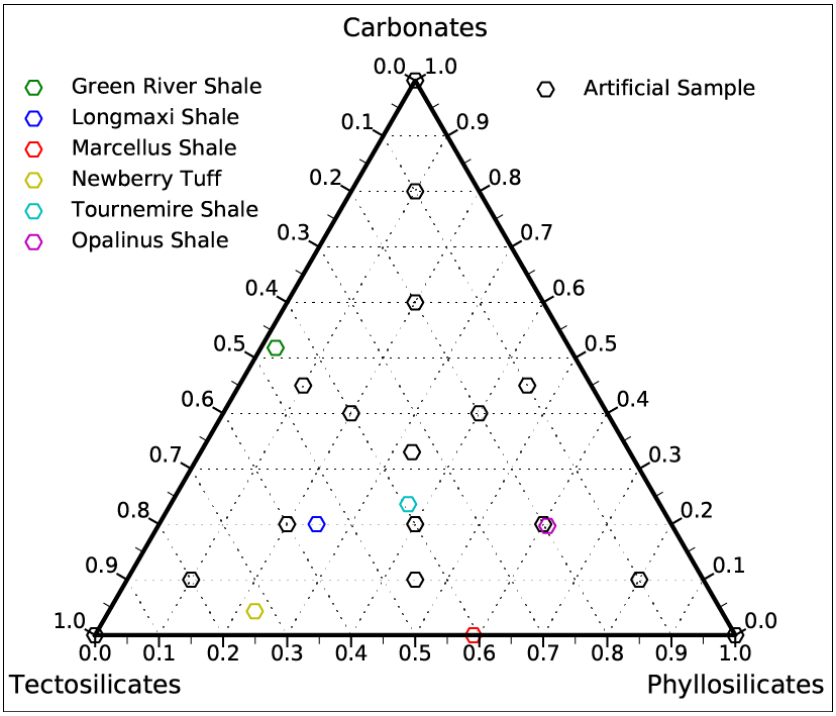

Figure **4-3**: Ternary diagram of mineral groups (tectosilicate, carbonate, and phyllosilicate) for both natural samples and artificial samples (wt.% data is listed in **Appendix Table 4-A4**)

2.3 Experimental Setup and Procedure

The friction-permeability experiments are performed in a triaxial testing apparatus that independently applies confining pressure and differential (end-to-end) pore pressure while the sample is sheared at a prescribed velocity (**Figure 4-4**). This allows the concurrent measurement of the evolution of fracture permeability and friction. The sample coupons are packed within a pair of steel shearing platens. The initial offset of platens is ~8 mm for slip displacement during sliding. The platen-offset gap is filled with filler as a seal. The side and bottom contacts between the sample coupon and the platen surfaces are packed with Teflon to prevent fluid leakage. The assembled platens are packed within a membrane to isolate from the confining fluid. A steel sleeve covers the load cell to prevent the effect of applied confining pressure.

To be consistent with the applied stress conditions of previous experimental studies [*Fang et al.*, 2017], we apply a confining stress (normal stress) of 3 MPa and set a constant upstream fluid pressure during axial shear displacement (at constant rate). The minimum flow rate of each pump is 0.001 ml/min and the display resolution of the pump pressure transducer is 1.0 kPa. A load cell with a resolution of 0.3 kPa is used to measure the axial stress. At room temperature, the minimum measurable permeability is $1.0 \times 10^{-16} m^2$.

We conduct velocity-stepping experiments to compare the hydraulic behavior response to varying velocities for both natural and sintered samples. The shear velocity is set to 10 μm/s (monotonic) and switched between down-steps and up-steps between 1 μm/s and 10 μm/s, until a displacement of ~6 to 7 mm is reached. All experiments are performed at room temperature (25 C°), with shear displacements recorded by LVDT (Linear Variable Differential Transformer) located outside the vessel.

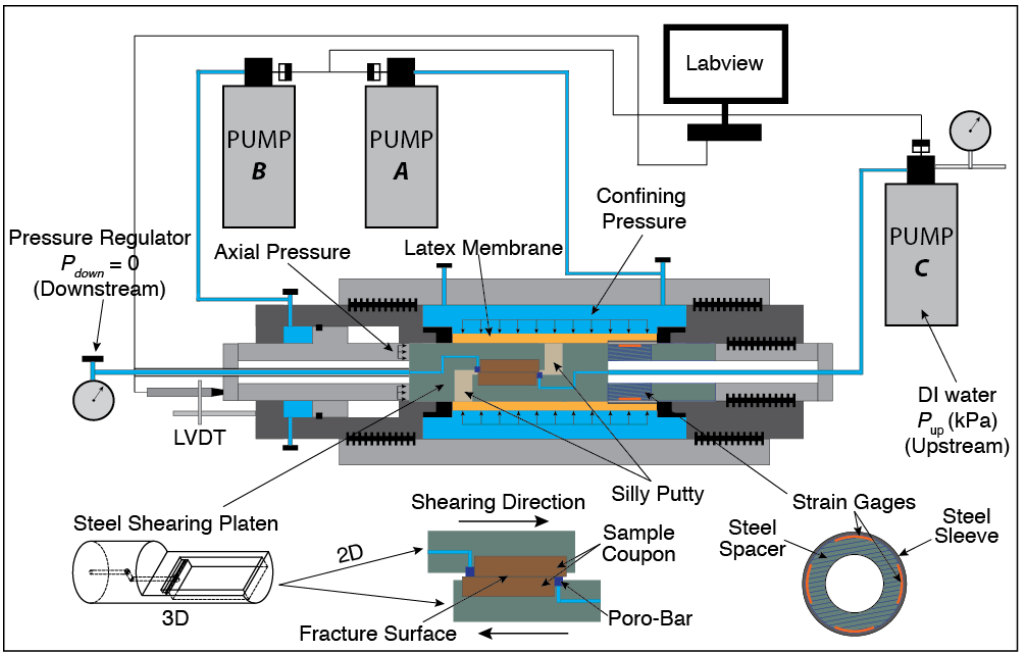

Figure **4-4**: Experimental setup to measure friction-permeability evolution: Pump A (ISCO 500D) controls the confining pressure (normal stress) applied on the fracture. Pump B (ISCO 500D) controls pressure that provides the source of shear stress applied on the fracture. Pump C (ISCO 500D) injects the fluid at a prescribed flow rate or pressure, allowing the fluid source located at the origin of the fracture and flow along the fractures.

3. Results and Discussions

In the following, we first interpret measurements of concurrent flow and deformation to recover friction-stability-permeability evolution in the context of rate-state friction models. We then correlate these friction-stability-permeability relationships with mineral assemblage to explore how mineralogy may control permeability evolution and link this with seismicity.

3.1 Analysis and Discussion

Frictional strength and stability are evaluated from **Eqs. (1)** to **(3)**. The measured fracture permeability k_m [m^2] is expressed in terms of averaged hydraulic aperture b_m [m] based on the cubic law of a single fracture:

$$b_m = -\left(\frac{12\mu_{vis} \cdot L(t) \cdot Q(t)}{W \cdot \Delta P_f} \right)^{1/3} \tag{4}$$

$$k_m = \frac{b_m^2}{12} \tag{5}$$

where μ_{vis} [Pa·s] is the viscosity of fluid; $L(t)$ [m] is the contact length of the fracture surface; W [m] is the fracture width; $Q(t)$ [m^3/s] is the measured flow rate and ΔP_f [Pa] is the differential pressure between the upstream and downstream extent of the fracture.

By solving **Eqs. (1)** to **(3)**, we model a (shearing) velocity step of each shale sample to confirm the frictional parameters. Meanwhile, we define two terms representing permeability change as follows,

$$\Delta k^i_n = \frac{k^i_{real} - k^i_{sim}}{k_0} \tag{6}$$

where Δk^i_n refers to the permeability change normalized to the initial fracture permeability k_0 before shearing; k^i_{real} is the measured permeability after the velocity step; k^i_{sim} is the simulated permeability that is assumed for unchanged velocity (*i.e.*, no velocity step). Index i refers to the i^{th} velocity step. However, as frictional parameters evolve with shearing, to correlate the transient permeability change to the concurrent frictional parameters, it is necessary to calculate the relative permeability change with respect to the permeability value at the point immediately before the shear velocity step:

$$\frac{\Delta k^i}{k^i_0} = \frac{k^i_{real} - k^i_{sim}}{k^i_0} \tag{7}$$

where Δk^i is the absolute permeability change from before until after the velocity step; k^i_0 is a reference permeability before the velocity step is applied. **Figure 4-5a** shows the results of one sample as an example of the net friction and permeability evolution with displacement. The calculated net fracture permeability monotonically decreases with displacement, consistent with previous observations [*Fang et al.*, 2017]. The data fitting method for simulating the permeability change is introduced in *Fang* et al., [2017]. Local frictional change and permeability evolution in response to shear velocity change are shown in **Figure 4-5b** and **Figure 4-5c**. The measured and modeled frictional parameters and permeability change of each sample are listed in Table **4-A5** and **4-A6**.

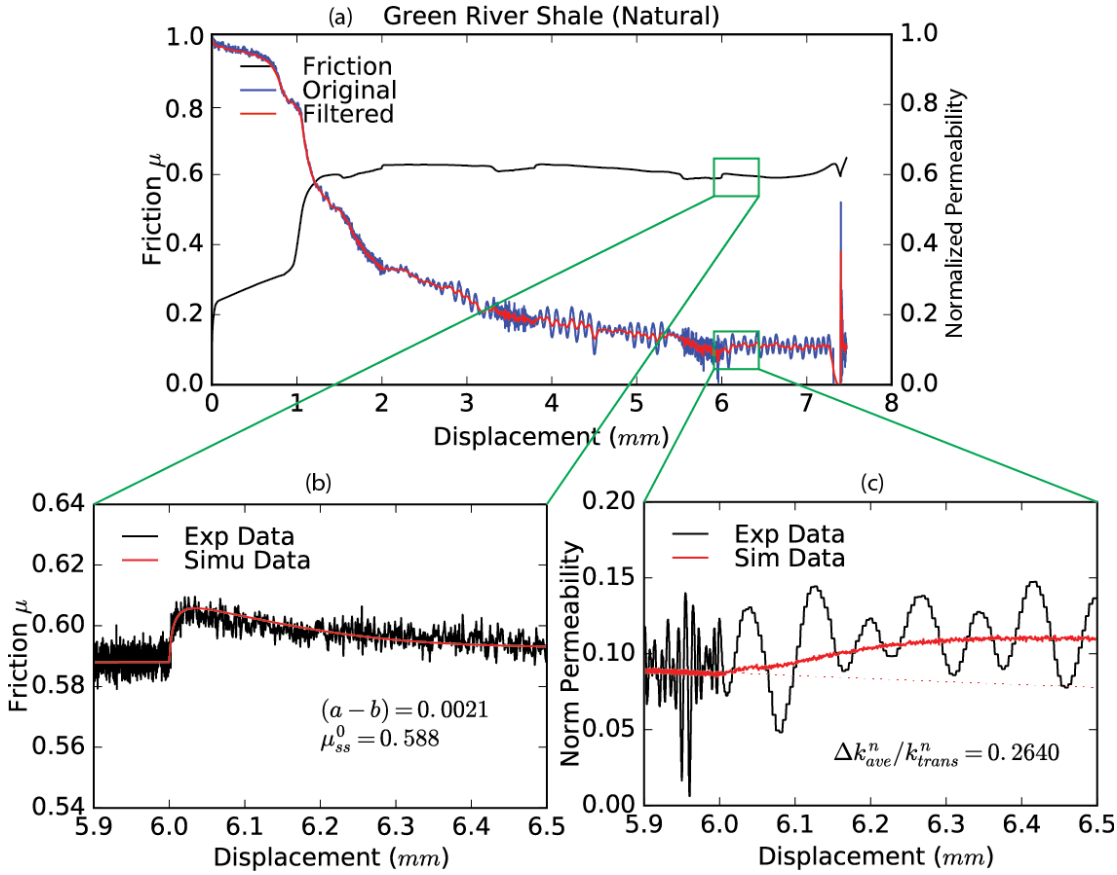

Figure **4-5**: (a) Net friction and permeability evolution during slip. (b) Frictional response to velocity change from 1 μm/s to 10 μm /s. (c) Permeability change with respect to velocity change from 1 μm/s to 10 μm /s

The analyzed frictional parameters and transient permeability change in response to velocity change are shown in **Figure 4-6** with respect to the selected mineral groups: phyllosilicates, carbonates and tectosilicates. Frictional strength μ and transient permeability change Δk_n and $\Delta k_n/\Delta k^i_0$ decrease with phyllosilicate content but increase with tectosilicate content. In contrast, a reverse trend is observed for frictional stability (*a*-*b*). However, the role of carbonate is distinct from the other two mineral groups. The permeability changes decrease with both frictional strength and stability, implying that in the very shallow crust (*i.e.*, low normal stress and low temperature), slip reactivation in calcite-bearing fault gouges is difficult and is unlikely to induce seismic events - and permeability is reduced during the resulting aseismic slip.

As surface contact state, which determines the flow path, is reflected in the frictional strength and stability, we directly correlate the permeability change with friction in **Figure 4-7**. The permeability change Δk has a positive correlation with concurrently measured frictional strength μ but a negative correlation with the corresponding frictional stability (*a*-*b*). This intrinsic linkage of friction and permeability change is directly determined by the asperity contact state and the material properties (*e.g.*, mechanical and swelling) that control the mechanical behaviors of fracture asperities. However, it is worth noting that the magnitude of permeability change in the natural samples is much larger than that of the artificial samples (shown as the solid black symbols in **Figure 4-6** and **4-7**) – this is due to the very distinct difference in the surface textures.

In summary, with known mineralogical compositions comprising the fracture, the frictional strength and stability of fractures can be estimated. Shear failure is less likely to occur for fractures with higher content of tectosilicates. However, once failure initiates, the fracture is more likely slip unstably. This process is opposite that for fractures with higher clay content - where the fracture is easier to reactivate and will slip stably. When an unstable fracture slides at

an accelerating rate, the transient change in fracture permeability can be speculated – those richer in tectosilicates exhibit larger permeability enhancement.

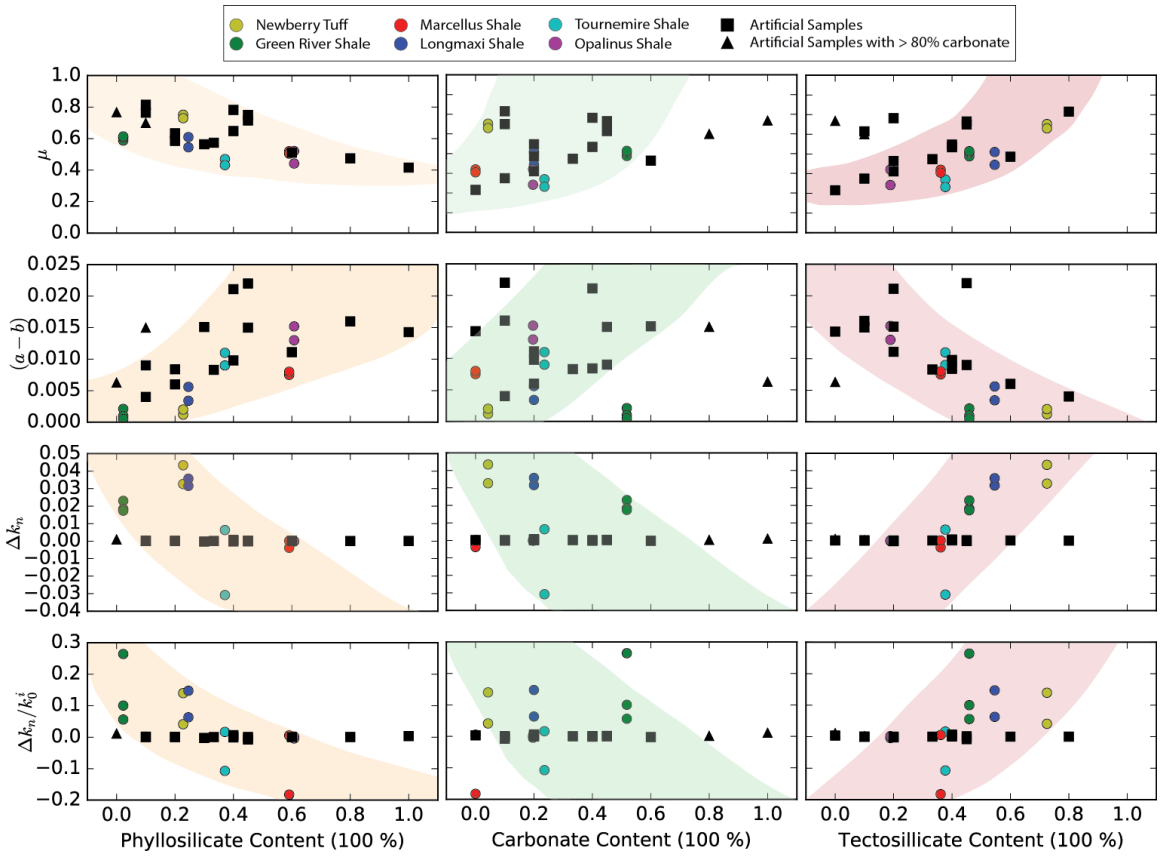

Figure **4-6**: Effect of mineral composition on friction response (*i.e.*, μ and (*a*-*b*)) and transient permeability evolution (*i.e.,* Δk_n and $\Delta k_n/\Delta k^i_0$) in response to shear velocity change. (a) Effect of phyllosilicate content; (b) Effect of carbonate content; (c) Effect of tectosilicate content

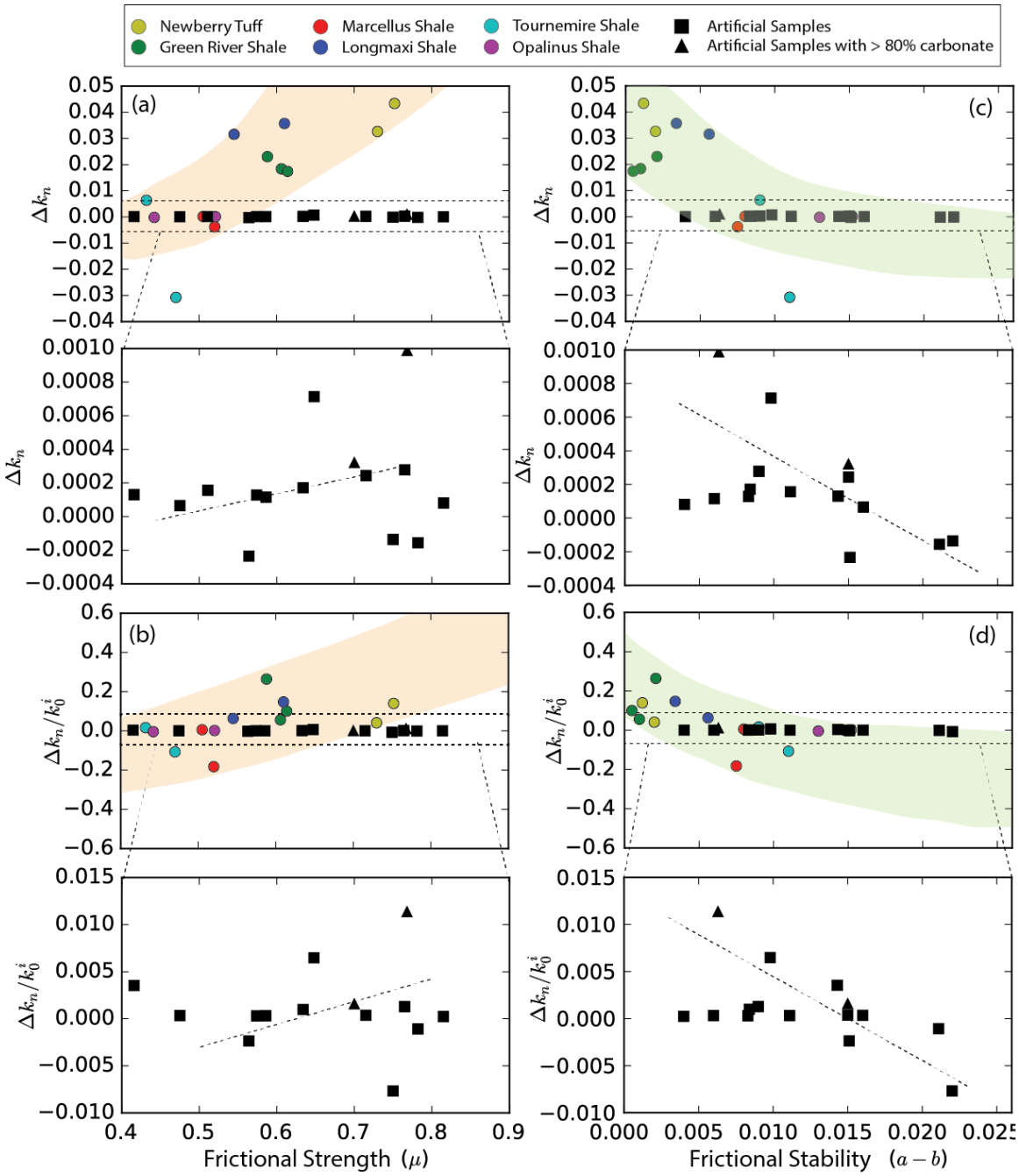

Figure **4-7**: (a) and (b) Correlation between frictional strength (μ) and permeability evolution (Δk_n and $\Delta k^i/\Delta k^i_0$); (c) and (d) Correlation between frictional stability (a-b) and permeability evolution (Δk_n and $\Delta k^i/\Delta k^i_0$).

3.2 Implication

Friction-permeability relationships defined with respect to mineralogy imply that fluid-rock interactions in fault zones may systematically impact the likelihood of reactivation, the mode of deformation as seismic or aseismic and the corresponding sense of permeability evolution. During the evolution of a natural fault, fluids can react with fault rocks. For example, fine-grained cataclasites in the fault core [*Evans and Chester*, 1995] may transform to new mineral phases (*e.g.*, phyllosilicate-rich) and structures (*e.g.*, foliation) that weaken the fault [*Collettini et al.*, 2008] and impact its mode of deformation. The impact of such fluid-rock interaction is represented in the substitution of mineralogical compositions selected in this work. For instance, when phyllosilicate-rich materials result from aluminosilicates, frictional strength is reduced due to the change in mineralogical content. Moreover, precipitation of new minerals (*e.g.*, carbonates) decreases the fracture aperture and potentially its permeability. Dissolution, however, can increase porosity and permeability and weaken the fault if sufficient dissolution takes place (*i.e.*, carbonates are significantly removed). Natural fluid-rock interaction process in fault zones operate over geologic time scales [*Kerrich*, 1986; *Lin et al.*, 2003]. However, anthropogenic fluid-injection (*i.e.*, enhanced geothermal energy recovery and geological sequestration of CO_2) may accelerate these transformations with fluids pushed far from equilibrium. In such cases, we expect (1) friction evolution due to silica dissolution on fault surfaces where interactions exist between the injected water and the reservoir rock over a long-term fluid circulation [*Xu et al.*, 2009]; and (2) a significant change in frictional strength of faults present in a CO_2 storage system when there is major carbonate precipitation in the fault damage zone due to rapid CO_2 leakage and degassing [*Bakker et al.*, 2016].

Thus, a new closed mechanical-hydro-chemical (MHC) coupling is speculated *via* linking the friction, mineralogy, and permeability of fault surfaces (**Figure 4-8)**: (1) pore pressure grows

in a fault zone, initiating fault slip at a critical state (Mohr-Coulomb criterion); (2) fault frictional behaviors, controlled by fault minerals [*Ikari et al*., 2011], define the mode of shear slip and its simultaneous permeability change; (3) altered fault permeability leads to a changed flow rate, breaking the equilibrium of initial mineral dissolution or precipitation [*Ellis et al.*, 2013]; (4) Newly formed mineral phases on fracture surfaces, in return, adjusts the frictional behaviors.

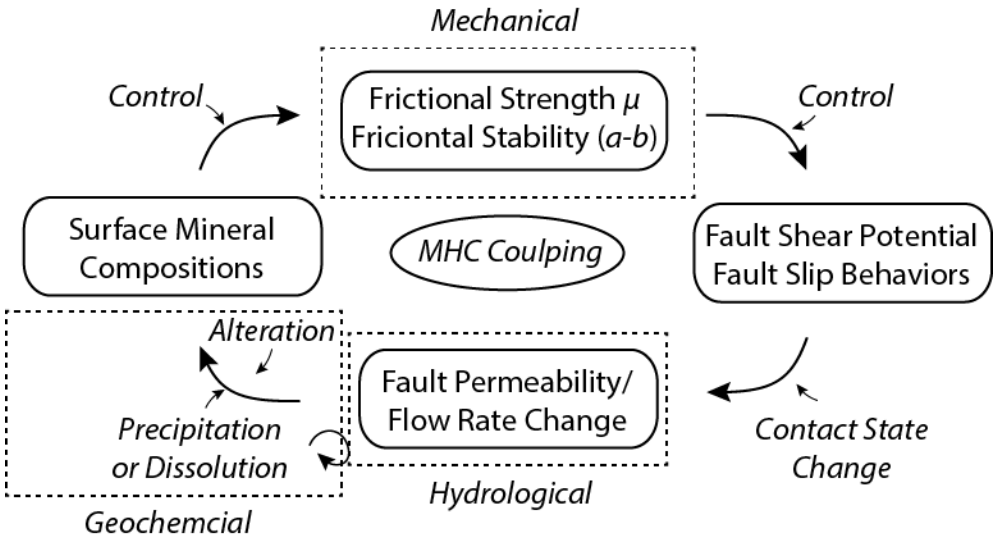

Figure **4-8**: Schematic diagram of new mechanical-hydrological-chemical (MHC) coupling logic

4. Conclusion

We report a series of direct-shear experiments with concurrent measurement of permeability to probe mineralogical controls on frictional strength, stability and permeability. These are conducted on saw-cut fractures in natural rocks with distinct mineral compositions as well as sintered samples with pre-defined mineralogical mixtures. Friction-permeability relationships are strongly controlled by mineralogy. Given the experimental conditions of low effective normal stress, room temperature and saw-cut planar fracture geometry, frictional strength and permeability change upon reactivation decreases with phyllosilicate content but

increases with tectosilicate content. In contrast, the reverse trend is observed for frictional stability (*a*-*b*). However, the effect of carbonate content on frictional stability and transient permeability change is different. The permeability change decreases with carbonate content while both frictional strength and stability increase. The permeability change always decreases with an increase in frictional stability. With this relationship, we speculate that planar fractures with low frictional stability exhibit permeability enhancement after seismic slip in the frame of rate-state friction theory. This relationship implies a new mechanical-hydro-chemical (MHC) coupling loop *via* a linkage of frictional properties, mineralogy and permeability. However, it is worth nothing that friction-permeability relationships are complex, and may also be affected by other external factors such as fracture surface roughness and material mechanical properties, which demands further experimental efforts.

Acknowledgement

We thank the help and insightful discussion and suggestions on the experiments from Professor Chris Marone. This work is the result of support provided by DOE Grant DE-FE0023354. This support is gratefully acknowledged. The data for this paper are available by contacting the corresponding author at yi.fang@psu.edu.

Appendix

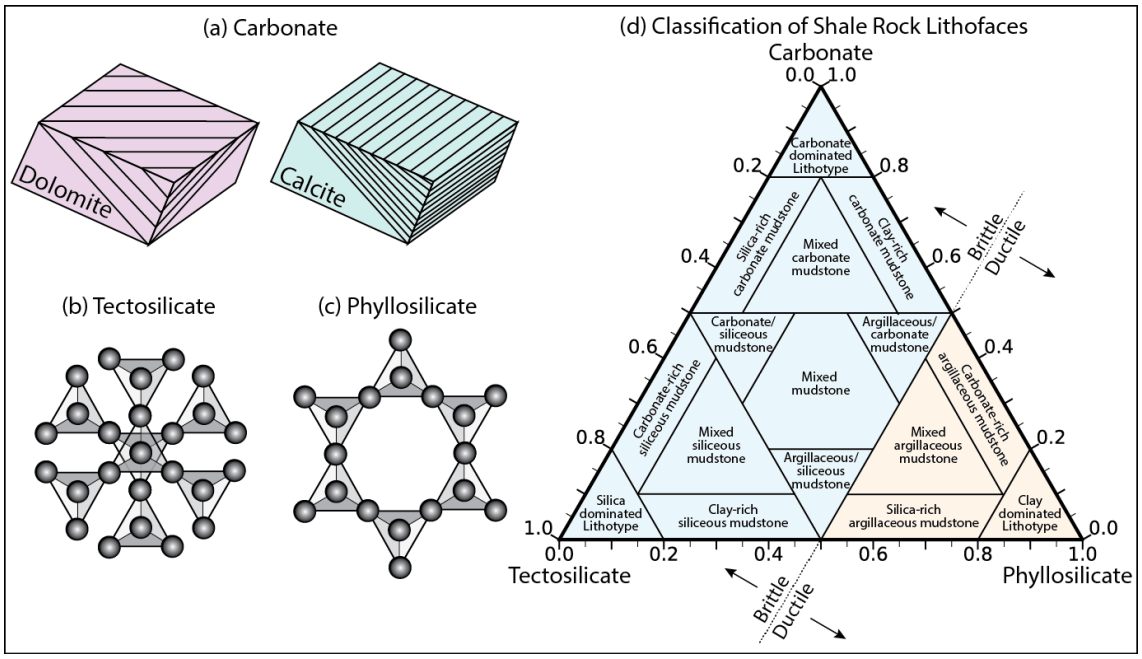

Figure **4-A1**: **(a)** Crystal structure of dolomite and. Dolomite has almost exactly the same structure as calcite except that layers of magnesium and calcium atoms alternate. The alternation means a complete unit cell of dolomite is not the same as a cleavage rhombohedron. **(b)** The tectosilicates or framework silicates have a structure wherein all of the 4 oxygens of SiO_4^{-4} tetrahedra are shared with other tetrahedra. **(c)** The basic structure of the phyllosilicates is based on interconnected six member rings of SiO_4^{-4} tetrahedra that extend outward in infinite sheets. **(d)** Ternary diagram of lithofaces classification with the three apexes representing the components carbonate, tectosilicate and phyllosilicate (CTP) (Modified from *Gamero-Diaz et al.*, [2013]).

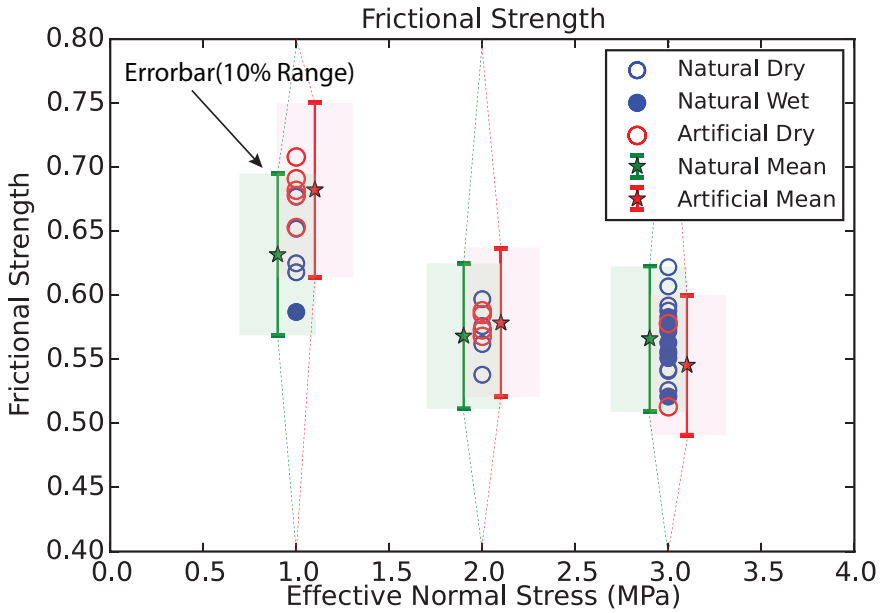

Figure **4-A2**: Frictional strength of both artificially consolidated and natural Green River Shale rocks under different effective normal stress. Error bar bounds 10% of the average frictional strength.

Table **4-A1**: Relationships of mineral compositions, frictional stability and frictional strength

Reference	Sample	σ_{eff} (MPa)	Mineral Composition (wt.%)			V_{lp} ($\mu m/s$)	Ave. Friction (μ_{ss})	Ave. Stability (a -b)
			P-Group	C-Group	T-Group			
[*Fang et al.*, 2015]	Newberry Tuff_1	15	0.0%	0.0%	100.0%	1 ~ 30	0.616	0.0015
	Newberry Tuff_2	15	27.8%	14.4%	57.7%	1 ~ 30	0.612	0.0018
	Newberry Tuff_3	15	17.2%	3.5%	79.3%	1 ~ 30	0.623	0.0006
	Newberry Tuff_4	15	13.8%	0.5%	85.7%	1 ~ 30	0.643	0.0018
	Newberry Tuff_5	15	5.0%	0.4%	94.6%	1 ~ 30	0.660	0.0006
[*Kohli and Zoback*, 2013]	Barnett_1	10	7.1%	23.4%	69.5%	0.1 ~ 10	0.784	-0.0032
	Barnett_2	10	32.5%	22.7%	44.8%	0.1 ~ 10	0.511	0.0023
	Barnett_3	10	39.5%	0.3%	60.2%	0.1 ~ 10	0.465	0.0049
	Barnett_4	10	42.2%	0.0%	57.8%	0.1 ~ 10	0.432	0.0062
	Haynesville_1	10	26.1%	56.5%	17.4%	0.1 ~ 10	0.612	-0.0025
	Haynesville_2	10	48.7%	23.4%	27.9%	0.1 ~ 10	0.427	0.0076
	Haynesville_3	10	52.2%	26.6%	21.1%	0.1 ~ 10	0.402	0.0084
	Eagleford_1	10	13.0%	73.2%	13.8%	0.1 ~ 10	0.698	-0.0029
	Eagleford_2	10	28.7%	62.6%	8.7%	0.1 ~ 10	0.567	-0.0018
[*Boulton et al.*, 2012] (fig.5)	CFR_GCS_U3P	31	31.7%	8.5%	59.8%	0.1 ~ 10	0.57	0.001
	CFR_GCS_U4F	31	58.6%	2.0%	39.4%	0.1 ~ 10	0.5	0.0036
	CFR_GCS_U4	30	20.8%	2.1%	77.1%	0.1 ~ 10	0.53	-0.0007
	CFR_GCT_U3	31	40.2%	5.9%	53.9%	0.1 ~ 10	0.31	0.0085
	CFR_WR_U3	31	19.4%	25.5%	55.1%	0.1 ~ 10	0.4	0.0063
	CFR_WR_U4	30	25.0%	7.0%	68.0%	0.1 ~ 10	0.555	-0.0008

Table **4-A1** Continued

Reference	Sample	σ_{eff} (MPa)	Mineral Composition (wt.%)			V_{lp} ($\mu m/s$)	Ave. Friction (μ_{ss})	Ave. Stability (a -b)
			P-Group	C-Group	T-Group			
[*Giorgetti et al.*, 2015]	Talc_Cal1	5	0.0%	100.0%	0.0%	0.1 ~ 30	0.65	-0.0031
fig.2 and fig.4(a)	Talc_Cal2	5	5.0%	95.0%	0.0%	0.1 ~ 30	0.56	0.0040
	Talc_Cal3	5	20.0%	80.0%	0.0%	0.1 ~ 30	0.51	0.0050
	Talc_Cal4	5	50.0%	50.0%	0.0%	0.1 ~ 30	0.25	0.0036
	Talc_Cal5	5	100.0%	0.0%	0.0%	0.1 ~ 30	0.20	0.0030
[*Smith and Faulkner*, 2010]	FG_L5.2	50	21.0%	44.0%	35.0%	0.1 ~ 1	0.42	0.0055
fig.6 and fig.10	FC_L4	25	5.0%	46.0%	49.0%	0.1 ~ 1	0.58	0.002
[*Verberne et al.*, 2014]	XJ_limestone	50	3.0%	95.0%	2.0%	0.1~ 10	0.72	0.0028
fig.5 and fig.6	CaCO3_gouge	50	0.0%	98.0%	2.0%	0.1~ 10	0.73	0.0034
[*Verberne et al.*, 2010]	SMG	30	29.0%	16.0%	55.0%	0.122 ~ 1.22	0.61	0.00445
Table 1 and Table	SSG	30	30.7%	2.0%	67.3%	0.122 ~ 1.22	0.59	0.00445
	NG	30	65.0%	0.0%	35.0%	0.122 ~ 1.22	0.42	0.00495
	SLG	30	2.0%	96.0%	2.0%	0.122 ~ 1.22	0.71	0.006
[*Stesky et al.*, 1974; *Ikari et al.*, 2011b] (Table 3)	Westerly	49.9	5.0%	0.0%	95.0%	1 ~ 30	0.69	0.0021
	Berea SS	49.9	3.0%	4.0%	93.0%	1 ~ 30	0.93	-0.0003
	Indiana SS	49.9	2.0%	94.9%	3.0%	1 ~ 30	0.93	-0.0016
[*Numelin et al.*, 2007]	A3	5	63.1%	2.3%	34.5%	10 ~ 50	0.65	0.0019
	A6	5	65.0%	8.9%	26.1%	10 ~ 50	0.42	0.0095

Table **4-A1** Continued

Reference	Sample	σ_{eff} (MPa)	Mineral Composition (wt.%)			V_{lp} $(\mu m/s)$	Ave. Friction (μ_{ss})	Ave. Stability $(a\text{-}b)$
			P-Group	C-Group	T-Group			
[*Carpenter et al.*, 2015]	SDZ_G26	25	31.1%	0.3%	68.6%	1 ~ 30	0.447	0.0027
(Table S1 and S2)	SDZ_G28	25	82.0%	0.2%	17.8%	1 ~ 30	0.127	0.0061
	SDZ_G31	25	56.9%	0.2%	42.9%	1 ~ 30	0.344	0.0046
	CDZ_G42A	25	27.6%	4.7%	67.7%	1 ~ 30	0.430	0.0052
	CDZ_G42B	10	93.0%	0.4%	6.6%	1 ~ 10	0.117	0.0055
	CDZ_G43A	7	97.4%	0.3%	2.3%	1 ~ 30	0.158	0.0061
	CDZ_G43B	22	82.7%	10.7%	6.6%	1 ~ 30	0.136	0.0040
	CDZ_G44	25	99.7%	0.0%	0.3%	1 ~ 30	0.120	0.0033
	CDZ_G45A	7	83.9%	2.5%	13.6%	1 ~ 30	0.167	0.0084
	CDZ_G45B	25	34.6%	17.2%	48.2%	1 ~ 30	0.307	0.0072
	CDZ_G46	22	16.2%	21.0%	62.7%	1 ~ 30	0.455	0.0016
	NBF_11150	25	46.0%	0.2%	53.8%	1 ~ 30	0.326	0.0063
	NBF_11180	25	48.3%	0.2%	51.5%	1 ~ 30	0.346	0.0047
	NBF_11190	25	45.6%	0.2%	54.2%	1 ~ 30	0.349	0.0048
	NBF_11200	25	46.2%	0.2%	53.6%	1 ~ 30	0.313	0.0053
	NBF_11210	25	43.6%	0.1%	56.3%	1 ~ 30	0.325	0.0059
	NBF_11220	25	41.5%	0.5%	58.0%	1 ~ 30	0.331	0.0054
	NBF_11250	25	43.5%	0.2%	56.3%	1 ~ 30	0.408	0.0052

Table **4-A1** Continued

Reference	Sample	σ_{eff} (MPa)	Mineral Composition (wt.%)			V_{lp} ($\mu m/s$)	Ave. Friction (μ_{ss})	Ave. Stability (a -b)
			P-Group	C-Group	T-Group			
[*Samuelson and Spiers*, 2012]	NST_Soll1	35	47.0%	43.0%	10.0%	0.2 ~ 10	0.485	0.0026
	NST_Rot1	35	59.0%	0.0%	41.0%	0.2 ~ 10	0.540	0.0032
	NST_Rot2	35	24.0%	1.0%	75.0%	0.2 ~ 10	0.570	0.0028
	NST_Hard1	35	0.0%	8.0%	92.0%	0.2 ~ 10	0.670	0.0025
	NST_Sol/Hard	35	23.5%	25.5%	51.0%	0.2 ~ 10	0.620	0.0031
[*Ikari et al.*, 2015]	Penn_Slate	50	54.0%	15.0%	31.0%	1~300	0.412	0.002
[*Moore and Lockner*, 2011]	Qrt_talc0	100	0.0%	0.0%	100.0%	0.01~1	0.710	-0.0002
Fig. 11a and Table A1	Qrt_talc5	100	5.0%	0.0%	95.0%	0.01~1	0.675	-0.0001
	Qrt_talc10	100	10.0%	0.0%	90.0%	0.01~1	0.660	0.0003
	Qrt_talc15	100	15.0%	0.0%	85.0%	0.01~1	0.615	-0.0010
	Qrt_talc25	100	25.0%	0.0%	75.0%	0.01~1	0.490	0.0016
	Qrt_talc50	100	50.0%	0.0%	50.0%	0.01~1	0.278	0.0066
	Qrt_talc75	100	75.0%	0.0%	25.0%	0.01~1	0.150	0.0050
	Qrt_talc100	100	100.0%	0.0%	0.0%	0.01~1	0.130	0.0034

Note:
(1) Mineral composition data are taken within three effective digit numbers.
(2) T, C, P are normalized using the equation: T/(T+C+P)*100%
(3) Steady State friction is calculated assuming that
(4) Frictional Stability (a-b) is calculated assuming that
(5) Temperature range is within 50 °C.
(6) Values might not add 100% due to rounding and reporting of trace phases, amorphous mineraloid, Neso-Cyclo-Soro-Ino-silicate.
(7) Values are normalized to fit the ternary diagram.

Table **4-A2**: Mineral compositions (wt.%) of natural samples

Minerals \ Samples	Green River Shale	Opalinus Shale	Marcellus Shale	Tournemire Shale	Longmaxi Shale	Newberry Tuff
Quartz	14.9	16.5	36.1	31.3	50.9	30.0
Analcime	16.7	0.0	0.0	0.0	0.0	0.0
Anorthite	7.8	0.0	0.0	0.0	0.0	0.0
Albite	0.0	0.0	0.0	0.0	3.7	42.4
Orthoclase	0.0	2.4	0.0	6.4	0.0	0
Microcline	6.5	0.0	0.0	0.0	0.0	0
Dolomite	39.4	0.0	0.0	0.0	3.4	2.8
Calcite	12.4	19.7	0.0	23.6	16.7	1.6
Muscovite	0.0	42.4	10.4	3.1	0.0	0
Illite	2.3	3.6	44.8	23.3	24.6	0
Chlorite	0.0	0.0	0.0	3.7	0.0	22.2
Clinochlore	0.0	3.9	0.0	0.0	0.0	0.6
Kaolinite	0.0	10.9	3.9	7.0	0.0	0
Montmorillonite	0.0	0.0	0.0	0.0	0.0	0
Others	0.0	0.6	4.8	1.8	0.7	0.3

Table **4-A3**: Basic mechanical and hydraulic properties of natural samples

Samples \ Properties	Young's Modulus (GPa)	Porosity ϕ (%)	Matrix Perm (k_{matrix} m^2)	Reference
GRS	24	3.5%	$1.0\text{-}5.0\times10^{-19}$	[*Yildirim*, 2014]
NRT	31	2-4%	4.0×10^{-19}	[*Wang et al.*, 2016]
LMX	25	3.9%	1.0×10^{-20}	[*Jia et al.*, 2017]
TNM	7.7	8-12%	1.0×10^{-20}	[*Guglielmi et al.*, 2015a]
MCS	25	6.25%	$1.0\text{-}5.0\times10^{-19}$	[*Yildirim*, 2014]
OPS	10-12	2-5%	4.5×10^{-21}	[*Keller*, 2016]

Table **4-A4**: Mineral compositions (wt.%) of artificial samples

Sample Number	Tectosilicate (wt. %)			Carbonate (wt. %)			Phyllosilicate (wt. %)	
	Quartz	Albite	Total	Calcite	Dolomite	Total	Illite	Total
AS001	40.0	40.0	80.0	5.0	5.0	10.0	10.0	10.0
AS002	5.0	5.0	10.0	5.0	5.0	10.0	80.0	80.0
AS003	5.0	5.0	10.0	40.0	40.0	80.0	10.0	10.0
AS004	16.65	16.65	33.3	16.65	16.65	33.3	33.3	33.3
AS005	10.0	10.0	20.0	30.0	30.0	60.0	20.0	20.0
AS006	10.0	10.0	20.0	10.0	10.0	20.0	60.0	60.0
AS007	30.0	30.0	60.0	10.0	10.0	20.0	20.0	20.0
AS008	5.0	5.0	10	22.5	22.5	45.0	45.0	45.0
AS009	22.5	22.5	45.0	22.5	22.5	45.0	10.0	10.0
AS0010	22.5	22.5	45.0	5.0	5.0	10.0	45.0	45.0
AS0011	10.0	10.0	20.0	20.0	20.0	40.0	40.0	40.0
AS0012	20.0	20.0	40.0	20.0	20.0	40.0	20.0	20.0
AS0013	20.0	20.0	40.0	10.0	10.0	20.0	40.0	40.0
AS0014	0.0	0.0	0.0	50.0	50.0	100.0	0.0	0.0
AS0015	0.0	0.0	0.0	0.0	0.0	0.0	100.0	100.0

Table **4-A5**: Data of friction and transient permeability changes for natural rock samples

Sample	Normal Stress (MPa)	Loading Velocity ($\mu m/s$)	Steady State Friction (μ_{ss})	Frictional Stability (a -b)	k_0 (10^{-12}m^2)	Δk_n (-)
GRS	3.0	1.0 to 10.0	0.606	0.001	69.503	0.01839
GRS	3.0	1.0 to 10.0	0.614	0.0005	69.503	0.01741
GRS	3.0	1.0 to 10.0	0.588	0.0021	69.503	0.02302
NBR	3.0	1.0 to 10.0	0.73	0.002	90.867	0.02497
NBR	3.0	1.0 to 10.0	0.752	0.0012	90.867	0.03316
LMX	3.0	1.0 to 10.0	0.61	0.0034	77.541	0.03200
LMX	3.0	1.0 to 10.0	0.545	0.0056	77.541	0.02830
TNM	3.0	1.0 to 10.0	0.432	0.009	14.814	0.02985
TNM	3.0	1.0 to 10.0	0.47	0.011	14.814	-0.14445
MCS	3.0	1.0 to 10.0	0.505	0.007	61.416	0.00019
MCS	3.0	1.0 to 10.0	0.52	0.0075	61.416	-0.00432
OPS	3.0	1.0 to 10.0	0.521	0.0152	8.801	0.00067
OPS	3.0	1.0 to 10.0	0.442	0.013	8.801	-0.00160

Table **4-A6**: Data of friction and transient permeability changes for artificial rock samples

Sample	Normal Stress (MPa)	Loading Velocity ($\mu m/s$)	Steady State Friction (μ_{ss})	Frictional Stability (a -b)	k_0 (10^{-12}m^2)	Δk_n (-)
AS001	3.0	1.0 to 10.0	0.815	0.004	0.187	0.03009
AS002	3.0	1.0 to 10.0	0.475	0.016	0.376	0.01199
AS003	3.0	1.0 to 10.0	0.7	0.015	3.558	0.00628
AS004	3.0	1.0 to 10.0	0.574	0.0083	0.914	0.00978
AS005	3.0	1.0 to 10.0	0.564	0.0151	1.989	-0.00820
AS006	3.0	1.0 to 10.0	0.511	0.0111	0.449	0.02414
AS007	3.0	1.0 to 10.0	0.586	0.006	1.568	0.00512
AS008	3.0	1.0 to 10.0	0.715	0.015	0.492	0.03442
AS009	3.0	1.0 to 10.0	0.765	0.009	2.87	0.00673
AS010	3.0	1.0 to 10.0	0.75	0.022	6.609	-0.00144
AS011	3.0	1.0 to 10.0	0.782	0.0211	0.655	-0.01650
AS012	3.0	1.0 to 10.0	0.634	0.0084	1.82	0.00655
AS013	3.0	1.0 to 10.0	0.648	0.0098	3.064	0.01618
AS014	3.0	1.0 to 10.0	0.768	0.0063	19.585	0.00351
AS015	3.0	1.0 to 10.0	0.416	0.0143	3.54	0.00255

References

Bakker, E., S. J. T. Hangx, A. R. Niemeijer, and C. J. Spiers (2016), Frictional behaviour and transport properties of simulated fault gouges derived from a natural CO 2 reservoir, *Int. J. Greenh. Gas Control*, *54*, 70–83.

Barton, N., S. Bandis, and K. Bakhtar (1985), Strength, deformation and conductivity coupling of rock joints, *Int. J. Rock Mech. Min. Sci.*, *22*(3), 121–140, doi:10.1016/0148-9062(85)93227-9.

Boulton, C., B. M. Carpenter, V. Toy, and C. Marone (2012), Physical properties of surface outcrop cataclastic fault rocks, Alpine Fault, New Zealand, *Geochemistry, Geophys. Geosystems*, *13*(1), n/a-n/a, doi:10.1029/2011GC003872.

Brune, J. N. (1970), Tectonic stress and the spectra of seismic shear waves from earthquakes, *J. Geophys. Res.*, *75*(26), 4997–5009, doi:10.1029/JB075i026p04997.

Carpenter, B. M., D. M. Saffer, and C. Marone (2015), Frictional properties of the active San Andreas Fault at SAFOD: Implications for fault strength and slip behavior, *J. Geophys. Res. Solid Earth*, *120*, 1–17, doi:10.1002/2015JB011963.Received.

Collettini, C., C. Cardellini, G. Chiodini, N. De Paola, R. E. Holdsworth, and S. A. F. Smith (2008), Fault weakening due to CO2 degassing in the Northern Apennines: short-and long-term processes, *Geol. Soc. London, Spec. Publ.*, *299*(1), 175–194.

Cornet, F. H., J. Helm, H. Poitrenaud, and a. Etchecopar (1997), Seismic and Aseismic Slips Induced by Large-scale Fluid Injections, *Pure Appl. Geophys.*, *150*(3–4), 563–583, doi:10.1007/s000240050093.

Davis, E. E., K. Becker, K. Wang, and B. Carson (1995), Long-term observations of pressure and temperature in Hole 892B, Cascadia accretionary prism, in *Proceedings of the Ocean Drilling Program. Scientific results*, vol. 146, pp. 299–311, Ocean Drilling Program.

Dieterich, J. H. (1978), Time-dependent friction and the mechanics of stick-slip, *Pure Appl. Geophys. PAGEOPH*, *116*, 790–806, doi:10.1007/BF00876539.

Dieterich, J. H. (1979), Modeling of rock friction: 1. Experimental results and constituve equations, *J. Geophys. Res.*, *84*(9), 2161–2168, doi:10.1007/BF00876539.

Ellis, B. R., J. P. Fitts, G. S. Bromhal, D. L. McIntyre, R. Tappero, and C. a Peters (2013), Dissolution-Driven Permeability Reduction of a Fractured Carbonate Caprock., *Environ. Eng. Sci.*, *30*(4), 187–193, doi:10.1089/ees.2012.0337.

Evans, J. P., and F. M. Chester (1995), Fluid‐rock interaction in faults of the San Andreas system: Inferences from San Gabriel fault rock geochemistry and microstructures, *J. Geophys. Res. Solid Earth*, *100*(B7), 13007–13020.

Fang, Y., S. A. M. den Hartog, D. Elsworth, C. Marone, and T. Cladouhos (2016), Anomalous distribution of microearthquakes in the Newberry Geothermal Reservoir: Mechanisms and implications, *Geothermics*, *63*, 62–73, doi:http://dx.doi.org/10.1016/j.geothermics.2015.04.005.

Fang, Y., D. Elsworth, C. Wang, T. Ishibashi, and J. P. Fitts (2017), Frictional stability-permeability relationships for fractures in shales, *J. Geophys. Res. Solid Earth*, *122*(3), 1760–1776, doi:10.1002/2016JB013435.

Faoro, I., A. Niemeijer, C. Marone, and D. Elsworth (2009), Influence of shear and deviatoric stress on the evolution of permeability in fractured rock, *J. Geophys. Res. Solid Earth*, *114*(1), doi:10.1029/2007JB005372.

Gamero-Diaz, H., C. K. Miller, and R. Lewis (2013), sCore: a mineralogy based classification scheme for organic mudstones, in *SPE Annual Technical Conference and Exhibition*, Society of Petroleum Engineers.

Giorgetti, C., B. M. Carpenter, and C. Collettini (2015), Frictional behavior of talc-calcite mixtures, *J. Geophys. Res. Solid Earth*, *120*(9), 6614–6633, doi:10.1002/2015JB011970.

Guglielmi, Y., D. Elsworth, F. Cappa, P. Henry, C. Gout, P. Dick, and J. Durand (2015a), In situ observations on the coupling between hydraulic diffusivity and displacements during fault reactivation in shales, *J. Geophys. Res. B Solid Earth*, doi:10.1002/2015JB012158.

Guglielmi, Y., F. Cappa, J.-P. Avouac, P. Henry, and D. Elsworth (2015b), Seismicity triggered by fluid injection–induced aseismic slip, *Sci.* , *348*(6240), 1224–1226, doi:10.1126/science.aab0476.

Ikari, M. J., C. Marone, and D. M. Saffer (2011), On the relation between fault strength and frictional stability, *Geology*, *39*(1), 83–86, doi:10.1130/g31416.1.

Ikari, M. J., A. R. Niemeijer, and C. Marone (2015), Experimental investigation of incipient shear failure in foliated rock, *J. Struct. Geol.*, *77*, 82–91, doi:10.1016/j.jsg.2015.05.012.

Johnson, T. L., and C. H. Scholz (1976), Dynamic properties of stick‐slip friction of rock, *J. Geophys. Res.*, *81*(5), 881–888.

Keller, L. M. (2016), Porosity anisotropy of Opalinus Clay: implications for the poroelastic behaviour, *Geophys. J. Int.*, *208*(3), 1443–1448.

Kerrich, R. (1986), Fluid infiltration into fault zones: chemical, isotopic, and mechanical effects, *Pure Appl. Geophys.*, *124*(1–2), 225–268.

Kohli, A. H., and M. D. Zoback (2013), Frictional properties of shale reservoir rocks, *J. Geophys. Res. Earth*, *118*(9), 5109–5125, doi:Doi 10.1002/Jgrb.50346.

Lin, A., N. Tanaka, S. Uda, and M. Satish-Kumar (2003), Repeated coseismic infiltration of

meteoric and seawater into deep fault zones: a case study of the Nojima fault zone, Japan, *Chem. Geol.*, *202*(1), 139–153.

Moore, D. E., and D. A. Lockner (2011), Frictional strengths of talc-serpentine and talc-quartz mixtures, *J. Geophys. Res. Solid Earth*, *116*(1), doi:10.1029/2010JB007881.

Niemeijer, A., and C. Collettini (2013), Frictional Properties of a Low-Angle Normal Fault Under In Situ Conditions: Thermally-Activated Velocity Weakening, *Pure Appl. Geophys.*, 1–24, doi:10.1007/s00024-013-0759-6.

Niemeijer, A. R., and C. J. Spiers (2007), A microphysical model for strong velocity weakening in phyllosilicate-bearing fault gouges, *J. Geophys. Res. Solid Earth*, *112*(10), doi:10.1029/2007JB005008.

Numelin, T., C. Marone, and E. Kirby (2007), Frictional properties of natural fault gouge from a low-angle normal fault, Panamint Valley, California., *Tectonics*, *26*(TC2004), doi:10.1029/2005TC001916, doi:10.1029/2005TC001916.

Ruina, A. (1983), Slip instability and state variable friction laws, *J. Geophys. Res. Solid Earth*, *88*(B12), 10359–10370, doi:10.1029/JB088iB12p10359.

Samuelson, J., and C. J. Spiers (2012), Fault friction and slip stability not affected by CO_2 storage: Evidence from short-term laboratory experiments on North Sea reservoir sandstones and caprocks, *Int. J. Greenh. Gas Control*, *11*(SUPPL), 78–90, doi:10.1016/j.ijggc.2012.09.018.

Scholz, C. H. (1998), Earthquakes and friction laws, *Nature*, *391*(6662), 37–42, doi:Doi 10.1038/34097.

Smith, S. A. F., and D. R. Faulkner (2010), Laboratory measurements of the frictional properties of the Zuccale low-angle normal fault, Elba Island, Italy, *J. Geophys. Res.*, *115*(B2), B02407, doi:10.1029/2008JB006274.

Stesky, R. M., W. F. Brace, D. K. Riley, and P. Y. F. Robin (1974), Friction in faulted rock at high temperature and pressure, *Tectonophysics*, *23*(1–2), 177–203, doi:10.1016/0040-1951(74)90119-X.

Verberne, B. A., C. He, and C. J. Spiers (2010), Frictional properties of sedimentary rocks and natural fault gouge from the Longmen Shan fault zone, Sichuan, China, *Bull. Seismol. Soc. Am.*, *100*(5B), 2767–2790.

Verberne, B. A., C. J. Spiers, A. R. Niemeijer, J. H. P. De Bresser, D. A. M. De Winter, and O. Plümper (2014), Frictional Properties and Microstructure of Calcite-Rich Fault Gouges Sheared at Sub-Seismic Sliding Velocities, *Pure Appl. Geophys.*, *171*(10), 2617–2640, doi:10.1007/s00024-013-0760-0.

Wang, J., W. Jung, Y. Li, and A. Ghassemi (2016), Geomechanical characterization of Newberry Tuff, *Geothermics*, *63*, 74–96.

Xu, T., P. Rose, S. Fayer, and K. Pruess (2009), On modeling of chemical stimulation of an enhanced geothermal system using a high pH solution with chelating agent, *Geofluids*, *9*(2), 167–177.

Yildirim, L. T. O. (2014), Evaluation Of Petrophysical Properties Of Gas Shale And Their Change Due To Interaction With Water,

Zoback, M. D., A. Kohli, I. Das, and M. Mcclure (2012), The Importance of Slow Slip on Faults During Hydraulic Fracturing Stimulation of Shale Gas Reservoirs, *Spe 155476*, (2011), SPE 155476, doi:10.2118/155476-MS.

Chapter 5

Investigation of Permeability Evolution and Frictional Behavior on Fabricated Fractures with Specified Roughness Features

Abstract

Understanding the role of fracture roughness on its frictional behavior and permeability evolution is vital for evaluating the potential of induced seismicity and associated fluid migration issues in subsurface fluid injection activities (*e.g.*, unconventional fractured reservoir stimulation, CO_2 sequestration, and waste water disposal). Previous experiments show that the permeability of smooth fractures declines monotonically with displacement due to the generation of wear products. Our recent laboratory tests investigate the role of roughness on permeability evolution and frictional behavior using artificially fabricated fractures with specified roughness features. The experimental results show that (1) both smooth and rough fracture surfaces exhibit velocity strengthening frictional behavior for small net displacement and the evolves to velocity neutral and velocity weakening with greater displacement. (2) Rougher surfaces exhibit higher velocity strengthening frictional behavior and higher frictional strength due to the presence of cohesive interlocking asperities during shearing. Seismicity may not be induced on rough fracture surfaces. (3) The roughness pattern exerts a dominant control on permeability evolution over the entire shearing history. Permeability evolves monotonically for smooth fractures but in a fluctuating pattern for highly roughened fractures. A higher roughness is likely to result in alternating compaction and dilation during shearing. Significant permeability damage may occur for rough samples when asperities are highly worn with wear products blocking fluid pathways. (4) There is no conspicuous correlation between permeability evolution and frictional behavior for rough

fracture samples when fractures are subject to sudden sliding velocity change. Implications of our lab-scale experimental results suggest that characterization of fracture geometry would be beneficial for better understanding and managing induced seismicity and permeability development.

Keywords: Friction, permeability, fabricated fractures, specified roughness

1. Introduction

Recent industrial activities, such as stimulation and production of hydrocarbon reservoir and enhanced geothermal systems (EGS), waste water disposal, have been recognized to induce seismicity due to massive fluid injection [*Majer et al.*, 2007; *Moeck et al.*, 2009; *Zoback et al.*, 2012; *Ellsworth*, 2013; *Walsh and Zoback*, 2015; *Fang et al.*, 2016]. The proposed CO_2 mitigation project, the geological carbon sequestration (GCS) also involves large-scale CO_2 fluid injection, which may induce seismicity and threaten the integrity of caprock formations for long term CO_2 storage [*Zoback and Gorelick*, 2012]. The induced seismicity occurs as seismic slip, slow slip and aseismic slip [*Cornet et al.*, 1997; *Zoback et al.*, 2012; *Guglielmi et al.*, 2015], which would result in shear dilation or compaction of fracture or faults and lead to permeability enhancement or reduction [*Jouanna*, 1972; *Maini*, 1972; *Barton et al.*, 1985; *Elsworth and Goodman*, 1986; *Segall and Rice*, 1995; *Faoro et al.*, 2009]. Hence, understanding the permeability evolution with respect to shear deformations is a key step for optimizing the stimulation and production of unconventional reservoirs and for protecting the geological sealing of fluid disposal repository.

It has long been recognized that these shear deformations result from the hydroshearing by increased fluid pressure on pre-existing fractures or faults [*Talwani*, 1997; *Segall and Fitzgerald*, 1998]. This physical process can be simply described by Coulomb-Mohr criteria as,

$$\tau = C_0 + \mu \cdot (\sigma_n - P_f) \tag{1}$$

where τ is shear stress; C_0 is cohesive strength; μ is the coefficient of friction (also known as the frictional strength); σ_n is normal stress applied on the fracture or fault plane; and P_f is fluid pressure acting on the fracture wall. When fluid pressure increases, the effective normal stress on a pre-existing fault surface is reduced, making it possible for fault to slip at a level of shear stress (**Figure 5-1a**). When the fault is reactivated at the beginning of slip, the fault movement is governed by the dynamic frictional behavior of the fault contact within the fault. This frictional behavior is empirically defined by the experimentally derived rate-and-state friction law [*Dieterich*, 1978, 1979; *Ruina*, 1983], in which the dynamic friction coefficient μ is written as:

$$\mu = \mu_0 + a \cdot \ln\left(\frac{V}{V_0}\right) + b \cdot \ln\left(\frac{V_0\theta}{D_c}\right) \tag{2}$$

$$\frac{d\theta}{dt} = 1 - \frac{V\theta}{D_c} \tag{3}$$

where μ_0 is the coefficient of friction at a reference fault slip velocity; θ is a state variable, a and b are friction parameters which represent the effect of instantaneous and displacement-dependent changes in friction from V_0 to V; and D_c is the critical slip distance over which evolution to a new steady state takes place. Frictional slip instability is determined in part by the parameter $(a-b)$ for a finite step in velocity, yielding:

$$a - b = \frac{\Delta\mu_{ss}}{\Delta \ln V} \tag{4}$$

where $\Delta\mu_{ss}$ is difference of static state friction between before and after velocity change; while $(a-b)$ values have been applied to examine whether the reservoirs fracture slip stable, aseismically (i.e., $a-b>0$), or instable, seismically (i.e., $a-b<0$) (**Figure 5-1b**).

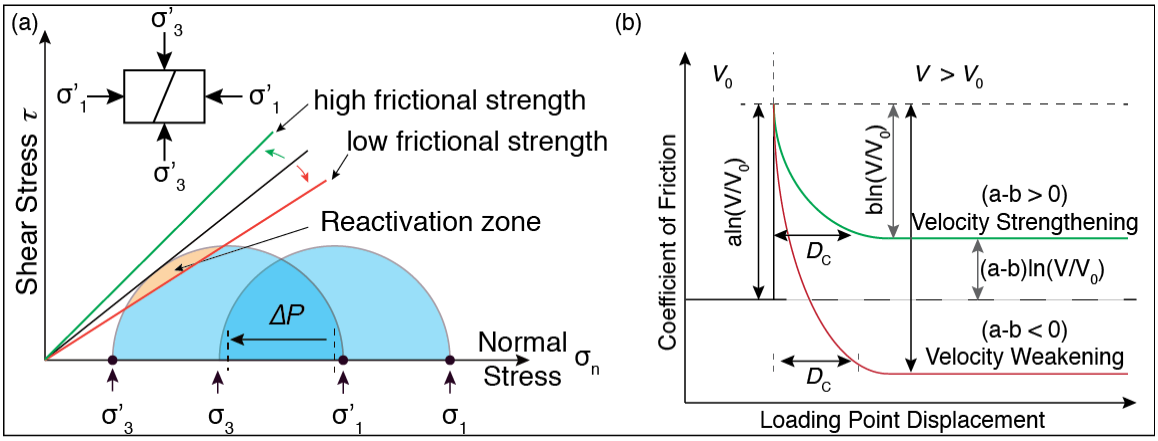

Figure **5-1**: **(a)**: Coulomb-Mohr Criteria for determining whether a fault can be reactivated or not; **(b)**: Rate-State Friction Law for determining whether a reactivated fault slips in stable or unstable behavior

Recent hydroshearing experiments on shale fractures indicate that permeability evolution of fracture can be linked to the frictional strength and stability because all of these physical parameters are controlled by the solid-solid contact of fracture surfaces during shearing. At low effective normal stress, phyllosilicate-rich shale exhibits weaker frictional strength but much stronger frictional stability and larger permeability reduction than that of carbonate-rich shale. The permeability evolution is due to the competition between wear product and fracture dilation, which depends on material strength and brittleness – strong-brittle asperities may result in higher frictional strength, lower frictional stability and larger permeability than that of weak-ductile asperities [*Fang et al*., 2017a, 2017b]. However, these conclusions may only reflect the friction-stability-permeability relationship at low confining pressure for fractures with low roughness with asperity size in order of micrometers. Previous shear deformation experiments suggest that fracture roughness at order of millimeters, play a different role in controlling the shear deformation and shear strength [*Barton*, 1973; *Barton and Choubey*, 1977], that is, when points of contact exist for the two fracture surfaces, the surface roughness can in fact control the fracture aperture, leading to significant dilation. The shearing of "saw-tooth" fractures indicates that the sliding occurred on intact asperity at low effective normal stress and resulted in strong shear

dilation and higher conductivity while the intact asperity cut each other at high effective stress and led to less shear dilation and lower conductivity [*Barton et al.*, 1985]. In addition, the mechanical behavior of fractures is strongly dependent on the geometry of asperities, such as size, shape, and distribution on surface, which means that the frictional strength and stability and permeability evolution may be controlled by the geometric pattern of asperities. To understand the role of surface roughness, we perform hydroshearing experiments on fracture samples with programmed roughness patterns. Those samples are fabricated with the assistance of 3D printing technology.

This study is organized as follows. First, we design a simple roughness pattern as analogues to natural fractures. Then we cast the fracture samples with known statistic roughness features (in terms of asperity height and wavelength) and we perform the hydroshearing experiments to measure the frictional strength, stability and permeability evolution of those roughness-featured fractures. We finally report the results and discussions of how the controlled surface roughness influences frictional stability and permeability evolution.

2. Experimental Methods

From the foregoing, we first examine the features of natural shale fractures. Then we create artificial fracture surfaces (as analogues to natural fractures), with controlled roughness features. At last, we perform the hydroshearing experiments with the artificial samples.

2.1 Characterization of Surface Roughness

The simplest rough surface is one having asperities with a pre-defined size and shape, such as the triangular and sinusoidal asperity that have been examined in shear experiments

[*Grasselli and Egger*, 2003; *Asadi et al.*, 2013]. However, these simple shapes lack the stochastical amplitude and wavelength that are characteristics of a real rough surface. With observation of natural pre-existing fractures (**Figure 5-2a**), the surface features can be described by the roughness - the characteristic deviation of the surface from a smooth plane. A statistical description of a rough surface, comprising peaks and valleys, requires information on deviations in the direction of the normal vector of the surface from its ideal form and on how the surface varies in the lateral directions. A typical mathematical model of a rough fracture surface suggests three main parameters: the fractal dimension, the RMS roughness at a reference length scale, and a length scale describing the describing the degree of mismatch [*Brown*, 1995]. The irregular profile of real fracture surface can be decomposed into a series of sinusoidal components (**Figure 5-2b**), each of which may play a role in shaping the surface textures as well as in influencing the fracture frictional strength, stability and permeability. To reduce the complexity, we make a simplification by focusing the role of the largest wavelength of fracture surface.

Hence, in this study, we assume that a fracture surface can be simply characterized by a combination of two geometric parameters (**Figure 5-2c**): (1) wavelength L_c, which describes the statistical independence of two points on a surface, and (2) the root mean square (RMS) height (S_q), defined as the root mean square values of asperity height within the sampling area A as:

$$S_q = \sqrt{\frac{1}{A}\iint_A z(x,y)\,dx\,dy} \tag{5}$$

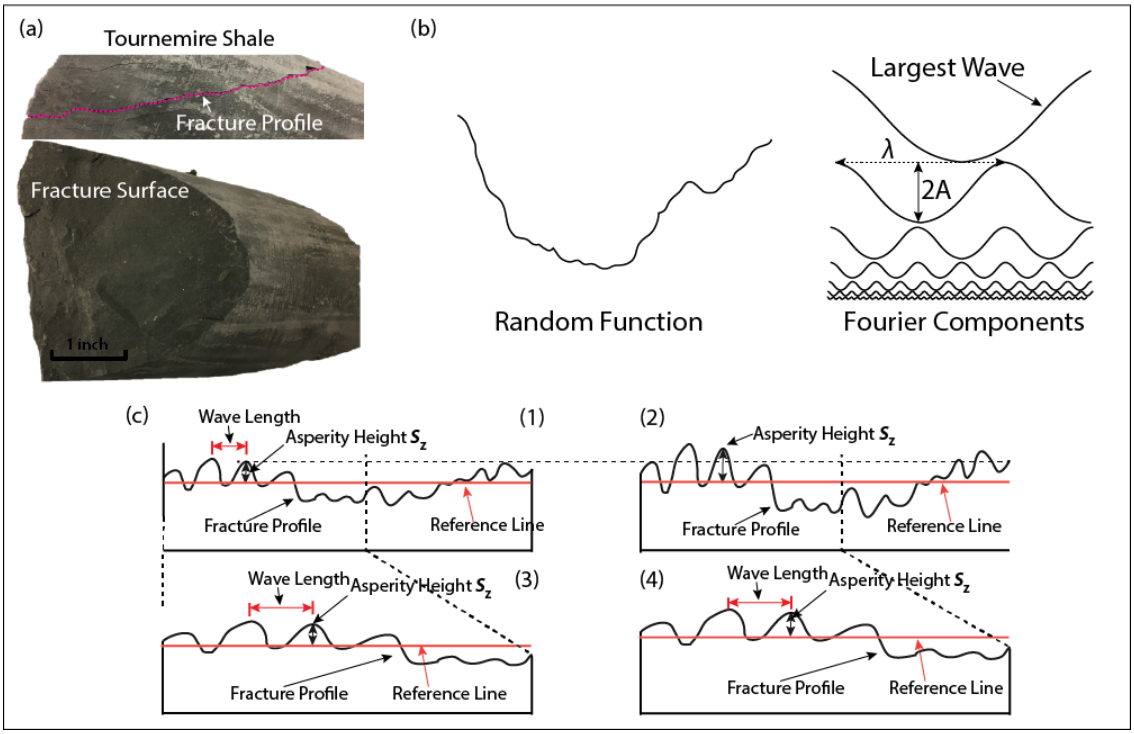

Figure **5-2**: **(a)** Example of fracture surface of natural sedimentary rock (Tournemire shale) where fracture outline is highlighted on cross-section. (b) The irregular surface profile represented by random function, which can be decomposed into a series of sinusoidal components (Modified from *Brown*, 1995). **(c)** Schematic graph of 1D fracture profile showing comparisons of asperity height and asperity wavelength: **(c1)** vs. **(c2)**: same wave length but different asperity height; **(c1)** vs. **(c3)** same asperity height but different wavelength; **(c1)** vs. **(c4)**: different wavelength and different asperity height.

Mechanically, when two well-matched rough surfaces slide against each other under a certain normal stress, the asperities must deform to accommodate the motion, which requires an elastic strain on the order of a ratio of asperity height and length [*Brodsky et al.*, 2016]. With this definition, we define an analogous term by applying the ratio of *RMS* height S_q and wavelength L_c (*i.e.*, S_q/L_c), which statistically integrates the contributions from all of the asperities on the fracture surfaces. Therefore, a higher S_q/L_c ratio may suggest that a larger elastic strain that is required accommodate the surface until plastic failure and truncation of the asperities are induced.

In addition to wavelength and RMS parameters, the physical features (*i.e.*, asymmetry and flatness) of the surface roughness model can also be characterized by the surface geometry parameters: skewness (S_{sk}) and kurtosis (S_{ku}), which are introduced in the appendix.

2.2 Preparation of Artificial Samples with Controlled Roughness

As random roughness with Gauss statistics is a well-accepted approximation of many real rough surfaces, we first generate an uncorrelated Gaussian distribution of random roughness height S_z, and then obtain the Gaussian-correlated profile $z_u(x,y)$ convoluted by a Gaussian filter [*Fung et al.*, 2010]. The designed 3D fracture surface profiles are illustrated in **Figure 5-3a**. The statistical roughness parameters of surface geometry are shown in **Figure 5-3b**, where four cases are highlighted: **(1)** same asperity height with different wavelength (*i.e.*, Case *A* vs. Case *B*); **(2)** same wavelength with different asperity height (*i.e.*, Case *B* vs. Case *C*); **(3)** different wavelength with different asperity height (*i.e.*, Case *A* vs. Case *C*); **(4)** same asperity height and wavelength but sheared at two different directions (*i.e.*, Case *A* vs. Case *D* or Case *B* vs. Case *D*). The values of surface roughness parameters are listed in **Table 5-1**.

From a physical interpretation, the highest positive skewness value (S_{sk} = 0.1543) suggests fracture (*B*) with smoothest surface. The negative skewness values of surfaces (*A*) and (*D*) indicate the presence of comparatively few peaks on fracture surfaces. Additionally, the kurtosis values of fracture (*A*) and (*D*) are relatively higher than that of fracture (*B*) and (*C*), suggesting that fracture (*A*) and (*D*) are spiky while fracture (*B*) and (*C*) are bumpy. These features are megascopic from the 3D geometries in **Figure 5-3a**. In summary, the integrated roughness of these samples is expressed as: $R_a > R_d > R_b > R_c$.

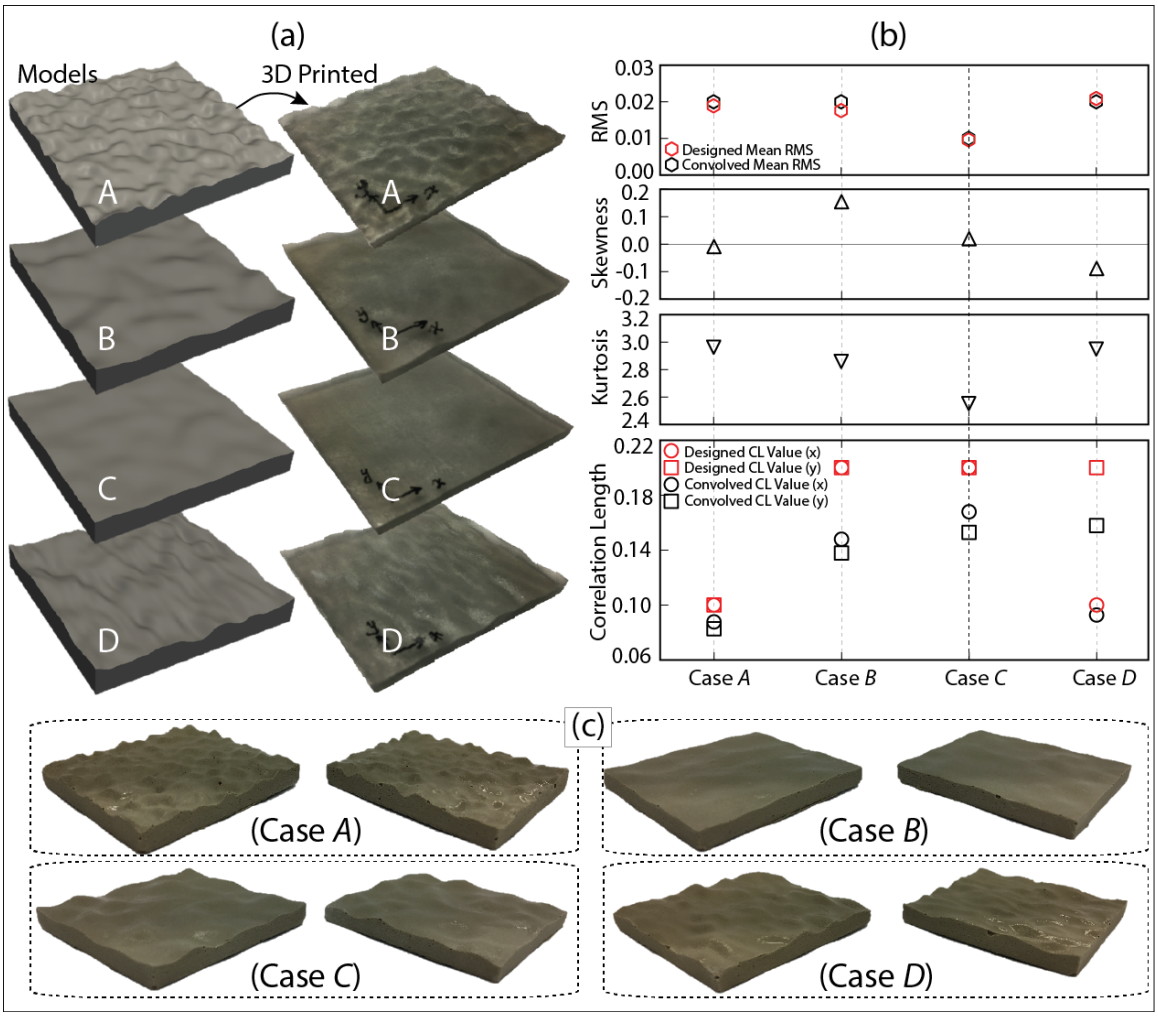

Figure **5-3**: **(a)** Designed fracture surface models and their 3D printed counterparts. **(b)** Statistical roughness parameters of modeled surface geometry: RMS height of asperity, surface skewness, surface kurtosis, and wavelength of surface geometry. **(c)** Artificial fractures casted with cemented calcite.

Table **5-1**: Statistical roughness parameters of fracture surface

Case No.	*RMS*	L_c(x)	L_c(y)	S_{sk}	S_{ku}	$\sigma_{(RMS)}$	μ
(a)	0.02	0.0877	0.0827	-0.0089	2.9625	0.0189	-0.0001
(b)	0.02	0.1479	0.1378	0.1543	2.8592	0.0176	0.0046
(c)	0.01	0.1679	0.1529	0.0196	2.5517	0.0096	-0.0030
(d)	0.02	0.0927	0.1579	-0.0886	2.9493	0.0181	-0.0028

With these 3D geometries, we applied 3D printing technique to create the solid parts for making resin mould for casting the artificial fracture samples (**Figure 5-3a**). The printed solids parts are printed by Object260 Connex3 (Stratasys Ltd) with digital material RGS8705. The resolution of the printed parts is at 16 micron. In order to make artificial samples that consist of natural minerals, we use the printed solid parts to crease a resin mould. Then we sieved the calcite powder and cement powder with particle size less than 106 μm and uniformly mixed 50 wt.% calcite and 50 wt.% cements with DI water. The slurry is eventually casted in the resin mould for three days. The artificial rock-like fracture samples are presented in **Figure 5-3c**. For providing a reference of experimental result, we cast an artificial fracture (Case *E*) with a saw-cut planar surface. The fracture surface is uniformly polished with grinding powder (#60 grit carbide) and the height of asperity is at least two orders of magnitude smaller than that of fracture case *A* to *D*.

2.3 Experimental Setup and Procedure

The friction-permeability experiments were performed in a triaxial testing apparatus that independently applies confining pressure and differential (end-to-end) pore pressure while the sample is sheared at a prescribed velocity (**Figure 5-4**). This allows the concurrent measurement of the evolution of fracture permeability and friction during shear slip. The sample coupons were packed within a pair of steel shearing platens. The initial offset of platens is ~ 8 mm for slip displacement during sliding. The platen-offset gap is filled with silly putty to prevent fluid extruding. The side and bottom contacts between the sample coupon and the platen surfaces are placed with Teflon to prevent fluid leaking from the injected fluid that is supposed to migrating through fracture surfaces. The assembled couple of platens are packed with membrane to be isolated from confining fluid. A steel sleeve covers the load cell to prevent the effect of applied confining pressure.

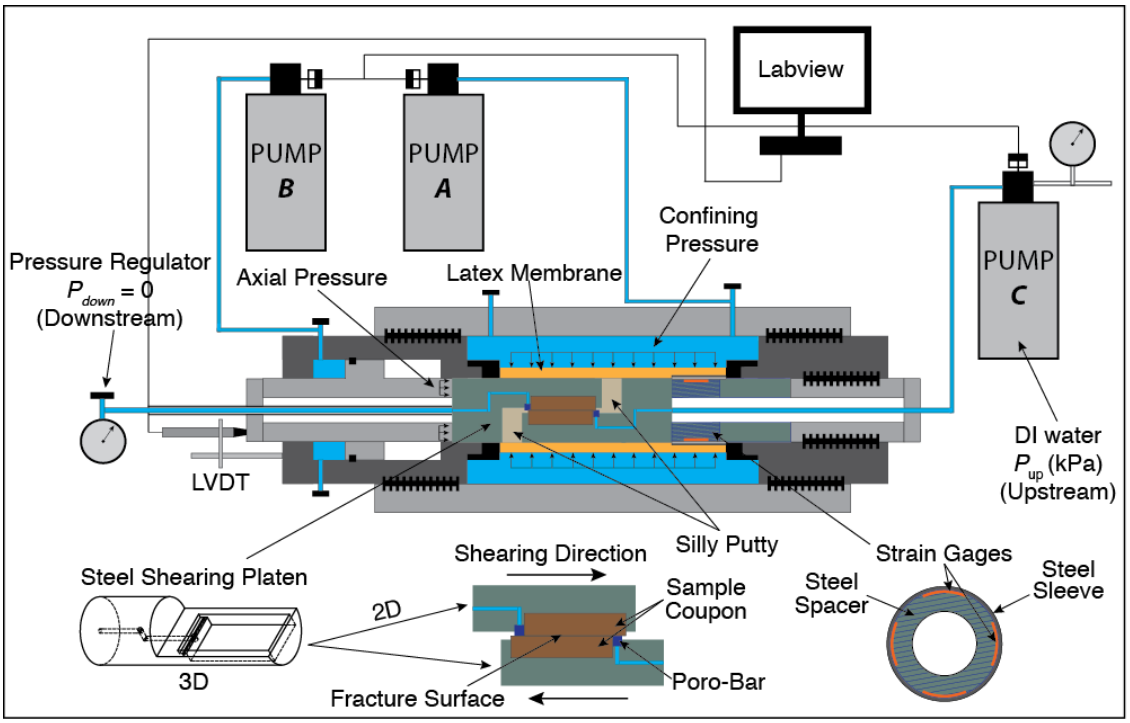

Figure **5-4**: Picture of experimental setup for friction-permeability evolution test: Pump A (ISCO 500D) controls the confining pressure (normal stress) applied on the fracture. Pump B (ISCO 500D) controls pressure that provides the source of shear stress applied on the fracture. Pump C (ISCO 500D) injects the fluid at a prescribed flow rate or pressure, allowing the fluid source locates at the origin of the fracture and flow along the fractures.

To be consistent with applied stress conditions of previous experimental studies [*Fang et al.*, 2016b], we apply a confining stress (normal stress) of 3 MPa (pump A) and set a constant upstream fluid pressure (pump C) during axial shear displacement at constant rate (pump B) and measured force. The minimum flow rate of each pump is 0.001 ml/min and the display resolution of the pump pressure transducer is 1.0 kPa. A load cell with a resolution of 0.3 kPa is used to measure the axial stress. At room temperature, the minimum measurable permeability is $1.0 \times 10^{-14} m^2$.

We conducted velocity-stepping experiments to compare the hydraulic behavior response to varying velocities for six different scenarios: Case *A*, *B*, *C*, D_x, D_y and *E*. It is worth noting that, sample *D* has an anisotropic correlation length along *x* and *y* direction, therefore, we run two experiments for sample *D*, one shear along *x* direction and the other shear along y direction. The

shear velocity was set to 10 μm/s (monotonic) and switched by down-steps and up-steps between 1 μm/s and 10 μm/s, until a displacement of ~6 to 8 *mm* was reached. All the experiments were performed at room temperature (25 C°), with shear displacements recorded by LVDT (Linear Variable Differential Transformer) located outside the vessel.

3. Results and Discussion

In this installment, we first introduce a broad observation of concurrent friction and permeability evolution during shearing. Then, we explore whether or not and how frictional strength, frictional stability and permeability change are controlled by the roughness variations of fracture surface.

3.1 Net Friction and Permeability Evolution

The measured frictional strength is calculated by the ratio of measured shear stress and applied constant effective normal stress as τ/σ_n. Given the assumption that the apertures of rough fractures are averaged over two parallel planar surfaces, the equivalent fracture permeability is calculated using the cubic law as,

$$b = -\left(\frac{12\mu_{vis} \cdot L(t) \cdot Q(t)}{W \cdot \Delta P_f} \right)^{1/3} \tag{6}$$

$$k = \frac{b^2}{12} \tag{7}$$

where b [m] is the equivalent hydraulic aperture; μ_{vis} [$Pa{\cdot}s$] is the viscosity of fluid; L(t) [m] is the contact length of the fracture surface; W [m] is the fracture width; Q(t) [m^3/s] is the measured flow rate and ΔP_f [Pa] is the differential pressure between the upstream and downstream extent of

the fracture.

Results of net friction and permeability evolution with displacement on samples *A* to *E*, and the corresponding images of fracture surface before and after the shear slip are individually shown in **Figure 5-5** to **5-10**. The measured frictional parameters and permeability change in response to velocity change are listed in **Table 5-2**. The dimensionless permeability is defined as the measured permeability normalized to the static permeability value before shearing.

A comparison of all friction-load point displacement curves of examined samples is illustrated in **Figure 5-11a**. For samples with large-size asperities, their friction evolutions share similar general trend, all ending up with a magnitude greater than 1, which is likely due to the effect of interlocking asperities. Accordingly, permeability of samples *A* to *D* during shearing evolves alternately up and down as a result of combined effects of dilation, compaction or clogging. By contrast, the frictional strength of sample *E* presents a much lower evolution profile as a result of low roughness of fracture surface. The permeability of sample *E* monotonically declined with displacement due to the continuing produced wear product filling the fracture aperture [*Fang et al.,* 2017].

The corresponding images of fracture surfaces before and after the shear slip are illustrated in **Figures 5-5** to **5-10**, showing shear-induced damage of asperities and demonstrating that fracture surface topography are likely to be significantly modified by wear and gouge accumulation within increasing slip. Therefore, the effects of contact junction size on fluid pathways are best indicated by the net permeability data rather than by the measured normal dilation displacement.

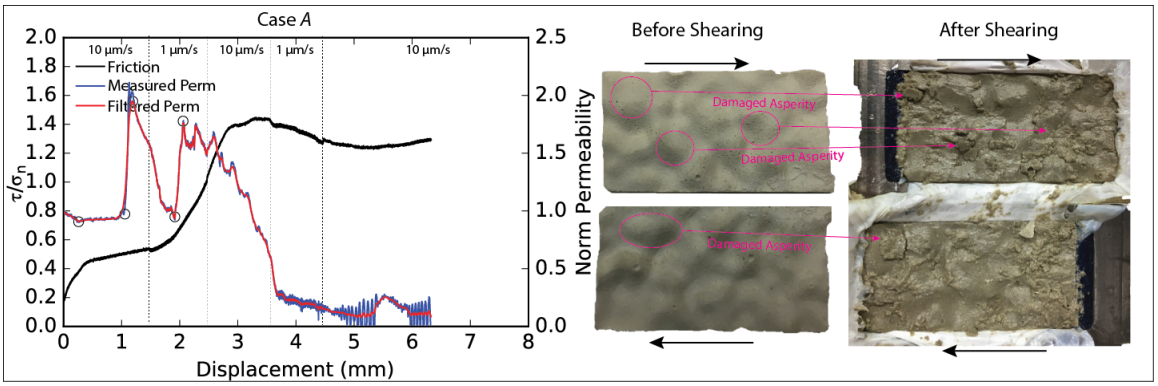

Figure **5-5**: Left: Net frictional strength and permeability evolutions with displacement for sample *A*. Right: Sample coupons before and after shear slip.

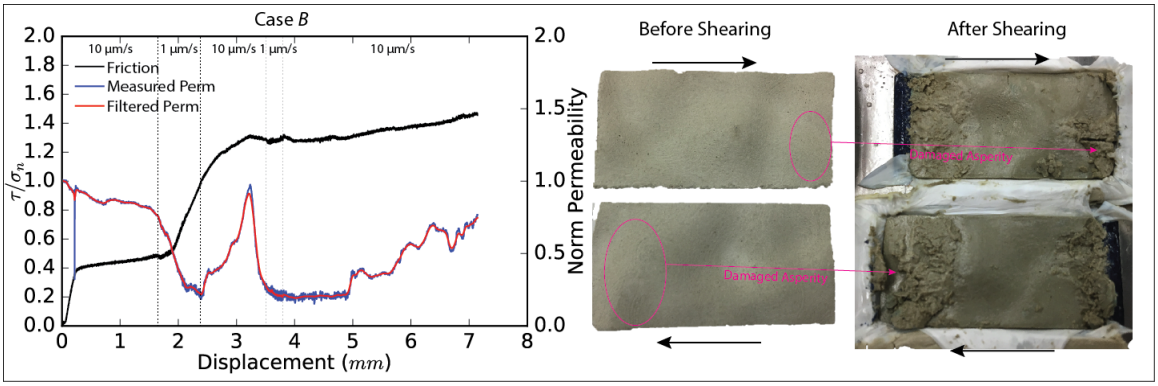

Figure **5-6**: Left: Net frictional strength and permeability evolutions with displacement for sample *B*. Right: Sample coupons before and after shear slip.

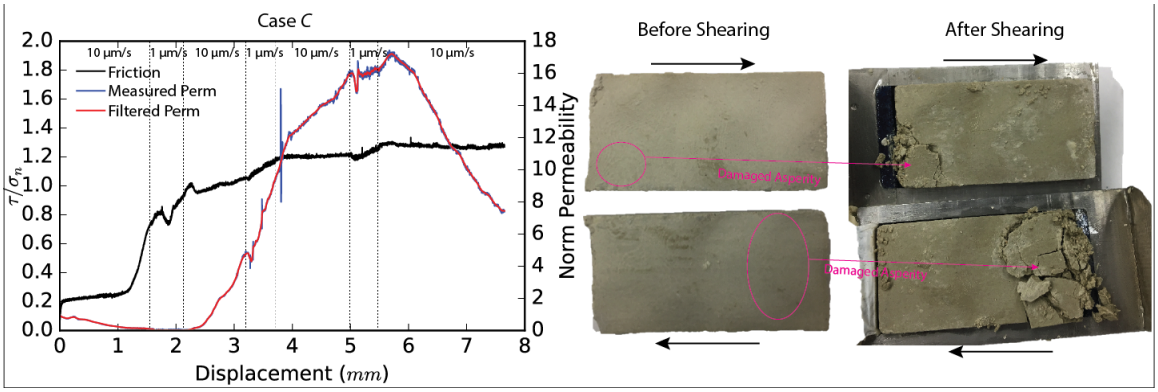

Figure **5-7**: Left: Net frictional strength and permeability evolutions with displacement for sample *C*. Right: Sample coupons before and after shear slip.

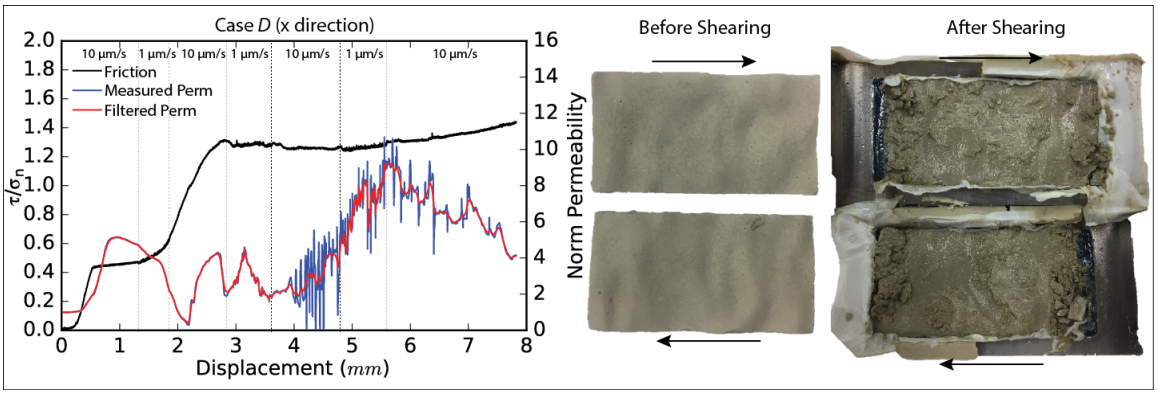

Figure **5-8**: Left: Net frictional strength and permeability evolutions with displacement for sample *D*. The shear direction is along *x* direction of sample *D* indicated in **Figure 5-3a**. Right: Sample coupons before and after shear slip.

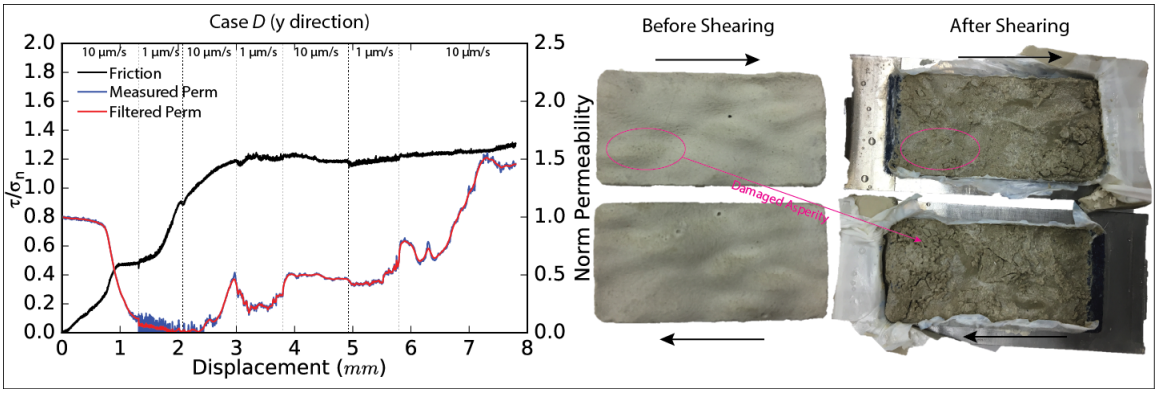

Figure **5-9**: Left: Net frictional strength and permeability evolutions with displacement for sample *D*. The shear direction is along *y* direction of sample *D* indicated in **Figure 5-3a**. Right: Sample coupons before and after shear slip.

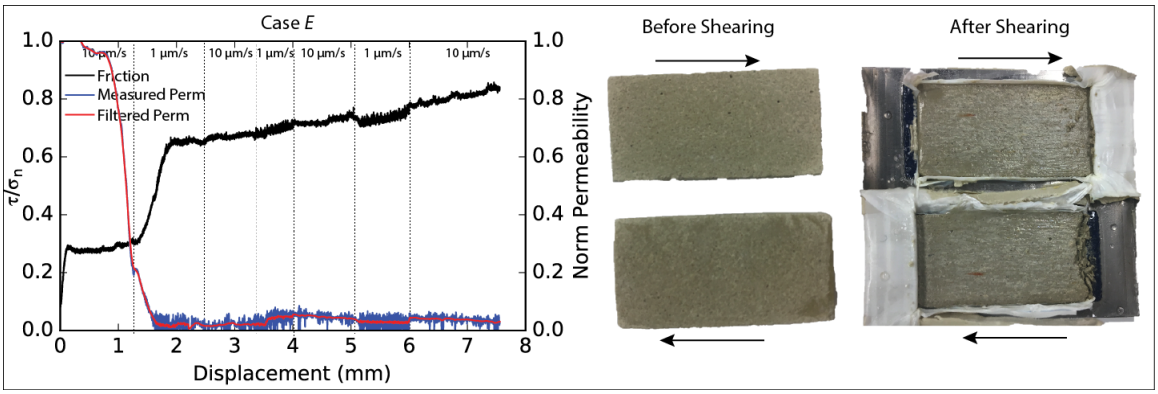

Figure **5-10**: Left: Net frictional strength and permeability evolutions with displacement for sample *E*. Right: Sample coupons before and after shear slip.

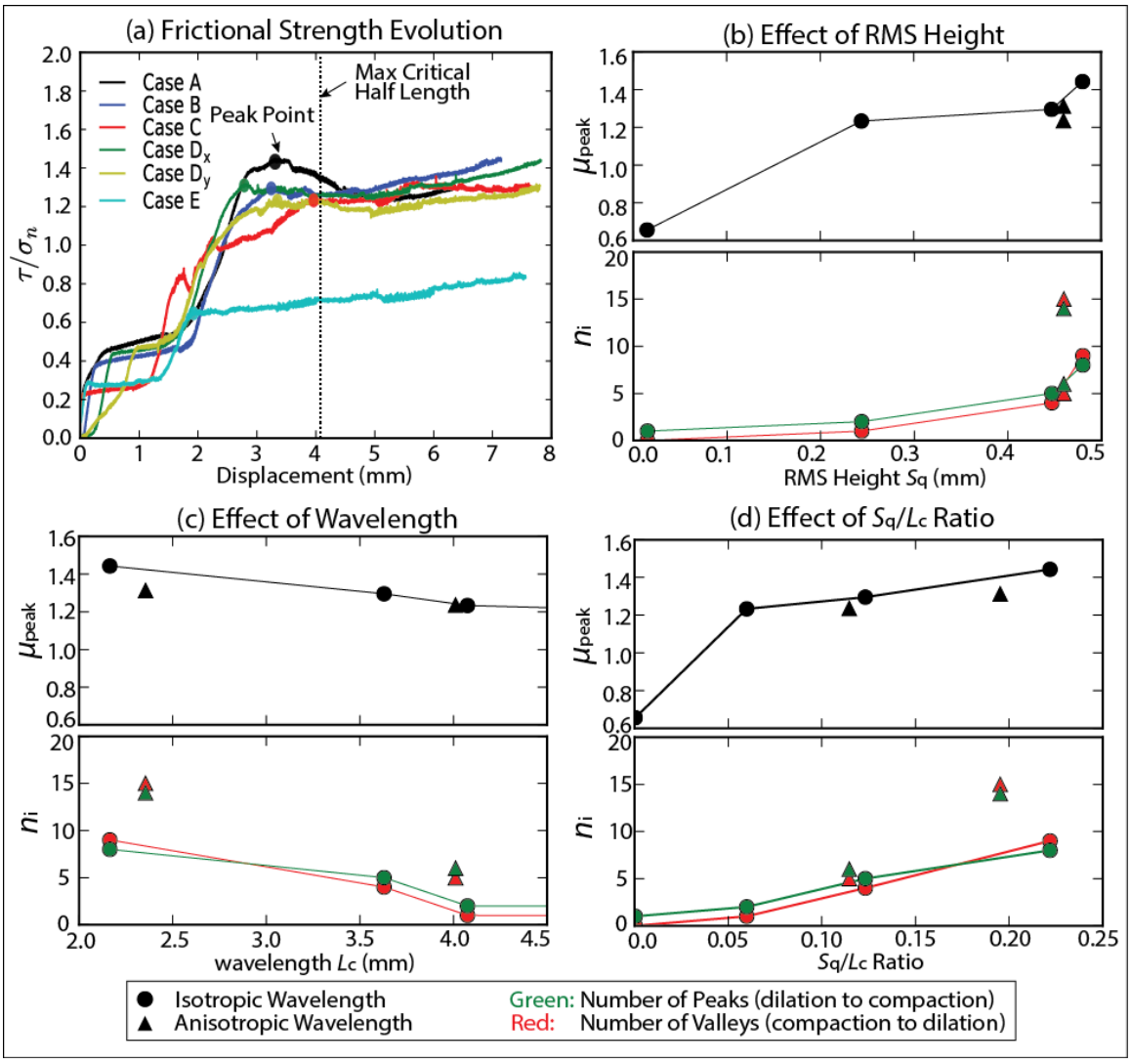

Figure **5-11**: **(a)** Friction-load point displacement curves of examined samples under effective normal stress of 3 MPa. A yielding point (peak point) is labeled before a displacement of half critical wavelength; **(b)** Effect of *RMS* height S_q; **(c)** Effect of Wavelength L_c; and **(d)** Effect of S_q/L_c ratio.

In addition to the effect of roughness diversity, the direction of shear slip with respect to surface wave direction could severely influence the permeability evolution history. Sample D_x and D_y, with identical asperity height and wavelength, are sheared at two different directions, showing that the highest dimensionless permeability of sample shear in the direction perpendicular to its larger wave is approximately (**Figure 5-8**) ~6 to ~7 times larger than that sheared in the direction parallel to its larger wave (**Figure 5-9**).

To explore the relationship between friction and surface roughness, we defined two parameters: (1) *peak frictional strength* (μ_{peak}) as the frictional yield value at a displacement less than half critical wavelength of fracture roughness, and (2) *number of permeability inflection point* (n_i) as the count number of peaks or valleys at the moment permeability changes from up-trend to down-trend or from down-trend to up-trend in shearing. This inflection points are partially highlighted in **Figure 5-5** for clarity.

A strong correlation between aforementioned two parameters (*i.e.*, μ_{peak} and n_i) and *RMS* height (S_q) and wavelength (L_c) is observed in **Figure 11b** and **11c**, presenting that the peak frictional strength (μ_{peak}) and the number of permeability inflection point (n_i) respectively decreases with wavelength but increases with both *RMS* height (S_q) and the S_q/L_c ratio in a non-linear trend. This is because (1) mechanically, fracture with higher S_q/L_c ratio demands a larger elastic deformation and requires larger shear stress to fail the asperity for fracture surface accommodation [*Brodsky et al.*, 2016]; and (2) hydraulically, higher S_q/L_c ratio leads more cycles of dilation and compaction during shearing. However, weak correlations are found between parameters (μ_{peak} and n_i) and surface features (*i.e.*, Skewness and Kurtosis), which are illustrated in **Figure 5-A1** in Appendix.

Table **5-2**: Measured frictional and permeability parameters of fracture samples

Sample	Normal Stress (MPa)	k_{ini} (m^2)	Velocity (μm/s)	τ/σ_n	(a-b)	u_s (mm)	D_c (μm)	Δu^i	k^i_0	Δk^i
rg_A	3	2.1335E-11	1 to 10	0.945	0.0009	2.46	90	0.4860	1.5398	0.1713
			1 to 10	1.29	-0.0002	4.46	50	0.4290	0.1565	0.0029
rg_B	3	1.53E-12	1 to 10	0.72	0.0003	2.12	15	0.2860	0.2795	0.0898
			1 to 10	1.267	-0.0021	3.79	50	0.4990	0.2074	0.0147
rg_C	3	7.42E-12	1 to 10	0.95	0.0007	2.15	80	0.0935	0.0144	0.0054
			1 to 10	1.18	-0.0004	3.7	50	0.1175	9.1366	0.0014
			1 to 10	1.28	-0.0008	5.5	50	0.2180	16.2394	0.8304
rg_D_x	3	2.90E-12	1 to 10	0.61	0.0022	1.8	150	0.0175	2.2096	0.2027
			1 to 10	1.283	0.0012	3.61	100	0.5180	9.0353	-1.1298
			1 to 10	1.28	0.0009	5.9	80	0.1825	1.7837	0.4963
rg_D_y	3	3.45E-12	1 to 10	0.668	0.0011	1.89	120	0.0775	0.0044	0.0085
			1 to 10	1.21	0.0007	3.78	35	0.2000	0.3245	0.1729
			1 to 10	1.193	0.0004	5.8	40	0.0350	0.5604	0.2258
rg_E	3	1.23E-11	1 to 10	0.65	-0.0004	2.2	40	0.2995	0.0232	0.0078
			1 to 10	0.705	-0.0005	4	60	0.4990	0.0445	0.0112
			1 to 10	0.75	-0.0012	5.9	50	0.4055	0.0299	0.0115

3.2 Friction Parameters and Permeability Change

For hydraulic rate-and-state friction experiments performed on fabricated samples, we determined the frictional parameters by a fitting method that solves Eqs. (2) and (3), and estimated the local permeability change using the modeling method described by *Fang et al*. [2017]. The up-close views of friction and permeability responses are shown in Appendix **Figure 5-A2** to **Figure 5-A7**. The evolution of the frictional strength and stability as a function of shear displacement is shown in **Figure 5-12**. Comparison of the constitutive parameters for rough and smooth surfaces shows several important results: First, the friction results as a whole indicate significant difference between the rough (sample *A* to *D*) and smooth surface (sample *E*). In **Figure 5-12a**, rougher surfaces show similar initial frictional strength as that of smooth surface, but indicate greater slip hardening from ~2 *mm* to 4 *mm*. The effect of slip hardening of rough surfaces deteriorates to a minimum level after a slip of 4 *mm*, implying that the interlocked large

asperities may have mechanically failed within a slip displacement of half wavelength. Rougher surfaces (sample *A* to *D*) also exhibit higher velocity-strengthening behavior during initial slip comparing to that of smooth surface (sample *E*) (**Figure 5-12b**). The frictional stability of rough and smooth surfaces slightly decreases with increasing displacement. However, whether this result extends to greater net displacement (> 10 *mm*) remains to be tested. This degradation of frictional stability suggests that aseismic fractures can evolve into seismic fracture with shear slip. The correlation of frictional parameters (*i.e.*, $\mu = \tau/\sigma_n$ and (a-b)) and fracture surface roughness ratio S_q/L_c is shown in **Figure 5-13**, where both frictional strength and stability increase with the roughness ratio. This relationship suggests that frictional strength and stability increasing with roughness, implying that fractures with low roughness are prone to reactivation and are more likely to fail seismically. This result is consistent with previous experimental work that shows roughness effects on fracture frictional behaviors in response to wear and gouge formation [*Marone and Cox*, 1994]. In contrast, these frictional parameters do not show conspicuous dependence on skewness and kurtosis, which is reported in **Figure 5-A8** in Appendix.

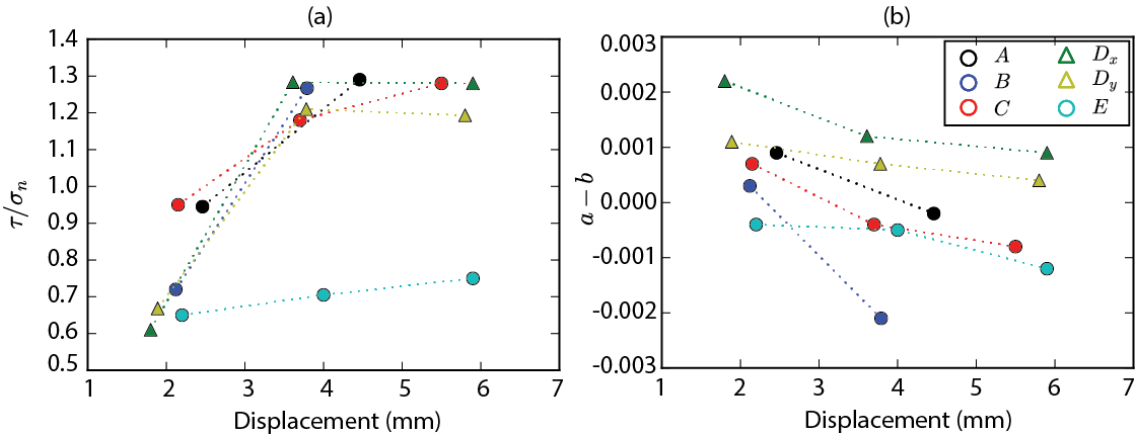

Figure **5-12**: **(a)** The apparent frictional strength (shear stress – normal stress ratio); and **(b)** the frictional stability values at the displacement where up-velocity steps are applied

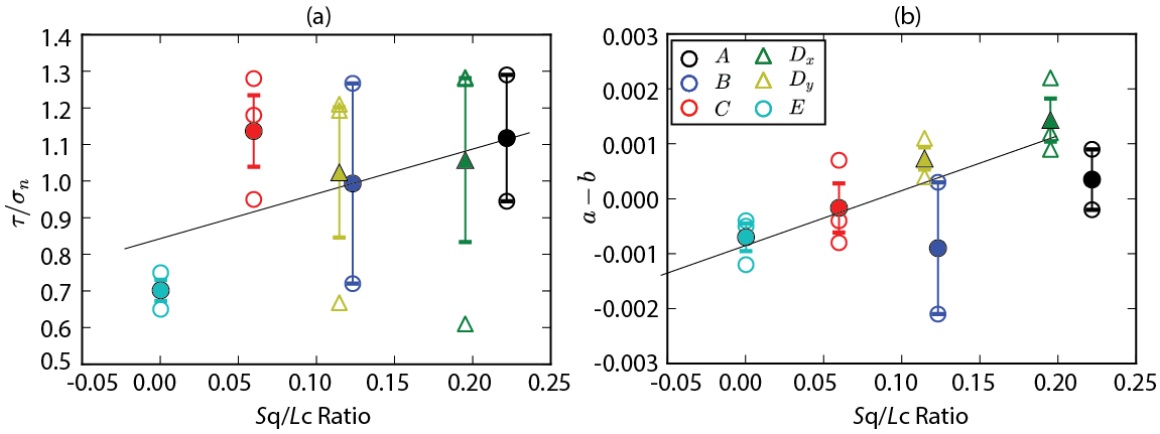

Figure **5-13**: **(a)** Correlation of the apparent frictional strength (*i.e.*, shear stress – normal stress ratio) and S_q/L_c ratio; **(b)** Correlation of frictional stability values and S_q/L_c ratio

Previous results suggest that the frictional parameters and net permeability evolution are controlled by the fracture roughness (**Figure 5-11** to **5-13**). In the following, we explore the direct relationship between frictional parameters and local transient permeability change in response to velocity steps. To compare the relative change magnitude of permeability, we first defined a normalized permeability change term as,

$$\frac{\Delta k^i}{k_0^i} = \frac{k_{real}^i - k_{sim}^i}{k_0^i} \tag{8}$$

where k^i_0 is the reference permeability before the instantaneous step of shear velocity change; i refers to the i^{th} velocity step; Δk^i is the permeability difference between the measured permeability k^i_{real} and the assumed permeability without velocity change k^i_{sim}. This normalized term describes the relative permeability change with respect to the permeability at the point before velocity change.

The correlations between permeability change and frictional parameters are shown in **Figure 5-14a** and **5-14b**, indicating that $\Delta k/ k^i_0$ is independent of (τ/σ_n) and (a-b) values. It is worth noting that such an uncorrelation or weak-correlation between permeability change and frictional stability may only be due to a small variation of (a-b) values measured from the same

materials. Most $\Delta k/ k^i_0$ values are close to zero, suggesting that for those fabricated samples, very small permeability change occur after fracture experience an instantaneous step of shear velocity change. The permeability changes (*i.e.*, $\Delta k/k^i_0$) with respect to fracture roughness S_q/L_c ratios are plotted in **Figure 5-14c**, showing uncorrelated trend between transient permeability changes and to fracture roughness S_q/L_c ratio. Such an uncorrelation between transient permeability changes and surface skewness and kurtosis are reported in **Figure 5-A9**.

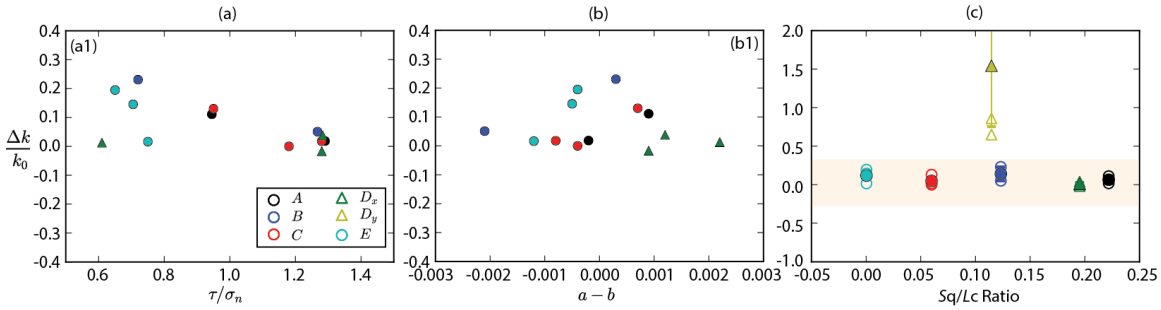

Figure **5-14**: **(a)** Correlation of $\Delta k/ k^i_0$ and (τ/σ_n) values; **(b)** Correlation of $\Delta k/ k^i_0$ and $(a\text{-}b)$ values **(c)** Correlation of $\Delta k/ k^i_0$ and S_q/L_c ratio

The net permeability evolution of smooth surface (sample *E* in **Figure 5-10**) shows similar monotonic declining trend with previous hydroshearing experiments of smooth natural fractures [*Fang et al.,* 2017], agreeing with the conclusion that the permeability decrease is due to gradually generated wear products although dilation is temperately triggered by the instantaneous shear velocity increase. For rougher surfaces, though instantaneous dilation due to sudden velocity change can be observed over a small displacement (**Figure 5-15a** to **5-15e**), the roughness effect significantly contributes to a distinct net permeability evolution, which means that instantaneous velocity change may only affect the permeability change in small magnitude over a short time or a small slip displacement after the velocity change, while over a large displacement, the roughness is the major influencing factor for changing the permeability.

From a microscopic point of view, above observation of permeability evolution is therefore summarized through two scenarios, as schematically illustrated in **Figure 5-16**:

(1) Smooth fracture surface characterized by micro asperity height S_{z_m} and micro wavelength L_{c_m} (**Figure 5-16a**). Considering that these asperities of fracture surfaces play significant roles for maintaining void spaces or propping two facing fracture planes [*Jaeger et al.*, 2007; *Ishibashi et al.*, 2016], in shearing process, destructions of these sinusoidal asperities generate granular wear products that are compacted within the fracture walls, resulting in a monotonic reduction of permeability.

(2) Rough fracture surface characterized by macro asperity height S_{z_M} and macro wavelength L_{c_M} (**Figure 5-16b**). For the case of rougher surface, the micro scale asperity features (*i.e.*, height S_{z_m} and wavelength L_{c_m}) can be identified on the macro asperity. When well-matched rough fracture walls begin colliding, two surfaces are settled and interlocked during initial closure and fine-size granular wear product may generate by cutting the micro asperities. The fracture permeability is likely to decrease during this period. By increasing shear displacement, since the real contact area between two rough surfaces is the sum of the areas of contact between facing asperities (i.e., the real contact area is a fraction of the nominal contact area), the real contact pressure is much higher than the nominal contact pressure, which results in plastic deformation of high-order asperities. In this process, when sheared-off asperities (*i.e.*, rock-forming minerals are broken down or crushed on the fracture surfaces) clog the flow pathways, the fracture permeability is significantly reduced. In contrary, with fracture sliding displacement increases, the damaged and half-damaged asperity debris may promote a strong dilation, leading to permeability enhancement (**Figure 5-16b**). Therefore, this physical process can explain the initial permeability decrease and later competed compaction and dilation behaviors of fracture in **Figure 5-5** to **5-10**.

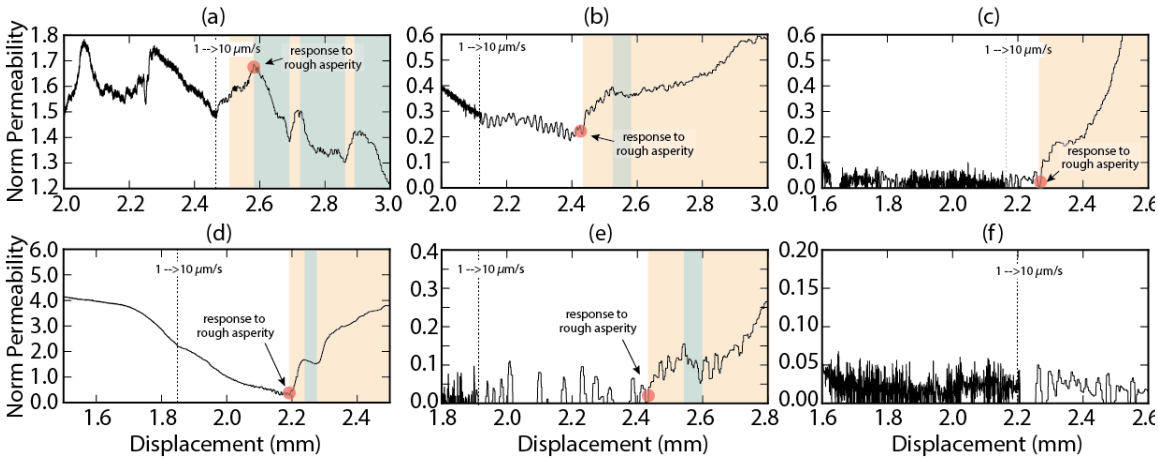

Figure **5-15**: Permeability evolution with effect of rougher asperities: (a): sample *A*; (b): sample *B*; (c) sample *C*; (d) sample D_x; (e) sample D_y; (f) sample *E*. The red shadow highlights the permeability change due to velocity change while the yellow and blue shadow highlight the dilation and compaction due to rough asperity.

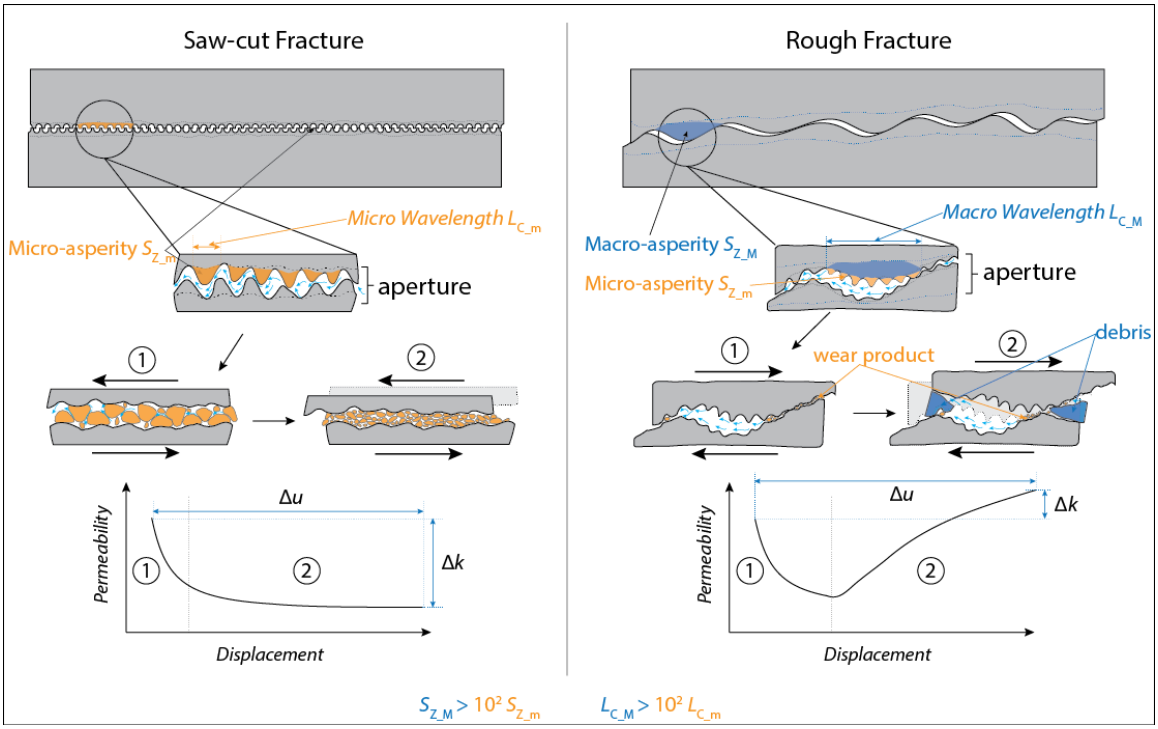

Figure **5-16**: Schematic diagram shows concepts of micro/macro asperity (S_{z_m}/S_{z_M}) and micro/macro wavelength ($L_{c\ m}/L_{c\ M}$) of saw-cut (smooth) fracture and rough fracture

3.3 Implication on Induced Seismicity of Fluid Injection Activities

The macroscopic, measured frictional behavior is an average of what happens at each individual asperity since the stress needed to shear off each asperity is relatively small - many asperities give a small contribution to the macroscopic behavior, so that it can be treated as a continuum. The lab-scale experimental results of frictional behavior suggest that seismic event is more likely to occur on fracture or faults with smoother surfaces due to the low frictional strength and stability, which is consistent with crustal-scale field observations that fault shear strength increases with curvature and mega-earthquakes preferentially occur on flat interfaces [*Bletery et al.*, 2016]. As implied by **Figure 5-12**, a rough fracture can fail aseismically initially and evolve to seismic failure mode with increasing sliding displacement, which is consistent with the observation that induced seismicity can be triggered by aseismic slip [*Guglielmi et al.*, 2015].

In addition to frictional behaviors that controls the occurrence of induced earthquakes, the permeability evolution during aseismic/seismic process, plays a key role of adjusting (*i.e.*, preventing or promoting) the timing of induced seismicity. For example, as the shear slip of a pre-existing fracture increases or decreases permeability of that fracture, a volume of fluid could be admitted into or blocked out of the fracture. Higher permeability could enhance the propagation of lower ΔP and would promote the progress of reactivation of faults that are prone to lower ΔP, as long as a sufficient volume of fluid and a pressure higher than the critical pore pressure for shear slip were supplied. On the contrary, lower permeability could prevent the propagation of fluid pressure and build up local fluid pressure and reactivate fractures with high shear strength. This process could explain our observations of the more extensive and faster propagation of lower ΔP or localized high fluid pressure zone very well. The plausibility of this process could be accepted based on an understanding of simple hydrology and geomechanical theory; however, the combination of the two independent data sets of microseismic migration and pore pressure

(stress information) used in this study, clearly provided a physical demonstration.

4. Conclusions

We performed hydro-shearing experiments on a group of fabricated fracture surfaces with specified roughness features. We studied the possible relationship between concurrent frictional behavior and permeability evolutions and analyzed the effect of surface roughness pattern.

Our experimental results show that (1) both smooth and rough fracture surfaces exhibit velocity strengthening frictional behavior for small net displacement evolves to velocity neutral and velocity weakening with displacement. (2) Rougher surfaces exhibit higher velocity strengthening frictional behavior and higher frictional strength due to cohesive interlocking asperities during shearing. Seismicity may not be induced on rough fracture surfaces. (3) The roughness pattern has a significant control on permeability evolution over the entire shearing history. Permeability evolves monotonically for smooth fracture while in a fluctuating pattern for highly roughed fractures. A higher roughness is likely to result in alterative compaction and dilation during shearing. Significant permeability damage could occur for rough samples when asperities are highly worn off and block the fluid pathways. (4) As experiments performed on the same material, there is no conspicuous correlation between local transient permeability evolution and local frictional behavior (*i.e.*, frictional strength and stability) for rough fracture samples when fractures subject to sudden sliding velocity change.

Acknowledgement

This work is the result of support provided by DOE Grant DE-EE0023354. This support is gratefully acknowledged. The data for this paper are available by contacting the corresponding author at yi.fang@psu.edu.

Appendix

Skewness is the ratio of the mean of the height values cubed and the cube of S_q within a sampling area expressed as,

$$S_{sk} = \frac{1}{S_q^3 \cdot A} \iint_A z^3(x,y)\,dx\,dy \tag{A1}$$

The skewness is derived from the amplitude distribution curve; it is the measure of the profile symmetry about the mean line. It describes the shape of the topography height distribution and represents the degree of bias either in the upward or downward direction of an amplitude distribution curve. This unit-less parameter can be positive (*i.e.,* the bulk of the material is below the mean line, suggesting a smoother surface), negative (*i.e.,* the bulk of the material is above the mean line, suggesting in rougher surface). However, a rougher surface could also be zero when the Gaussian height distribution has symmetrical topography. In such a case, it is necessary to apply kurtosis value to confirm the roughness of a fracture with symmetrical topography. The kurtosis is a measure of the sharpness of the surface height distribution and is the ratio of the mean of the fourth power of the height values and the fourth power of S_q within the sampling area as,

$$S_{ku} = \frac{1}{S_q^4 \cdot A} \iint_A z^4(x,y)\,dx\,dy \tag{A2}$$

Kurtosis is strictly positive and unit-less, and measures the spread of the height distribution. A surface with a Gaussian height distribution has a kurtosis value of three. This parameter detects whether the profile spikes are evenly distributed and provides a measure of the spikiness of the area. If Kurtosis value is smaller than 3 the surface is flat while if the Kurtosis is higher than 3, the surface has more peaks than valleys.

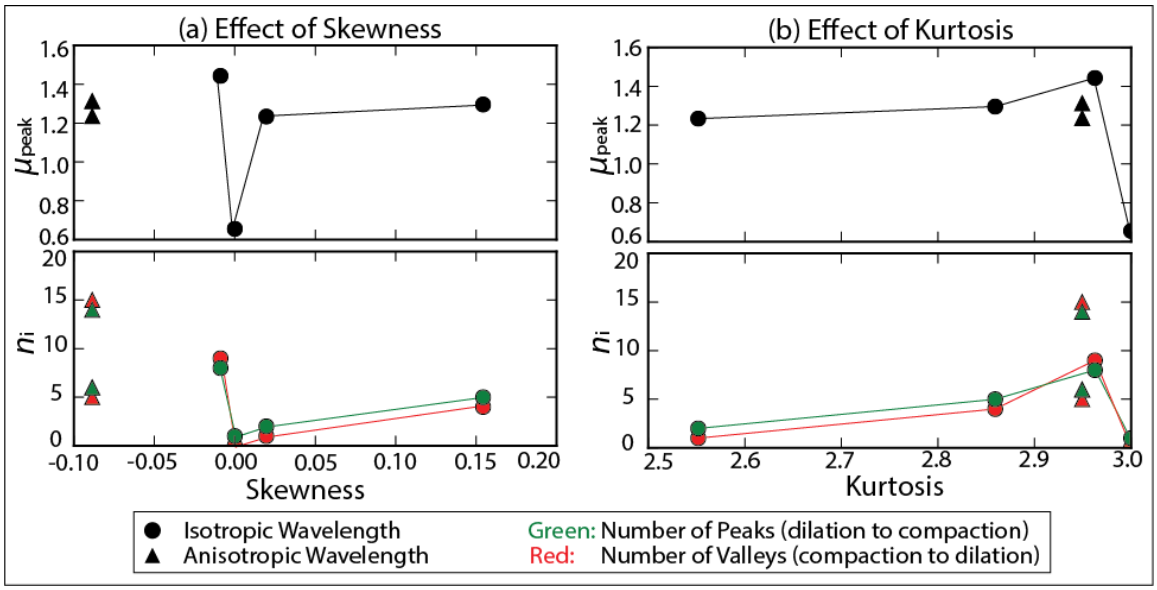

Figure **5-A1**: **(a)** Relationship of skewness and μ_{peak}, and n_i; **(b)** Relationship of Kurtosis and μ_{peak}, and n_i

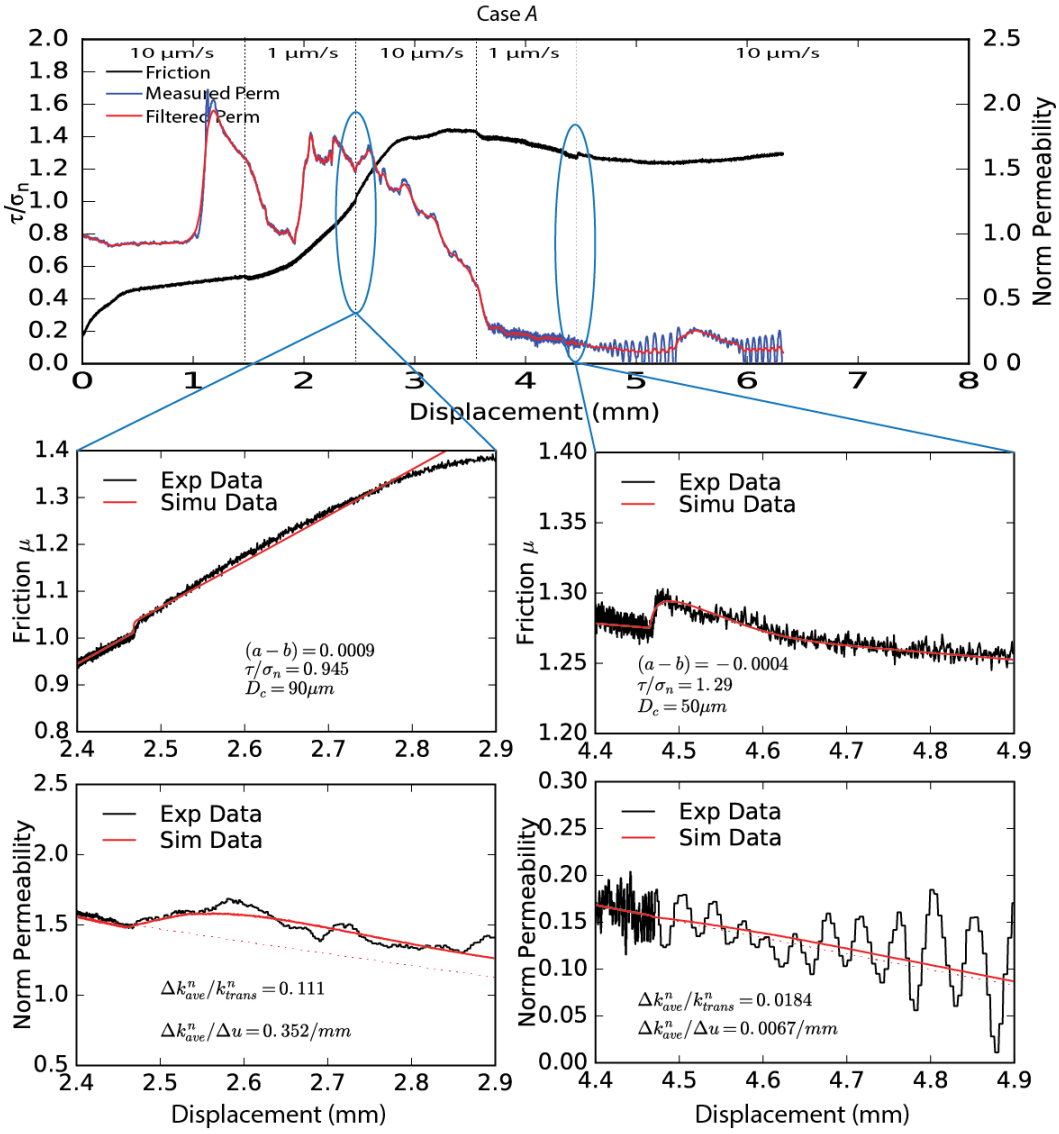

Figure **5-A2**: Friction data and numerical simulations for surface *A*. In each case data represent the friction response to an up-velocity step change in load point velocity.

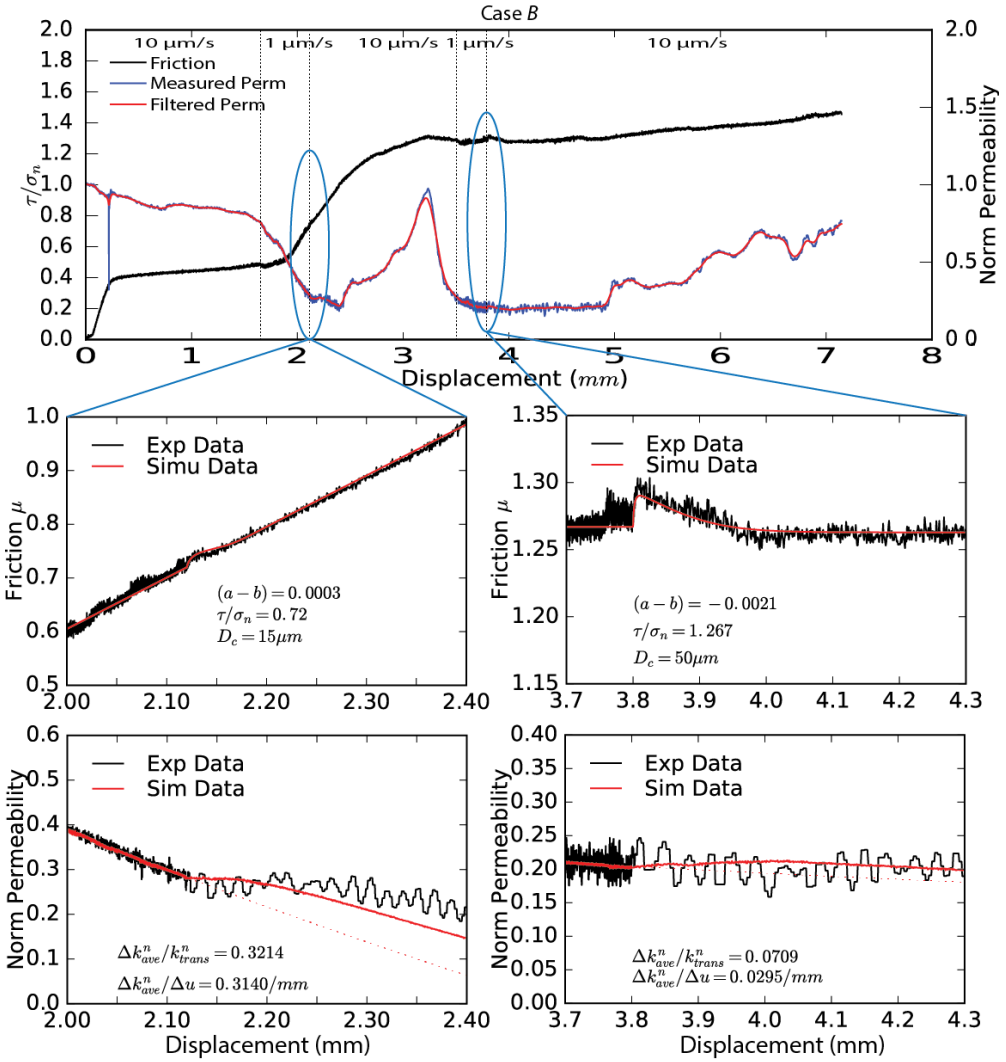

Figure **5-A3**: Friction data and numerical simulations for surface *B*. In each case data represent the friction response to an up-velocity step change in load point velocity.

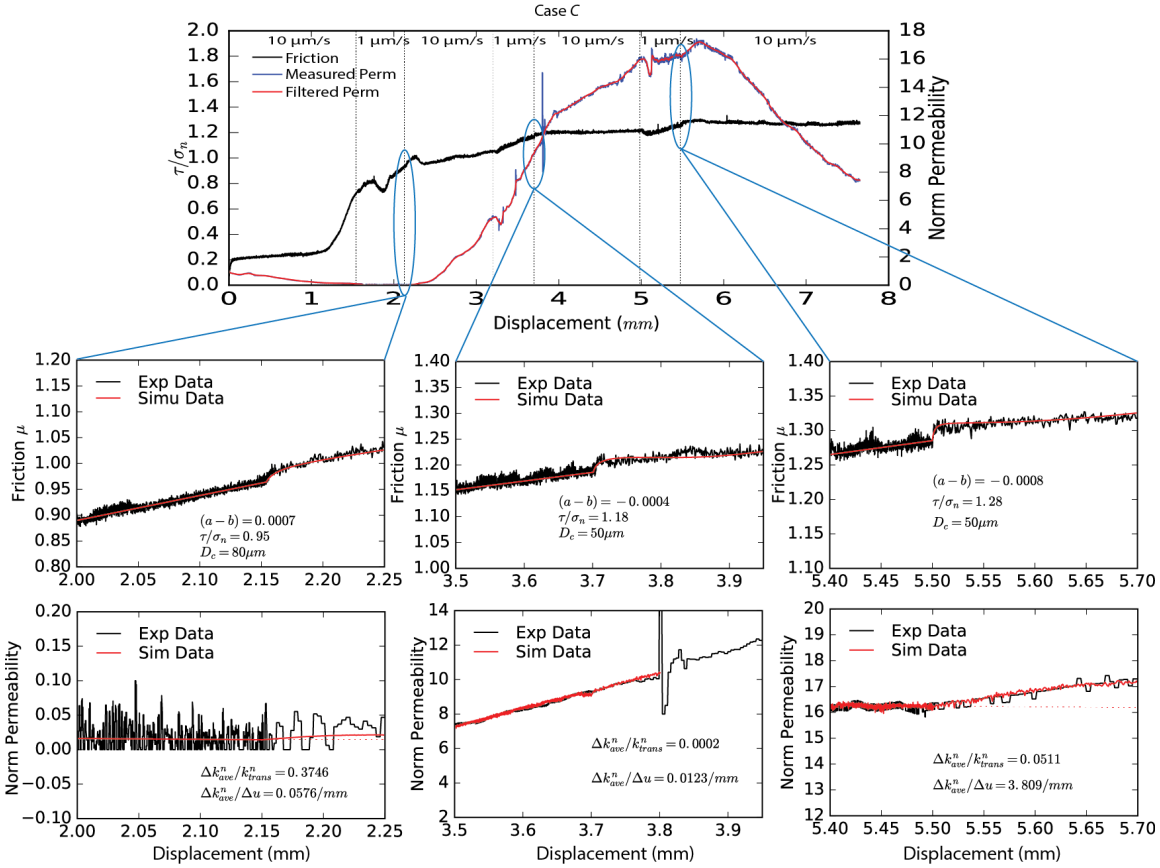

Figure **5-A4**: Friction data and numerical simulations for surface *C*. In each case data represent the friction response to an up-velocity step change in load point velocity.

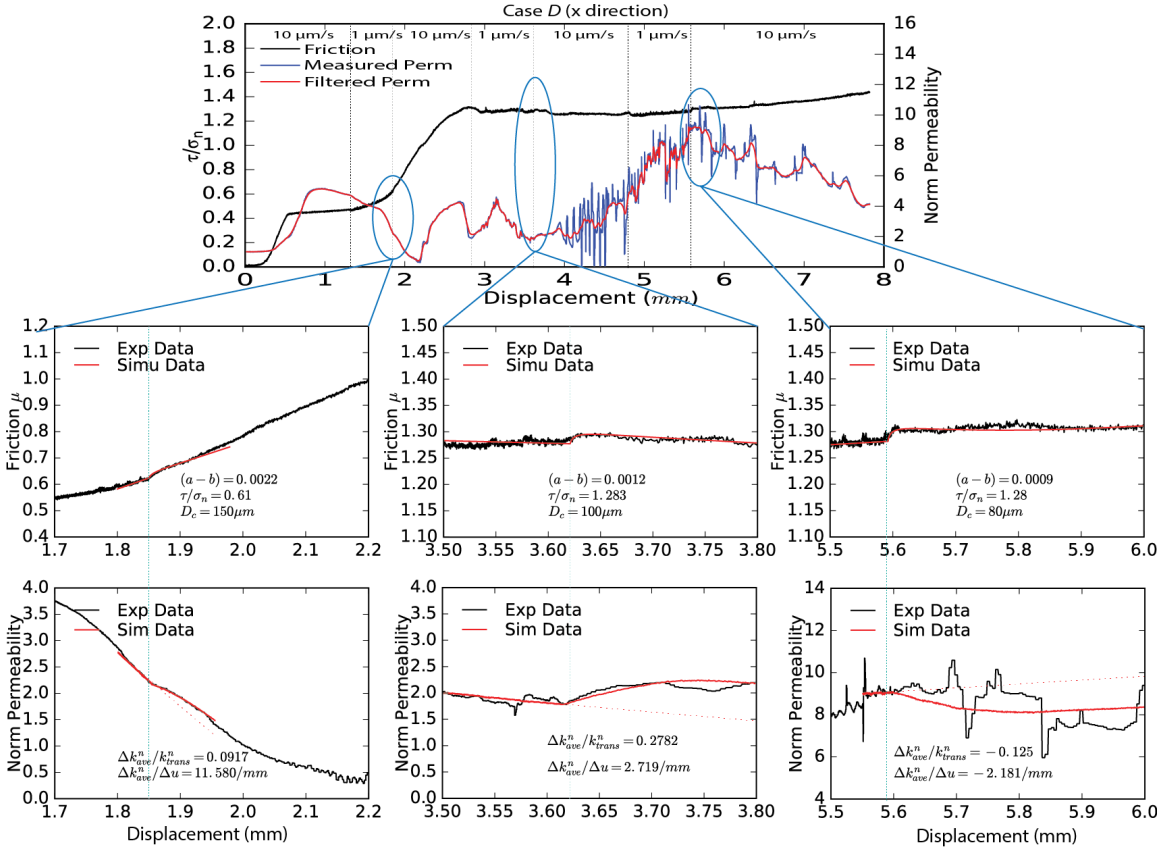

Figure **5-A5**: Friction data and numerical simulations for surface D_x. In each case data represent the friction response to an up-velocity step change in load point velocity.

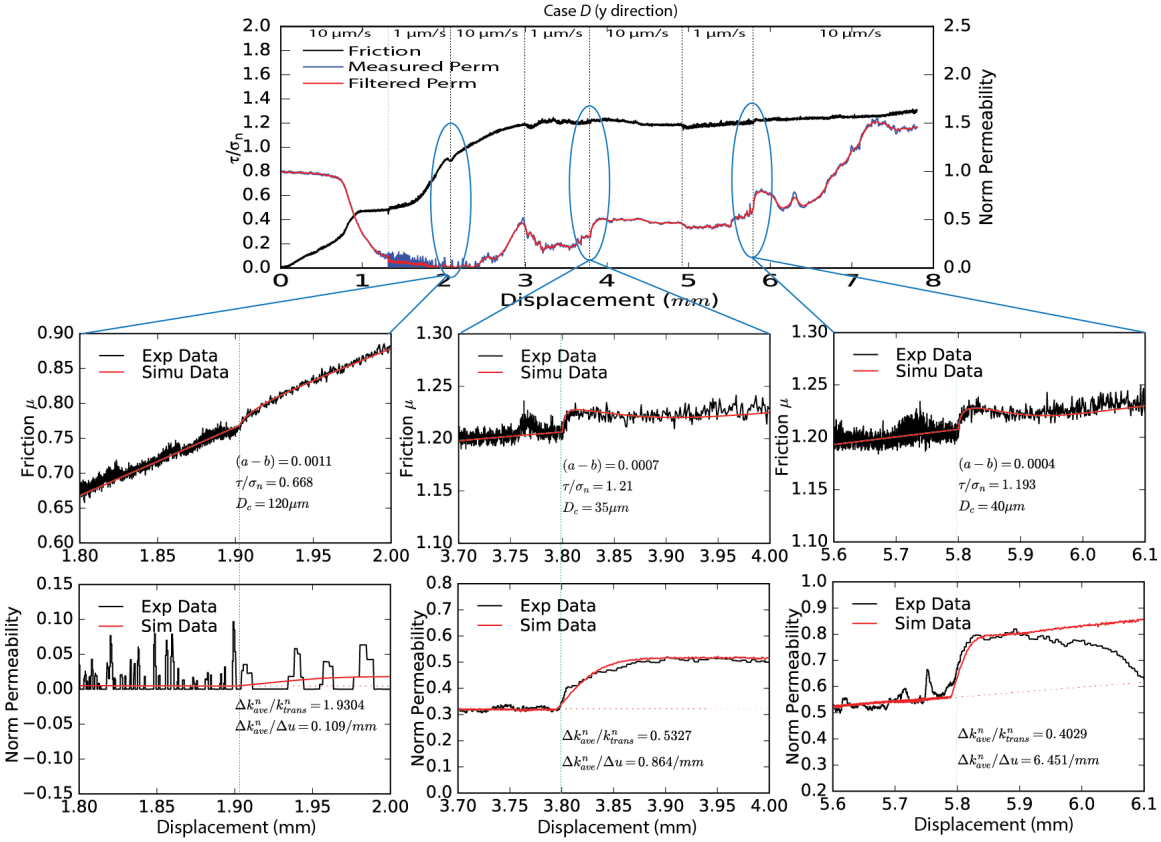

Figure **5-A6**: Friction data and numerical simulations for surface D_y. In each case data represent the friction response to an up-velocity step change in load point velocity.

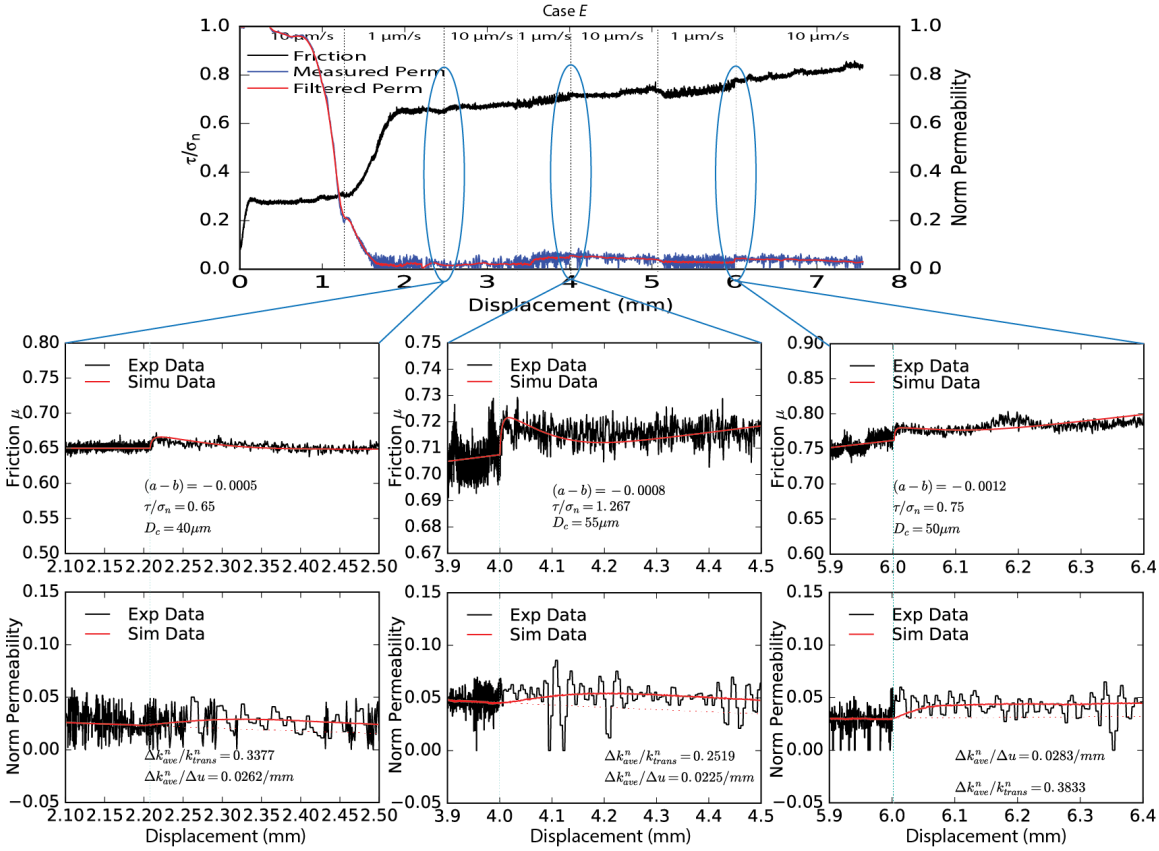

Figure **5-A7**: Friction data and numerical simulations for surface *E*. In each case data represent the friction response to an up-velocity step change in load point velocity.

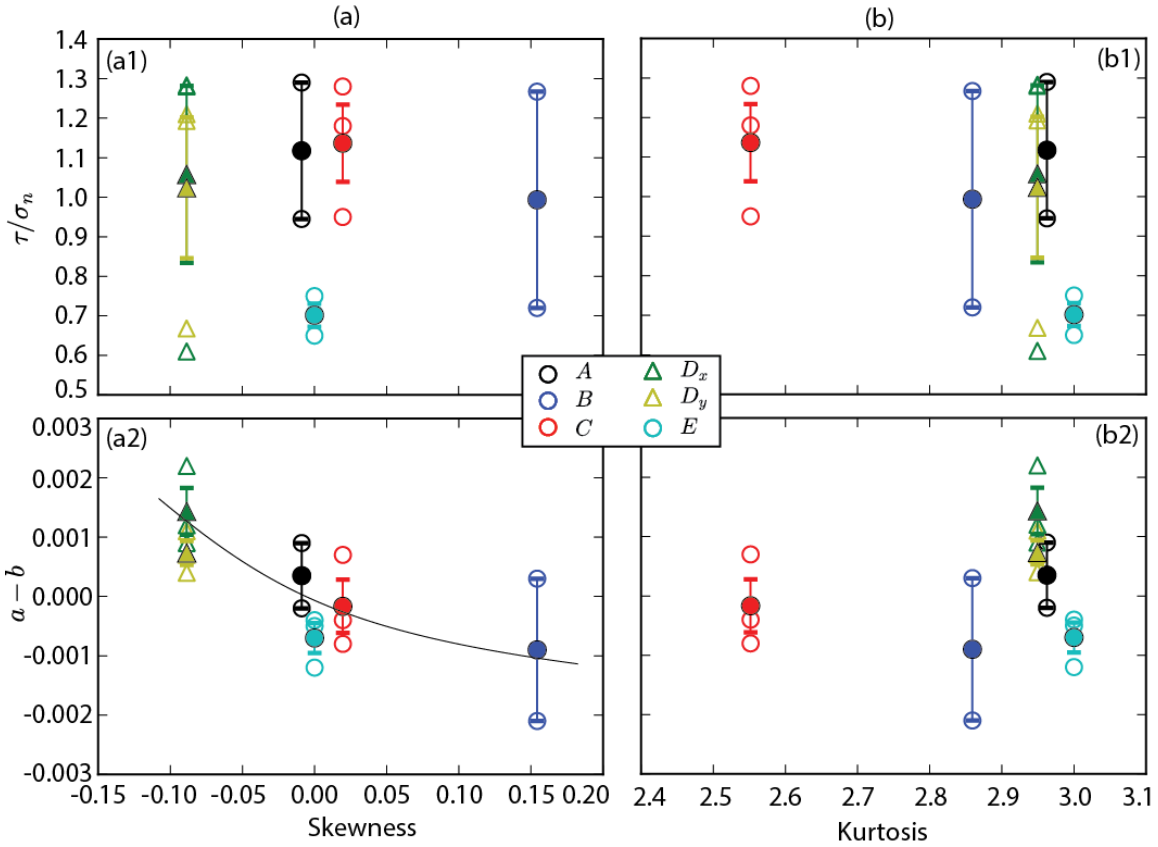

Figure **5-A8**: **(a)** Correlation of frictional parameters (*i.e.*, frictional strength and stability) and Skewness; **(b)** Correlation of frictional parameters and Kurtosis

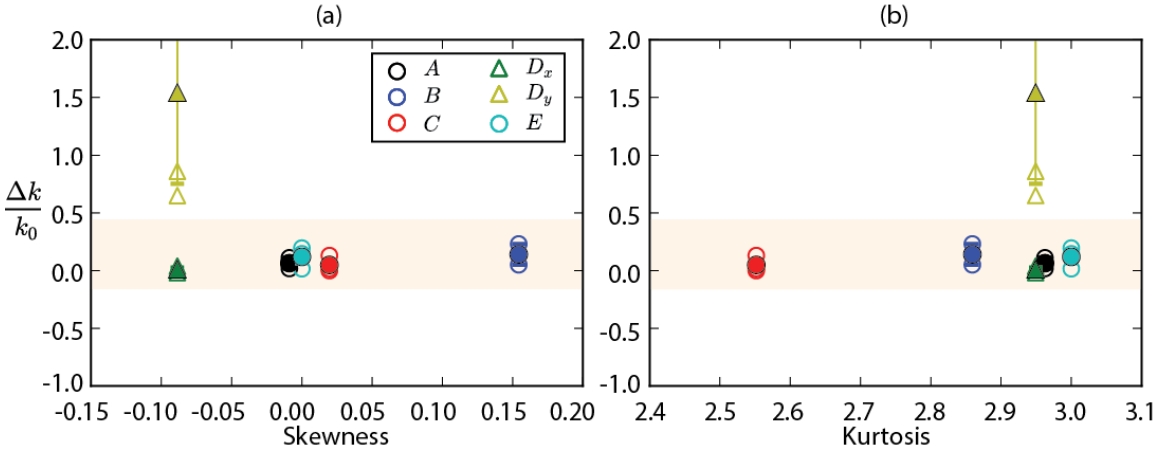

Figure **5-A9**: **(a)** Correlation of $\Delta k/\ k^i_0$ and skewness values; **(b)** Correlation of $\Delta k/\ k^i_0$ and kurtosis values

References

Asadi, M. S., V. Rasouli, and G. Barla (2013), A laboratory shear cell used for simulation of shear strength and asperity degradation of rough rock fractures, *Rock Mech. Rock Eng.*, *46*(4), 683–699, doi:10.1007/s00603-012-0322-2.

Barton, N. (1973), Review of a new shear-strength criterion for rock joints, *Eng. Geol.*, *7*(4), 287–332, doi:10.1016/0013-7952(73)90013-6.

Barton, N., and V. Choubey (1977), The shear strength of rock joints in theory and practice, *Rock Mech.*, *10*(1–2), 1–54, doi:10.1007/BF01261801.

Barton, N., S. Bandis, and K. Bakhtar (1985), Strength, deformation and conductivity coupling of rock joints, *Int. J. Rock Mech. Min. Sci.*, *22*(3), 121–140, doi:10.1016/0148-9062(85)93227-9.

Bletery, Q., A. M. Thomas, A. W. Rempel, L. Karlstrom, A. Sladen, and L. De Barros (2016), Mega-earthquakes rupture flat megathrusts, *Science (80-.).*, *354*(6315), 1027–1031, doi:10.1126/science.aag0482.

Brodsky, E. E., J. D. Kirkpatrick, and T. Candela (2016), Constraints from fault roughness on the scale-dependent strength of rocks, *Geology*, *44*(1), 19–22, doi:10.1130/G37206.1.

Brown, S. R. (1995), Simple Mathematical-Model of a Rough Fracture, *J. Geophys. Res. Earth*, *100*(B4), 5941–5952, doi:10.1029/94JB03262.

Cornet, F. H., J. Helm, H. Poitrenaud, and a. Etchecopar (1997), Seismic and Aseismic Slips Induced by Large-scale Fluid Injections, *Pure Appl. Geophys.*, *150*(3–4), 563–583, doi:10.1007/s000240050093.

Dieterich, J. H. (1978), Time-dependent friction and the mechanics of stick-slip, *Pure Appl. Geophys. PAGEOPH*, *116*, 790–806, doi:10.1007/BF00876539.

Dieterich, J. H. (1979), Modeling of rock friction 1. Experimental results and constitutive equations, in *Journal of Geophysical Research: Solid Earth*, vol. 84, pp. 2161–2168.

Ellsworth, W. L. (2013), Injection-Induced Earthquakes, *Science (80-.).*, *341*(6142), 142–149, doi:10.1126/science.1225942.

Elsworth, D., and R. E. Goodman (1986), Characterization of rock fissure hydraulic conductivity using idealized wall roughness profiles, *Int. J. Rock Mech. Min. Sci. Geomech. Abstr.*, *23*(3), 233–243, doi:http://dx.doi.org/10.1016/0148-9062(86)90969-1.

Fang, Y., S. A. M. den Hartog, D. Elsworth, C. Marone, and T. Cladouhos (2016), Anomalous

distribution of microearthquakes in the Newberry Geothermal Reservoir: Mechanisms and implications, *Geothermics*, *63*, 62–73, doi:http://dx.doi.org/10.1016/j.geothermics.2015.04.005.

Faoro, I., A. Niemeijer, C. Marone, and D. Elsworth (2009), Influence of shear and deviatoric stress on the evolution of permeability in fractured rock, *J. Geophys. Res. Solid Earth*, *114*(1), doi:10.1029/2007JB005372.

Fung, A. K., K.-S. Chen, and K. S. Chen (2010), *Microwave scattering and emission models for users*, Artech house.

Grasselli, G., and P. Egger (2003), Constitutive law for the shear strength of rock joints based on three-dimensional surface parameters, *Int. J. Rock Mech. Min. Sci.*, *40*(1), 25–40.

Guglielmi, Y., F. Cappa, J.-P. Avouac, P. Henry, and D. Elsworth (2015), Seismicity triggered by fluid injection–induced aseismic slip, *Sci.* , *348*(6240), 1224–1226, doi:10.1126/science.aab0476.

Jouanna, P. (1972), Effet des sollicitations mécaniques sur les écoulements dans certains milieux fissurés,

Maini, Y. N. (1972), In situ hydraulic parameters in jointed rock: their measurement and interpretation,

Majer, E. L., R. Baria, M. Stark, S. Oates, J. Bommer, B. Smith, and H. Asanuma (2007), Induced seismicity associated with Enhanced Geothermal Systems, *Geothermics*, *36*(3), 185–222, doi:http://dx.doi.org/10.1016/j.geothermics.2007.03.003.

Marone, C., and S. J. D. Cox (1994), Scaling of rock friction constitutive parameters: The effects of surface roughness and cumulative offset on friction of gabbro, *pure Appl. Geophys.*, *143*(1), 359–385, doi:10.1007/BF00874335.

Moeck, I., G. Kwiatek, and G. Zimmermann (2009), Slip tendency analysis, fault reactivation potential and induced seismicity in a deep geothermal reservoir, *J. Struct. Geol.*, *31*(10), 1174–1182, doi:10.1016/j.jsg.2009.06.012.

Ruina, A. (1983), Slip instability and state variable friction laws, *J. Geophys. Res. Solid Earth*, *88*(B12), 10359–10370, doi:10.1029/JB088iB12p10359.

Segall, P., and S. D. Fitzgerald (1998), A note on induced stress changes in hydrocarbon and geothermal reservoirs, *Tectonophysics*, *289*(1), 117–128.

Segall, P., and J. R. Rice (1995), Dilatancy, compaction, and slip instability of a fluid-infiltrated fault, *J. Geophys. Res.*, *100*(B11), 22155–22171, doi:10.1029/95jb02403.

Talwani, P. (1997), On the nature of reservoir-induced seismicity, *Pure Appl. Geophys.*, *150*(3–4), 473–492, doi:Doi 10.1007/S000240050089.

Walsh, F. R., and M. D. Zoback (2015), Oklahoma's recent earthquakes and saltwater disposal, *Sci. Adv.*, *1*(5).

Zoback, M. D., and S. M. Gorelick (2012), Earthquake triggering and large-scale geologic storage of carbon dioxide, *Proc. Natl. Acad. Sci. U. S. A.*, *109*(26), 10164–10168, doi:Doi 10.1073/Pnas.1202473109.

Zoback, M. D., A. Kohli, I. Das, and M. Mcclure (2012), The Importance of Slow Slip on Faults During Hydraulic Fracturing Stimulation of Shale Gas Reservoirs, *Spe 155476*, (2011), SPE 155476, doi:10.2118/155476-MS.

Chapter 6

General Conclusions and Suggestions for Further Research

1. General Conclusions

Fluid-injection induced seismicity is widely observed in enhanced geothermal reservoir stimulation. With the in-situ microearthquakes (MEQs) data in the first phase of Newberry geothermal reservoir stimulation, we apply theoretical analysis and experimental method to reveal the mechanisms of a bimodal depth distribution of fluid-injection-induced MEQs. Differing from other expected distribution patterns of induced MEQs with depth, this bimodal depth distribution of MEQs at the Newberry geothermal reservoir suggests unusual controls by fluid permeation and reservoir mineralogy and state. Our analyses introduce the following conclusions: **(1)** the unusual and unexpected penetration of excess fluid pressures in the shallow zone is plausible mainly due to the casing leak in the shallow reservoir. This result is further confirmed by the second observation that indeed the casing is damaged at shallow depth (~700 m). **(2)** The diminished seismicity in the deep open zone is plausibly associated by fluid loss (wellhead pressure drop) as a result of the shallow leak. **(3)** An upward-migrating fluid pressure pulse is incapable of inducing seismicity in the shallow reservoir (above ~1000 m), but may partially contribute to the occurrence of seismicity near the top of casing shoe (~1800 m). **(4)** The observation of missing seismic events between ~1800 m and ~2500 m during the stimulation plausibly results from slight velocity strengthening properties in the reservoir and in particular on local preexisting fractures. Aseismic events may still occur in this intermediate zone, in the form of slow sliding slip or creep events, but may be below the threshold observed by the seismic monitoring. In the second phase

of Newberry geothermal reservoir stimulation, the magnitudes and locations of microseismic events are recorded.

With in-situ MEQs data, a reservoir permeability mapping method is developed to constrain the evolution of in-situ permeability at sufficiently fine resolution. In this work we present a model that links observed MEQs to the permeability of the fractured reservoir. The model couples the established physical coupling between hydraulic and mechanical properties of fractures, hydroshearing-induced seismicity, and fracture permeability. The parametric study of controlling parameters in the governing equations suggests that the most significant geophysical properties are frictional evolution, fracture dilation angle, moment magnitude and the distribution of spatial seismicity (*i.e.* fracture populations, locations, spacing). We apply both the cubic law and *Oda*'s crack tensor theory to a synthetic reservoir model as a demonstration. We then evaluate the permeability distribution and its evolution using MEQ data from the stimulation of the Newberry EGS reservoir. Comparison of predicted permeabilities derived from each method identifies that **(1)** the resolution of permeability is largely determined by the cellular grid size and the fracture size for both *Oda*'s crack tensor theory and cubic law methods while the evaluated equivalent permeability is independent of the limitation of the REV size. **(2)** With identical parameters, although *Oda*'s crack tensor theory produces a more accurate estimation of permeability than that of the cubic law, the difference between the two estimates is less than one order magnitude. **(3)** In the reservoir, the most permeable zone is located within the densest zone of MEQs. This model has potential application for mapping permeability evolution using in-situ monitored MEQ data in both conventional and unconventional reservoirs at various scales. The study also suggests that higher reliability of the results can be achieved through improving the accuracy of the parameters that are used in the model. Particularly in practical operations, the quality of the observed moment tensors recovered through microseismic monitoring is key in

determining the accuracy of the properties of the in-situ fractures and the recovered permeability of the EGS reservoir.

The stimulation of shale reservoirs or geological CO_2 sequestration (GCS) may also induce seismicity, which may change reservoir permeability due to fault slip. In order to understand the mode of fracture reactivation and permeability evolution in shales in a low effective normal stress regime, we perform direct-shearing experiment to measure the frictional strength and stability while also measuring permeability changes. We find that, under low effective normal stress, phyllosilicate-rich shale (OPS) exhibits weaker frictional strength but much stronger frictional stability and larger permeability reduction than that of carbonate-rich shale (GRS). Our experimental and analytical results show that this observed friction-stability-permeability relationship may be explained via an integration of three interconnected physical mechanisms: **(1)** different mineral composition of fractures has a distinct effect on frictional strength and frictional stability. At low effective normal stress, phyllosilicate-rich OPS tends to be more frictionally stable than that of carbonate-rich GRS. **(2)** Generated wear products of low surface roughness fractures, would seal the fluid conduits of fracture aperture, countering the effect of fracture dilation. The competition between wear product and fracture dilation depends on material strength and brittleness – strong-brittle asperities may result in higher frictional strength, lower frictional stability and larger permeability than that of weak-ductile asperities. **(3)** Swelling of clay-rich asperities and clay-rich wear products directly seals the fracture aperture, and therefore reduces the permeability. This relationship implies that a comprehensive mineralogical characterization of reservoir rock and fractures may help in a preliminary understanding of potential permeability evolution subject to fluid injection in shale rocks.

Thereafter, a series of direct-shear experiments with concurrent measurement of permeability are performed to probe mineralogical controls on frictional strength, stability and permeability. These are conducted on saw-cut fractures in natural rocks with distinct mineral

compositions as well as sintered samples with pre-defined mineralogical mixtures. Friction-permeability relationships are strongly controlled by mineralogy. Given the experimental conditions of low effective normal stress, room temperature and saw-cut planar fracture geometry, frictional strength and permeability change upon reactivation decreases with phyllosilicate content but increases with tectosilicate content. In contrast, the reverse trend is observed for frictional stability (*a*-*b*). However, the effect of carbonate content on frictional stability and transient permeability change is different. The permeability change decreases with carbonate content while both frictional strength and stability increase. The permeability change always decreases with an increase in frictional stability. With this relationship, we speculate that planar fractures with low frictional stability exhibit permeability enhancement after seismic slip in the frame of rate-state friction theory. This relationship implies a new mechanical-hydro-chemical (MHC) coupling loop *via* a linkage of frictional properties, mineralogy and permeability.

However, it is worth nothing that friction-permeability relationships are complex, and may also be affected by other external factors such as fracture surface roughness and material mechanical properties, which demands further experimental efforts. Hence, the effect of roughness on permeability evolution and frictional behavior is investigated through performing direct-shear experiments on fabricated fractures with specified roughness features. The rough fractures show distinct frictional behavior and permeability evolution comparing to that of smooth fractures. Rougher surfaces exhibit higher velocity strengthening frictional behavior and higher frictional strength due to the presence of cohesive interlocking asperities during shearing, suggesting that seismicity may not be induced on rough fracture surfaces. Permeability evolves monotonically for smooth fractures but in a fluctuating pattern for highly roughened fractures, implying alternating compaction and dilation during shearing. Significant permeability damage may occur when asperities are highly worn with wear products blocking fluid pathways.

Implications of our lab-scale experimental results suggest that characterization of fracture geometry would be beneficial for better understanding and managing induced seismicity and permeability development. These conclusions suggest that friction-permeability relationships are complicated, and are affected by various factors such as fracture materials and surface characteristics.

Finally, in shale reservoir stimulation, fractures are propped to increase the permeability of the formation. Meanwhile, the proppants may also influence the frictional strength of fractures. Thus, we explore the evolution of friction and permeability of a propped fracture using shearing-concurrent measurements of permeability during constant velocity shearing experiments. We separately examine the effects of normal stress, proppant thickness, proppant size and rock texture on the frictional and transport response of proppant packs confined between planar fracture surfaces. The results indicate that proppant-absent and proppant-filled fractures show different frictional strength, implying that proppants could change the friction of natural fractures and influence the potential for shear failure. For fractures with proppants, we observed that (1) the frictional response is mainly controlled by the normal stress and proppant thickness. High normal stress results in the crushing of proppant particles although this change in size has almost no impact on the frictional response of the proppant-fracture system. The observed post-shearing striations on fracture surfaces suggest that the magnitude of proppant embedment is controlled by the applied normal stress. Moreover, under high normal stress, the reduced friction implies that shear slip is more likely to occur for the propped fractures in deeper reservoirs. The increase in the number of proppant layers, from mono-layer to triple-layers, significantly increases the friction of the propped fracture due to the inter-locking of the particles and jamming, suggesting that high proppant density during emplacement would help stabilize the fractures during injection. (2) Permeability of propped fracture is mainly controlled by the magnitude of the normal stress, the proppant thickness and the proppant size. Permeability of the propped fracture

decreases during shearing due to proppant particle crushing and related clogging. Compared to the multi-layered specimen, the mono-layer case which has fewer displacement degrees-of-freedom exhibits the smallest initial permeability due to proppant embedment. Proppants become prone to crushing if the shear loading evolves concurrently with the normal loading. Above combined conclusions suggest the use of high-density proppants in the field, which not only provides high hydraulic conductivity for hydro-carbon production, but also help to mitigate the risk of induced seismicity.

2. Suggestions for Further Research

Understanding the feedback of induced seismicity and friction-permeability evolution of fractures is challenging due to the complexity of the problem itself and the limitation of in-situ geophysical instruments and in-house experimental conditions.

For geo-engineering activities, such as geologic sequestration of CO_2, enhanced geothermal reservoir stimulation, and shale gas reservoir stimulation, many issues still remain to be addressed and are worth of further in-depth scientific investigations. The author proposes following questions, which could be the topics for the future work of this thesis:

(1) In engineering activities such as EGS stimulation or wastewater disposal, is there a model that can constrain the probable maximum event of induced earthquake if given the injection rate? What's the maximum range of permeability evolution under such extreme conditions?

(2) For geological sequestration of CO_2, what is the influence of fluid-rock interaction on the mechanical properties of fracture material? What mechanical properties are they? Which property will be influenced most by the fluid-rock interaction?

(3) Experimental work in Chapter 3 to 5 has explored the friction-permeability relationship for natural fracture surface with low roughness, artificially consolidated fracture surface with low

roughness and artificially cases fracture surface with specified roughness. However this work is conducted under low confining stress (3 MPa). If the experimental apparatus is improvable, what are the results under high confining pressure? What are the effects of high temperatures?

(4) It is also worth mentioning that in the shear experiments of propped fractures, the distribution of proppant after shearing cannot be measured, thus crucial information on proppant clogging is missing. However, this can be solved by the imaging techniques such as xCT scanning.

Efforts to answer above questions would help us better understand the mechanism of induced seismicity and the corresponding hydraulic behavior of fractured reservoir, which would provide helpful insights into the geo-engineering practices.

Appendix

Evolution of Friction and Permeability in a Propped Fracture under Shear

Abstract

We explore the evolution of friction and permeability of a propped fracture using shearing-concurrent measurements of permeability during constant velocity shearing experiments. We separately examine the effects of normal stress (1 MPa, 3 MPa and 5 MPa), proppant thickness (mono-, double- and triple-layer), proppant size (40/80 mesh, 30/50 mesh and 20/40 mesh) and fracture wall texture (Green River shale and Westerly granite) on the frictional and transport response of proppant packs confined between planar fracture surfaces. The results indicate that proppant-absent and proppant-filled fractures show different frictional strength, implying that proppants could change the friction of natural fractures and influence the potential for shear failure. For fractures with proppants, we observe that (1) the frictional response is mainly controlled by the normal stress and proppant thickness. High normal stress results in the crushing of proppant particles although this change in particle size distribution has almost no impact on the frictional response of the proppant-fracture system. The depth of shearing-concurrent striations on fracture surfaces suggests that the magnitude of proppant embedment is controlled by the applied normal stress. Moreover, under high normal stress, the reduced friction implies that shear slip is more likely to occur on propped fractures in deeper reservoirs. The increase in the number of proppant layers, from mono-layer to triple-layers, significantly increases the friction of the propped fracture due to the inter-locking of the particles and jamming, suggesting that high proppant density during emplacement would help stabilize the fractures during injection. (2) Permeability of the propped fracture is mainly controlled by the

magnitude of the normal stress, the proppant thickness and the proppant size. Permeability of the propped fracture decreases during shearing due to proppant particle crushing and related clogging. Compared to the multi-layered specimen, the mono-layer case which has fewer displacement degrees-of-freedom exhibits the smallest initial permeability due to proppant embedment. Proppants are prone to crushing if the shear loading evolves concurrently with the normal loading. These combined conclusions suggest that the use of high-density proppants not only provides high hydraulic conductivity for hydrocarbon production but may also help to mitigate the risk of induced seismicity.

Key words: Friction; Permeability; Propped fracture; Shearing; Proppant embedment; Proppant Crushing

1. Introduction

Hydraulic fracturing has been a major well stimulation technique since the 1940s (Economides and Nolte 2000). The process involves the injection of fracturing fluid into a targeted reservoir layer through a wellbore. The high pressure fluid drives the propagation of hydraulic fractures with proppant particles carried with the penetrating fluid along the fracture and into the reservoir formation (Detournay 2016). Following the injection phase, the fracturing fluid flows back into the wellbore and the created hydraulic fractures will compact due to the release of fluid pressure. The proppant particles however hold the hydraulic fractures open, allowing the propped fractures to act as highly permeable flow paths for the extraction of hydrocarbons.

Over the past decade, massive hydraulic fracturing has been broadly applied for the extraction of tight gas, shale gas and other unconventional resources (King 2010). This broad

application of horizontal drilling and stimulation, with multiple horizontal wells per pad, multiple fracturing stages per well, and multiple clusters per stage has resulted in the successful recovery of hydrocarbons from ultra-low permeability reservoirs. These include the recovery of unconventional resource from shales and tight sandstones (International Energy Agency 2014). Hydraulic fracturing in unconventional reservoirs can be significantly different from the hydraulic fracturing of conventional reservoirs. This is due to the presence of pre-existing natural fractures or weak planes in the formation that may significantly affect the propagation of the fluid driven fractures. Based on various theories of conventional hydraulic fracturing, a bi-wing type fracture is typically assumed to result from the stimulation of a vertical well (Perkins and Kern 1961). However, based upon field production data, as well as microseismic observations, it is believed that so-called "fracture complexity" may result from interactions between the created hydraulic fracture and pre-existing natural fractures. This is especially prevalent in unconventional reservoirs where the contrast in permeabilities between matrix and natural fracture are very high (Warpinski 2009; Maxwell and Cipolla 2011; Maxwell 2014). When a propagating hydraulic fracture intersects a natural fracture, multiple scenarios for the form of the crossing are possible. These include direct crossing, hydraulic fracturing arrested by the natural fracture, crossing with an offset, or even more complicated scenarios when the third dimension is considered (Blanton 1982; Thiercelin et al. 1987; Warpinski and Teufel 1987; Renshaw and Pollard 1995; Zhang et al. 2007, 2017; Dahi-Taleghani and Olson 2011; Fu et al. 2013). Therefore, fracture branching and the development of complex fracture networks are generally created during multistage hydraulic fracturing (**Figure A-1a**) with implications for the state of stress applied on such oblique fractures.

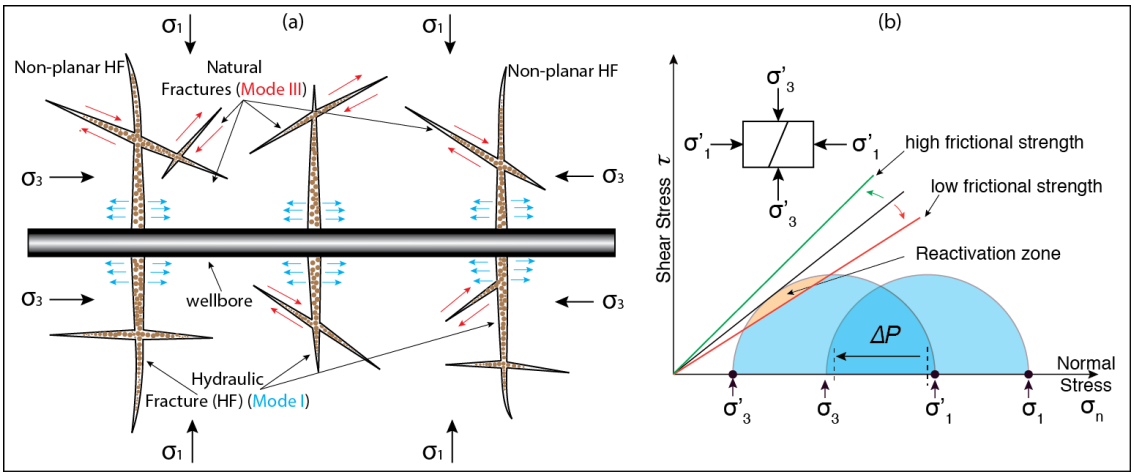

Figure **A-1**: (a) Schematic of complex fracturing system filled with proppant after multistage hydraulic fracturing; (b) Mohr-Coulomb criterion for determining whether a pre-existing fracture would be sheared after a combined effect of local stress reorientation and frictional alteration.

Significant effort has been applied to understand mechanisms involved in creating hydraulic fracture networks in unconventional reservoirs (Weng 2015). However, less attention has been given to understand the role of shear deformation (*e.g.*, induced seismicity by hydroshearing) and permeability evolution of the complex fracture system that may evolve during long-term depletion. Injection-induced seismicity has been associated with both the operation of waste water reinjection (Keranen et al. 2014) and due to hydraulic fracturing (Bao and Eaton 2016). Nevertheless, whether induced seismicity can occur during long-term depletion of unconventional fractured reservoirs is of significant scientific interest but remains poorly understood. In the usual conceptual model of conventional hydraulic fracturing, the created fracture plane is perpendicular to the minimum stress direction – thus, there is no shear stress on the fracture as it propagates and before the depletion stage of reservoir production. Post-stimulation, additional shear stresses induced during the depletion process should also be negligible for simple fracture geometry. Once depletion begins, considering the Mohr-Coulomb failure criterion, the gradual decrease in pore pressure will increase the effective clamping stress on the fracture plane (Biot coefficient < 1) and further stabilize the fracture planes (Biot 1956).

Therefore, it can be concluded that the expectation of induced seismicity during conventional hydraulic fracturing is trivial.

However, for unconventional reservoirs, induced seismicity may result due to the more complex and oblique fracturing geometry. First, the hydraulic fracture planes are not necessary aligned with the maximum horizontal stress, due to the presence of pre-existing natural fractures and related fracture complexity. Second, non-uniform depletion due to heterogeneous permeability fields can cause stress reorientation and additional shear stress on the fracture planes due to poroelastic effects (Segall and Fitzgerald 1998; Roussel and Sharma 2012). Third, some field operations, such as the failure of diversion during re-fracturing and undesired well connection when fracturing a new well (*i.e.*, cross-well communication or frac-hit) can lead to fluid leakage into the pre-existing hydraulic fractures which have been under depletion and result in additional slip on pre-existing fractures (Sardinha et al. 2015). Fourth, re-injecting fluid into wells under depletion has been implemented in the field to boost the production under some circumstances, *e.g.*, if there is a sharp decline of production, or delineated depleted zone around the producing well (Dohmen et al. 2017). Finally, numerous experimental studies show that the interaction between propagating hydraulic fractures and pre-existing natural fractures is significantly influenced by differential stress and fracture orientation and frictional strength (Blanton 1982; Renshaw and Pollard 1995). As the frictional strength of propped fractures in the first fracturing phase may be altered, it may significantly influence the behavior of fracture propagation in the later re-fracturing phase. These circumstances make the potential for induced seismicity finite for unconventional resource recovery. Induced seismicity typically results from the shear reactivation of a pre-existing fracture, which, in turn, is governed by frictional behavior of the fracture surface contact (Fang et al. 2017). Moreover, for both conventional and unconventional hydraulic fracturing, the main purpose is to create propped fractures and to increase the permeability of the formation. Thus the evolution of permeability of the propped

fractures is the key parameter that ultimately affects well production. In the course of production, the permeability of propped hydraulic fractures are expected to decrease due to the impacts of proppant embedment and crushing, concomitant with the gradual increase in the effective clamping stress. However, detailed coupling mechanisms involved in shearing and permeability evolution for propped fractures remains unclear. In this study, we explore the first- and second-order frictional and fluid transport response of propped fractures as the fundamental controlling parameters involved in the reactivation of pre-existing fractures (**Figure A-1b**). This experimental and analytical work reveals the co-evolution of permeability with friction of a propped fracture under shear.

2. Experimental methods

We explore the evolution of friction and permeability on propped fractures. We first present the procedure of sample preparation for the experiments. Then, we introduce the experimental setup and testing procedure implemented to explore the evolution of permeability and friction of a propped fracture under shearing. Finally, theories and methods to calculate the evolution of friction and permeability are discussed.

2.1 Sample preparation

The experiments are completed on Green River shale (GRS) as an appropriate analog of a shale reservoir. To provide a contrast in rock texture, Westerly granite (WG) was also used as a reference, because it has been extensively studied and is well suited for comparison due to its homogeneous and isotropic structure. The mineralogical compositions and mechanical properties of GRS and WG are listed in **Table 3-1**. The rock samples were first cored to a length of 2 inches

and diameter of 1 inch and then carefully saw cut into two halves, representing a parallel plate model (**Figure A-2**). The planar surfaces were uniformly polished with abrasive powder (#60 Grit carbide) to provide consistent surface roughness for all fracture analogues. To prevent the dislocation of proppant particles during the process of sample reassembly, a very thin layer of washable glue was placed on the fracture surfaces to temporarily fix the proppant particles. The proppant particles were uniformly and tightly placed on the surface of the fractures, forming a monolayer. To evaluate the effect of proppant thickness, samples with double and triple layers of proppants were also assembled and tested. The reassembled split samples, with proppants embedded, were packed within a latex membrane with an initial offset of 8 mm to accommodate the shear offset applied during shearing. To reduce the friction between the outer wall of the sample and the membrane, we used Teflon tape to cover the outer wall of the sample, through which the extra friction by the system can be significantly reduced.

Three typical proppant sizes, *i.e.*, 40/80 mesh (180 ~ 425 μm), 30/50 mesh (300 ~ 600 μm) and 20/40 mesh (420 ~ 840 μm), were used in the experiments of this study. The proppant size is often referred to as the sieve cut and is typically in the range between 8 and 140 mesh (105 μm ~ 2.38 mm). The exact distributions of proppant grain size in this experiment are shown in **Figure A-3**. The 40/80 mesh was used as a baseline for the purpose of comparison, while the 30/50 mesh and 20/40 mesh was utilized to study the effect of proppant size.

Table **A-1**: Mineralogical and mechanical properties of GRS and WG

Mineral Group	**Green River Shale**	**Westerly Granite**
Carbonates (%)	51.8	0
Tectosilicates (%)	45.9	5
Phyllosilicates (%)	2.3	95
Reference	(Fang et al., 2017)	(Stesky et al. 1974)

Mechanical Property	**Green River Shale**	**Westerly Granite**
Young's Modulus (GPa)	3.2-3.8	76
Poisson Ratio	0.345-0.365	0.27
Reference	(Yildirim 2014)	(Karner and Marone 2001)

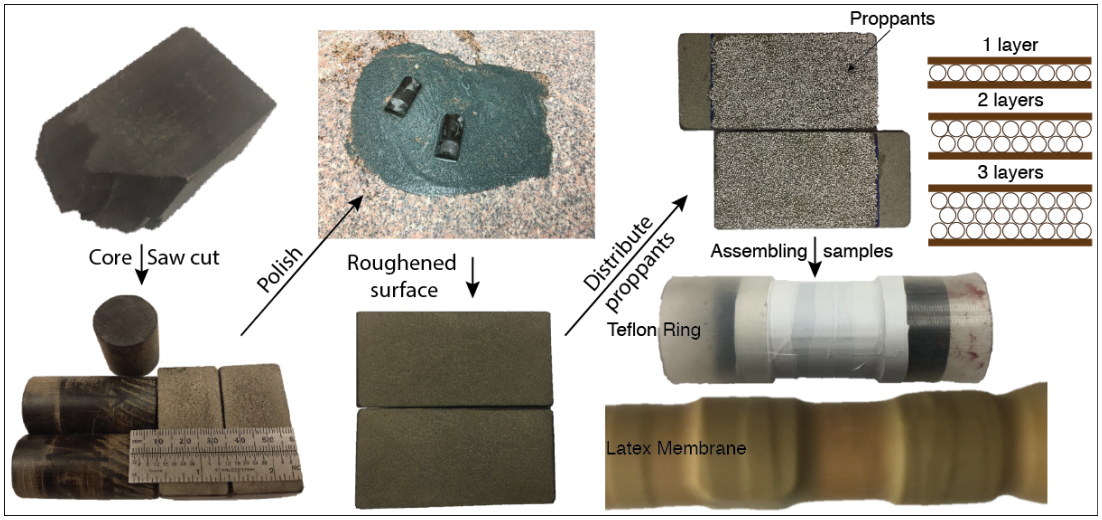

Figure **A-2**: Procedures of sample preparation

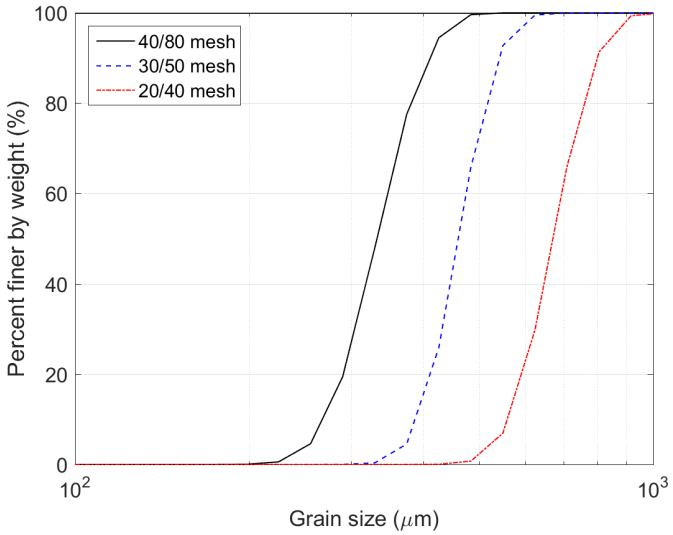

Figure **A-3**: Grain size distributions of the three types of proppant used in the experiments

2.2 Experimental setup and testing procedure

The experiments were performed in a triaxial testing apparatus that is able to independently apply confining pressure, pore pressure, and shear displacement at prescribed (constant) velocity. The evolution of fracture permeability during the experiments can also be concurrently monitored (**Figure A-4a**). The packed sample was then assembled in the cylindrical vessel. The confining stress (normal stress in this configuration) was gradually applied until the desired magnitude was reached. With the desired normal stress applied, deionized water was circulated through the fracture with a constant upstream pressure for 5 mins to dissolve and remove the glue that was used to fix the proppant during sample assembly. Once a steady flow rate was attained, monotonic shearing at constant velocity was applied. The shear velocity was controlled at 3 μm/s and the shearing was stopped after a displacement of 6 mm was reached. All experiments were performed at room temperature. The shear displacement was recorded by LVDT installed at the end of the displacing piston. Pre- and post-experiment, samples were characterized by white light optical profilometry to observe the possible interaction (*e.g.*,

embedment or striations) between proppant particles and the shale surface due to shearing. White light profilometry was performed using a Zygo NewView 7300 profilometer with a 10X objective lens with data processed with Mx^{TM} software (**Figure A-4b**). Furthermore, to examine the shear-induced damage or crushing of proppants, the proppant particles were scanned and sized both pre- and post-experiment by a laser particle size analyzer.

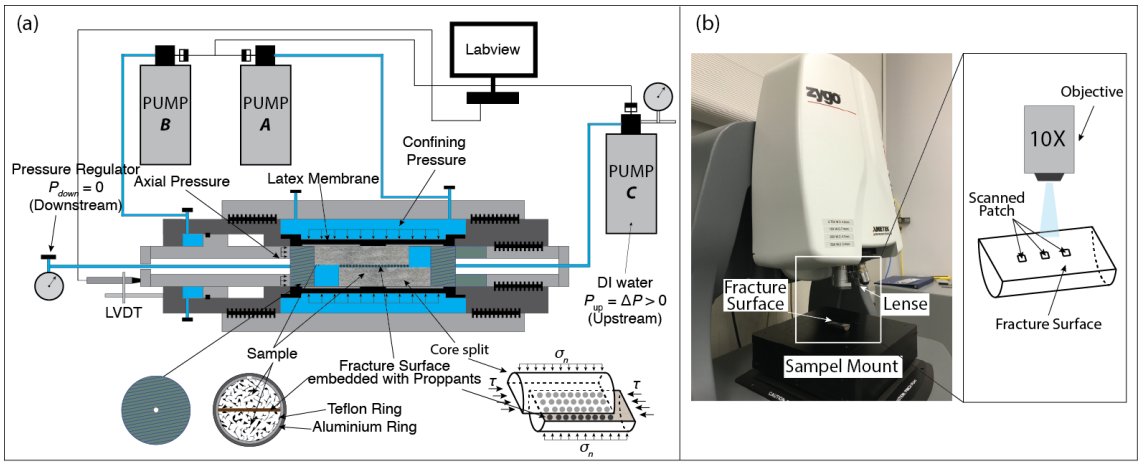

Figure **A-4**: (a) Schematic of experimental arrangement for the measurement of evolution of permeability-friction. Pump A controls the confining pressure (normal stress) applied across the fracture. Pump B controls pressure that provides the source of shear stress applied to the fracture. Pump C injects the fluid at a prescribed flow rate or pressure, allowing the fluid source located at the origin of the fracture to flow along the fractures. (b) 3D optical surface profiler for characterizing statistical roughness of the fracture surface. The fracture surface is located ready for white light interferometric scanning

2.3 Friction and permeability calculation

We calculated the coefficient of friction μ as a function of shear displacement using the ratio of measured shear stress to applied normal stress as $\mu = \tau/\sigma_n$, and ignoring cohesion. A parallel plate model for the cubic law is typically employed to describe fluid flow within a fracture (Witherspoon et al. 1980), however, as the proppant layers inside the fracture increases, the pattern of fluid flow experiences a transition from parallel plate flow to porous medium flow (Slichter, 1899; Kozeny, 1927; Carman, 1937; Li, 2017) (**Figure A-5**). In the direct-shear

experiment, the proppant particles may dislocate, deform and even break in shearing. Nevertheless, we define an equivalent hydraulic permeability k_f based on Darcy's law as,

$$k_f = \frac{Q(t)\mu_{vis}L(t)}{W b_e}$$

where μ_{vis} (Pa·s) is the viscosity of fluid; $L(t)$ (m) is the contact length of the fracture surface; W (m) is the fracture width; Q(t) (m^3/s) is the measured flow rate and ΔP_f (Pa) is the differential pressure between the upstream and downstream extent of the fracture.

The permeability of a porous medium can be estimated based on the Kozeny-Carman equation (Bear 1972) as,

$$k = \frac{1}{180}\frac{\epsilon^3}{(1-\epsilon)^2}{d_p}^2$$

The permeability is then related to the porosity of the packed bed ϵ and the particle diameter d_p.

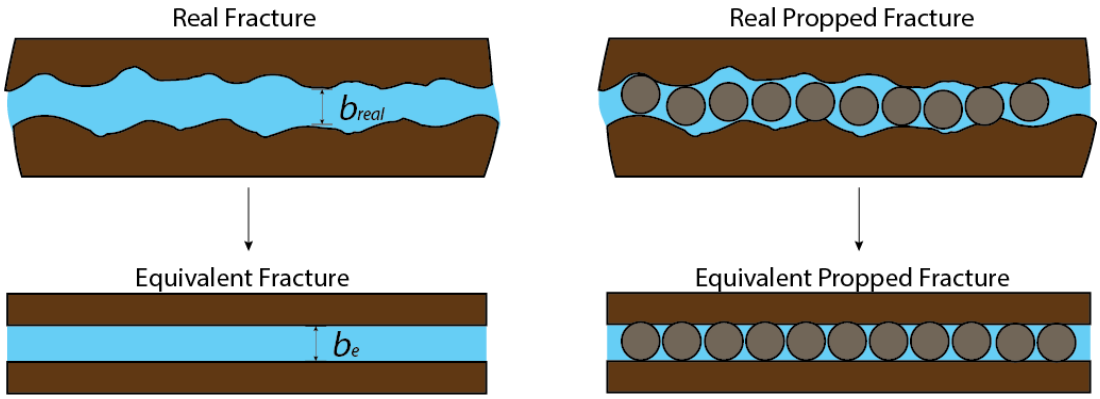

Figure **A-5**: Simplified fracture models with parallel plate flow and porous medium flow

3. Experimental results

In this section, the results are presented to highlight key experimental observations related to the effects of normal stress, proppant thickness, proppant size and rock texture on the friction-permeability relationships of propped fractures.

3.1 Effect of normal stress

Figure A-6a to **A-6c** show the evolution of permeability, normalized permeability and friction for the propped fracture during shearing under different normal stress, *i.e.*, 1 MPa, 3 MPa and 5 MPa, respectively. A mono-layer of proppant is present in all three cases with a corresponding proppant size in the range 0.18 mm to 0.425 mm (40/80 mesh). The total shear displacement is 5 mm. As expected, the initial permeability before shearing decreases with an increase in normal stress due to the combined influence of reduced porosity and fracture closure (**Figure A-6a**). Permeability gradually declines during the shearing for all three cases. The normalized permeability indicates that the reduction in permeability is most profound for the case with the highest normal stress. At the end of loading, the permeability for the three cases decreases to be ~70%, 40% and 20% of the initial values. A plausible mechanism for explaining this phenomenon is that the proppants crush the most during shearing for the case with the highest normal stress, which causes the largest relative decrease in apparent fracture aperture. Particle crushing is apparent from the grain size distributions collected pre- and post-shearing shown in Figure A-6d, where the particle damage increases with normal stress, inferring its influence on permeability evolution. Note that for the case of 1 MPa normal stress, there is nearly no change in the grain size distribution before and after testing (*i.e.*, no crushing of particles during shearing). Thus the grain size distribution of the initial proppant packing is not shown in the plot.

The frictional resistance of the propped fracture in Figure A-6c also displays a dependence on the normal stress. The coefficient of friction decreases as the normal stress increases, which is consistent with friction-normal stress relationships from previous experimental studies on simulated gouge (Mair and Marone 1999; Fang et al. 2016). The reduction in frictional strength may be attributed to two possible causes. First, at higher normal stresses, the normalized membrane restraint between the sample surface and the membrane is

reduced. As the normal stress increases, the coefficient of friction converges to the actual value representing the contact behavior between proppant particles and the fracture surface. Second, higher normal stress will compact the proppant particles and result in the crushing and embedment of proppants, which changes the contact response at the interface between proppant particles and fracture surfaces. **Figure A-7** explicitly compares the topography of the fracture surfaces both pre- and post-slip and for different normal stresses. Each experiment is performed with a virgin fracture. A notable feature is that there are an increasing number of post-shearing striations on the fracture surface as the normal stress increases. These striations result from the embedment of proppant particles into the fracture surface with grooving owing to the shear loading. To further characterize the striations, the fracture surfaces were scanned with white light profilometry. **Figure A-8** compares the profiles of fracture surfaces both before and after shearing for the case of 5 MPa normal stress. The dark channel represents a striation with a depth of about 100 μm. As the normal stress increases, the frictional behavior then gradually transits from being governed by the sliding of particles along the fracture surface to along the surface of striations. Since the surface of the striation is less rough than the initial fracture surface, the friction may decrease for the highest normal stress as shown in **Figure A-6c**.

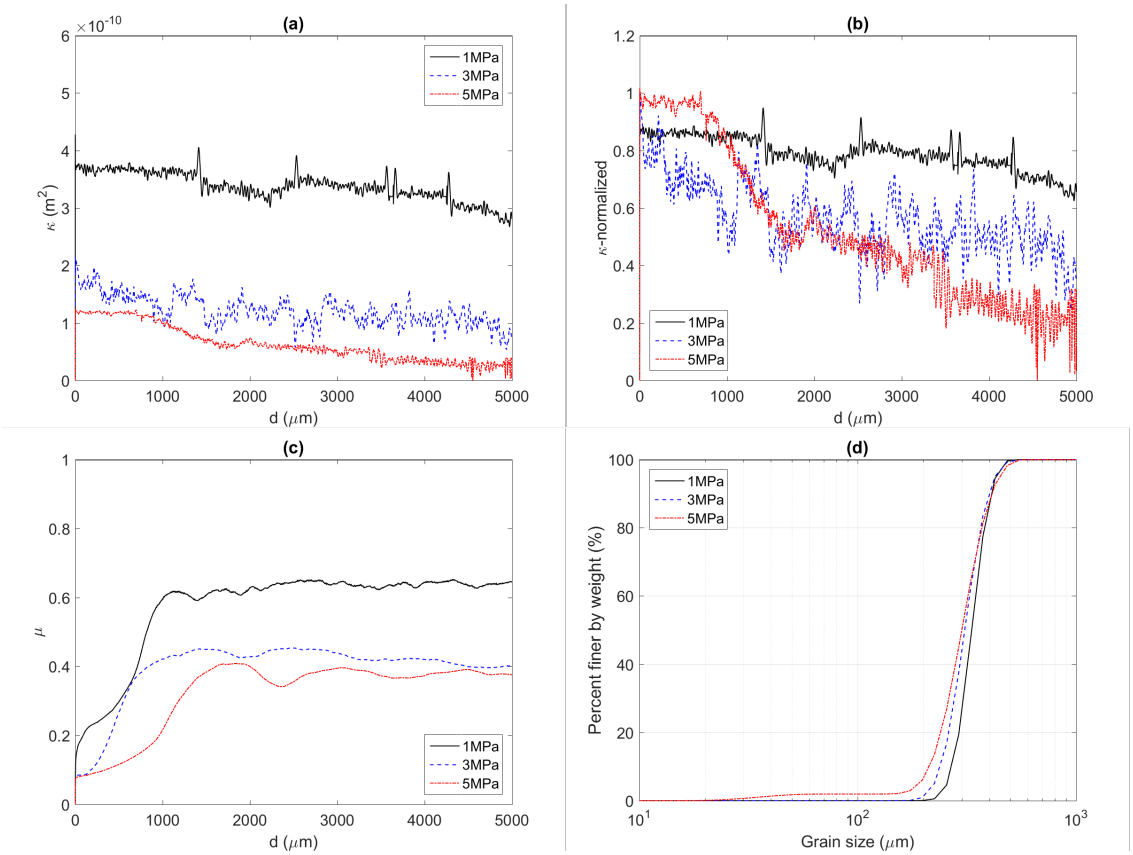

Figure **A-6**: Evolution of (a) permeability, (b) normalized permeability (with respect to the initial permeability value), and (c) friction for the propped fracture during shearing under three different normal stresses of, 1 MPa, 3 MPa and 5 MPa with displacement; (d) particle size distributions of proppants post-experiments – at 1 MPa, grain size distribution before and after testing does not change much, thus the distribution at 1 MPa is representative of the virgin particle distribution (i.e., 40/80 mesh).

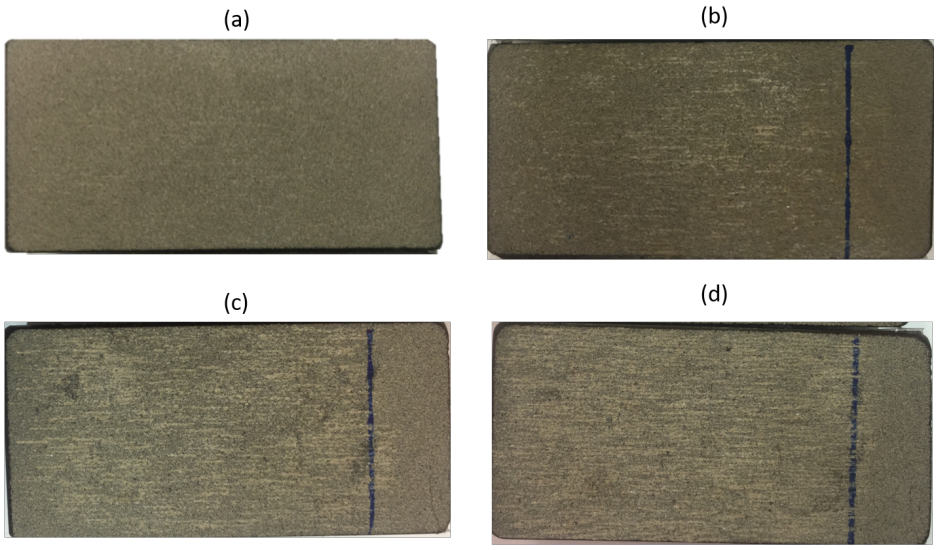

Figure **A-7**: (a) Fracture surface before shearing, (b) fracture surface after shearing at a normal stress of 1 MPa, (c) fracture surface after shearing at a normal stress of 3 MPa, and (d) fracture surface after shearing at a normal stress of 5 MPa. The number of striations increases as the normal stress increases.

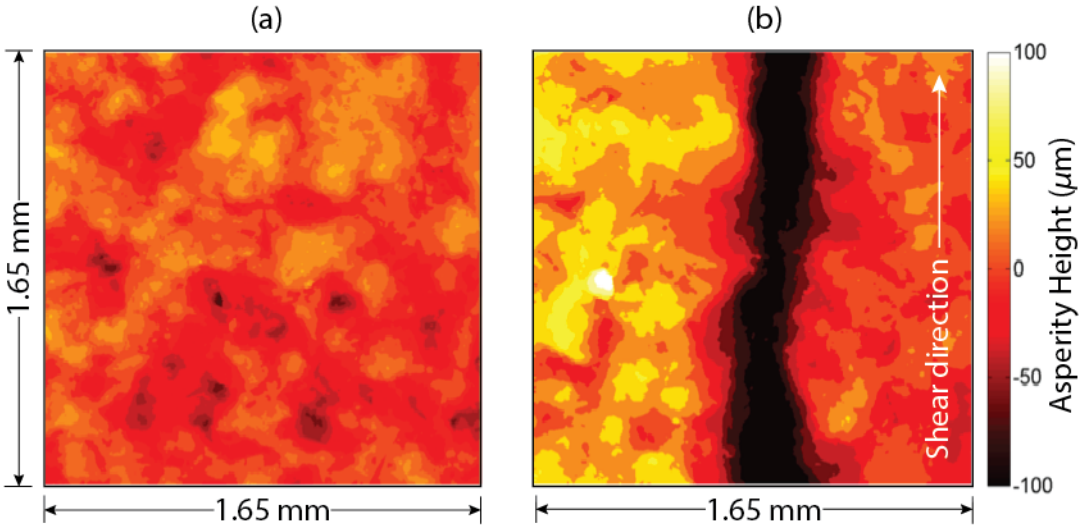

Figure **A-8**: White light profilometry of fracture surface (a) before shearing (Figure A-7a) and (b) after shearing at 5 MPa normal stress (Figure A-7d). The dark channel represents a striation with a depth of ~100 μm.

3.2 Effect of proppant thickness

Figure A-9 presents the evolution of permeability, normalized permeability and friction during shearing for different proppant thickness as influenced by the number of proppant layers. Four cases are represented, showing the behavior for bare surfaces (*i.e.*, no proppants embedded), and with mono-, double- and triple-layers of proppant. The normal stress for all four cases is 3 MPa and the proppant size is 40/80 mesh. For idealized close-packing of mono-sized particles filled between two parallel plates, the mono-layer structure has the largest porosity (0.3954) while the porosity approaches the minimum magnitude (0.2595) as the number of layers increase and the aggregate conforms to a face-centered cubic (FCC) structure (Figure A-10). From this rationale, and with mono-disperse particle sizes, the permeability for a mono-layer of proppant is expected to be the largest among all the cases. However, **Figure A-9a** shows that the initial permeability of a mono-layer of proppant is actually smaller than that for double and triple layers. This may be attributed to the permeability decrease due to proppant embedment where the case with a mono-layer of proppant is affected the most. In the case of a mono-layer, the fewer displacement degrees-of-freedom offered where the proppant is sandwiched between rigid faces, rather than compacting to the interior, results in a greater embedment.

Permeability gradually decreases during shearing for all four cases, however the mechanisms of permeability reduction between bare surfaces and proppant embedded surfaces are different. For the bare surfaces, the permeability decreases due to the generated wear products (Fang et al., 2017), while for proppant embedded fractures, the permeability is reduced due to proppant crushing, embedment, and clogging during shearing. Furthermore, the normalized permeabilities indicate that the relative decrease in permeability increases as the proppant thickness decreases. The case without proppants has the largest permeability drop (*i*.e., more than 80%), while the case with a triple-layer of proppants has less than a 20% decrease in

permeability. The grain size distributions of proppants, both before and after the experiments (Figure A-9d), indicate that the case with double-layer of proppants suffers the most profound crushing of the proppant. However, the reason why the double-layer of proppants has the most particle crushing (relative to both single- and triple-layers) is not yet clear.

The friction of the propped fracture for these three cases with proppants shows a clear trend that more proppant layers result in an increase in frictional strength. This is possibly due to the increase in inter-locking forces and jamming between particles when multiple proppant layers are present during shearing. The case without proppant exhibits a frictional strength similar to that of the case with a double-layer of proppants, but larger than the friction value for a mono-layer of proppants.

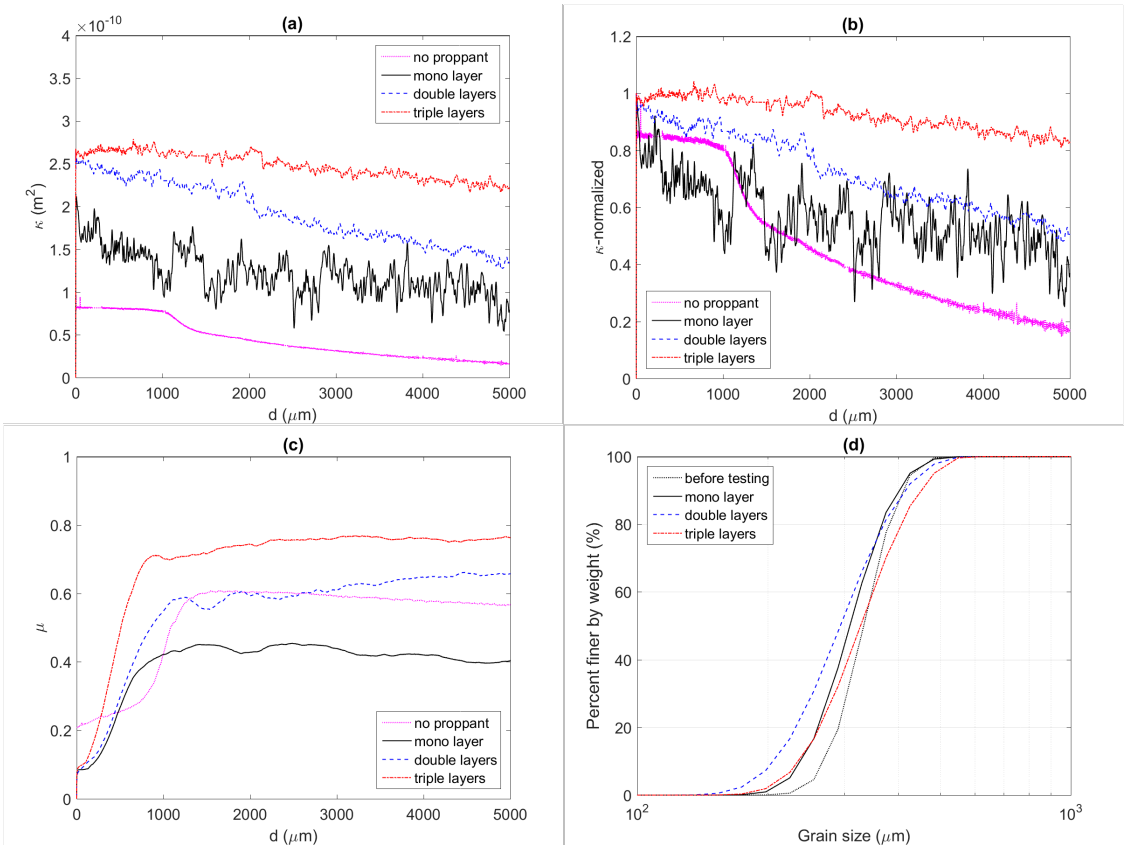

Figure **A-9**: Evolution of (a) permeability, (b) normalized permeability (with respect to the initial permeability value), and (c) friction for the propped fracture during shearing under different proppant thickness, no proppant, mono layer, double layers and triple layers with displacement; (d) grain size distributions of proppants before and after the experiments. The confining stress is 3 MPa and proppant size is 40/80 mesh for all cases.

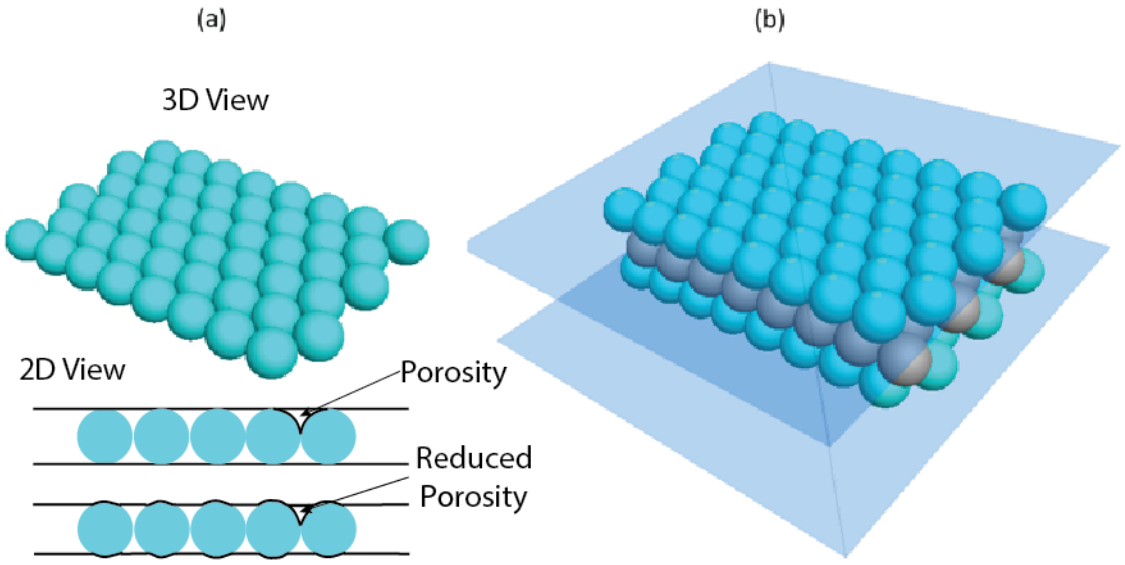

Figure **A-10**: Idealized close-packing of mono-sized particles as, (a) a mono-layer and (b) as multiple-layers (FCC structure)

3.3 Effect of proppant size

Figure A-11 shows the evolution of permeability, normalized permeability and friction for the propped fracture during shearing for the three different proppant sizes shown in Figure A-3. All three cases are for a mono-layer of proppant at a normal stress of 3 MPa. As expected, the initial permeability decreases as the proppant size decreases owing to the smaller initial apparent aperture and pore-throat size.

The normalized permeability for the 20/40 mesh proppant remains near constant during shearing, while that for the 30/50 mesh decreases by ~20% and that for the 40/80 mesh proppant decreases by ~50%. To explain why the smaller proppant is subject to a larger permeability drop during shearing, **Figure A-11d** plots the grain size distributions of the proppants both before and after the experiments for each proppant size. The smallest proppant size (40/80 mesh) shows significant particle crushing, however, particle crushing is not clearly identified with either the 30/50 mesh or 20/40 mesh proppants. While particle crushing could explain the severe

permeability drop during shearing for the case with 40/80 mesh, it may not resolve the paradox of permeability drop for the 30/50 mesh proppant. Another possible reason for the permeability drop, besides that of particle crushing, is the potential reorganization of particles during shearing and the possibility of particle clogging. Although not verified in the experiments, due to limitations of measurement, clogging is highly possible since the initial particle packing is relatively loose.

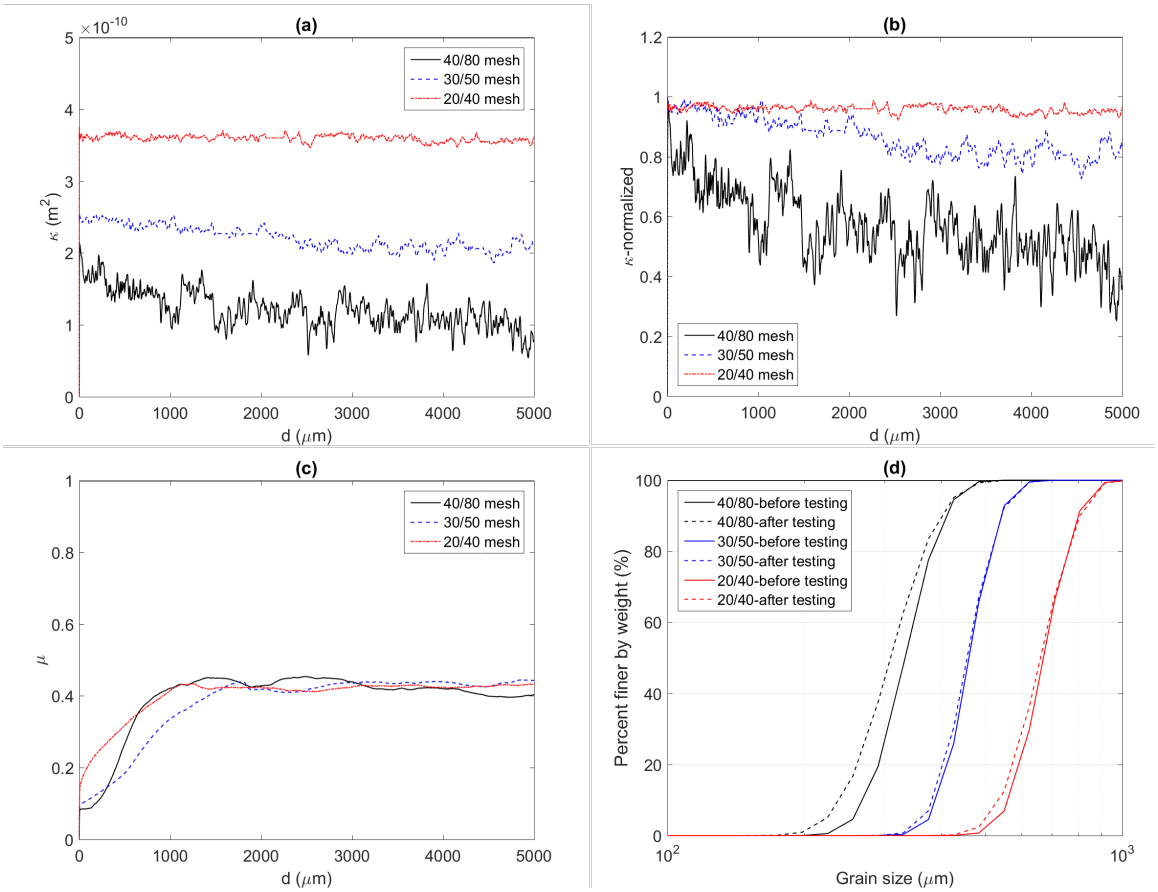

Figure **A-11**: Evolution of (a) permeability, (b) normalized permeability (with respect to the initial permeability value), and (c) friction for the propped fracture during shearing for three different proppant sizes, viz. 40/80 mesh, 30/50 mesh and 20/40 mesh with displacement; (d) particle size distributions of proppants both before and after shearing. The confining stress is 3 MPa for all cases.

The friction of the propped fracture for these three cases is nearly identical which suggests that, given the identical normal stress, though the proppant size varies, the contact state between the proppant surface and the fracture surface is equivalent in each case. The results

indicate that friction is mainly governed by the stress state as well as the degree of embedment between proppant particles and fracture surface.

3.4 Effect of rock texture

To investigate the effect of texture of the fracture surfaces and to eliminate the role of striation-formation on the response, the experiments were repeated with Westerly granite at 3 MPa normal stress and with a mono-layer of proppant (40/80 mesh). **Figure A-12a** to **A-12c** show the evolution of permeability, normalized permeability and friction during shearing for the two different rock textures. The case with granite has a slightly larger initial permeability than that with shale, although both cases show a decrease in permeability during shearing. Granite is stiffer and of higher strength than shale, therefore the proppant embedment is smaller than shale under the same normal stress. This may explain the higher initial permeability for the granite before shearing. The permeability for both granite and shale sandwiching-fractures converge to similar magnitudes at the end of shearing. The normalized permeability indicates that the decrease in permeability for granite is slightly larger than that for shale. This is because there is more particle crushing in the case with granite than with shale – as apparent in the post-experiment reduction in the particle size distribution for granite (**Figure A-12d**).

Friction of the propped fracture for granite is also slightly larger than that for shale, which could be attributed to the mineral-particle contact state (*i.e.*, proppant-quartz for WG and proppant-calcite for GRS) and the larger amount of generated small particles as a result of particle crushing.

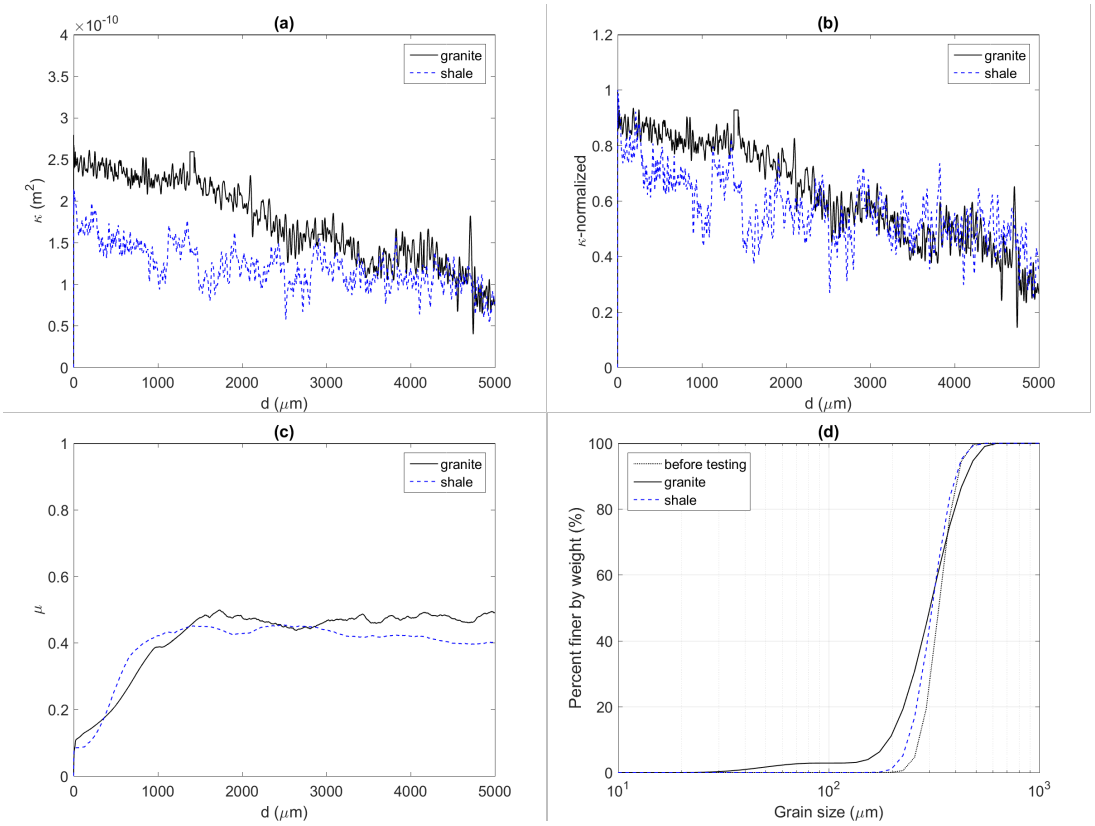

Figure **A-12**: Evolution of (a) permeability, (b) normalized permeability (with respect to the initial permeability value), and (c) friction for the propped fracture during shearing for two different sandwiching fracture rock types - shale and granite with displacement; (d) particle size distributions (PSD) of proppants both before and after the experiments. The confining stress is 3 MPa and the proppant size is 40/80 mesh for both cases.

4. Discussion

The experimental results show that the main factors controlling the frictional behavior of a propped fracture are the normal stress and proppant thickness. High normal stress results in the crushing of proppant particles, reducing the mean size of the proppant PSD (**Figure A-6d**). However, this change in size has only limited impact on the frictional response of the encasing fractures (**Figure A-10c**). Under high normal stress, the normalized membrane restraint between the sample surface and the membrane is reduced, implying that at higher normal stress this contributes proportionally less to the frictional resistance and yielding a strength closer to the real

strength of the assemblage. This strength is smaller than at lower stresses, due to the absence of the spurious shear restraint provided by the membrane. High normal stress also generates striations on the fracture surfaces during shearing, which allows a smoother contact between proppant particles and the fracture surface. As a result, the overall friction reduces as the normal stress increases. The proppant thickness also plays an important role in defining the friction of a propped fracture. Inter-locking of particles and jamming is not expected between proppant particles for the mono-layer proppant configuration. However, given the saw-cut fracture surface geometry, as the number of proppant layers increases from one to three, the inter-locking forces between particles largely increases the friction of the propped fracture. The effects of proppant size and rock texture on the friction of a propped fracture are secondary. In terms of the response of proppants in fractures, the friction of the fracture without proppant is significantly different from that with proppant (**Figure A-9c**). For a single layer propped fracture, the reduced friction implies that for re-fracturing in a propped fractured reservoir, the hydraulic fracture may be arrested by a propped fracture. It should be noted that the impact of fracture asperities on the friction of a propped fracture is ignored in this study. This particular fracture analogue comprises two flat surfaces with a uniform but minimal roughness (controlled by the PSD of the grinding powder), while in reality, the resulting fracture surfaces may have a considerably higher amplitude roughness.

The permeability of a propped fracture is mainly governed by the normal stress, the proppant thickness and the proppant size. The normal stress controls the amount of proppant embedment and thus the dilation of the fracture aperture during shearing. High normal stress not only causes the compaction of the fracture and of the proppant bed, but also leads to the crushing of proppant particles that accelerates the fracture closure. Compared to the multi-layered specimen, the mono-layer case exhibits the smallest initial permeability due to proppant embedment. Although a larger proppant size favors a higher initial permeability of the propped

fracture, the in-fracture transport of large diameter proppants during completion of slickwater fracturing is difficult - the issue of proppant size selection is beyond the scope of this study.

Except for the case with a mono-layer of 20/40 mesh proppant, the permeability of the propped fracture decreases during the shearing process for all other cases. The comminution-related decline in permeability during shearing dominates over the effect of shear-induced dilation for a fracture with flat surface geometry. However, it is not excluded that permeability enhancement by shear slip of a fracture with high surface roughness would dominate over the proppant-crushing induced permeability decline. Another unexpected conclusion drawn from this study is that significant proppant crushing occurs during shearing even at a normal stress of 5 MPa. Since proppants are typically designed to withstand normal stresses as high as 50 MPa, they become vulnerable if the shear loading evolves concurrently with the normal loading.

It is also worth mentioning that there are some limitations in the experiments. First, the direct observations of proppant crushing and embedment are not feasible while keeping specimens in an in-situ stress state. These results are indirectly reflected by the measurements of particle size and surface characteristics after the experiments. Second, the distribution of proppant after shearing cannot be measured, thus crucial information on proppant clogging is missing. The real time proppant clogging status may only be tested *via* the imaging techniques such as xCT scanning. Last, the normal stress applied by the apparatus is modulated by the strength of the aluminum ring (shown in **Figure A-4a**) used to protect the void left by the offset distance between the two fractures. To prevent radial deformation of aluminum ring, the highest normal stress applied in the experiments is required to less than 6 MPa. Although the normal stress in the experiments can be interpreted as the effective stress applied on the fracture wall, it is still lower than a typical magnitude in the field.

5. Conclusions

In this study, we explore the evolution of friction and permeability of a propped fracture using shearing-concurrent measurements of permeability during constant velocity shearing experiments. We separately examine the effects of normal stress (1 MPa, 3 MPa and 5 MPa), proppant thickness (mono-, double- and triple-layer), proppant size (40/80 mesh, 30/50 mesh and 20/40 mesh) and rock texture (Green River shale and Westerly granite) on the frictional and transport response of proppant packs confined between planar fracture surfaces. The results indicate that proppant-absent and proppant-filled fractures show different frictional strength, implying that proppants could change the friction of natural fractures and influence the potential for shear failure. For fractures with proppants, we observed that (1) the frictional response is mainly controlled by the normal stress and proppant thickness. High normal stress results in the crushing of proppant particles although this change in size has almost no impact on the frictional response of the proppant-fracture system. The observed post-shearing striations on fracture surfaces suggest that the magnitude of proppant embedment is controlled by the applied normal stress. Moreover, under high normal stress, the reduced friction implies that shear slip is more likely to occur for the propped fractures in deeper reservoirs. With this simple specific fracture configuration (*i.e.*, saw-cut surface), the increase in the number of proppant layers, from mono-layer to triple-layers, significantly increases the friction of the propped fracture due to the inter-locking of the particles and jamming, suggesting that high proppant density during emplacement would help stabilize the fractures during injection. (2) Permeability of the propped fracture is mainly controlled by the magnitude of the normal stress, the proppant thickness and the proppant size. Permeability of the propped fracture decreases during shearing, which is plausibly due to proppant particle crushing and related clogging. Compared to the multi-layered specimen, the mono-layer case which has fewer displacement degrees-of-freedom exhibits the smallest initial

permeability due to proppant embedment. Proppants become prone to crushing if the shear loading evolves concurrently with the normal loading. Above combined conclusions suggest the use of high-density proppants in the field, which not only provides high hydraulic conductivity for hydro-carbon production, but also help to mitigate the risk of induced seismicity.

Acknowledgement

The authors acknowledge the support provided by the Young 1000 Talent Program of China, Tongji Civil Engineering Peak Discipline Plan (CEPDP), National Natural Science Foundation of China under grant 41772286 and 51674267, and U.S. Department of Energy (DOE) under grant DE-FE0023354. The useful discussions with Professor Chris Marone are also greatly appreciated.

References

Bao X, Eaton DW (2016) Fault activation by hydraulic fracturing in western Canada. Science (80-). doi: 10.1126/science.aag2583

Bear J (1972) Dynamics of Fluids in Porous Media. Soil Sci 120:162–163. doi: 10.1097/00010694-197508000-00022

Biot MA (1956) General solutions of the equations of elasticity and consolidation for a porous material. J Appl Mech 23:91–96.

Blanton TL (1982) An experimental study of interaction between hydraulically induced and pre-existing fractures. SPE Unconv. Gas Recover. Symp.

Dahi-Taleghani A, Olson JE (2011) Numerical modeling of multistranded-hydraulic-fracture propagation: accounting for the interaction between induced and natural fractures. SPE J. doi: 10.2118/124884-PA

Detournay E (2016) Mechanics of hydraulic fractures. Annu Rev Fluid Mech 48:311–339. doi: doi:10.1146/annurev-fluid-010814-014736

Dohmen T, Zhang J, Barker L, Blangy JP (2017) Microseismic magnitudes and b-Values for delineating hydraulic fracturing and depletion. SPE J. doi: https://doi.org/10.2118/186096-PA

Economides M, Nolte K (2000) Reservoir Stimulation, 3rd edn. Wiley

Fang Y, den Hartog SAM, Elsworth D, et al (2016) Anomalous distribution of microearthquakes in the Newberry Geothermal Reservoir: Mechanisms and implications. Geothermics 63:62–73. doi: http://dx.doi.org/10.1016/j.geothermics.2015.04.005

Fang Y, Elsworth D, Wang C, et al (2017) Frictional stability-permeability relationships for fractures in shales. J Geophys Res Solid Earth 122:1760–1776. doi: 10.1002/2016JB013435

Fu P, Johnson SM, Carrigan CR (2013) An explicitly coupled hydro-geomechanical model for simulating hydraulic fracturing in arbitrary discrete fracture networks. Int J Numer Anal Methods Geomech 37:2278–2300. doi: 10.1002/nag.2135

International Energy Agency (2014) World energy outlook 2014. International Energy Agency

Karner SL, Marone C (2001) Frictional restrengthening in simulated fault gouge- Effect of shear load perturbations. J Geophys Res 106:19319–19337.

Keranen KM, Weingarten M, Abers GA, et al (2014) Sharp increase in central Oklahoma

seismicity since 2008 induced by massive wastewater injection. Science (80-) 345:448–451.

King GE (2010) Thirty Years of Gas Shale Fracturing: What Have We Learned? SPE Annu. Tech. Conf. Exhib.

Mair K, Marone C (1999) Friction of simulated fault gouge for a wide range of velocities and normal stresses. J Geophys Res Solid Earth 104:28899–28914. doi: 10.1029/1999JB900279

Maxwell S (2014) Microseismic imaging of hydraulic fracturing: improved engineering of unconventional shale reservoirs. Society of Exploration Geophysicists

Maxwell S, Cipolla C (2011) What does microseismicity tell us about hydraulic fracturing? SPE Annu. Tech. Conf. Exhib.

Perkins TK, Kern LR (1961) Widths of hydraulic fractures. J Pet Technol. doi: 10.2118/89-PA

Renshaw CE, Pollard DD (1995) An experimentally verified criterion for propagation across unbounded frictional interfaces in brittle, linear elastic materials. Int J Rock Mech Min Sci Geomech Abstr 32:237–249. doi: http://dx.doi.org/10.1016/0148-9062(94)00037-4

Roussel NP, Sharma MM (2012) Role of stress reorientation in the success of refracture treatments in tight gas sands. SPE Prod Oper 27:346–355.

Sardinha C, Petr C, Lehmann J, et al (2015) Determining interwell connectivity and reservoir complexity through fracturing pressure hits and production-interference analysis. In: Journal of Canadian Petroleum Technology. pp 88–91

Segall P, Fitzgerald SD (1998) A note on induced stress changes in hydrocarbon and geothermal reservoirs. Tectonophysics 289:117–128.

Stesky RM, Brace WF, Riley DK, Robin PYF (1974) Friction in faulted rock at high temperature and pressure. Tectonophysics 23:177–203. doi: 10.1016/0040-1951(74)90119-X

Thiercelin MJ, Roegiers JC, Boone TJ, Ingraffea AR (1987) An investigation of the material parameters that govern the behavior of fractures approaching rock interfaces. In: 6th International Congress of Rock Mechanics. International Society for Rock Mechanics,

Warpinski N (2009) Microseismic monitoring: inside and out. J Pet Technol. doi: 10.2118/118537-JPT

Warpinski NR, Teufel LW (1987) Influence of geologic discontinuities on hydraulic fracture propagation . J Pet Technol. doi: 10.2118/13224-PA

Weng X (2015) Modeling of complex hydraulic fractures in naturally fractured formation. J Unconv Oil Gas Resour 9:114–135. doi: http://dx.doi.org/10.1016/j.juogr.2014.07.001

Witherspoon PA, Wang JSY, Iwai K, Gale JE (1980) Validity of Cubic Law for fluid flow in a deformable rock fracture. Water Resour Res 16:1016–1024. doi: 10.1029/WR016i006p01016

Yildirim LTO (2014) Evaluation Of Petrophysical Properties Of Gas Shale And Their Change Due To Interaction With Water, MS Thesis, The Pennsylvania State University.

Zhang F, Dontsov E, Mack MG (2017) Fully coupled simulation of a hydraulic fracture interacting with natural fractures with a hybrid discrete□continuum method. Int J Numer Anal Methods Geomech. doi: 10.1002/nag.2682

Zhang X, Jeffrey RG, Thiercelin M (2007) Deflection and propagation of fluid-driven fractures at frictional bedding interfaces: A numerical investigation. J Struct Geol 29:396–410. doi: http://dx.doi.org/10.1016/j.jsg.2006.09.013

CURRICULUM VITA

YI FANG

Department of Energy & Mineral Engineering
Address: 230A Hosler Building, University Park, PA, 16802
Email: yi.fang@psu.edu

EDUCATION

2013 – 2017 Ph.D. in Energy and Mineral Engineering, Pennsylvania State University, USA
2011 – 2013 M.S. in Geology, California State University, Long Beach, USA
2007 – 2011 B.E. in Civil Engineering, China University of Geoscience, Wuhan, China

RESEARCH EXPERIENCE

2016 & 2017 Aramco Services Company (Houston Research Center): Summer Graduate Intern
2013 – 2017 Penn State G3 Center and Energy Institute: Research Assistant
2011 – 2013 Cal State Long Beach Stable Isotope Geochemistry Lab: Research Assistant

TEACHING EXPERIENCE

2017 Spring Penn State: Production Process Engineering (PNG480): TA
2017 Spring Penn State: Petroleum Engineering Design (PNG475): TA
2016 Spring Penn State: Computational Reservoir Geomechanics (EGEE520): TA
2015 Spring Penn State: Contaminant Hydrogeology (EnvSE408): Co-Instructor
2013 Spring Cal State, Long Beach: Physical Geology (GEOL102): Instructor

PUBLICATIONS

Peer-Reviewed Journal Articles (1st author or *corresponding author)

1. **Fang, Y***., S.M. den Hartog, D. Elsworth, C. Marone, and T.T. Cladouhos. 2016. Anomalous Distribution of MEQs in Geothermal Reservoir: Mechanisms and Implications. *Geothermics*. Vol. 63, p. 62-73.
2. **Fang, Y**., C. Wang, D. Elsworth*, and T. Ishibashi. 2017. Seismicity-permeability coupling in the behavior of gas shale, CO2 storage and deep geothermal energy. *Geomech. Geophys Geo-Energ Geo-Resour*. V. 3, No. 2, p. 189-198.
3. **Fang, Y***., D. Elsworth, C. Wang, T. Ishibashi, and J.P. Fitts. 2017. Frictional Stability-Permeability Relationships for Fractures in Shales. *J. Geophys. Res. Solid Earth*. V. 122, No. 3, p. 1760-1776.
4. **Fang, Y***., D. Elsworth, and T.T. Cladouhos. 2017. Reservoir permeability mapping using MEQ data. *Geothermics* (In Revision)
5. **Fang, Y***., D. Elsworth, C. Wang, and Y. Jia. 2017. Mineralogical controls on frictional strength, stability and shear permeability of fractures. (*Submitted to JGR*)
6. **Fang, Y***., D. Elsworth, T. Ishibashi, and F. Zhang. 2017. Investigation of permeability evolution and frictional behavior on fabricated fractures with specified roughness features. (*Submitted to JGR*)
7. Zhang, F., **Y. Fang***, D. Elsworth, C. Wang, and X. Yang. 2017. Evolution of friction and permeability in a propped fracture under shear. (*Submitted to Geofluids*)